

# Numerical Integrators for Physical Applications

## Dissertation

der Mathematisch-Naturwissenschaftlichen Fakultät  
der Eberhard-Karls-Universität Tübingen  
zur Erlangung des Grades eines  
Doktors der Naturwissenschaften  
(Dr. rer. nat)

vorgelegt von  
Dipl.-Phys. Jonathan Kurt Hermann Seyrich  
aus Tübingen

Tübingen  
2016

---

Veröffentlicht mit Genehmigung der Mathematisch-Naturwissenschaftlichen Fakultät der Eberhard Karls Universität Tübingen.

Tag der mündlichen Qualifikation: 13.06.2016

Dekan: Prof. Dr. Wolfgang Rosenstiel  
1. Berichterstatter: Prof. Dr. Christian Lubich  
2. Berichterstatter: Prof. Dr. Christian Hainzl

---

This thesis is based on the following papers (status as of June 2016):

- a) G. Lukes-Gerakopoulos, J. Seyrich, and D. Kunst. “Investigating spinning test particles: spin supplementary conditions and the Hamiltonian formalism.” *Phys. Rev. D* **90**, 104019 (2014).
- b) D. Kunst, T. Ledvinka, G. Lukes-Gerakopoulos, and J. Seyrich. “Comparing Hamiltonians of a spinning test particle for different tetrad fields.” *Phys. Rev. D* **93**, 044004 (2016).
- c) C. Hainzl and J. Seyrich. “Comparing the full time-dependent BCS equation to its linear approximation: A numerical investigation.” *Eur. Phys. J. B* **89** (5), 1-10 (2016).
- d) J. Seyrich. “Splitting integrators for the BCS equations of superconductivity.” To be submitted. Preprint: arXiv:1505.03417.

The author’s share of contribution to the above-mentioned papers was:

- a) 45 %.
- b) 20 %.
- c) 66 %.
- d) 100 %.

---

---

**To Elena,  
the most wonderful person on earth!**

---

# Zusammenfassung

Die vorliegende Dissertationsschrift bündelt Arbeiten zu zwei fundamentalen Theorien, welche die theoretische Physik bisher vergeblich zu vereinen sucht. Zum einen betrachten wir das Phänomen der Supraleitung auf dem Gebiet der ganz kleinen Teilchen, in grundlegendster Weise beschrieben durch die Theorie der Quantenmechanik. Zum anderen befassen wir uns mit Gravitationswellen, genauer gesagt mit diese erzeugenden Binärsystemen schwerer Himmelskörper. Die physikalische Beschreibung dieser Vorgänge basiert auf der Allgemeinen Relativitätstheorie der ganz großen Objekte. Aus unserer numerischen Perspektive sind die Probleme jedoch durchaus vereinbar, denn unser Ziel ist es jeweils, numerische Werkzeuge zu entwickeln, um fundamentale physikalische Vorgänge zu simulieren.

In Bezug auf die Binärsysteme schwerer Himmelskörper betrachten wir zwei verschiedene Bewegungsgleichungen zur Beschreibung der Evolution der Konstituenten. Zunächst wenden wir uns den Gleichungen von *Mathisson–Papapetrou* zu. Hierbei stehen wir vor der Herausforderung, dass die Bewegungsgleichungen zum Teil implizit sind. Nichtsdestotrotz ist es uns gelungen, basierend auf den sogenannten *Gauß–Runge–Kutta–Verfahren* einen äußerst effizienten und zudem genauen Integrator zu entwickeln, welcher insbesondere die Konstanten der Bewegung erhält. Anschließend möchten wir die Simulationsresultate der *Mathisson–Papapetrou–Gleichungen* mit einer Hamilton’schen Näherung vergleichen. Hierzu stellen wir, wieder auf Basis der Gauß–Runge–Kutta–Verfahren, einen Algorithmus zur Zeitintegration der Hamilton’schen Gleichungen vor. Auch dieser bleibt selbst für lange Integrationszeiten sehr nahe bei der exakten Lösung und schafft es, die Energie während der Simulation nahezu konstant zu halten. In einem nächsten Schritt untersuchen wir, inwieweit die Hamilton’sche Näherung physikalisch sinnvolle Ergebnisse produzieren kann. Mit Blick auf relevante Erhaltungsgrößen stellen wir fest, dass der Hamilton’schen Näherung in ihrer ursprünglich veröffentlichten Form physikalisch falsche Annahmen zugrunde liegen. Dies lieferte unseren Kooperationspartnern von Seiten der Theoretischen Physik den Anlass, nach einer verbesserten Näherung in Hamilton-Form zu forschen. Die dabei hervorgebrachten Verbesserungen untersuchen und verifizieren wir mit unseren numerischen Algorithmen. Die Hamilton’sche Struktur dieser physikalisch richtigen Näherungen eignet sich besonders zur Untersuchung der physikalischen Systeme mittels sogenannter *Surface-Sections*. Deshalb nutzen wir die Kollisionsseigenschaft der Gauß–Runge–Kutta–Integratoren aus, um ein effizientes und genaues Rechenverfahren zur Berechnung dieser Sections zu implementieren.

Im zweiten Teil der Arbeit befassen wir uns mit den *zeitabhängigen BCS–Gleichungen*. Dies sind gekoppelte partielle Differentialgleichungen zur mikroskopischen Beschreibung der Cooperpaardichte in einem supraleitenden Material. Ein in der Theoretischen Physik viel diskutierter Punkt ist die Frage, ob sich nahe der kritischen Temperatur nicht eine einfachere Gleichung zur Approximation der relevanten supraleitenden Vorgänge auf makroskopischer Skala finden ließe. Um dieser Frage nachzugehen, untersuchen wir in einer numerischen Studie das Verhalten der zeitabhängigen BCS–Gleichungen und einer linearen Approximation für Systeme mit Kontakt-Wechselwirkung. Hierbei betrachten wir den Sonderfall eines translationsinvarianten Systems. Wir entwickeln zwei numerische Lösungsverfahren basierend auf sogenannten *Splitting-Methoden*, d.h. wir unterteilen die Differentialgleichungen geschickt in mehrere Teilprobleme, welche sich jeweils bequem lösen lassen. Die Teillösungen kombinieren wir dann geeignet zu akkuraten Integrationsverfahren, deren Rechenaufwand lediglich linear mit der Anzahl der zur Raumdiskretisierung verwendeten Basisfunktionen ansteigt. Mithilfe der

---

*Schnellen Fourier Transformation (FFT)* können wir unsere Verfahren in natürlicher Weise auf Systeme mit allgemeinen Potentialen erweitern. Auch hier steigt der Rechenaufwand nur langsam mit der Anzahl der Basisfunktionen an.

Für den physikalisch wichtigen Fall von Systemen mit Kontakt-Wechselwirkung führen wir mit unseren entwickelten Werkzeugen umfangreiche Simulationen für verschiedene Werte der Temperatur nahe der kritischen Temperatur durch. Wir beobachten einen exponentiellen Abfall der Cooperpaardichte für die lineare Näherung, aber kontinuierliche Oszillationen der Cooperpaardichte um einen endlichen Wert im Falle der ursprünglichen Gleichung. Hieraus können wir schließen, dass die in bisherigen makroskopischen Theorien angenommene Diffusion des supraleitenden Parameters lediglich ein Artefakt einer ungerechtfertigten Linearisierung ist. Damit können wir nicht nur neue numerische Verfahren für wesentliche physikalische Bewegungsgleichungen präsentieren, sondern zudem noch einen wichtigen Beitrag zur noch immer angehenden Diskussion in der Physik leisten.

Um unsere Arbeit kurz zusammenzufassen: Es ist uns gelungen, auf zwei wichtigen Gebieten der Physik effiziente Werkzeuge zur Simulierung grundlegender Vorgänge zu entwickeln. Hiermit konnten wir unseren Kooperationspartnern wichtige Einblicke in die Eigenheiten der relevanten Bewegungsgleichungen ermöglichen und neue theoretische Betrachtungen anstoßen.

# Abstract

In this thesis, we report on our work in two very fundamental fields of physics which still have not been merged in a satisfactory way by a combining physical theory. One area is the field of very small particles, most accurately described by quantum mechanics. Here, we are interested in the phenomenon of superconductivity. The other area is that of the very heavy objects of our universe. Their most fundamental description is based on the theory of general relativity. Our particular interest lies in binary systems of compact objects rotating around each other, constantly radiating gravitational waves in the process. Although quantum mechanics and general relativity are worlds apart from a physical point of view, they inhibit some analogies when seen from our numerical perspective. For our aim is the same in both fields: We want to provide numerical tools for the simulations of interesting physical processes.

Regarding binary systems we want to compare two descriptions of their motion in space. The first is given by the *Mathisson–Papapetrou equations*. In order to study the evolution as given by these equations, we develop an efficient integration scheme based on Gauss Runge–Kutta methods. An intriguing challenge is given by the fact that part of the equations of motion have only be given implicitly. All obstacles notwithstanding, we present an efficient integrator which preserves the constants of motion even over long times. The second description of a binary’s motion is given by a Hamiltonian approximation of the Mathisson–Papapetrou equations. We want to study whether this prescription yields physically valid results. To this aim, we first come up with an efficient numerical evolution scheme, again recurring to Gauss Runge–Kutta integrators. Our scheme conserves the Hamiltonian structure, thus yielding reliable results for long time spans. Then, we test the Hamiltonian approach in different aspects. When studying the behavior of important constants of motion, we have found out that the Hamiltonian in its originally published form must be based on unphysical assumptions. This triggered new theoretical studies by our collaborators from physics with the aim of finding better suited alternatives. Their new results and suggestions are tested with the help of our algorithms. The –now physically reasonable– Hamiltonian descriptions are well-suited to investigate the binary systems for chaos with the help of *surface sections*. Hence, we take use of the collocation property of the Gauss Runge–Kutta schemes to present an accurate and convenient algorithm for the calculation of such sections.

In the realm of superconductivity, we consider the time-dependent BCS equations. These are quite involved partial differential equations describing the evolution of the Cooper pair density within a superconducting material or a superfluid. A very hot topic in the theoretical physics community concerns the question as to whether there exists, close to the critical temperature, a more convenient equation for a reliable approximation on a macroscopic scale. We take on this question from a numerical point of view. For this, we compare the evolution of a system with contact interaction given by the BCS equations to the one obtained via a linearized approximation by means of a thorough numerical study. We concentrate on a translation invariant system and develop two new numerical solvers based on so-called *splitting methods*. Splitting the coupled equations into more convenient subproblems and aptly combining the partial results, we come up with efficient and accurate schemes whose CPU times depend only linearly on the number of basis functions of the space discretization. With the help of the *Fast Fourier Transform (FFT)* algorithm, we can even extend our integrators to general potentials in a very natural way. In this case, too, the CPU effort grows only mildly as a function of the number of basis functions.

---

In the physically relevant case of a fermionic system interacting via a contact interaction, we employ our newly developed schemes to conduct numerous simulations for temperatures closer and closer to the critical one. From these simulations, we conclude that the linearization deviates far from the original equations. More precisely, the linear approximation leads to an exponential decay of the Cooper pair density whereas the full equations yield oscillations about a finite value. Consequently, the diffusion which is inherent to all hitherto existing macroscopic theories can only be an unphysical artifact. With this, we add an important fact to the still ongoing discussion in the physics community.

In short, we successfully developed convenient tools for the simulation of important physical phenomena in two fundamental fields of physics. This allowed our collaborators to gain valuable insights into the behavior of their equations of interest, thus contributing to the advance of fundamental science.

# Contents

<b>Zusammenfassung</b>	<b>7</b>
<b>Abstract</b>	<b>9</b>
<b>1. Introduction</b>	<b>15</b>
1.1. Introduction to relativistic binary systems . . . . .	15
1.1.1. Mathisson–Papapetrou equations . . . . .	16
1.1.2. Spin supplementary conditions . . . . .	18
1.1.3. Hamiltonian approximation . . . . .	19
1.2. Introduction to superconductivity . . . . .	20
1.2.1. Ginzburg–Landau equation . . . . .	21
1.2.2. Stationary BCS theory . . . . .	22
1.2.3. Superconductivity in BCS theory . . . . .	23
1.2.4. From microscopic to macroscopic scale . . . . .	23
1.2.5. Time-dependence . . . . .	24
1.2.6. The argument over a time-dependent Ginzburg–Landau equation . . .	25
<b>2. Objectives of this work</b>	<b>27</b>
2.1. Mathisson–Papapetrou equations and Hamiltonian approximation . . . . .	27
2.2. Time-dependent BCS equations and possible approximations . . . . .	28
2.3. List of the objectives . . . . .	29
<b>3. Summary of the results</b>	<b>31</b>
3.1. On the Mathisson–Papapetrou equations and their Hamiltonian approximations	31
3.1.1. Initial values for the Mathisson–Papapetrou equations . . . . .	32
3.1.2. Gauss Runge–Kutta methods . . . . .	34
3.1.3. Integrating the Mathisson–Papapetrou equations . . . . .	37
3.1.4. Symplectic structure of the Hamiltonian approximation . . . . .	39
3.1.5. Integrating the Hamiltonian equations . . . . .	41
3.1.6. Triggering the search for physical tetrads . . . . .	42
3.1.7. Calculating surfaces of sections . . . . .	43
3.2. On the integration of the time-dependent BCS equations . . . . .	45
3.2.1. Space discretization . . . . .	47
3.2.2. Linear BCS equations . . . . .	48
3.2.3. Initial values for the BCS simulations . . . . .	49
3.2.4. Numerical calculation of $T_c$ and $\Delta$ . . . . .	50
3.2.5. Properties of the discrete BCS equations . . . . .	51
3.2.6. Splitting methods . . . . .	54
3.2.7. Nonlinear BCS integrator . . . . .	55
3.2.8. Triple splitting integrator . . . . .	56
3.2.9. Measuring the integrators’ accuracy . . . . .	56
3.2.10. Splitting integrators for general potentials . . . . .	57
3.2.11. Physical results . . . . .	58
3.3. On the particular hardships of implementation and simulation . . . . .	58

<b>Acknowledgements</b>	<b>61</b>
<b>A. Investigating spinning test particles: spin supplementary conditions and the Hamiltonian formalism</b>	<b>63</b>
Abstract . . . . .	63
A.1. Introduction . . . . .	63
A.2. Mathisson-Papapetrou equations . . . . .	64
A.2.1. Spin four-vector . . . . .	66
A.2.2. Calculating the tangent vector . . . . .	67
A.3. The Hamiltonian formalism for the spinning particle . . . . .	68
A.3.1. The Hamiltonian for the Kerr spacetime . . . . .	70
A.4. Comparison of Tulczyjew and Newton-Wigner SSC . . . . .	72
A.4.1. Preliminaries . . . . .	72
A.4.2. Comparison for large spin . . . . .	74
A.4.3. Comparison for very small spin . . . . .	75
A.4.4. Constants of motion . . . . .	76
A.5. Numerical comparison of the MP equations with the corresponding Hamiltonian equations . . . . .	77
A.5.1. Preliminaries . . . . .	77
A.5.2. Comparison for large spin . . . . .	78
A.5.3. Comparison for very small spin . . . . .	79
A.5.4. Behavior of the constants of motion and scaling with the spin . . . . .	80
A.6. Conclusions . . . . .	83
Acknowledgements . . . . .	84
A.7. Numerical integration of the MP equations . . . . .	84
A.8. Numerical integration of the Hamiltonian equations . . . . .	87
<b>B. Comparing Hamiltonians of a spinning test particle for different tetrad fields</b>	<b>91</b>
Abstract . . . . .	91
B.1. Introduction . . . . .	91
B.2. The Hamiltonian formalism . . . . .	93
B.3. The Hamiltonian Function in Boyer-Lindquist coordinates compared with Cartesian Isotropic coordinates . . . . .	96
B.3.1. A tetrad in Boyer-Lindquist coordinates . . . . .	96
B.3.2. The Hamiltonian function in isotropic cartesian coordinates . . . . .	102
B.4. The Hamiltonian function in Kerr-Schild coordinates . . . . .	106
B.4.1. ZAMO Tetrad . . . . .	107
B.4.2. Non-ZAMO tetrad . . . . .	109
B.5. Conclusions . . . . .	111
Acknowledgements . . . . .	112
B.6. Numerical integration of the Hamiltonian equations . . . . .	112
B.7. Plunging orbits . . . . .	114
<b>C. Comparing the full time-dependent Bogoliubov–de-Gennes equations to their linear approximation: A numerical investigation</b>	<b>117</b>
Abstract . . . . .	117
C.1. Introduction . . . . .	117
C.2. Physical and mathematical background . . . . .	118

---

C.2.1. Energy functional and BCS equations . . . . .	118
C.2.2. Contact interactions . . . . .	119
C.2.3. Initial values . . . . .	120
C.2.4. Ginzburg–Landau and macroscopic parameter . . . . .	120
C.2.5. The linear approximation . . . . .	121
C.3. Recent mathematical results . . . . .	121
C.4. Simulations . . . . .	122
C.4.1. Gap as a function of $h$ . . . . .	122
C.4.2. Results for $h = 1/4$ . . . . .	123
C.4.3. Results for $h = 1/8$ . . . . .	124
C.4.4. Results for $h = 1/16$ . . . . .	124
C.5. Summary . . . . .	126
Acknowledgements . . . . .	126
C.6. Critical temperature and initial energy gap . . . . .	126
C.7. Numerical treatment of the equations . . . . .	127
C.7.1. Finite extension and discrete system . . . . .	127
C.7.2. The equations for a delta potential . . . . .	128
C.7.3. Space discretization . . . . .	128
C.7.4. Solving the system of ordinary differential equations . . . . .	129
C.7.5. Time discretization . . . . .	130
C.7.6. Fixing the time discretization parameter . . . . .	130
C.7.7. Fixing the space discretization parameters . . . . .	131
<b>D. Splitting integrators for the BCS equations of superconductivity</b>	<b>133</b>
Abstract . . . . .	133
D.1. Introduction . . . . .	133
D.2. The BCS Equations . . . . .	135
D.2.1. Superconductivity . . . . .	136
D.2.2. The discrete BCS equations . . . . .	136
D.3. Space Discretization . . . . .	136
D.3.1. System of ordinary differential equations . . . . .	137
D.3.2. System for a contact interaction . . . . .	137
D.3.3. Constants of motion . . . . .	138
D.3.4. Numerical notation . . . . .	139
D.4. Calculating the Convolution Terms . . . . .	139
D.5. Nonlinear Splitting Integrator . . . . .	140
D.5.1. Decoupled system . . . . .	140
D.5.2. BCSInt . . . . .	141
D.5.3. Number of operations . . . . .	142
D.6. Triple Splitting Integrator . . . . .	143
D.6.1. Calculating $\Phi_{\tau,g}$ . . . . .	143
D.6.2. Calculating $\Phi_{\tau,h}$ . . . . .	144
D.6.3. SplitBCS . . . . .	146
D.6.4. Number of operations . . . . .	147
D.7. Numerical Experiments . . . . .	148
D.8. Conclusion . . . . .	150
Acknowledgements . . . . .	151

---



# 1. Introduction

General relativity and quantum mechanics are possibly two of the most amazing things humankind has ever invented and surely two of the most important descriptions of physical processes in their respective areas of validity. No wonder, then, that one of the most exciting challenges for theoretical physics is to combine these two fundamental models. Unfortunately, such a combination has turned out to be out of reach until today. Yet, although defying every effort so far to being put on common ground, the two theories share quite some properties.

For example both of their fundamental equations, i.e., the Einstein field equations in the general relativistic case and the Schrödinger equation in the realm of quantum mechanics, are much too complex for calculations in systems which comprise many constituents. As a consequence, the respective communities have tried to and succeeded in finding less cumbersome equations which are well-suited for the description of specific physical phenomena. From a physical point of view, this thesis is concerned with two particularly fascinating processes –one in each of the broad areas mentioned above. Regarding these processes, the physics community wants to know how far their approximations derive from the real truth<sup>1</sup>. From a numerical point of view, this thesis is about helping the physicists finding out. For this, we have to come up with highly accurate integration schemes and implement simulations for all the equations in play. The result of our endeavor are four papers and further ongoing projects in two areas of physics which we want to present in this script.

In the first part, we turn our attention towards binary systems consisting of one comparably light star and another much heavier one such as a black hole or a neutron star. The most popular equations of motion for this setting will be presented in the next Section 1.1. In Chapter 2 we explain what special numerical interest we had in these equations. Our results in this area and their impact are discussed in Chapter 3 whereas Chapters A and B contain the corresponding original publications.

The second part of this thesis is concerned with superconductivity. This is the ability of certain materials, when cooled beneath a characteristic threshold temperature, to let electrons move unhindered by any resistance, thus rendering obsolete the well-known relation between voltage, resistance and current from school. We give an introduction to this phenomenon and the relevant equations in the next but one next Section 1.2. Again, the numerical tasks in this area are outlined in Chapter 2 and our new contributions to science gathered in Chapter 3. The papers produced in the course of this undertaking can be found in Chapters C and D.

## 1.1. Introduction to relativistic binary systems

When the renowned German newspaper *Die Zeit* composed a list of the twenty most fascinating projects in the history of science, it rightly included<sup>2</sup> the search for *gravitational waves*. These wavelike ripples and distortions of spacetime were first predicted by Einstein (1916) as possible solutions to his famous field equations, first presented in (Einstein, 1915), which are, until the present day, the most accurate theory for the distribution of matter in the universe.

---

<sup>1</sup>‘The real truth‘ meaning the most accurate but still computationally feasible description of the given phenomenon available.

<sup>2</sup>Alongside more well-known topics such as the *Large Hadron Collider* at CERN, *The Human Genome Project*, etc., see <http://www.zeit.de/online/2008/02/bg-weltraetsel>.

---

At first, these waves had not been paid much attention to. This changed when Hulse and Taylor (1975) achieved an indirect proof of the existence of gravitational waves as a by-product of their investigation of pulsar stars<sup>3</sup>. This triggered a rush to finally measure gravitational waves directly. As a consequence, a lot of scientific resources and taxpayers' money<sup>4</sup> has been poured into the construction of land-based detectors, such as VIRGO in France and Italy (Giazotto, 1992), GEO 600 in Germany and the UK (Lück *et al.*, 1997), KAGRA in Japan (Kuroda *et al.*, 2010), and LIGO in the USA (Abramovici *et al.*, 1992). Physically speaking, these antennae are huge interferometers with arms that are some kilometers long<sup>5</sup>. Presumably in two decades from now, even a space-based telescope, consisting of an array of satellites, will be launched by the European space agency ESA under the name eLISA. However, despite all this effort the gravitational waves have stayed hidden up to this day<sup>6</sup>. In order to increase the chances of an eventual detection, astronomers need accurate templates of signals from the most promising sources. These have been singled out to be binary systems consisting of inspiraling compact objects, see, e.g. (Blanchet, 2002), such as neutron stars or black holes. In this thesis, we are interested in binaries where one of the two stellar bodies is much heavier than the other. They are called *Extreme mass ratio inspirals (EMRIs)*.

### 1.1.1. Mathisson–Papapetrou equations

The most profound model of the universe was introduced by Einstein (1915). He showed that the distribution of mass is nothing else than curvature of spacetime<sup>7</sup>, which is encoded in a metric  $g_{\mu\nu}$ . Mathematically speaking, the metric is a tensor-valued function of the spacetime variables. It is subject to the field equations

$$R_{\mu\nu} - \frac{1}{2}g_{\mu\nu}R = T_{\mu\nu}, \quad (1.1)$$

where  $R_{\mu\nu}$  is the *Ricci tensor* which is the trace of the Riemann curvature tensor,

$$R_{\mu\nu} = R_{\mu\lambda\nu}^{\lambda} = \partial_{\lambda}\Gamma_{\mu\nu}^{\lambda} - \partial_{\nu}\Gamma_{\mu\lambda}^{\lambda} + \Gamma_{\mu\nu}^{\lambda}\Gamma_{\lambda\alpha}^{\alpha} - \Gamma_{\mu\alpha}^{\lambda}\Gamma_{\nu\lambda}^{\alpha}, \quad (1.2)$$

with the Christoffel-symbols

$$\Gamma_{\beta\gamma}^{\alpha} = \frac{1}{2}g^{\alpha\delta} \left( \frac{\partial g_{\gamma\delta}}{\partial x^{\beta}} + \frac{\partial g_{\beta\delta}}{\partial x^{\gamma}} - \frac{\partial g_{\beta\gamma}}{\partial x^{\delta}} \right). \quad (1.3)$$

$R$  is the *Gauss curvature* given by the contraction of the Ricci tensor,

$$R = R_{\mu}^{\mu}. \quad (1.4)$$

The *stress-energy tensor*  $T_{\mu\nu}$ , in turn, is a source term including, for example, energy and matter. The field equations (1.1) are very complex to handle computationally. Fortunately, for

---

<sup>3</sup>For this, they were awarded the Nobel Prize in Physics in 1993.

<sup>4</sup>Such as the DFG grant SFB transregio 7 our group has proudly been part of.

<sup>5</sup>As gravitational waves are assumed to have a very long wavelength, an antenna for their interception has to be very large as well.

<sup>6</sup>Update to submitted version of this thesis: On February 11th, 2016, Abbott *et al.* (2016) announced the first direct measurement of gravitational waves by the LIGO interferometer. The waves were emitted during the merger of a binary of two black holes, which were long been supposed to be promising candidates (cf. the explanations above).

<sup>7</sup>Spacetime is the four-dimensional ensemble of time and space.

special systems such as the EMRIs introduced above, much less intractable descriptions have been found over the years. For EMRIs, one assumes the much heavier body to be stationary and unperturbed by the much lighter one orbiting it<sup>8</sup>. The heavy body is represented by a solution to the *free field equation*, which means the partial differential Eq. (1.1) with  $T_{\mu\nu} = 0$ . Normally, one chooses one of the two analytic solutions found so far, namely the metric of Schwarzschild (1916)<sup>9</sup> or the one of Kerr and Schild (1963). The central object fixed, one can turn towards the lighter body.

In the most basic approach, this lighter body is characterized as a point particle with position  $x^\mu$  and momentum  $p^\mu$  moving in the space which is curved according to the metric  $g_{\mu\nu}$ <sup>10</sup>. In most applications, one also wants to take into account the rotation of the lighter body around its own axis –commonly denoted as that body’s *spin*. This spin is encoded in an antisymmetric tensor  $S^{\mu\nu}$ . The equations for a spinning test body were first introduced by Mathisson (1937) and Papapetrou (1951). They consider the lighter body to be a small perturbation of the central massive object which is singular at the position of the test body. They then introduce multipole moments to describe this perturbation. The quadrupole and higher moments are of the order of  $\mathcal{O}(S^2)$ , with

$$S^2 = \frac{1}{2} S^{\mu\nu} S^{\mu\nu}. \quad (1.5)$$

As, in physically valid situations, the spin has to be small, Mathisson (1937) and Papapetrou (1951) neglect quadrupoles and higher moments. The resulting pole-dipole approximation for the equations of motion of the spinning particle are the *Mathisson–Papapetrou (MP) equations*, named after the just-mentioned theoretical physicists<sup>11</sup>. In the commonly used reformulation of Dixon (1970), the equations of motion are

$$\frac{Dp^\mu}{d\tau} = -\frac{1}{2} R^\mu{}_{\nu\kappa\lambda} v^\nu S^{\kappa\lambda}, \quad (1.6)$$

$$\frac{DS^{\mu\nu}}{d\tau} = p^\mu v^\nu - v^\mu p^\nu. \quad (1.7)$$

Here,  $\tau$  denotes the proper time,  $v^\mu = dx/d\tau$  the tangent vector to the world line of the test particle, and  $Da^\mu/d\tau$  denotes the covariant derivative of some given vector  $a^\mu$  in direction of  $v^\mu$ , defined as

$$\frac{Da^\mu}{d\tau} := \frac{da^\mu}{d\tau} + \Gamma^\mu{}_{\alpha\beta} v^\alpha a^\beta. \quad (1.8)$$

---

<sup>8</sup>Just as one can, to good accuracy, describe the two-particle system sun–earth by a fixed sun and the earth orbiting it.

<sup>9</sup>Schwarzschild wrote a letter to Einstein from a trench at the west front of World War I, happily introducing to him the first solution to the newly introduced field equations. Shortly afterwards he died of his injuries..., see, e.g. [http://en.wikipedia.org/wiki/Karl\\_Schwarzschild](http://en.wikipedia.org/wiki/Karl_Schwarzschild).

<sup>10</sup>A numerical integration scheme tailored to the motion of such a particle –called *geodesic motion*– was developed in the author’s diploma thesis (Seyrich, 2012).

<sup>11</sup>A nice introduction to the MP equations and their derivation is given by Dixon (1964).

---

Everything put together, we get the following system of ordinary differential equations (ODEs):

$$\frac{dx^\mu}{d\tau} = v^\mu, \quad (1.9)$$

$$\frac{Dp^\mu}{d\tau} = -\frac{1}{2} R^\mu{}_{\nu\kappa\lambda} v^\nu S^{\kappa\lambda}, \quad (1.10)$$

$$\frac{DS^{\mu\nu}}{d\tau} = p^\mu v^\nu - v^\mu p^\nu. \quad (1.11)$$

### 1.1.2. Spin supplementary conditions

As it is antisymmetric, the spin tensor  $S^{\mu\nu}$  contains 6 independent data. Adding the positions and the momenta, the test particle is described by 14 variables. If we take into account the four-velocity conservation<sup>12</sup>

$$v_\mu v^\mu = -c^2, \quad (1.12)$$

the number of degrees of freedom is reduced to 13. But, as the set (1.9)-(1.11) consists of only 10 relevant equations<sup>13</sup>, we need some additional information to close the system. The physical explanation is that general relativity does not fix a reference system, i.e., we have to prescribe an observer. This is done with the help of a so-called *spin supplementary condition (SSC)* –supplementary constraints on the system representing physical features<sup>14</sup>. Depending on which SSC is chosen, a different reference frame is given. Physically speaking, this ‘freedom of choice’ is caused by the fact that the lighter body must have a finite extension as it would rotate with velocities larger than the speed of light otherwise. Each SSC fixes another center of mass for the extended test particle and the MP equations describe the evolution from the perspective of an observer for whom the center of mass is the one given by the SSC. Two interesting SSCs on which we focus in this thesis are the *Tulczyjew* SSC

$$S^{\mu\nu} p_\nu \stackrel{!}{=} 0 \quad (1.13)$$

and the more general *Newton–Wigner* SSC

$$S^{\mu\nu} \omega_\nu \stackrel{!}{=} 0, \quad (1.14)$$

where  $\omega_\nu$  is a timelike four-vector whose form is specified in Chapters A and B as well as in the next Subsection.

When multiplying the SSC (1.13) with  $p_\mu$  from the left, we see that the originally 4 equations are linearly dependent. Similarly, we can multiply the SSC (1.14) with  $\omega_\mu$ . Thus, the SSCs provide us with 3 more independent equations with the help of which we can close the system (1.9)-(1.11). More specifically, based on the relations (1.13) and (1.12) one can derive the expression

$$v^\mu = N \left( \frac{p^\mu}{\mu} + \frac{2S^{\mu\nu} u^\lambda R_{\nu\lambda\rho\sigma} S^{\rho\sigma}}{4\mu^2 + R_{\alpha\beta\gamma\delta} S^{\alpha\beta} S^{\gamma\delta}} \right), \quad (1.15)$$

---

<sup>12</sup>In the units we used in our works, we have  $c = 1$ . Accordingly, the four-velocity conservation is given by  $v_\mu v^\mu = -1$  in what follows.

<sup>13</sup>Eqs. (1.9) are just a definition.

<sup>14</sup>A nice overview of the different SSCs and their physical interpretation can be found in (Semerák, 1999) and (Kyrian and Semerák, 2007).

where  $N$  is a normalization constant defined by Eq. (1.12). When employing the Newton–Wigner SSC instead, one can start with the covariant derivative of (1.14) to arrive at

$$v^\mu = \frac{1}{\omega_\nu p^\nu} \left( (\omega_\nu v^\nu) p^\mu + S^{\mu\nu} \frac{D\omega_\nu}{d\tau} \right). \quad (1.16)$$

For a more thorough discussion, we refer the interested reader to Subsection A.2. and rather stress that, as a pole-dipole approximation, the MP equations supplemented by a physical SSC are considered valid up to first order in the lighter body’s spin.

The Tulczyjew SSC has already been used in various EMRI simulations, see, e.g. (Hartl, 2003a,b; Suzuki and Maeda, 1997; Verhaaren and Hirschmann, 2010), as it yields a convenient, explicit expression for the calculation of the tangential velocity  $v^\mu$ . Presumably due to the not-so-convenient expression it yields for  $v^\mu$ , the Newton–Wigner SSC has not been used in practical simulations so far. However, for certain choices of the timelike vector  $\omega_\nu$ , it has some nice analytical implications as we want to explain now.

### 1.1.3. Hamiltonian approximation

The Mathisson–Papapetrou equations are much easier to handle than the partial differential field equations (1.1). But, although they can be obtained via a total variation of a suitable Lagrangian<sup>15</sup>, there is no straightforward Hamiltonian formulation for them. This motivated Barausse *et al.* (2009) to look into the matter. Here, we give a short summary of their important work. A more detailed introduction to the topic can be found in Section A.3.

Barausse *et al.* (2009) consider the Newton–Wigner SSC with

$$w_\nu = p_\nu - \mu \tilde{e}_\mu^T, \quad (1.17)$$

where  $\mu$  is the mass of the test particle and  $\tilde{e}_\mu^T$  is the timelike future oriented component of a tetrad to be specified, i.e., a vierbein with respect to which they measure the particle’s spin. They introduce a three-dimensional spin vector  $S_I$ ,  $I = 1, 2, 3$ , via

$$S_I = \frac{1}{2} \epsilon_{IJK} S^{JK}, \quad (1.18)$$

where  $S^{JK}$  are the spacelike components of the projection of  $S^{\mu\nu}$  onto the tetrad<sup>16</sup>. They further define a three-dimensional canonical momentum vector  $P_i$ ,  $i = 1, 2, 3$ , as the partial derivative of the MP equations’ Lagrangian with respect to  $v^i$ . They use coordinate time  $t = x^0$  as the relevant parameter and introduce a Hamiltonian  $H$  as a function of  $x^i$ ,  $P_i$  and  $S_I$ <sup>17</sup> for which they state the following

**Theorem 1.1.** *The Dirac brackets<sup>18</sup> with regard to the Hamiltonian  $H$  of the introduced phase*

---

<sup>15</sup>Cf. (Barausse *et al.*, 2009) and references therein or Theorem 3.1 in Subsection 3.1.3 below.

<sup>16</sup> $\epsilon_{IJK}$  denotes the *Levi–Civita* tensor.

<sup>17</sup>The Hamiltonian, which consists of many terms, is presented in detail in Section A.3 from our publication of Chapter A.

<sup>18</sup>The Dirac brackets are the analog of the Poisson brackets from classical mechanics, see, e.g. (Yang and Hirschfelder, 1980) for an introduction.

---

space variables  $x^i$ ,  $P_i$  and  $S_I$  satisfy

$$\{x^i, x^j\}_{DB} = \mathcal{O}(S^2), \quad (1.19)$$

$$\{x^i, P_j\}_{DB} = \delta_j^i + \mathcal{O}(S^2), \quad (1.20)$$

$$\{P_i, P_j\}_{DB} = \mathcal{O}(S^2), \quad (1.21)$$

$$\{x^i, S^J\}_{DB} = \mathcal{O}(S^2), \quad (1.22)$$

$$\{P_i, S^J\}_{DB} = \mathcal{O}(S^2), \quad (1.23)$$

$$\{S^I, S^J\}_{DB} = \epsilon_{IJK} S^K + \mathcal{O}(S^2), \quad (1.24)$$

$$(1.25)$$

where  $S^2$  is the Euclidean norm of  $S_I$ .

in other words, up to errors of  $\mathcal{O}(S^2)$ , the evolution of the test particle is governed by the Hamiltonian equations

$$\frac{dx^i}{dt} = \frac{\partial H}{\partial P_i}, \quad (1.26)$$

$$\frac{dP_i}{dt} = -\frac{\partial H}{\partial x^i}, \quad (1.27)$$

$$\frac{dS_I}{dt} = \epsilon_{IJC} \frac{\partial H}{\partial S_J} S^C. \quad (1.28)$$

This immediately raises the question of how far the solutions to the Hamiltonian equations (1.26)-(1.28) deviate from those of the MP equations. Since an approximate Hamiltonian structure can only be derived for MP equations supplemented by the Newton–Wigner SSC (Barausse *et al.*, 2009), and since the MP equations with this SSC have never been looked at in simulations, the subsequent question is how far the results of the MP equations with Newton–Wigner SSC differ from those of the MP equations supplemented by the Tulczyjew SSC.

We further detail our interest in the topic in the first part of Chapter 2. Let us leave the very massive objects behind for the moment and turn towards an intriguing phenomenon on much smaller scales.

## 1.2. Introduction to superconductivity

When Onnes (1911) worked on the resistance of ultra cold mercury over a century ago, not only did he discover a hitherto unknown phenomenon<sup>19</sup>, but also did he give rise to a completely new field of physics: When he measured the resistance  $R$  of the alloy against the temperature  $T$ , he found out that at first the resistance declined alongside the temperature –just as everyone would expect from his or her experience in school. However, at a temperature of roughly 4.1K, the resistance broke down completely, thus allowing the electrons to flow freely through the conductor. The qualitative behavior of  $R(T)$  can be seen in Fig. 1.1.

---

<sup>19</sup>Wherefore he received the Nobel Prize in Physics in 1913.

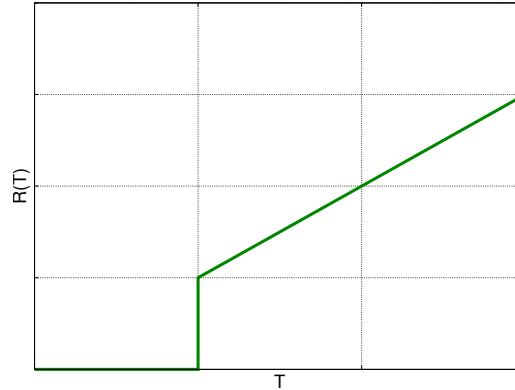


Figure 1.1: Sketch of the resistance  $R$  as a function of the temperature  $T$  for superconducting materials.

Soon, other materials, too, were found to show perfect conductivity when reaching a specific temperature  $T_c$ . Not much later, people realized that the alloys in question exhibited further characteristic behaviors. More specifically, Meissner and Ochsenfeld (1933) observed that magnetic fields were expelled from superconductors. This so-called Meissner effect was first described by London and London (1935) who showed that the magnetic field decays exponentially as a function of the penetration depth  $x$  into the material. In detail, the magnitude of the magnetic field  $B$  at depth  $x$  within the conductor is given by

$$B(x) = B_0 \exp\left(-\frac{x}{\lambda_L}\right), \quad (1.29)$$

where  $\lambda_L$  is a characteristic length.

### 1.2.1. Ginzburg-Landau equation

Intriguingly, the magnetic field is expelled and decays following the same law no matter whether it already has been around before the material is cooled down or whether it is switched on after the temperature has shrunk below the critical temperature. This means that superconductivity is in fact a thermodynamic state which is independent of the process through which the system got there. Further physical experiments showed that, at  $T_c$ , the system undergoes a so-called second order transition from a disordered into an ordered phase<sup>20</sup>. Such phase transitions had already been looked at by Landau (1937)<sup>21</sup>. They are commonly described by a parameter which is zero in the normal state and positive in the ordered one. Building on this, Landau and Ginzburg (1950) introduced a parameter  $\psi(\mathbf{x})$ , the squared magnitude of which they interpreted as the density of superconducting particles in the material. Assuming that  $\psi$  was small for systems close to the critical temperature, they derived a phenomenological expression of the free energy density  $\mathcal{E}^{\text{GL}}$  as an expansion in  $|\psi(x)|^2$  and  $|\nabla\psi|^2$ . They got

$$\mathcal{E}^{\text{GL}}(\psi) = c_1 |(-i\nabla + 2A(x))\psi(x)|^2 + c_2 W(x)|\psi(x)|^2 + c_3(1 - |\psi(x)|^2)^2, \quad (1.30)$$

<sup>20</sup>An illustrative example of a second order phase transition is given by the spontaneous magnetization of a ferromagnet when the external magnetic field exceeds a certain threshold.

<sup>21</sup>For his related work on liquid helium, Landau received the Nobel Prize in Physics in 1962.

---

where  $W(x)$  is the electric potential,  $A(x)$  is the magnetic potential for which  $B(x) = \nabla \times A(x)$ , and  $c_i$ ,  $i = 1, 2, 3$ , are some constants. We recall that a stationary physical system always arranges in such a way that it minimizes the describing energy. A minimizer of an energy functional satisfies the corresponding *Euler–Lagrange* equations which in the present case are obtained by minimizing  $\mathcal{E}^{\text{GL}}$  with respect to  $\psi$ . This yields the well-known *Ginzburg–Landau* equations

$$c_1 (-i\nabla + 2A(x))^2 \psi(x) + (c_2 W(x) - 2c_3)\psi(x) + 2c_3 |\psi(x)|^2 \psi(x) = 0. \quad (1.31)$$

If this equation has a nontrivial solution, then the system is in a superconducting state with the density of superconducting particles at a given point  $x$  inside the conductor given by  $|\psi(x)|^2$ . With Ginzburg and Landau’s theory this space dependence could be calculated for the first time. Furthermore, theirs was the first theory able to describe type-II superconductors in which magnetic flux penetrates the conductor in a regular hexagonal structure<sup>22</sup>. But, all its practical relevance notwithstanding, it is only a macroscopic theory.

### 1.2.2. Stationary BCS theory

The first and still most widely used microscopic theory for superconductivity was published by Bardeen *et al.* (1957), commonly known as BCS, in 1957<sup>23</sup>. In this work, the algebraic structure of the second quantization and unitary transformations introduced by Bogoliubov (1947) are used to derive a Hamiltonian of pairs of electrons with opposed spin, the famous *Cooper pairs*. From a physical point of view, the system is in a superconducting state whenever it is energetically advantageous for two electrons of opposed spin to form an entangled pair. The higher the share of paired electrons, the more superconducting the system will be. Here, we concentrate on the mathematical framework as it was that very formulation we have worked with for our research<sup>24</sup>.

Just as the statistical physical description, the mathematical formulation of BCS theory for a system of fermions is based on operators acting on the Hilbert space. In our case the relevant operators are the *density operator*  $\gamma : L^2(\mathbb{R}^3) \mapsto L^2(\mathbb{R}^3)$  and the (*cooper*) *pair density operator*  $\alpha : L^2(\mathbb{R}^3) \mapsto L^2(\mathbb{R}^3)$ . These operators are represented by their respective kernels  $\gamma(x, y) \in L^2(\mathbb{R}^3 \times \mathbb{R}^3)$  and  $\alpha(x, y) \in L^2(\mathbb{R}^3 \times \mathbb{R}^3)$ . Later on, we will especially be interested in  $\alpha(x, y)$  which is interpreted physically as the probability of finding one half of a Cooper pair at position  $x$  and the other at position  $y$ . In order to streamline notation, the convention is to combine the two density operators in the  $2 \times 2$  matrix

$$\Gamma = \begin{pmatrix} \gamma & \alpha \\ \bar{\alpha} & 1 - \bar{\gamma} \end{pmatrix}, \quad (1.32)$$

with the bar denoting complex conjugation. For a given chemical potential  $\mu$ <sup>25</sup>, a fermionic system on a domain  $D \subset \mathbb{R}^3$  at temperature  $T$  in a given state  $\Gamma$  is described by the energy

---

<sup>22</sup>A nice overview of the various phenomena connected with superconductivity and of Ginzburg–Landau theory in particular can be found in (Cyrot, 1973).

<sup>23</sup>The relevance of this work can best be seen by noting that, according to Google Scholar, it has been cited more than 10000 times. Very rightly, thus, the authors were rewarded with a Nobel Prize in Physics in 1972.

<sup>24</sup>A detailed presentation of the mathematical framework for BCS theory can be found in (Bach *et al.*, 1994).

<sup>25</sup>From a mathematical point of view, the chemical potential is nothing other than a Lagrange multiplier which comes into play due to the conservation of the number of particles.

functional

$$\begin{aligned} \mathcal{F}_T(\Gamma) = & \text{Tr} \left( [(-i\nabla + A(x))^2 - \mu + W(x)] \gamma \right) - TS(\Gamma) \\ & + \int_D V(x-y) |\alpha(x,y)|^2 dx dy, \end{aligned} \quad (1.33)$$

where  $V$  is the interaction between the particles and where  $S$  is the entropy defined as

$$S(\Gamma) = -\text{Tr} [\text{Tr}_{\mathbb{C}^2}(\Gamma \ln \Gamma)]. \quad (1.34)$$

In some works, an exchange term  $\int_D V(x-y) |\gamma(x,y)|^2 dx dy$  and a direct term  $\int_D V(x-y) \gamma(x,x) \gamma(y,y) dx dy$  are added to the functional, see, e.g., (Hainzl *et al.*, 2010). Following the original work of Bardeen *et al.* (1957), we omit these contributions in what follows. For later use, we mention that for temperatures above  $T_c$  the minimizer of  $F_T$  is given by the normal state

$$\Gamma^N = \begin{pmatrix} \gamma^N & 0 \\ 0 & 1 - \bar{\gamma}^N \end{pmatrix}, \quad (1.35)$$

$$\gamma^N = \frac{1}{1 + \exp(((-i\nabla + 2A(x))^2 - \mu + W(x)/T)}. \quad (1.36)$$

This means the system is not superconducting and the electrons are distributed according to the *Fermi–Dirac statistics* for fermions.

### 1.2.3. Superconductivity in BCS theory

According to the theory of BCS, a system is said to be superconducting whenever the Cooper pair density  $\alpha$  takes a finite value. Consequently, the critical temperature  $T_c$  for the onset of superconductivity is defined as that very temperature  $T$  below which the minimizer of the free energy functional (1.33) is minimized by states  $\Gamma$  with nonvanishing  $\alpha$ . In this case, there exists an *energy gap* between the superconducting state and a non-superconducting state. This gap is conventionally denoted by  $\Delta(p)$ . The larger the gap, the more energetically advantageous it is for the system to form Cooper pairs which flow freely through the material under consideration. The energy gap  $\Delta$  satisfies the implicit equation

$$\Delta(p) = - \left( \hat{V} * \frac{\Delta}{K_T^\Delta} \right) (p), \quad (1.37)$$

with

$$K_T^\Delta(p) = \frac{\sqrt{(p^2 - \mu)^2 + |\Delta(p)|^2}}{\tanh \frac{\sqrt{(p^2 - \mu)^2 + |\Delta(p)|^2}}{2T}}. \quad (1.38)$$

Considering  $K_T^\Delta$  as a multiplication operator in momentum space, one can also define the critical temperature as that value  $T_c \geq 0$ , for which

$$\inf \text{spec} (K_T^0 + V) < 0, \quad \text{if } T < T_c, \quad (1.39)$$

$$K_T^0 + V \geq 0, \quad \text{if } T \geq T_c. \quad (1.40)$$

---

Similarly, one can define the energy gap for a given temperature  $T$  as that  $\Delta$ , for which

$$K_T^{\Delta} + V \tag{1.41}$$

has 0 as an isolated eigenvalue. It was shown by Hainzl *et al.* (2008) that these definitions are analogous to the more physical ones above.

#### 1.2.4. From microscopic to macroscopic scale

As opposed to Ginzburg–Landau theory, the microscopic formalism of BCS is considered valid for all temperatures. Still, bearing in mind the satisfying results obtained via Ginzburg–Landau close to the critical temperature, the question arises as to whether the latter is indeed an approximation of the former. A positive answer to this questions for systems in a domain with an extension of  $\mathcal{O}(1/h)$  at temperature  $T = (1 - h^2)T_c$ , with  $h$  being a small parameter, was given by Gorkov (1959). A rigorous analysis of the matter was carried out by Frank *et al.* (2012). They obtained the following

**Theorem 1.2.** *Let  $\alpha_0(x, y)$  be a minimizer of the translation invariant energy functional, i.e.,  $F_T$  with vanishing  $W$  and  $A$ . Let  $\Gamma$  be a minimizer of  $\mathcal{F}_T$  and  $\psi$  be a minimizer of  $\mathcal{F}^{GL} = \int_D \mathcal{E}^{GL} dx$ .*

*Then, one has*

$$\mathcal{F}_T(\Gamma) - \mathcal{F}_T(\Gamma_0) = h^3(\mathcal{F}^{GL}(\psi) - c_3) + \mathcal{O}(h^{3+1/3}), \tag{1.42}$$

$$\alpha(x, y) = \frac{1}{h^2} \tilde{\psi} \left( \frac{x+y}{2} \right) \alpha_0 \left( \frac{x-y}{h} \right) + \xi(x, y), \tag{1.43}$$

*with*

$$\|\xi(x, y)\|_{L^2} = \mathcal{O}(h^{3+\frac{1}{3}}), \tag{1.44}$$

$$\mathcal{F}^{GL}(\tilde{\psi}) = \mathcal{F}^{GL}(\psi) + \mathcal{O}(h^{\frac{1}{3}}). \tag{1.45}$$

In a few words, this means that close to the critical temperature the centers of mass of the Cooper pairs are distributed, up to a very small error, as given by an almost minimizer of the Ginzburg–Landau functional. Hence, Ginzburg–Landau yields a physically correct macroscopic picture<sup>26</sup>. This told, in the stationary case everything seems fine. But what about time-dependent processes?

#### 1.2.5. Time-dependence

Resorting to the transformations of Bogoliubov (1947), De Gennes (1966) derived the time-dependent equations corresponding to the BCS energy functional<sup>27,28</sup>. In the mathematical

---

<sup>26</sup>The attentive reader may have noticed that, as opposed to the BCS functional, the magnetic potential enters the Ginzburg–Landau functional with a factor of 2. If we took account of the physical constants, it would be  $2e$  instead of  $e$  ( $e$  being the charge of an electron). This is further ‘proof’ of the fact that the Ginzburg–Landau equation describes the center of motion of two particles.

<sup>27</sup>Therefore, the time-dependent BCS equations are often referred to as *Bogoliubov–de-Gennes equations* in the literature.

<sup>28</sup>De Gennes received the Nobel Prize in Physics in 1991, although not for his work on superconductivity, but for his work on polymers and crystals.

setting of this work, the evolution equations of the –now time-dependent–  $2 \times 2$  operator valued  $\Gamma_t$  can formally be written quite compactly as

$$i\dot{\Gamma}_t = [H_{\Gamma_t}, \Gamma_t], \quad (1.46)$$

where the dot indicates differentiation with respect to time and  $H_{\Gamma_t}$  is the self-consistent Hamiltonian

$$H_{\Gamma_t} = \begin{pmatrix} -\Delta + W & V\alpha_t \\ V\bar{\alpha}_t & \Delta - W \end{pmatrix}. \quad (1.47)$$

With regard to the individual constituents of  $\Gamma_t$ , this translates into

$$i\dot{\gamma}_t = [-\Delta + W, \gamma_t] + iG_{\alpha_t}, \quad (1.48)$$

with the operator  $G_{\alpha_t}$  defined via its integral kernel

$$G_{\alpha_t}(x, y) = i \int_D (\alpha_t(x, z)\bar{\alpha}_t(y, z) [V(y - z) - V(x - z)]) dz, \quad (1.49)$$

and

$$\begin{aligned} i\dot{\alpha}_t(x, y) = & (-\Delta_x + W(x) - \Delta_y + W(y) + V(x - y))\alpha_t(x, y) \\ & - \int_D (\gamma_t(x, z)V(z - y)\alpha_t(z, y)) dz - \int_D (\gamma_t(y, z)V(z - x)\alpha_t(x, z)) dz. \end{aligned} \quad (1.50)$$

Although we will see below that these equations simplify for some special cases, they are very complex to handle in general. Therefore, it would be nice to have a good approximation at least on the macroscopic scale, i.e., a description of the important phenomena by a macroscopic phase parameter subject to a time-dependent analog of the Ginzburg-Landau Eq. (1.31). Thus, the search for a nonlinear, diffusive time-dependent partial differential equation started.

### 1.2.6. The argument over a time-dependent Ginzburg–Landau equation

After first attempts by Stephen and Suhl (1964); Schmid (1966); Abrahams and Tsuneto (1966) among others, Gorkov and Eliashberg (1968) pointed out that, if anything, a nonlinear equation could only be valid in the special case of so-called gapless superconductors. Ever since, a lot of discussion has been going on in the theoretical superconductivity community about whether or not a time-dependent Ginzburg–Landau-type equation does indeed exist, see, e.g., (Cyrot, 1973; De Melo *et al.*, 1993; Randeria, 1995). If so, It would be related to a linearization of the equation of motion (1.50) for  $\alpha$  which is obtained by replacing  $\gamma_t$  in the coupling term by the corresponding initial particle density  $\gamma_0$ . This linearization yields the following equation of motion for the Cooper pair density:

$$\begin{aligned} i\dot{\alpha}_t(x, y) = & (-\Delta_x + W(x) - \Delta_y + W(y) + V(x - y))\alpha_t(x, y) \\ & - \int_D (\gamma_0(x, z)V(z - y)\alpha_t(z, y)) dz - \int_D (\gamma_0(y, z)V(z - x)\alpha_t(x, z)) dz. \end{aligned} \quad (1.51)$$

---

Advocates of the existence of a time-dependent Ginzburg–Landau equation reason that, when expressing  $\gamma_t$  as

$$\gamma_t = \gamma_0 + \eta_t, \tag{1.52}$$

$\|\eta_t\|/\|\gamma_t\| = \mathcal{O}(h)$  holds for  $T$  near the critical temperature. Thus, all relevant information of the Cooper pair density can already be deduced from the linear Eq. (1.51). On the contrary, a second camp among theoretical physicists says,  $\|\eta_t\|$  cannot be guaranteed to be small at all. Consequently, they say, the linearization of the equations can lead to nonphysical artifacts and the dissipative character of a time-dependent Ginzburg–Landau is just a such.

Right here, we enter the game as we will point out in the second part of the next Section.

## 2. Objectives of this work

As told above, from a physical point of view this work is concerned with two very different areas. Seen from a numerical point of view, they are not so different at all. Plainly speaking, this thesis is about developing efficient and accurate integration tools for evolution equations describing important physical processes and implementing and running smooth simulations<sup>29</sup>, thus helping the physics community gathering precious insights into the nature of the equations of interest. Let us detail the specific numerical problems and their physical background.

### 2.1. Mathisson–Papapetrou equations and Hamiltonian approximation

Up to now, when astrophysicists wanted to find templates of signals of gravitational waves coming from an EMRI, they have run simulations of the MP equations (1.9)-(1.11) supplemented by the Tulczyjew SSC (1.13), see, e.g. (Suzuki and Maeda, 1997; Hartl, 2003a). A useful template for the detectors consists of a characteristic frequency pattern. In order to obtain a such, numerical simulations have to run over long times to gather enough sampling points for the necessary *Fourier transform* from the time domain into the frequency domain. So far, simulations have always been run with standard explicit integration schemes from Flannery *et al.* (1992) which are not suited for long-term integrations, c.f. (Hairer *et al.*, 2006).

This makes it interesting in its own right to search for a more effective integration scheme for the portrayed setting. However, in the course of this thesis, this has only been part of an even more extensive undertaking. That is to say, physicists would really like to work with the convenient Hamiltonian approximation of Barausse *et al.* (2009), if only they knew whether it was trustworthy. This is not guaranteed by theorem 1.1 above because, firstly, the Hamiltonian structure depends on using the Newton–Wigner SSC, which has to the best of the author’s and his co-workers’ knowledge never been used in simulations so far, and, secondly, the tetrad the authors introduced for their definition appears more or less out of the blue. Consequently, as the SSC (1.14) depends on the tetrad, the MP solutions could be unphysical in the first place.

In this work, we want to clarify the two points. For this, we first have to compare the MP solutions for the SSC (1.13) to those obtained via the Newton–Wigner SSC with  $w_\nu = p_\nu - \mu \tilde{e}_T^\mu$ . More precisely, we have to look at the respective solutions to the initial value problem

$$\left\{ \begin{array}{l} \frac{d x^\mu}{d\tau} = v^\mu, \\ \frac{d p^\mu}{d\tau} = -\frac{1}{2} R^\mu{}_{\nu\kappa\lambda} v^\nu S^{\kappa\lambda} - \Gamma_{\nu\kappa}^\mu v^\nu p^\kappa, \\ \frac{d S^{\mu\nu}}{d\tau} = p^\mu v^\nu - v^\mu p^\nu + \Gamma_{\kappa\lambda}^\mu S^{\nu\kappa} v^\lambda - \Gamma_{\kappa\lambda}^\nu S^{\mu\kappa} v^\lambda, \\ x^\mu(\tau = 0) = x_0^\mu, \\ p^\mu(\tau = 0) = p_0^\mu, \\ S^{\mu\nu}(\tau = 0) = S_0^{\mu\nu}, \end{array} \right. \quad (2.1)$$

where the tangential velocity  $v^\mu$  has to be calculated with the help of Eq. (1.15) in case of the Tulczyjew SSC or via Eq. (1.16) when employing the Newton–Wigner SSC instead. This already poses some very intriguing problems. To start with, we have to find similar initial

<sup>29</sup>An explanation of the difficulties of the ‘running and implementing’ part is given in Section 3.3.

---

data for both simulations<sup>30</sup>. Then, we have to find an efficient and still accurate integration scheme for the MP equations which is reliable for simulations over long times. In the case of the Newton–Wigner SSC, the implicitness of Eq. (1.14) poses a very interesting additional challenge.

As a second step, we have to compare the solutions of the system (1.9)-(1.11) plus (1.14) to the solutions of the Hamiltonian approach. In order to do so, we have to find and implement a suitable long-time integrator for the Hamiltonian system of Barausse *et al.* (2009). A further challenge is given by the fact that the MP equations are parametrized by the proper time, whereas the Hamiltonian approach rests on a parametrization by the coordinate time. So we have to find a way to compare the respective solutions at the same times.

Anticipating the next Section, we have found that the tetrad of Barausse *et al.* (2009) gives unphysical results in a certain limit. This was the starting point for the theoretical physics community to look for better tetrads. Anticipating the next Section once again, we could show that the Hamiltonians based on the new tetrads yield good results. Moreover, we investigate the integrability of the corresponding systems. As the symplectic structure is a necessary condition for a trustworthy investigation of EMRIs for chaos via surface of sections, this work is also concerned with the implementation of an efficient algorithm for the calculation of these sections.

## 2.2. Time-dependent BCS equations and possible approximations

After convergence of the stationary minimizer of the BCS functional towards the solution of Ginzburg–Landau was proven in the sense of theorem 1.2 by Frank *et al.* (2012), the authors turned their attention towards the time-dependent case with the aim of applying their analytical tools which they had honed further in convergence proofs for other physical settings, see, e.g. (Hainzl and Seiringer, 2012; Hainzl and Schlein, 2013). But, in the case of time-dependent BCS around the critical temperature, the situation was quite muddled even from a physical point of view as we outlined in Subsection 1.2.6. Thus, in order to get an understanding of the situation, the mathematical physics community was in need of some simulations of the systems of interest. Delivering them was, in a few words, our numerical task.

More specifically, in this work we consider the time-dependent BCS equations (1.48),(1.50) for systems at temperatures  $T = (1 + h^2)T_c$ , with  $h$  being a small parameter, for initial data close to the minimizer of the BCS energy functional<sup>31</sup>. This immediately leads to the first task, which is to find a way to obtain physically valid initial conditions.

Then, we have to evolve the system as governed by the equations of motion and track, in particular, the behavior of the macroscopic quantity  $\psi_t$  defined as the projection of the Cooper pair density  $\alpha_t$  onto the translation invariant minimizer  $\alpha_0$ , i.e., the time-dependent analog of  $\psi$  of theorem 1.2. As the existence of a time-dependent Ginzburg–Landau equation first and foremost depends on the validity of the linear approximation (1.51) of the Cooper pair

---

<sup>30</sup>Specifying physically valid initial values for general relativistic systems is no easy task and an area of research on its own, see, e.g. (Walther *et al.*, 2009) and references therein.

<sup>31</sup>Starting with a minimizer would not yield any interesting results because the system would simply remain in the minimizing state, of course.

density's equation of motion, we evolve both the full and the linearized equations. Regarding the particle interaction  $V$ , we concentrate on contact interactions  $V(x) = -a\delta(x)$  with positive interaction constant  $a$ . These are the most popular interactions in particle physics. From a numerical point of view, we then want to extend our tools to general potentials.

As the system (1.48),(1.50) would be very complex to solve in the most general form, we focus on systems without external potentials, i.e., we set  $W(x) = 0$  and  $A(x) = 0$  and consider translation invariant systems. This means that for the kernels of the operators  $\gamma$  and  $\alpha$  we have

$$\gamma(x, y) = \gamma(x - y), \tag{2.2}$$

$$\alpha(x, y) = \alpha(x - y). \tag{2.3}$$

Even in this situation, the resulting equations of motion represent an interesting problem to work on from a numerical point of view. An additional difficulty lies in the fact that the macroscopic quantify  $\psi_t$  varies on scales of the order  $\mathcal{O}(1/h)$  in units of the microscopic variables of BCS system. This implies that we have to work on different scales simultaneously.

## 2.3. List of the objectives

For the reader to have a compact overview, we sum up the tasks of the thesis in a list as follows:

- Find and implement an efficient and accurate integration scheme for the Mathisson–Papapetrou (MP) equations (1.9)-(1.11) supplemented by the spin supplementary condition (SSC) (1.13).
- Find and implement an efficient and accurate integration scheme for the Mathisson–Papapetrou (MP) equations (1.9)-(1.11) supplemented by the SSC (1.14). In particular, find a suitable way to cope with the nonlinearity of the ODE's right hand side due to Eq. (1.14).
- Find and implement an efficient and accurate integration scheme for the Hamiltonian system (1.26)-(1.28).
- Implement efficient and accurate schemes for the respective Hamiltonian equations of motion based on the various tetrads introduced in Chapter B, including an efficient and reliable algorithm for the calculation of surfaces of sections.
- Find and implement reliable algorithms to find physically realistic initial values for the equations of motion listed above.
- Find and implement an efficient and accurate solution scheme for the time-dependent partial differential BCS equations (1.48),(1.50) for a translation invariant system with contact interactions and vanishing external potentials.
- Find and implement reliable algorithms to find physically realistic initial values for the BCS equations.
- Simulate the time-dependent BCS equations and its linear approximation (1.51) for different sets of data and compare the resulting evolutions.
- Extend the numerical integration tools to general potentials.

---

The results of our works on these tasks are summarized in the next Chapter. The detailed results are given in Chapters A, B, C and D.

## 3. Summary of the results

The codes for the simulations of the Mathisson-Papapetrou equations, cf. Chapter A, have been written in *FORTRAN*. All the other codes have been written in *c++*.

In this Chapter, we want to summarize what these codes were about and what was achieved in the course of this thesis. This summary is meant to be self-contained so that the reader can get an understanding of the publications corresponding to this thesis without having to go through them. However, it is not meant to repeat the details published in our papers. On the other hand, there are aspects which could only be mentioned briefly in the publications. As they have been important nevertheless, we use the opportunity to be more specific about them in this summary. We start with literally the heavier part.

### 3.1. On the Mathisson–Papapetrou equations and their Hamiltonian approximations

As mentioned in the introduction, simulating an EMRI first of all requires a model for the much heavier central body, i.e., a background metric  $g^{\mu\nu}$ . For all projects in the course of this thesis, we worked with the *Kerr metric* as it is this the most astrophysically relevant solution to the Einstein field equations (1.1). It represents an interesting class of stationary, axisymmetric black holes with mass  $M$  rotating around their own axis with angular momentum  $a$ . Conventionally,  $a$  is denoted as the *spin* of the black hole. The most common description of a Kerr black hole uses the so-called *Boyer-Lindquist coordinates*. These are generalized spherical coordinates  $r, \theta, \phi$  which are related to the Cartesian coordinates  $x, y, z$  via the transformation

$$x = \sqrt{r^2 + a^2} \sin(\theta) \cos(\phi), \quad (3.1)$$

$$y = \sqrt{r^2 + a^2} \sin(\theta) \sin(\phi), \quad (3.2)$$

$$z = r \cos(\theta). \quad (3.3)$$

From this relation, we see that the Boyer-Lindquist coordinates simplify to the usual spherical coordinates in the case of a nonspinning black hole. Using these coordinates, the Kerr spacetime metric is given by

$$g_{tt} = -1 + \frac{2Mr}{\Sigma}, \quad (3.4)$$

$$g_{t\phi} = -\frac{2aMr \sin^2 \theta}{\Sigma}, \quad (3.5)$$

$$g_{\phi\phi} = \frac{\Lambda \sin^2 \theta}{\Sigma}, \quad (3.6)$$

$$g_{rr} = \frac{\Sigma}{\Delta}, \quad (3.7)$$

$$g_{\theta\theta} = \Sigma, \quad (3.8)$$

---

with

$$\Sigma = r^2 + a^2 \cos^2 \theta, \quad (3.9)$$

$$\Delta = \varpi^2 - 2Mr, \quad (3.10)$$

$$\varpi^2 = r^2 + a^2, \quad (3.11)$$

$$\Lambda = \varpi^4 - a^2 \Delta \sin^2 \theta. \quad (3.12)$$

All non-specified components of the metric vanish identically. We easily see that the metric does neither depend on the time  $t$  nor on the azimuthal angle  $\phi$ . Thus, by a generalization of *Noether's theorem*<sup>32</sup> to general relativity, the energy,

$$E = -p_t + \frac{1}{2} g_{t\mu,\nu} S^{\mu\nu}, \quad (3.13)$$

and the  $z$ -component of the total angular momentum,

$$J_z = p_\phi - \frac{1}{2} g_{\phi\mu,\nu} S^{\mu\nu}, \quad (3.14)$$

are constants of motion of the Mathisson-Papapetrou equations<sup>33</sup>. These preserved quantities came in handy for our first problem to solve.

### 3.1.1. Initial values for the Mathisson–Papapetrou equations

When we want to compare the different evolutions of the initial value problem (2.1) obtained with the respective prescriptions (1.15) and (1.16) for the calculation of the tangential velocity, we first have to make sure that both systems start very close to each other. This is no trivial task because we cannot simply stipulate the values of  $x_0^\mu$ ,  $p_0^\mu$  and  $S_0^{\mu\nu}$ . If so, we would, firstly, risk to get unphysical values for physically important quantities such as the above-introduced energy (3.13) and, secondly, we would miss another conceptual point: As the different SSCs (1.13) and (1.14) prescribe two different reference frames, the phase space points  $(x_0^\mu, p_0^\mu, S_0^{\mu\nu})$  are not the same in both cases. Hence, even if we gave them the same numerical value at the start of our simulations, one of the respective systems of constraints would not be satisfied.

A way out is to resort to constraints and physically relevant scalar quantities. Each fixed value of such a scalar and each fixed constraint eliminates one variable among  $x_0^\mu$ ,  $p_0^\mu$  and  $S_0^{\mu\nu}$ . In our work on the different SSCs for the MP equations, cf. Chapter A, we could take use of the energy (3.13), the angular momentum (3.14), the mass of the test particle,

$$\mu^2 = -p^\mu p_\mu, \quad (3.15)$$

the spin length,

$$S^2 = \frac{1}{2} S^{\mu\nu} S_{\mu\nu}, \quad (3.16)$$

---

<sup>32</sup> The theorem states that every symmetry of a system leads to a corresponding conserved quantity.

<sup>33</sup>  $g_{\kappa\mu,\nu}$  denotes the derivative with respect to  $x^\nu$  of the metric component  $g_{\kappa\mu}$ .

as well as of the three constraints of the respective SSC in order to reduce the number of variables from 14 to seven. Thanks to the metric’s axisymmetry and its independence of coordinate time, we could further set  $t_0 = \phi_0 = 0$  without any loss of generality. This means that we had to stipulate values for the four physical quantities  $E$ ,  $J_z$ ,  $\mu^2$  and  $S^2$  as well as for five phase space variables<sup>34</sup>. The remaining quantities can then be calculated with the help of the seven relations at hand. In our paper, cf. Subsection A.4.1, we further reduced the number of equations with the help of the following relations: For the SSCs one can introduce a spin four-vector via

$$S_\mu = -\frac{1}{2}\eta_{\mu\nu\rho\sigma}u^\nu S^{\rho\sigma}, \quad (3.17)$$

where  $u^\nu = p^\nu/\mu$ , in case of the Tulczyjew SSC, and via

$$S_\mu = -\frac{1}{2\mu}\eta_{\mu\nu\rho\sigma}\omega^\nu S^{\rho\sigma} \quad (3.18)$$

for the Newton–Wigner SSC. The Levi–Civita density tensor  $\eta_{\mu\nu\rho\sigma}$  is introduced in (A.16) below. With the help of the SSCs, one can also infer the inverse relations

$$S^{\rho\sigma} = -\eta^{\rho\sigma\gamma\delta}S_\gamma u_\delta \quad (3.19)$$

and

$$S^{\rho\sigma} = \eta^{\rho\sigma\gamma\delta}S_\gamma \frac{\mu\omega_\delta}{\omega_\nu\omega^\nu}, \quad (3.20)$$

respectively. In terms of the spin four-vectors, the SSCs take the form

$$S_\mu p^\mu \stackrel{!}{=} 0 \quad (3.21)$$

and

$$S_\mu \omega^\mu \stackrel{!}{=} 0. \quad (3.22)$$

For a more thorough discussion on these relations, we refer the interested reader to Subsection A.2.1.

We can ‘spent’ two of the three SSC constraints to go from the spin tensor with six independent data to the four-vector. Furthermore, setting  $t_0 = \phi_0 = 0$ , we can reduce the number of free phase space variables from 14 to ten. Fixing the energy  $E$ , the total angular momentum  $J_z$ , the spin length  $S^2$  and the mass  $\mu^2$  and adding the remaining SSC constraint (3.21) or (3.22), one remains with five phase space variables to stipulate. In the work of Chapter A, we implemented a scheme which takes initial values for  $r$ ,  $\theta$ ,  $p^r$ ,  $S^r$  and  $S^\theta$  as well as values for  $E$ ,  $J_z$ ,  $\mu^2$  and  $S^2$  and then calculates the remaining quantities  $p^t$ ,  $p^\theta$ ,  $p^\phi$ ,  $S^t$  and  $S^\phi$  with a Newton–Raphson

---

<sup>34</sup>Here, we do neither count  $t_0$  nor  $\phi_0$ .

---

root finder applied to the nonlinear system<sup>35</sup>

$$0 = E + p_t + \frac{1}{2\mu} g_{t\mu,\nu} \eta^{\mu\nu\gamma\delta} S_\gamma p_\delta, \quad (3.23)$$

$$0 = J_z - p_\phi - \frac{1}{2\mu} g_{\phi\mu,\nu} \eta^{\mu\nu\gamma\delta} S_\gamma p_\delta, \quad (3.24)$$

$$0 = \mu^2 + g^{\mu\nu} p_\mu p_\nu, \quad (3.25)$$

$$0 = S^2 - g^{\mu\nu} S_\mu S_\nu, \quad (3.26)$$

$$0 = g^{\mu\nu} S_\mu p_\nu, \quad (3.27)$$

see Subsection A.4.1 for more details<sup>36</sup>. Physical experience has it that the terms  $g_{t\mu,\nu} \eta^{\mu\nu\gamma\delta} S_\gamma p_\delta$  and  $g_{\phi\mu,\nu} \eta^{\mu\nu\gamma\delta} S_\gamma p_\delta$  are small compared to  $p_t$  and  $p_\phi$ . Taking this into account, we got very good initial guesses for the iteration by setting  $p_t = E$ ,  $p_\phi = J_z$ , and calculating the initial guess for  $p^\theta$  via Eq. (3.25). As for the spins, we chose  $S^t = S^\theta$  and determined the initial guess for  $S^\phi$  by relation (3.26). With this, we solved the nonlinear equations up to rounding errors within three or four iterations in all our tests.

This told, we could deliver reasonable data with the same physical properties for both settings to start the simulations of the MP equations with. The next step was to provide the appropriate tools to run them. These tools, as all the integration schemes for the evolution of binary systems in this work, rely on Gauss Runge–Kutta methods. Therefore we next give a short summary of their important properties.

### 3.1.2. Gauss Runge–Kutta methods

An  $s$ -stage Gauss Runge–Kutta method is an implicit Runge–Kutta scheme

$$\mathbf{y}_{n+1} = \mathbf{y}_n + h \sum_{i=1}^s b_i f(\mathbf{Y}_i), \quad (3.28)$$

$$\mathbf{Y}_i = \mathbf{y}_n + h \sum_{j=1}^s a_{ij} f(\mathbf{Y}_j), \quad i = 1, \dots, s, \quad (3.29)$$

which belongs to the subclass of the so-called *collocation methods*.

Given an interval  $[\tau_n, \tau_{n+1} = \tau_n + h]$ , stages  $0 \leq c_1 < \dots < c_s \leq 1$ , and an initial value problem

$$\begin{cases} \mathbf{y}(\tau_n) = \mathbf{y}_0, \\ \frac{d\mathbf{y}}{d\tau} = f(\tau, \mathbf{y}), \end{cases} \quad (3.30)$$

the polynomial  $u(\tau)$  of degree  $s$ , satisfying

$$\begin{cases} u(\tau_n) = \mathbf{y}_0, \\ \dot{u}(\tau_n + c_i h) = f(\tau_n + c_i h, u(\tau_n + c_i h)), \quad i = 1, \dots, s, \end{cases} \quad (3.31)$$

---

<sup>35</sup>In the case of the Newton–Wigner SSC, Eq. (3.26) is replaced by Eq. (A.23) and Eq. (3.27) is substituted by  $0 = g^{\mu\nu} S_\mu \omega_\nu$ .

<sup>36</sup>We chose  $r$ ,  $\theta$ ,  $p^r$ ,  $S^r$  and  $S^\theta$  as the free parameters for our initial value finder as these are the quantities which have already been used in (Hartl, 2003a).

is called a *collocation polynomial*.

In order to solve an initial value problem (3.30) *by collocation*, one has to find the polynomial  $u(\tau)$  which satisfies the collocation conditions (3.31). This gives an approximate solution of the initial value problem after a time step  $h$  by setting

$$\mathbf{y}(\tau_{n+1})_{\text{col}} := u(\tau_{n+1}). \quad (3.32)$$

It can now readily be shown, see, e.g., (Hairer *et al.*, 1993), that a collocation method is equivalent to an implicit  $s$ -stage Runge-Kutta scheme (3.28),(3.29) with coefficients

$$a_{ij} = \int_0^{c_i} l_j(\tau) d\tau, \quad (3.33)$$

$$b_j = \int_0^1 l_i(\tau) d\tau. \quad (3.34)$$

Here,  $l_i(\tau)$  denote the *Lagrange-polynomials* of degree  $s$ ,

$$l_i(\tau) = \prod_{i \neq j} \frac{\tau - c_j}{c_i - c_j}. \quad (3.35)$$

Depending on which set of stages  $0 \leq c_1 < \dots < c_s \leq 1$  is chosen, different collocation methods can be constructed<sup>37</sup>. By setting

$$c_i = \frac{1}{2}(1 + \tilde{c}_i), \quad (3.36)$$

with  $\tilde{c}_i$  being the roots of the *Legendre-polynomial* of degree  $s$ , one obtains a *Gauss collocation method* or *Gauss Runge–Kutta method* as they are referred to throughout most of our works. Very importantly, they have the following properties<sup>38</sup>:

- (i) The schemes have a convergence order  $2s$ , i.e., one has

$$\mathbf{y}(\tau_n) - \mathbf{y}_n = \mathcal{O}(h^{2s}), \quad (3.37)$$

which is the highest possible order among all Runge–Kutta schemes, see, e.g., Hairer *et al.* (1993).

- (ii) The collocation polynomial  $u(\tau)$  satisfying the collocation conditions (3.31) is given by the interpolation polynomial through the points  $(\tau_n, \mathbf{y}_n), (\tau_n + c_1 h, \mathbf{Y}_1), \dots, (\tau_n + c_s h, \mathbf{Y}_s)$ . It further satisfies

$$\mathbf{y}(\tau) - u(\tau) = \mathcal{O}(h^s) \quad (3.38)$$

for all  $\tau \in [\tau_n, \tau_{n+1}]$ .

---

<sup>37</sup>A detailed introduction to collocation methods can be found in (Hairer *et al.*, 1993).

<sup>38</sup>An extensive analysis of the listed properties can be found in the monograph (Hairer *et al.*, 2006).

- 
- (iii) The schemes are *symplectic*, i.e., with  $\Phi_h$  denoting their numerical flow which maps the solution  $\mathbf{y}_n$  at one step to the one at the next step via

$$\mathbf{y}_{n+1} = \Phi_h(\mathbf{y}_n), \quad (3.39)$$

one has

$$\left( \frac{\partial \Phi_h(\mathbf{y})}{\partial \mathbf{y}} \right)^T J \left( \frac{\partial \Phi_h(\mathbf{y})}{\partial \mathbf{y}} \right) = J, \quad (3.40)$$

$$J = \begin{pmatrix} 0 & \text{Id} \\ -\text{Id} & 0 \end{pmatrix}.$$

Therefore, Gauss Runge–Kutta methods preserve the structure of symplectic systems. These are systems described by autonomous initial value problems (3.30) whose right hand side is given by

$$f(\mathbf{y}) = J^{-1} \nabla H(\mathbf{y}), \quad (3.41)$$

with a differentiable real valued function  $H$  which is most commonly denoted as *the Hamiltonian*.

- (iv) The schemes are *variational integrators*, i.e., for physical systems described by an action

$$S = \int_{\tau_n}^{\tau_{n+1}} L(\mathbf{y}(\tau), \dot{\mathbf{y}}(\tau)) d\tau \quad (3.42)$$

one can show, cf. Marsden and West (2001), that

$$\mathbf{y}_{n+1} = u(\tau_{n+1}), \quad (3.43)$$

where  $u(t)$  is a minimizer of the discretized action

$$\tilde{S} = \sum_{i=1}^s L(u(\tau_n + c_i h), \dot{u}(\tau_n + c_i h)). \quad (3.44)$$

- (v) The schemes, when applied to systems they share some structure with, preserve the constants of motion up to arbitrarily small errors over extremely long time scales. Furthermore, the overall numerical error growths only linearly in time which is much slower than for explicit standard integration schemes.

When executing a step with a Gauss Runge–Kutta scheme, one first has to solve the system of implicit equations (3.29) via a fixed-point iteration

$$\mathbf{Y}_i^{k+1} = \mathbf{y}_n + h \sum_{j=1}^s a_{ij} f(\mathbf{Y}_j^k). \quad (3.45)$$

This, of course, requires more calculations per time step than an explicit scheme with the same number of stages. But, this extra effort is more than offset by the high accuracy of Gauss Runge–Kutta methods which allows to apply them with a much larger step size. Detailed information on their efficient implementation is given in Seyrich (2013, Section 7) and Hairer *et al.* (2006, Chapters VIII.5 and VIII.6).

Let us now turn towards the evolution of the MP equations.

### 3.1.3. Integrating the Mathisson–Papapetrou equations

From a numerical point of view, we had to solve an initial value problem

$$\begin{cases} \frac{d\mathbf{y}}{d\tau} = f(\mathbf{y}), \\ \mathbf{y}(\tau = 0) = \mathbf{y}_0, \end{cases} \quad (3.46)$$

with  $\mathbf{y} = (t, r, \dots, S^{\theta\phi}, S^{\theta\theta})^T \in \mathbb{R}^{24}$  and  $f : \mathbb{R}^{24} \rightarrow \mathbb{R}^{24}$  specified by the first three lines of the system (2.1) together with the respective SSC we were considering. As of the vector of initial values  $\mathbf{y}_0 \in \mathbb{R}^{24}$ , it can be obtained by our method introduced in Section 3.1.1 above.

As a first step, we noticed that due to the antisymmetry of the tensor  $S^{\mu\nu}$ , the axisymmetry and the stationarity of the Kerr metric, it is sufficient to just evolve

$$\tilde{\mathbf{y}} = \left( r, \theta, p^t, p^r, p^\theta, p^\phi, S^{tr}, S^{t\theta}, S^{t\phi}, S^{r\theta}, S^{r\phi}, S^{\theta\phi} \right)^T \in \mathbb{R}^{12} \quad (3.47)$$

without any loss of information. For the sake of readability, we will skip the tilde in the following.

For the next step, we took use of the following

**Theorem 3.1.** *There exists some Lagrangian function such that the Mathisson–Papapetrou equations of motion can be obtained by minimizing the corresponding action.*

This fact was shown by Porto (2006) based on previous works by Westpfahl (1969) and Bailey and Israel (1975) and says that the Mathisson–Papapetrou equations can be considered as the Euler–Lagrange equations of a suitable Lagrangian<sup>39</sup>. Consequently, they approximately share a common structure with Gauss Runge–Kutta schemes which are in fact variational integrators as we have just explained in the last Subsection 3.1.2. Bearing in mind property (v) mentioned in that Subsection, we thus employed Gauss Runge–Kutta schemes to the initial value problem (3.46) –or rather its 12-dimensional subproblem. In the case of the MP equations supplemented by the Tulczyjew SSC, this yielded an integrator which preserves the constants of motion over very long times as can be seen in Fig. A.9. Additionally, it is much faster than standard explicit schemes as it can be employed with much larger step sizes, cf. Section A.7 from our corresponding publication of Chapter A.

With regard to the Newton–Wigner SSC, we still had to find a way to cope with the implicit specification of the tangential velocity (1.16). Calculating the covariant derivative of  $w_\nu$ , this equation takes the form

$$v^\mu = \frac{1}{\omega_\nu p^\nu} \left( (\omega_\nu v^\nu) p^\mu + S^{\mu\nu} \left[ \frac{d\omega_\nu}{d\tau} - \Gamma_{\nu\mu}^\kappa v^\mu \right] \right), \quad (3.48)$$

i.e.,  $v^\mu$  also appears in the second part of the right hand side. From a mathematical point of view, Eq. (3.48) takes the form

$$\vec{v} = A(x^\mu, p^\mu, S^{\mu\nu}) \vec{v}, \quad (3.49)$$

with  $A \in \mathbb{R}^{4 \times 4}$  and

$$\vec{v} := \left( v^t, v^r, v^\theta, v^\phi \right)^T \in \mathbb{R}^4. \quad (3.50)$$

---

<sup>39</sup> See also (Barausse *et al.*, 2009, Sec. III.A) for a detailed discussion of the topic.

For every inner-stage value  $\mathbf{Y}_i$ ,  $i = 1, \dots, s$ ,  $f(\mathbf{Y}_i)$  has to be calculated for use in the Runge–Kutta implicit system (3.29). Each of this calculations requires the solution of

$$\vec{v}_i = A(\mathbf{Y}_i^x, \mathbf{Y}_i^p, \mathbf{Y}_i^S) \vec{v}_i, \quad (3.51)$$

where  $\mathbf{Y}_i^x$  denote the components of  $\mathbf{Y}_i$  associated with the position variables and where  $\mathbf{Y}_i^p$ ,  $\mathbf{Y}_i^S$  are defined accordingly.

The first idea we introduced was to augment the implicit system (3.29) that has to be solved anyway by adding Eq. (3.51), thus obtaining

$$\begin{pmatrix} \vec{v}_i \\ \mathbf{Y}_i^x \\ \mathbf{Y}_i^p \\ \mathbf{Y}_i^S \end{pmatrix} = \begin{pmatrix} A(\mathbf{Y}_i^x, \mathbf{Y}_i^p, \mathbf{Y}_i^S) \vec{v}_i \\ \mathbf{y}_n^x + h \sum_{j=1}^s a_{ij} \vec{v}_i \\ \mathbf{y}_n^p + h \sum_{j=1}^s a_{ij} f^p(\mathbf{Y}_i^x, \mathbf{Y}_i^p, \mathbf{Y}_i^S, \vec{v}_i) \\ \mathbf{y}_n^S + h \sum_{j=1}^s a_{ij} f^S(\mathbf{Y}_i^x, \mathbf{Y}_i^p, \mathbf{Y}_i^S, \vec{v}_i) \end{pmatrix},$$

$$i = 1, \dots, s. \quad (3.52)$$

But, when implementing this idea, we encountered problems with the convergence regardless of the iteration we applied to the system, cf. Section A.7. As a consequence, the mathematical beauty of the idea notwithstanding, we had to discard it and to search for another solution. For this, we used the following result from linear algebra:

**Theorem 3.2.** *For every matrix  $A \in \mathbb{R}^{n \times n}$ , there exist orthogonal matrices  $U \in \mathbb{R}^{n \times n}$  and  $V \in \mathbb{R}^{n \times n}$  and so-called singular values  $\sigma_1, \dots, \sigma_n$ , such that the singular value decomposition*

$$A = U \Sigma V^T \quad (3.53)$$

holds with  $\Sigma = \text{diag}(\sigma_1, \dots, \sigma_n)$ .

Furthermore, the number of finite valued  $\sigma_i$  is equal to the rank of  $A$  and the nullspace  $\ker(A)$  of  $A$  is given by

$$\ker(A) = \text{span}(v_j | \sigma_j = 0), \quad (3.54)$$

i.e., it is spanned by the columns of  $V$  corresponding to vanishing singular values.

A very stable iterative method for the calculation of the singular value decomposition (3.53) based on  $QR$ -decompositions was developed by Golub and Kahan (1965).

From the fact that Eq. (3.51) can, of course, be written in the form

$$0 = (I - A(\mathbf{Y}_i^x, \mathbf{Y}_i^p, \mathbf{Y}_i^S)) \vec{v}_i =: B(\mathbf{Y}_i^x, \mathbf{Y}_i^p, \mathbf{Y}_i^S) \vec{v}_i, \quad (3.55)$$

we see that  $\vec{v}_i$  is an element of the nullspace of the just-defined matrix  $B$ . Taking into account the physical constraint (1.12), we can further specify  $\vec{v}_i$  to be that very element of  $\ker(B)$ , for which  $v^\mu v_\mu = -1$  holds<sup>40</sup>. Consequently, we could introduce a scheme which takes use of the singular value decomposition algorithm of Golub and Kahan (1965) as follows:

- Calculate

$$B(\mathbf{Y}_i^x, \mathbf{Y}_i^p, \mathbf{Y}_i^S) = I - A(\mathbf{Y}_i^x, \mathbf{Y}_i^p, \mathbf{Y}_i^S). \quad (3.56)$$

<sup>40</sup>From physical considerations, cf. Subsection A.2.2, we know that  $\dim \ker(B) = 1$ .

- Calculate the singular value decomposition of  $B$  and therewith the column of the orthogonal matrix  $V_{.,i}$  corresponding to the only singular value  $\sigma_i$  which is equal to 0.
- Obtain the tangential velocity by renormalizing  $V_{.,i}$  in order to have  $v^\mu v_\mu = -1$ .

In numerical tests it turned out that the computation of the matrix  $B$  and its singular value decomposition was much faster than the other computations in the calculation of the equation of motion’s right hand side<sup>41</sup>, cf. Section A.7.

With the help of our algorithms, the long-time behavior of the Mathisson–Papapetrou equations with the two different SSCs (1.13) and (1.14) could be compared in a thorough numerical study, see Section A.4. The result, in a few words, was that there is a discrepancy between the two prescriptions which is negligible for small spins  $S$  of the test particle but grows linearly as a function of this spin. Namely, the relative error in the mass of the test particle  $\mu^2$ , which is a constant of motion for the MP equations supplemented by the Tulczyjew SSC, has been shown by our numerical investigation to scale with  $S^2$  in the case of the Newton–Wigner SSC. Furthermore, the length of the spin itself is not preserved either. In the range of physically relevant spins, however, the two approximations are in good agreement. This implies that the Hamiltonian approach of Barausse *et al.* (2009) is based on sound foundations, i.e., on a reasonable SSC. In order to check whether the approach itself is justified, we had to develop a long time integration scheme for the arising Hamiltonian equations (1.26)–(1.28).

The according scheme, as well as all our further works on binary systems, relied on a coordinate transformation of the Hamiltonian system which we present next.

### 3.1.4. Symplectic structure of the Hamiltonian approximation

Mathematically speaking, the Hamiltonian equations considered in the course of this thesis possess a so-called *Poisson structure*, i.e., with

$$\mathbf{y} = (P_1, P_2, P_3, x^1, x^2, x^3, S_1, S_2, S_3)^T \in \mathbb{R}^9, \quad (3.57)$$

they can be written as

$$\dot{\mathbf{y}} = B(\mathbf{y})\nabla H(\mathbf{y}), \quad (3.58)$$

where  $B : \mathbb{R}^9 \rightarrow \mathbb{R}^{9 \times 9}$  is a skew-symmetric matrix-valued function given by

$$B(\mathbf{y}) = \begin{pmatrix} 0 & -I_{3 \times 3} & 0 \\ I_{3 \times 3} & 0 & 0 \\ 0 & 0 & B_1(\mathbf{y}) \end{pmatrix}, \quad (3.59)$$

with

$$I_{3 \times 3} = \begin{pmatrix} 1 & 0 & 0 \\ 0 & 1 & 0 \\ 0 & 0 & 1 \end{pmatrix}, \quad (3.60)$$

$$B_1(\mathbf{y}) = \begin{pmatrix} 0 & -S_3 & S_2 \\ S_3 & 0 & -S_1 \\ -S_2 & S_1 & 0 \end{pmatrix}. \quad (3.61)$$

---

<sup>41</sup> This is although the calculation of the singular value decomposition requires quite some iterations. But, still, this effort is negligible in comparison with the calculation of all the tensors appearing in the MP equations. This shows once more how time-consuming simulations in general relativity are (see also Section 3.3).

---

This structure allows us to adapt to our setting a previous result of the author in the realm of post-Newtonian equations, see (Seyrich, 2013). Namely, for the system (3.58) the Euclidean norm  $S$  of the spin vector

$$\mathbf{S} = \begin{pmatrix} S_1 \\ S_2 \\ S_3 \end{pmatrix} \quad (3.62)$$

is preserved due to

$$\frac{dS^2}{dt} = 2 \mathbf{S} \cdot \frac{d\mathbf{S}}{dt} = 2 \mathbf{S} \cdot (\nabla_{\mathbf{S}} H \times \mathbf{S}) = 2 \nabla_{\mathbf{S}} H \cdot (\mathbf{S} \times \mathbf{S}) = 0. \quad (3.63)$$

Hence, the three dimensional spin (3.62) can be written as a function of two variables  $\alpha \in [0, 2\pi)$  and  $\xi \in [0, S]$  as

$$\mathbf{S} = \begin{pmatrix} \sqrt{S^2 - \xi^2} \cos(\alpha) \\ \sqrt{S^2 - \xi^2} \sin(\alpha) \\ \xi \end{pmatrix}. \quad (3.64)$$

Regarding the evolution of the two new variables, we could show the following

**Theorem 3.3.** *The time evolution of the variables  $\alpha$  and  $\xi$ , introduced in relation (3.64), is governed by*

$$\frac{d\xi}{dt} = -\frac{\partial H}{\partial \alpha}, \quad (3.65)$$

$$\frac{d\alpha}{dt} = \frac{\partial H}{\partial \xi}. \quad (3.66)$$

The proof is similar to the one for the post-Newtonian equations in (Seyrich, 2013). We first notice that by definition of  $\alpha$  and  $\xi$ , we have

$$\frac{\partial H}{\partial \alpha} = \frac{\partial H}{\partial S_1} \frac{\partial S_1}{\partial \alpha} + \frac{\partial H}{\partial S_2} \frac{\partial S_2}{\partial \alpha}, \quad (3.67)$$

$$\frac{\partial H}{\partial \xi} = \frac{\partial H}{\partial S_1} \frac{\partial S_1}{\partial \xi} + \frac{\partial H}{\partial S_2} \frac{\partial S_2}{\partial \xi} + \frac{\partial H}{\partial S_3} \frac{\partial S_3}{\partial \xi}, \quad (3.68)$$

$$\frac{\partial S_1}{\partial \alpha} = -\sqrt{S^2 - \xi^2} \sin(\alpha) = -S_2, \quad (3.69)$$

$$\frac{\partial S_2}{\partial \alpha} = \sqrt{S^2 - \xi^2} \cos(\alpha) = S_1, \quad (3.70)$$

$$S_3 = \xi. \quad (3.71)$$

Deriving relation (3.71) with respect to  $t$  yields

$$\frac{d\xi}{dt} = \frac{dS_3}{dt} = \frac{\partial H}{\partial S_1} S_2 - \frac{\partial H}{\partial S_2} S_1. \quad (3.72)$$

Replacing  $S_1$  and  $S_2$  with the help of relations (3.69) and (3.70), respectively, and then applying Eq. (3.67), we arrive at

$$\frac{d\xi}{dt} = -\frac{\partial H}{\partial S_1} \frac{\partial S_1}{\partial \alpha} - \frac{\partial H}{\partial S_2} \frac{\partial S_2}{\partial \alpha} = -\frac{\partial H}{\partial \alpha}, \quad (3.73)$$

which proves the equality (3.65).

Concerning the second statement of the theorem, we equate the time derivatives of  $S_1$  and  $S_2$  given by the equation of motion (3.58) to the ones obtained with the chain rule applied to definition (3.64). This yields

$$\frac{\partial H}{\partial S_2} S_3 - \frac{\partial H}{\partial S_3} S_2 = \frac{dS_1}{dt} = \frac{\partial S_1}{\partial \xi} \frac{d\xi}{dt} + \frac{\partial S_1}{\partial \alpha} \frac{d\alpha}{dt}, \quad (3.74)$$

$$\frac{\partial H}{\partial S_3} S_1 - \frac{\partial H}{\partial S_1} S_3 = \frac{dS_2}{dt} = \frac{\partial S_2}{\partial \xi} \frac{d\xi}{dt} + \frac{\partial S_2}{\partial \alpha} \frac{d\alpha}{dt}. \quad (3.75)$$

Subtracting the second equation multiplied by  $\frac{\partial S_1}{\partial \xi}$  from the first equation multiplied by  $\frac{\partial S_2}{\partial \xi}$  leads to

$$\begin{aligned} & \left( \frac{\partial S_1}{\partial \alpha} \frac{\partial S_2}{\partial \xi} - \frac{\partial S_2}{\partial \alpha} \frac{\partial S_1}{\partial \xi} \right) \frac{d\alpha}{dt} = \frac{\partial H}{\partial S_2} \frac{\partial S_2}{\partial \xi} S_3 - \frac{\partial H}{\partial S_3} \frac{\partial S_2}{\partial \xi} S_2 \\ & - \frac{\partial H}{\partial S_3} \frac{\partial S_1}{\partial \xi} S_1 + \frac{\partial H}{\partial S_1} \frac{\partial S_1}{\partial \xi} S_3. \end{aligned} \quad (3.76)$$

This equation, in turn, can be transformed to

$$S_3 \frac{d\alpha}{dt} = S_3 \left( \frac{\partial H}{\partial S_1} \frac{\partial S_1}{\partial \xi} + \frac{\partial H}{\partial S_2} \frac{\partial S_2}{\partial \xi} + \frac{\partial H}{\partial S_3} \frac{\partial S_3}{\partial \xi} \right). \quad (3.77)$$

The term in brackets can be replaced with the help of relation (3.68) whereafter a division by  $S_3$  yields the second equality of the above theorem.

Crucially, theorem 3.3 states that the Hamiltonian approximation to the Mathisson–Papapetrou equations, when expressed in new variables

$$\mathbf{z} := (P_1, P_2, P_3, \xi, x^1, x^2, x^3, \alpha) \in \mathbb{R}^8, \quad (3.78)$$

is of symplectic form, i.e., the equations of motion are given by

$$\frac{d\mathbf{z}}{dt} = J^{-1} \nabla H(\mathbf{z}). \quad (3.79)$$

Let us now explain how we used this fact for the numerical treatment of the equations.

### 3.1.5. Integrating the Hamiltonian equations

Having shown that the Hamiltonian equations of Barausse *et al.* (2009) possess a symplectic structure, we applied the Gauss Runge–Kutta schemes introduced in Subsection 3.1.2<sup>42</sup>. Doing so, we could provide an accurate and efficient scheme which easily outperforms its explicit rivals as is illustrated in Fig. A.10 of our corresponding paper, cf. Chapter A. With the help of our scheme, the Hamiltonian formalism of Barausse *et al.* (2009) could be compared to the evolution governed by the Mathisson–Papapetrou equations supplemented by the Newton–Wigner SSC in numerical long time studies, cf. Section A.5. But, before being able to compare the respective results, one further obstacle had to be removed:

<sup>42</sup>With the results of the last Subsection in mind, this now seems to be a trivial exercise. However, implementing an integrator for the general relativistic kind of Hamiltonian equations is no easy task, c.f. Section 3.3.

---

The evolution of the Mathisson–Papapetrou equations were calculated with respect to proper time  $\tau$ . The Hamiltonian approximation, in turn, relies on a parametrization by coordinate time  $t$ . As we did not want to reformulate the MP equations and implement and run them again<sup>43</sup>, we instead pursued the following idea: Having the time-component of the velocity,  $v^t$ , at hand, we could calculate the coordinate time  $t_{\text{MP}}$  corresponding to the proper time of each output we had from the MP evolutions. These times were fed as input to the Hamiltonian simulations. Then, if in the simulation of the Hamiltonian system one of these times was crossed between two time steps  $t_i$  and  $t_{i+1}$ , we used the collocation property of the Gauss schemes, cf. property (ii) in Subsection 3.1.2. More precisely, we calculated, at negligible computational costs, the values of the collocation polynomial  $u$  at time  $t_{\text{MP}}$ . Owing to the approximation property (3.38) of  $u(t)$ , we thus obtained the results of the Hamiltonian equations of motion up to  $\mathcal{O}(h^s)$ . These results could then be compared to the projection onto the Hamiltonian subspace of the MP phase space variables at  $t_{\text{MP}}$ .

The numerical studies showed clear discrepancies between the respective evolutions for large spins. Similarly to the differences between the particular SSCs, these discrepancies declined with the spin magnitude. Hence, for physically reasonable spins of  $10^{-6} \leq S \leq 10^{-4}$ , the Hamiltonian approximation was in good agreement with the MP equations. This proved that the Hamiltonian approach does indeed yield a good approximation to the Mathisson–Papapetrou equations with NW SSC.

But as mentioned above, the Hamiltonian in (Barausse *et al.*, 2009) is based on a reference system fixed by a not-well-motivated choice of tetrad<sup>44</sup>. Not surprisingly, we wanted to check the viability of this tetrad. Let us talk about the according endeavor in the following.

### 3.1.6. Triggering the search for physical tetrads

One of the most reliable ways of investigating the viability of physical assumptions is to check whether scalar physical quantities, which are known to be constants of motion, are preserved under the assumptions in consideration. In Kerr spacetime both the energy (3.13) and the  $z$ -component of the total angular momentum (3.14) are constants of the MP equations, no matter which SSC is used, i.e., regardless of whether or not some tetrad field appears in the SSC. Therefore, we looked at the physically interesting limit of a Schwarzschild spacetime. This historically first and easier analytic solution to Einstein’s field equations (1.1) represents the nonrotating limit  $a \rightarrow 0$  of the Kerr spacetime. It is well-known, see, e.g., (Suzuki and Maeda, 1997), that in a Schwarzschild the total angular momentum is preserved. This gave us two more criteria to check the tetrad field with. For this, we set  $a = 0$  and repeated our Hamiltonian simulations, measuring  $J_x$  and  $J_y$  in the process. It turned out, cf. Fig B.1 in Section B.3, that neither of the additional constants of motion was preserved. With this, we showed that the Hamiltonian approach in its original form in (Barausse *et al.*, 2009) leads to artifacts when physically important quantities are looked at.

This was the starting point of the search for a better suited tetrad field, i.e., a more physical observer frame, to build a Hamiltonian upon. In the wake of this enterprise, our collaborators from the theoretical physics community came up with various new tetrads based on a refined formalism of Barausse and Buonanno (2010). These new tetrads are introduced and analyzed

---

<sup>43</sup>Cf. Section 3.3.

<sup>44</sup>The exact form of this tetrad can be found in Eqs. (A.51).

in the paper corresponding to Chapter B together with an improved tetrad of Barausse and Buonanno (2010). The numerical investigation of their behavior required integration tools for some more Hamiltonian equations of motion. As, from a numerical point of view, all the Hamiltonians obtained with the respective tetrads have the same structure (3.58) as the original one, we could again take use of their symplectic structure and employ Gauss Runge–Kutta methods in order to obtain efficient integrators. Theoretically, this sounds nice. However, each new tetrad gives rise to a completely different Hamiltonian, which then has to be derived with respect to  $x^i$ ,  $P_i$  and  $S^I$ . This yields a totally new set of equations of motion to be implemented.

What is more, the new Hamiltonians are based on different coordinates. The tetrads introduced in Section B.4 from our publication of Chapter B use the so-called *Kerr–Schild* coordinates. By doing so, one disadvantage of the Boyer–Lindquist coordinates could be circumvented. To be more precise, the Kerr metric in Boyer–Lindquist coordinates (3.4)–(3.8) has two singularities. One is given by  $\Sigma = 0$ , the other by  $\Delta = 0$ . It turns out that the singularity  $\Delta = 0$  is a coordinate singularity<sup>45</sup>. As a consequence, numerical simulations, when approaching this singularity, risk to break down although the test particle is still somewhat away from the central anomaly. The metric in Kerr–Schild coordinates (B.49) does not have this singularity<sup>46</sup>, thus allowing numerical simulations to go closer to the central black hole. This convenient property of the Kerr–Schild coordinates is illustrated in Fig. B.6 from our publication of Chapter B. On the other hand, the Hamiltonian equations in these coordinates, although sharing the same Poisson structure, consist of even more terms than the Hamiltonian equations in Boyer–Lindquist coordinates.

From a physical point of view, the newly suggested tetrad fields behave much better than the original one as is detailed in Subsections B.4.1 and B.4.2 of our corresponding publication. Combining these findings with the results above, it has thus been shown that a Hamiltonian approximation to the MP equations based on a sensible tetrad field yields reliable results. As a consequence, other convenient properties of a Hamiltonian formalism can be used to further analyze the behavior of extreme mass ratio binary systems. One important aspect is the investigation of a system for chaos with the help of surface sections which was done for the first time in our publication of Chapter B. As the concerning procedure was only outlined very concisely in the publication, we explain it now.

### 3.1.7. Calculating surfaces of sections

For a symplectic system with two degrees of freedom, one of the most reliable tools to check the system for chaos with are so-called *Poincaré sections*<sup>47</sup>. Summarizing their nature in a few words, each time the variable describing one of the two degrees of freedom takes a fixed value, i.e., passes a fixed section, the variable and the corresponding canonically conjugate variable of the other degree of freedom are plotted against each other. Doing so for many sections yields characteristic patterns which look similar to the example in the left panel of Fig. 3.1 for nonchaotic orbits and resemble the example in the right panel of Fig. 3.1 for chaotic systems.

For symplectic systems with more degrees of freedom the calculation of Poincaré sections is

---

<sup>45</sup>Its physical meaning is that of the black hole’s horizon.

<sup>46</sup>Due to this fact, the Kerr–Schild coordinates are said to be ‘horizon penetrating’.

<sup>47</sup>An introduction to Poincaré sections can be found in (Seyrich, 2012, Chapter 2.1).

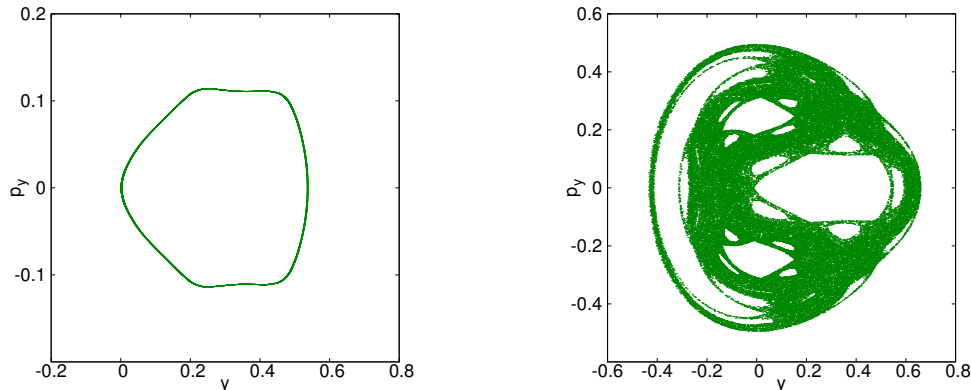


Figure 3.1: Illustration of a Poincaré section for an integrable orbit (left panel) and a chaotic orbit (right panel). Courtesy of Seyrich (2012).

more involved<sup>48</sup>. However, one can still get a first impression of the dynamical behavior with the help of two-dimensional surfaces of section. Here, one again fixes a certain surface and plots two variables at these sections against each other. In our publication of Chapter B, we calculated such sections for the improved Hamiltonian of Barausse and Buonanno (2010). For this, we considered the  $\theta = \pi/2$ -plane and tracked the values at this plane of  $r$  and  $P_r$ . The resulting plots, cf. Fig. B.3, indicate chaotic motion for spinning particles in a Kerr background. This is an interesting physical finding because the hitherto assumption has been that linear-in-spin approximations of spinning test particles cannot yield chaotic motion, c.f. (Hinderer *et al.*, 2013).<sup>49</sup>

The calculation of these sections is also interesting from the numerical point of view, as one cannot expect the simulation to reach the  $\theta = \pi/2$ -plane exactly at the discrete times of the numerical integration. For the implementation of a reliable and convenient algorithm, we could take use of the Gauss Runge-Kutta schemes' collocation property, i.e. property (ii) introduced in Subsection 3.1.2.

In detail, let us suppose we have crossed the plane in the step from  $t_n \rightarrow t_{n+1}$ , i.e.,  $\cos(\theta_n) \cdot \cos(\theta_{n+1}) < 0$ . We can then use the collocation property to calculate the  $\theta$ -component of the collocation polynomial  $u(t)$  and calculate its root  $t_{\text{section}}$  by means of a fast bisection method<sup>50</sup>. With this method, the root is located up to an error of  $\mathcal{O}(h^s)$ . We can then calculate all the other required phase space variables by evaluating  $u(t)$  at time  $t_{\text{section}}$ . Thanks to property (3.38), this yields an approximation to the correct phase space values at the section up to  $\mathcal{O}(h^s)$ . In order to illustrate the accuracy of our proposed approach, we plot the relative error of the Hamiltonian at the sections of Fig. B.3, defined as

$$\Delta H_{\text{section}} = \left| \frac{H(\mathbf{y}(t_{\text{section}})) - H(\mathbf{y}(0))}{H(\mathbf{y}(0))} \right|, \quad (3.80)$$

<sup>48</sup> A study of test particles in a Kerr background which aims to combine constants of motion and an approach for three degrees of freedom of Katsanikas and Patsis (2011) in order to calculate meaningful Poincaré sections is currently in the making.

<sup>49</sup>In the publication of Chapter B, we used a further surface of section, c.f. Fig. B.2, as another proof of the unphysical behavior of the original tetrad of Barausse *et al.* (2009).

<sup>50</sup>Or rather the root of  $u^\theta(t) - \pi/2$ , to be more precise.

in Fig. 3.2.

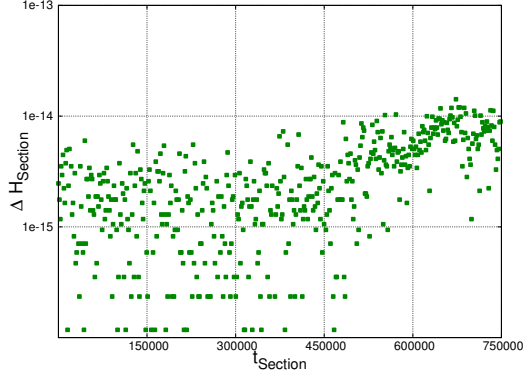


Figure 3.2: The relative error of the Hamiltonian,  $\Delta H_{\text{Section}}$ , calculated for the phase space points of the sections of Fig. B.3.

With this result, we end the summary of our results and contributions concerning the very massive objects. Now, we want to lose some weight and consider the comparably much smaller Cooper electrons. As outlined in the Introduction, their motion in a superconducting material is governed by the time-dependent BCS equations which were the topic of the second part of this thesis.

### 3.2. On the integration of the time-dependent BCS equations

For a given temperature  $T$ , the one-dimensional translation invariant systems of superconducting particles we considered in this thesis are described by the free energy functional

$$\mathcal{F}_T(\Gamma) = \int_{\mathbb{R}} (p^2 - \mu) \hat{\gamma}(p) dp + \int_{\mathbb{R}} |\alpha(x)|^2 V(x) dx - TS(\Gamma), \quad (3.81)$$

where the entropy is now given by

$$S(\Gamma) = - \int_{\mathbb{R}} \text{Tr}_{\mathbb{C}^2} (\Gamma(p) \log \Gamma(p)) dp. \quad (3.82)$$

For such systems with a contact interaction, the critical temperature is implicitly given by

$$\frac{2\pi}{a} = \int_{\mathbb{R}} \frac{\tanh\left(\frac{p^2 - \mu}{2T_c}\right)}{p^2 - \mu} dp, \quad (3.83)$$

and the implicit equation for the energy gap at temperatures  $T < T_c$  takes the form

$$\frac{2\pi}{a} = \int_{\mathbb{R}} \frac{1}{K_T^\Delta} dp, \quad (3.84)$$

with  $K_T^\Delta$  as defined in Eq. (1.38), see, e.g. (Frank *et al.*, 2013).

---

In this setting, the corresponding time-dependent BCS equations are conventionally written in terms of the Fourier transforms, i.e., the momentum space representations

$$\hat{\gamma}_t(p) = \frac{1}{2\pi} \int_{\mathbb{R}} \gamma_t(x) e^{ipx} dx, \quad (3.85)$$

$$\hat{\alpha}_t(p) = \frac{1}{2\pi} \int_{\mathbb{R}} \alpha_t(x) e^{ipx} dx. \quad (3.86)$$

In this basis, the self-consistent equations take the form

$$i\dot{\Gamma}_t(p) = [H_{\Gamma_t(p)}, \Gamma_t(p)], \quad p \in \mathbb{R}, \quad (3.87)$$

where the Hamiltonian is given by

$$H_{\Gamma_t}(p) = \begin{pmatrix} p^2 - \mu & 2[\hat{V} * \hat{\alpha}_t](p) \\ 2[\hat{V} * \overline{\hat{\alpha}_t}](p) & \mu - p^2 \end{pmatrix}, \quad (3.88)$$

with  $*$  denoting the convolution of  $\hat{V}$  with  $\hat{\alpha}_t$ .

As explained in Section 2.2, we were interested in systems at temperatures  $T = T_c(1 + \hbar^2)$  with extensions of  $\mathcal{O}(1/\hbar)$  which is the scale on which physical effects are expected to occur<sup>51</sup>, see e.g. (Frank *et al.*, 2012). In order to render the system computationally feasible, one has to restrict it to a domain  $D = [0, L2\pi]$ ,  $\mathbb{N} \ni L > 1/\hbar$ , and to assume periodic boundary conditions. On the finite domain  $D$ , the momenta consist of the discrete set  $k \in 1/L\mathbb{Z}$ . The momentum space representations of  $\alpha$  and  $\gamma$  are given by

$$\hat{\gamma}_t(k) = \frac{1}{L2\pi} \int_0^{L2\pi} \gamma_t(x) e^{ikx} dx, \quad (3.89)$$

$$\hat{\alpha}_t(k) = \frac{1}{L2\pi} \int_0^{L2\pi} \alpha_t(x) e^{ikx} dx. \quad (3.90)$$

In terms of these representations, the BCS equations read

$$i\dot{\Gamma}_t(k) = [H_{\Gamma_t(k)}, \Gamma_t(k)], \quad k \in \frac{1}{L}\mathbb{Z}, \quad (3.91)$$

where the convolution appearing in the Hamiltonian is now to be understood as

$$(\hat{V} * \hat{\alpha}_t)(k) = \sum_{j \in \mathbb{Z}} \hat{V}_{k-j} \hat{\alpha}_t(j). \quad (3.92)$$

The first step we had to make was to discretize the equations of motion (3.91) in space in order to obtain a system of ordinary differential equations (ODEs).

---

<sup>51</sup>The microscopic scale is  $\mathcal{O}(1)$  for the units we have chosen.

### 3.2.1. Space discretization

As the BCS equations are given in their momentum space representation anyway, the standard way for a space discretization is by means of the so-called *Fourier collocation*. This means that for a fixed number  $K \in \mathbb{N}$ , a  $L2\pi$ -periodic function  $f(x) = \sum_{j \in \mathbb{Z}} \hat{f}(j) e^{ik/Lx}$  is approximated by

$$f^K(x) = \sum_{k=-\frac{K}{2}}^{\frac{K}{2}-1} \hat{f}^K(k) e^{i\frac{k}{L}x}, \quad (3.93)$$

where the coefficients  $\hat{f}^K(k)$  are obtained by the discrete Fourier transform of the values  $f_j = f(L2\pi/K \cdot j)$ ,  $j = -K/2, \dots, K/2 - 1$ . From numerical analysis, cf. (Lubich, 2008, Chapter III.1), we cite the following well-known

**Theorem 3.4.** *Let  $f$  be periodic and  $s$  times continuously differentiable. Let  $f^K$  be the corresponding collocation polynomial (3.93). Then,*

$$\|f(x) - f^K(x)\| \leq CK^{-s}L^s \left\| \frac{d^s f}{dx^s} \right\| \quad (3.94)$$

holds for some constant  $C$  independent of the number of basis functions  $K$ .

In order to obtain an ODE system, we inserted the ansatz

$$\gamma_t^K(x) = \sum_{k=-\frac{K}{2}}^{\frac{K}{2}-1} \hat{\gamma}_t^K(k) e^{i\frac{k}{L}x}, \quad (3.95)$$

$$\alpha_t^K(x) = \sum_{k=-\frac{K}{2}}^{\frac{K}{2}-1} \hat{\alpha}_t^K(k) e^{i\frac{k}{L}x}, \quad (3.96)$$

into the infinite dimensional system (3.91) and used that the contact interactions  $V(x) = -a\delta(x)$  we were interested in are given in momentum the subspace by

$$\hat{V}(k) = -\frac{a}{2L\pi}, \quad -\frac{K}{2} \leq k \leq \frac{K}{2} - 1. \quad (3.97)$$

After some manipulations, c.f. Subsection D.3, this yielded the system

$$\dot{\gamma}_t^K(k) = \frac{2a}{L\pi} \left( q_t(k) \sum_{j=-K/2}^{K/2-1} p_t(j) - p_t(k) \sum_{j=-K/2}^{K/2-1} q_t(j) \right), \quad (3.98)$$

$$i\dot{\alpha}_t^K(k) = 2 \left( \frac{k^2}{L^2} - \mu \right) \alpha_t^K(k) + \frac{a}{L\pi} \sum_{j=-K/2}^{K/2-1} \alpha_t^K(j) (2\gamma_t^K(k) - 1), \quad (3.99)$$

$$-\frac{K}{2} \leq k \leq \frac{K}{2} - 1,$$

where we have defined

$$p_t(k) := \operatorname{Re} \alpha_t^K(k), \quad (3.100)$$

$$q_t(k) := \operatorname{Im} \alpha_t^K(k). \quad (3.101)$$

---

It can readily be seen from Eq. (3.98) that  $\gamma_t^K(k)$  is a real quantity whenever  $\gamma_0^K(k)$  is so. As  $\gamma^K$  represents the physical particle density which is real by definition, we can safely assume  $\gamma_t^K(k)$  to be real in the following.

Concerning the number of basis functions  $K$ , we had to make sure that it was large enough for the resolution of small scales. Resolving small scales in quantum mechanics means taking into account large momenta. This can also be seen from theorem 3.4 and the fact that events on small scales are described by highly oscillating functions  $f$ . In our studies of Chapter C,  $K = 256 \cdot L$  turned out to yield satisfactory results, c.f. Subsection C.7.7.

From a formal mathematical point of view, the system (3.98),(3.99), when supplemented by some initial data, represents an initial value problem

$$\begin{cases} \frac{d\mathbf{y}(t)}{dt} = f(\mathbf{y}(t)), \\ \mathbf{y}(0) = \mathbf{y}_0, \end{cases} \quad (3.102)$$

for

$$\mathbf{y}(t) = \begin{pmatrix} \vec{\gamma}(t) \\ \vec{\alpha}(t) \end{pmatrix} \in \mathbb{C}^{2K}, \quad (3.103)$$

$$\vec{\gamma}(t) = (\gamma_t^K(-K/2) \ \dots \ \gamma_t^K(K/2-1))^T \in \mathbb{R}^K, \quad (3.104)$$

$$\vec{\alpha}(t) = (\alpha_t^K(-K/2) \ \dots \ \alpha_t^K(K/2-1))^T \in \mathbb{C}^K. \quad (3.105)$$

### 3.2.2. Linear BCS equations

In order to obtain the linear approximation to the BCS equations which is the first step towards a possible Ginzburg–Landau formalism, we replaced  $\gamma_t^K(k)$  in the equation of motion for  $\alpha_t^K(k)$  with  $\gamma_0^K(k)$ . This yielded the linear system of equations

$$\begin{aligned} i\dot{\alpha}_t^K(k) &= 2 \left( \frac{k^2}{L^2} - \mu \right) \alpha_t^K(k) + \frac{a}{L\pi} \sum_{j=-K/2}^{K/2-1} \alpha_t^K(j) (2\gamma_0^K(k) - 1), \\ -\frac{K}{2} &\leq k \leq \frac{K}{2} - 1. \end{aligned} \quad (3.106)$$

Seen through our numerical prism, we were given an initial value problem

$$\begin{cases} \frac{d\vec{\alpha}(t)}{dt} = \tilde{f}(\vec{\alpha}(t)), \\ \vec{\alpha}(0) = \vec{\alpha}_0, \end{cases} \quad (3.107)$$

In order to compare its evolutions to those of the full equations, we took the same initial values for both cases and ran simulations over long enough time spans for interesting physical phenomena to occur.

But before we could think about algorithms to run simulations, we first had to find physically reasonable initial values  $\mathbf{y}_0$  to start these simulations with.

### 3.2.3. Initial values for the BCS simulations

Suitable initial data for our simulations had be such that they fell into the range of validity of a possible Ginzburg–Landau description. For the stationary case it was shown by Frank *et al.* (2012) that the Ginzburg–Landau approximation can only hold if the density matrix  $\Gamma$  of the system is such that

$$\mathcal{F}_T(\Gamma) - \mathcal{F}_T(\Gamma^N) \leq \mathcal{O}(h^4) \quad (3.108)$$

holds for  $T = T_c(1 + h^2)$ , with  $h \in \mathbb{R}$  small. This means that the system must be close to the minimizer of the free energy functional, which for temperatures above the critical one is given by the normal state (1.35). As we wanted to find out whether a time-dependent Ginzburg–Landau equation existed, we had to start with initial data  $\Gamma_0$  that fulfilled the constraint (3.108). In order to obtain such data, we used that for temperatures slightly beneath  $T_c$ , i.e.,  $T = T_c(1 - h^2)$ , the minimizer of the free energy functional (1.33) is given by

$$\Gamma^{\min} = \frac{1}{1 + e^{H_\Delta/T}}, \quad (3.109)$$

with

$$H_\Delta = \begin{pmatrix} p^2 - \mu & -\Delta \\ -\Delta & \mu - p^2 \end{pmatrix}, \quad (3.110)$$

where  $\Delta$  is the energy gap defined in (1.37) which for the present setting is implicitly given by (3.84).

Taken this into account, our idea was to proceed as follows:

- For a given  $h$ , determine  $T_c$  with the help of relation (3.83) and set  $T = T_c(1 - h^2)$ .
- For this  $T$ , determine the corresponding energy gap  $\Delta$  via Eq. (3.84).
- Set  $T = T_c(1 + h^2)$  and insert this, together with the just-determined  $\Delta$ , into  $\Gamma^{\min}$  which then, of course, is not a minimizer of the free energy functional anymore, but nearby.
- Choose the initial condition  $\Gamma_0 = \Gamma^{\min}$ .

Calculating the right-hand side of the matrix Eq. (3.109) gives

$$\Gamma_0 = \begin{pmatrix} \hat{\gamma}_0 & \hat{\alpha}_0 \\ \hat{\alpha}_0 & 1 - \hat{\gamma}_0 \end{pmatrix} = \begin{pmatrix} \frac{1}{2} - \frac{p^2 - \mu}{2K_T^\Delta(p)} & \frac{\Delta(p)}{2K_T^\Delta(p)} \\ \frac{\Delta(p)}{2K_T^\Delta(p)} & \frac{1}{2} + \frac{p^2 - \mu}{2K_T^\Delta(p)} \end{pmatrix}. \quad (3.111)$$

As  $\Delta$  is of the order of the small parameter  $h$ , c.f. (Frank *et al.*, 2013), the constraint (3.108) can be shown to hold.

However, when calculating  $T_c$  and  $\Delta$  via the implicit equations (3.83) and (3.84), respectively, we would have determined these values for the continuous system. But, as outlined above, we work with a discrete system. So we had to make sure that the critical temperature we worked with was the critical temperature with respect to our system. Otherwise, it could have happened that we were not close enough to  $T_c$  of the system and, hence, the results of our simulations would only be numerical artifacts.

This said, we resorted to the critical temperature’s equivalent definition (1.39) where we restrict  $V$  and  $K_T$  to the subspace spanned by the  $K$  first eigenfunctions of the Laplacian. Similarly, we use Eq. (1.37) for the calculation of  $\Delta$ . As we outlined the procedure only shortly in our corresponding publication of Section C, we now explain the calculation in detail here.

---

### 3.2.4. Numerical calculation of $T_c$ and $\Delta$

For the following derivation, we use the Dirac bra–ket notation for states on our approximation space. In this notation, the  $L_2$  inner product of two functions  $f^K$  and  $g^K$  on our subspace is given by  $\langle f | g \rangle$ , i.e.,

$$\langle f | g \rangle := \sum_{k=-\frac{K}{2}}^{\frac{K}{2}-1} \widehat{f}(k) g_k. \quad (3.112)$$

The delta potential  $V(x) = -a\delta(x)$  restricted to our subspace can be written as

$$V = -\frac{a}{L2\pi} |\phi\rangle \langle\phi|, \quad (3.113)$$

where  $|\phi\rangle$  is the state

$$\phi(k) = 1, \quad -\frac{K}{2} \leq k \leq \frac{K}{2} - 1. \quad (3.114)$$

Inserting this expression into the implicit Eq. (1.37) for  $\Delta$  and setting  $\psi(p) = \Delta(p)/K_T^\Delta(p)$ , we have

$$\Delta(p) = -c |\phi\rangle \langle\phi| \psi =: \Delta_0 |\phi\rangle. \quad (3.115)$$

Hence,  $\Delta$  is just a multiple of the state  $|\phi\rangle$ . In order to determine  $\Delta_0$ , we start with the second definition of  $\Delta$ , i.e.,

$$\left( K_T^{\Delta_0 \phi} + V \right) |v\rangle = 0, \quad (3.116)$$

where  $|v\rangle$  is the eigenfunction corresponding to the zero eigenvalue. Subtracting  $V |v\rangle$  and dividing by  $K_T^{\Delta_0 \phi}$ , we get

$$|v\rangle = -\frac{1}{K_T^{\Delta_0 \phi}} V |v\rangle, \quad (3.117)$$

or, if we insert expression (3.113),

$$|v\rangle = \frac{a}{L2\pi} \frac{1}{K_T^{\Delta_0 \phi}} |\phi\rangle \langle\phi| v\rangle. \quad (3.118)$$

By multiplying from the left with  $\langle\phi|$  and dividing by  $\langle\phi| v\rangle$ , we arrive at

$$\frac{L2\pi}{a} = \langle\phi| \frac{1}{K_T^{\Delta_0 \phi}} |\phi\rangle. \quad (3.119)$$

Starting with the definition

$$(K_{T_c}^0 + V) |v\rangle = 0, \quad (3.120)$$

and repeating the outlined procedure, we get

$$\frac{L2\pi}{a} = \langle\phi| \frac{1}{K_{T_c}^0} |\phi\rangle. \quad (3.121)$$

In order to obtain  $T_c$  with the help of this equation, we used a bisection method on the interval  $[0, 10]$ <sup>52</sup> to search for the root of

$$f(T_c) = \sum_{k=-K/2}^{K/2-1} \frac{\tanh\left(\frac{\frac{k^2}{L^2} - \mu}{2T_c}\right)}{\frac{k^2}{L^2} - \mu} - \frac{L2\pi}{a}. \quad (3.122)$$

When plotting  $T_c$  as a number of the basis functions  $K$  for fixed  $h$  and  $L$ , c.f. Fig. C.9 from our publication of Chapter C, we found out that  $T_c$  can indeed deviate significantly from the solution of the continuous Eq. (3.83). On the other hand, when choosing a large enough basis  $K = 256 \cdot L$ , no numerical artifacts had to be feared.

We then used a second bisection to find the corresponding  $\Delta$  as the root of

$$f(\Delta) = \sum_{k=-K/2}^{K/2-1} \frac{\tanh\left(\frac{\sqrt{\left(\frac{k^2}{L^2} - \mu\right)^2 + \Delta^2}}{2T_c}\right)}{\sqrt{\left(\frac{k^2}{L^2} - \mu\right)^2 + \Delta^2}} - \frac{L2\pi}{a}. \quad (3.123)$$

The thus obtained  $\Delta$  depended linearly on  $h$ , as can be seen from Fig. C.1 from our work of Chapter C. This is in agreement with the behavior for continuous systems, vide supra.

With  $T_c$  and  $\Delta$  at hand, we could insert them into the discrete analog of Eq. (C.12) and obtained

$$\hat{\gamma}_0^K(k) = \frac{1}{2} - \frac{\frac{k^2}{L^2} - \mu}{2} \frac{\tanh\left(\frac{\sqrt{\left(\frac{k^2}{L^2} - \mu\right)^2 + |\Delta|^2}}{2T}\right)}{\sqrt{\left(\frac{k^2}{L^2} - \mu\right)^2 + |\Delta|^2}} \quad (3.124)$$

$$\hat{\alpha}_0^K(k) = \frac{\Delta}{2} \frac{\tanh\left(\frac{\sqrt{\left(\frac{k^2}{L^2} - \mu\right)^2 + |\Delta|^2}}{2T}\right)}{\sqrt{\left(\frac{k^2}{L^2} - \mu\right)^2 + |\Delta|^2}}. \quad (3.125)$$

As we did not want to run bisection algorithms at the beginning of every simulation, we calculated  $T_c$  and  $\Delta$  for various  $h$  once, and then gave them as input.

Having shown how initial data for the initial value problem (3.102) can be obtained, we now turn towards its time integration. In numerical terms, we want to find a numerical approximation to the exact flow of such an initial value problem. For this, we denote a time step by  $\tau$  and the flow over such a time, i.e., the smooth map between  $\mathbf{y}(t)$  and  $\mathbf{y}(t + \tau)$ , by  $\Phi_{\tau,f}(\mathbf{y}(t))$ . Its numerical approximation will be denoted by  $\Phi_{\tau,f}^{\text{num}}$ . While looking for a suitable  $\Phi_{\tau,f}^{\text{num}}$ , we had to keep in mind the following points.

### 3.2.5. Properties of the discrete BCS equations

When integrating the discrete BCS equations (3.98),(3.99), some properties had to be taken into account. Firstly, we were confronted with a high-dimensional problem as the number of

<sup>52</sup>The upper bound 10 of the interval was chosen very large so that we were sure not to look for  $T_c$  on the wrong interval.

---

basis functions of the space discretization had to be large. This made it particularly urgent to find an integration scheme whose CPU effort increased not too fast as a function of the dimension  $K$ . Secondly, looking at the equation of motion (3.99) for  $\hat{\alpha}^K$ , one can notice that it resembles the linear Schrödinger equation supplemented by a coupling term. In particular, it has the same kinetic part, i.e., the same multiplication operator  $k^2/L^2 - \mu$ . In combination with the first point, this means that the right hand side has a very large Lipschitz constant. Therefore, standard explicit integration tools, such as those of Flannery *et al.* (1992), are of as little help as for the Schrödinger equation. An illustration of this fact can be found in Fig. D.11 from the publication of Chapter D. With regard to this plot, the need for the construction of more suitable integration schemes is obvious. For the construction and testing of such schemes, we could rely on some constants of motion, which we gather in the following

**Theorem 3.5.** *Along solutions of the discrete BCS equations (3.98),(3.99), the eigenvalues of the density matrix  $\Gamma_t^K(k)$ , given by*

$$\lambda_{1,2}(k) = \frac{1}{2} \pm \sqrt{\left(\hat{\gamma}_t(k) - \frac{1}{2}\right)^2 + |\hat{\alpha}_t(k)|^2}, \quad (3.126)$$

and the discretization of the free energy  $\mathcal{F}_T(\Gamma)$ , given by

$$\begin{aligned} F^K(\hat{\gamma}_t^K, \hat{\alpha}_t^K) &= \sum_{k=-K/2}^{K/2-1} \left(\frac{k^2}{L^2} - \mu\right) \hat{\gamma}_t(k) - \frac{1}{L2\pi} \int_0^{L2\pi} |\alpha_t^K(x)|^2 V(x) dx \\ &\quad + T \sum_{k=-K/2}^{K/2-1} [\lambda_1(k) \log(\lambda_1(k)) + \lambda_2(k) \log(\lambda_2(k))], \end{aligned} \quad (3.127)$$

are preserved.

The conservation of the eigenvalues of  $\Gamma^K$  can easily be seen from the fact that its time evolution, as prescribed by its equation of motion (3.87), is unitary. Concerning  $F^K$ , we first notice that the entropy term

$$T \sum_{k=-K/2}^{K/2-1} [\lambda_1(k) \log(\lambda_1(k)) + \lambda_2(k) \log(\lambda_2(k))] \quad (3.128)$$

only depends on the constant eigenvalues and, hence, is preserved, too. In order to show the conservation of the remaining part, we first calculate

$$\begin{aligned} \frac{1}{L2\pi} \int_0^{L2\pi} |\alpha_t^K(x)|^2 V(x) dx &= \sum_{j,k,l} \overline{\hat{\alpha}_t^K(k)} \hat{\alpha}_t^K(j) \hat{V}(l) \frac{1}{L2\pi} \int_0^{L2\pi} e^{ix(-k+j+l)} dx \\ &= \sum_{j,k} \overline{\hat{\alpha}_t^K(k)} \hat{\alpha}_t^K(j) \hat{V}(k-j) \\ &= \sum_k \overline{\hat{\alpha}_t^K(k)} \left(\hat{\alpha}_t^K * \hat{V}\right)(k). \end{aligned} \quad (3.129)$$

For real potentials satisfying  $V(x) = V(-x)$ , we can similarly deduce

$$\frac{1}{L2\pi} \int_0^{L2\pi} |\alpha_t^K(x)|^2 V(x) dx = \sum_k \hat{\alpha}_t^K(k) \left( \overline{\hat{\alpha}_t^K} * \widehat{V} \right) (k). \quad (3.130)$$

With this, we have

$$\frac{dF^K}{dt} = \sum_{k=-K/2}^{K/2-1} \left[ \left( \frac{k^2}{L^2} - \mu \right) \frac{d\hat{\gamma}_t(k)}{dt} + \frac{d\overline{\hat{\alpha}_t^K(k)}}{dt} \left( \hat{\alpha}_t^K * \widehat{V} \right) (k) + \frac{d\hat{\alpha}_t^K(k)}{dt} \left( \overline{\hat{\alpha}_t^K} * \widehat{V} \right) (k) \right]. \quad (3.131)$$

Regarding the term with the time derivative of  $\gamma$ , we can write

$$\left( \frac{k^2}{L^2} - \mu \right) \frac{d\hat{\gamma}_t(k)}{dt} = \frac{1}{2} \text{Tr} \left( \begin{pmatrix} \frac{k^2}{L^2} - \mu & 0 \\ 0 & \mu - \frac{k^2}{L^2} \end{pmatrix} \dot{\Gamma}_t^K(k) \right). \quad (3.132)$$

The other terms can be rewritten as

$$\begin{aligned} & \frac{d\overline{\hat{\alpha}_t^K(k)}}{dt} \left( \hat{\alpha}_t^K * \widehat{V} \right) (k) + \frac{d\hat{\alpha}_t^K(k)}{dt} \left( \overline{\hat{\alpha}_t^K} * \widehat{V} \right) (k) \\ &= \frac{1}{2} \text{Tr} \left( \begin{pmatrix} 0 & 2 \left( \hat{\alpha}_t^K * \widehat{V} \right) (k) \\ 2 \left( \overline{\hat{\alpha}_t^K} * \widehat{V} \right) (k) & 0 \end{pmatrix} \dot{\Gamma}_t^K(k) \right). \end{aligned} \quad (3.133)$$

Inserting the last two reformulations into Eq. (3.131) yields

$$\frac{dF^K}{dt} = \frac{1}{2} \sum_{k=-K/2}^{K/2-1} \text{Tr} \left( H_{\Gamma_t^K(k)} \dot{\Gamma}_t^K(k) \right). \quad (3.134)$$

We can now replace  $\dot{\Gamma}^K$  with its equation of motion (3.87) and use the cyclicity of the trace to obtain

$$\begin{aligned} \frac{dF^K}{dt} &= \frac{1}{2} \sum_{k=-K/2}^{K/2-1} \text{Tr} \left( -i H_{\Gamma_t^K(k)} \left[ H_{\Gamma_t^K(k)}, \Gamma_t^K(k) \right] \right) \\ &= \frac{-i}{2} \sum_{k=-K/2}^{K/2-1} \text{Tr} \left( H_{\Gamma_t^K(k)} H_{\Gamma_t^K(k)} \Gamma_t^K(k) \right) - \text{Tr} \left( H_{\Gamma_t^K(k)} H_{\Gamma_t^K(k)} \Gamma_t^K(k) \right) \\ &= 0. \end{aligned} \quad (3.135)$$

Thus, the discrete energy  $F^K$  is preserved.

Both integration algorithms we developed for this thesis are based on a splitting approach. Therefore, we next give a short introduction to this idea.

---

### 3.2.6. Splitting methods

Splitting methods were first employed for advection equations by Strang (1968) and Marchuk (1968). For quantum dynamical problems, they were applied for the first time by Feit *et al.* (1982) who split the linear Hamiltonian into a kinetic and a potential part. The respective solutions were then concatenated in a suitable way in order to obtain a reliable integration method.

In more detail, let us assume that the right hand side of an initial value problem (3.102) can be written as the sum of two parts

$$f(\mathbf{y}) = f_1(\mathbf{y}) + f_2(\mathbf{y}), \quad (3.136)$$

such that the exact flows  $\Phi_{t,f_1}$  of the problem

$$\begin{cases} \frac{d\mathbf{y}(t)}{dt} = f_1(\mathbf{y}(t)), \\ \mathbf{y}(0) = \mathbf{y}_0, \end{cases} \quad (3.137)$$

and  $\Phi_{t,f_2}$  of the problem

$$\begin{cases} \frac{d\mathbf{y}(t)}{dt} = f_2(\mathbf{y}(t)), \\ \mathbf{y}(0) = \mathbf{y}_0, \end{cases} \quad (3.138)$$

can be obtained more easily than the one of the whole system. Then, a suitable way to obtain a numerical approximation  $\mathbf{y}_1^{\text{num}}$  to the exact solution after a time step  $\tau$ , is to set

$$\mathbf{y}_1^{\text{num}} = \Phi_{\tau,f}^{\text{num}}(\mathbf{y}_0) = (\Phi_{\tau/2,f_2} \circ \Phi_{\tau,f_1} \circ \Phi_{\tau/2,f_2})(\mathbf{y}_0) \quad (3.139)$$

or

$$\mathbf{y}_1^{\text{num}} = \tilde{\Phi}_{\tau,f}^{\text{num}}(\mathbf{y}_0) = (\Phi_{\tau/2,f_1} \circ \Phi_{\tau,f_2} \circ \Phi_{\tau/2,f_1})(\mathbf{y}_0). \quad (3.140)$$

This is the so-called *Strang splitting*. Successively applying the approximated flow  $\Phi_{\tau,f}^{\text{num}}$  yields an approximation to the exact solution at times  $t = n\tau$ ,  $n = 1, 2, \dots$ . With regard to its approximation error, as long as  $\Phi_{t,f_2}$  and  $\Phi_{t,f_1}$  are of second-or-higher order, we have the following

**Theorem 3.6.** *The difference, at time  $t = n\tau$ , between the exact solution  $\mathbf{y}(n\tau)$  to the initial value problem (3.102) and its numerical approximation by the Strang splitting  $\mathbf{y}_n^{\text{num}}$  satisfies*

$$\|\mathbf{y}(n\tau) - \mathbf{y}_n^{\text{num}}\| \leq C(t)\tau^2,$$

where  $C(t)$  is independent of the time discretization parameter  $\tau$ .

We are now in the position to introduce the integration methods we developed for the discrete BCS equations. As both methods have been presented in much detail in the publications of Chapters C and D, we only summarize the main points. Let us start with our first idea.

### 3.2.7. Nonlinear BCS integrator

As the eigenvalues of the density matrix  $\Gamma^K$  are preserved along evolutions of the discrete BCS equations, we have the possibility to express  $\hat{\gamma}_t^K(k)$  in terms of  $\hat{\alpha}_t^K(k)$  and the initial data. After some transformations, c.f. Section D.5, we obtained

$$\hat{\gamma}_t^K(k) = \frac{1}{2} \pm \sqrt{h(k) - |\hat{\alpha}_t^K(k)|^2}, \quad (3.141)$$

with the auxiliary function

$$h(k) := \left( \hat{\gamma}_0^K(k) - \frac{1}{2} \right)^2 + |\hat{\alpha}_0^K(k)|^2. \quad (3.142)$$

The signs in Eq. (3.141) could be inferred from the initial values of for simulations. As can be seen from Eqs. (3.124),(3.125), they were such that  $\hat{\gamma}_0^K(k)$  was greater than  $1/2$  for  $\mu > k^2/L^2$  and less than or equal to  $1/2$  for  $\mu \leq k^2/L^2$ .

With this, we eliminated  $\hat{\gamma}_t^K(k)$  in the equation of motion (3.99) for  $\hat{\alpha}_t^K(k)$ . This resulted in the system

$$\begin{aligned} i\dot{\hat{\alpha}}_t^K(k) &= 2 \left( \frac{k^2}{L^2} - \mu \right) \hat{\alpha}_t^K(k) \pm \frac{a}{L\pi} \langle \phi | \alpha^K \rangle \sqrt{h(k) - |\hat{\alpha}_t^K(k)|^2}, \\ -\frac{K}{2} &\leq k \leq \frac{K}{2} - 1, \end{aligned} \quad (3.143)$$

where we have expressed the contact interaction via the bra-ket notation (3.113). The equation of motion (3.143) is exactly of the form (3.136), with

$$f_2(\vec{\alpha}) = A\vec{\alpha} = \text{diag} \left( 2 \left( \frac{(-K/2)^2}{L^2} - \mu \right), \dots, 2 \left( \frac{(K/2 - 1)^2}{L^2} - \mu \right) \right) \vec{\alpha}. \quad (3.144)$$

The flow of the corresponding subproblem (3.138) can be calculated exactly as

$$\Phi_{\tau,A}(\vec{\alpha}) = \text{diag} \left( e^{-i2 \left( \frac{(-K)^2}{4L^2} - \mu \right) \tau}, \dots, e^{-i2 \left( \frac{(K-2)^2}{4L^2} - \mu \right) \tau} \right) \vec{\alpha}. \quad (3.145)$$

Regarding  $f_1$ , it has a much smaller Lipschitz constant than the complete right hand side  $f$ , wherefore  $\Phi_{\tau,f_1}$  can be approximated by some standard integration scheme. We than followed the idea of the last Subsection and set

$$\Phi_{\tau,f}^{\text{num}}(\vec{\alpha}(0)) = (\Phi_{\tau/2,A} \circ \Phi_{\tau,f_1}^{\text{num}} \circ \Phi_{\tau/2,A})(\vec{\alpha}(0)). \quad (3.146)$$

Very importantly, the calculation of the individual sub-flows only requires  $\mathcal{O}(K)$  operations per step, c.f. Tab. D.1. As  $\Phi_{\tau,A}$  satisfies the group property

$$\Phi_{t,A} \circ \Phi_{s,A} = \Phi_{t+s,A}, \quad (3.147)$$

we could further save CPU costs by combining the last sub-step of the previous step with the first sub-step of the next step. A detailed presentation of the integrator, which we have given the name BCSInt, can be found in Subsection D.5.

The integrator turned out to be very accurate, as can be seen in Fig. C.8 from the publication of Chapter C. However, after we had finished the simulations with the nonlinear BCS equations and had already turned towards the integration of its linear approximation (3.106), we realized that there was an even more efficient and accurate way to integrate the discrete BCS equations with a contact interaction. We also introduce the main ideas behind this scheme.

---

### 3.2.8. Triple splitting integrator

The main idea behind our other algorithm, called *SplitBCS*, is to split the right hand side of the full system (3.98),(3.99) into the three parts

$$f(\vec{\gamma}(t), \vec{\alpha}(t)) = \tilde{A}\mathbf{y}(t) + g(\vec{\alpha}(t)) + h(\vec{\gamma}(t), \vec{\alpha}(t)), \quad (3.148)$$

$$\tilde{A} \begin{pmatrix} \vec{\gamma}(t) \\ \vec{\alpha}(t) \end{pmatrix} = \begin{pmatrix} \vec{\gamma}(t) \\ A\vec{\alpha}(t) \end{pmatrix}, \quad (3.149)$$

$$g(\vec{\alpha}(t)) = \frac{2a}{L\pi} \left( q_t(k) \sum_{j=-K/2}^{K/2-1} p_t(j) - p_t(k) \sum_{j=-K/2}^{K/2-1} q_t(j) \right), \quad (3.150)$$

$$h(\vec{\gamma}(t), \vec{\alpha}(t)) = \frac{a}{L\pi} \sum_{j=-K/2}^{K/2-1} \alpha_t^K(j) (2\gamma_t^K(k) - 1). \quad (3.151)$$

Split in this particular way, the flows of all three subproblems can be calculated exactly in  $\mathcal{O}(K)$  operations. This is shown in detail in the Subsections D.6.1 and D.6.2 of our corresponding publication. The three exact sub-flows are then combined via the composition

$$\Phi_{\tau,f}^{\text{num}} = \Phi_{\tau,AghgA} := \Phi_{\tau/2,A} \circ \Phi_{\tau/2,g} \circ \Phi_{\tau,h} \circ \Phi_{\tau/2,g} \circ \Phi_{\tau/2,A}. \quad (3.152)$$

Leaving out the sub-steps  $\Phi_{\tau/2,g}$ , we also had a convenient integrator for the linear BCS equations. A very detailed description of the algorithm is given in Subsection D.6. In that Subsection, we also analyze the complexity of the respective sub-algorithms which calculate the exact flows of the subproblems. The results of this undertaking are listed in Tab. D.2. It is apparent that SplitBCS requires much less operations than BCSInt for the physically relevant simulation with a delta potential. When testing the accuracy with the method we will outline next, SplitBCS was again ahead of BCSInt.

### 3.2.9. Measuring the integrators' accuracy

A very reliable tool for the investigation of an integrator's reliability is to consider a first integral of the equations of motion under consideration. In our case, we can use the discrete free energy (3.127), or, to be more precise, its relative error along a numerical trajectory defined as

$$\Delta F^K(t) = \left| \frac{F^K(\vec{\gamma}(t), \vec{\alpha}(t)) - F^K(\vec{\gamma}(0), \vec{\alpha}(0))}{F^K(\vec{\gamma}(0), \vec{\alpha}(0))} \right|. \quad (3.153)$$

Tracking  $\Delta F^K(t)$  during our simulations, we could make sure that they were very accurate. With the help of this tool, we could also demonstrate that SplitBCS shows even smaller integration errors than BCSInt. More detail on this can be found in Section D.7 of Chapter D. There, we also show that SplitBCS almost preserves the eigenvalues (3.126) of  $\Gamma^K$ , exactly preserved by construction for BCSInt. As a next step, we extended the integration schemes to systems with general potentials as we outline now.

### 3.2.10. Splitting integrators for general potentials

For general potentials  $V$ , the space discretized BCS equations read

$$i\dot{\gamma}_k(t) = 2 \left[ \alpha_k(t) \overline{(\hat{V} * \alpha)_k} - \overline{\alpha_k(t)} (\hat{V} * \alpha)_k \right], \quad (3.154)$$

$$i\dot{\alpha}_k(t) = 2 \left( \frac{k^2}{L^2} - \mu \right) \alpha_k(t) - 2(2\gamma_k(t) - 1) (\hat{V} * \alpha)_k, \quad (3.155)$$

$$-\frac{K}{2} \leq k \leq \frac{K}{2} - 1,$$

where the convolution of two  $K$ -periodic vectors  $\mathbf{a}$  and  $\mathbf{b}$  is given by

$$(\mathbf{a} * \mathbf{b})_k = \sum_{j=K/2}^{K/2-1} a_{k-j} b_j. \quad (3.156)$$

These convolutions require some extra effort. Fortunately, the terms comprising those convolutions are still well-behaved in the sense that they have a small Lipschitz constant. Furthermore, it is well-known from numerical analysis that the convolution of two  $K$  dimensional vectors can be calculated efficiently with the help of the Fast Fourier Transform (FFT) algorithm as outlined in Section D.4 of our concerning publication<sup>53</sup>.

Thanks to these favorable properties, one can use the same splittings as for the delta case. The flows for the subproblems involving the convolutions can be calculated conveniently with explicit standard integration schemes such as the explicit midpoint rule or the classical Runge–Kutta method. We observed that the numerical errors in the calculation of these subflows were vanishingly small compared to the already small error caused by the splitting of the original problem. As a consequence, we had found accurate integration schemes, whose CPU times per time step are  $\mathcal{O}(\log(K) \cdot K)$ . When comparing the efforts of both schemes, c.f. Subsections D.5.3 and D.6.4, we see that in the general case BCSInt is a bit faster as it requires one convolution less per time step. On the other hand, SplitBCS is even more accurate, c.f. Section D.7.

Additionally, the subproblem

$$i \frac{d\alpha_k(t)}{dt} = h(\vec{\gamma}(0), \vec{\alpha}(t))_k = (2\gamma_k(0) - 1) (\hat{V} * \alpha)_k \quad (3.157)$$

is linear in  $\vec{\alpha}$ . Therefore, its flow  $\Phi_{\tau, h}$  can be approximated up to exponentially small errors with the Lanczos method introduced, for example, in (Lubich, 2008, Chapter III.2.2) with only some additional cost as compared to an integration using the classical Runge–Kutta method. This is useful in applications where the norm of  $\vec{\alpha}$  is of particular interest since the Lanczos method is norm-preserving by construction.

Having generalized our integrators, we can finally summarize the interesting physical results of our simulations.

---

<sup>53</sup>The English version of wikipedia contains a very nice presentation of the FFT algorithm.

---

### 3.2.11. Physical results

We considered the physically important case of systems with a contact interaction. For various values of the small parameter  $\hbar$ , we generated physically interesting initial data via the procedure outlined in Subsection 3.2.4 above. We then simulated the motion as governed by the full BCS equations (3.98),(3.99) and the evolution prescribed by the linear approximation (3.106). In both cases we integrated the system until a final time  $t_{\text{end}} = \mathcal{O}(1/\hbar^2)$ , as this is the time the system needs to show physically relevant effects, see, e.g. (Hainzl and Schlein, 2013). During both simulations, we tracked the behavior of the discretized  $L_2$  norm of the Cooper pair density  $\alpha$ , given by

$$\frac{1}{\hbar^2} \|\alpha_t\|_2^2 = \frac{1}{\hbar^2} \sum_{k=-K/2}^{K/2-1} |\alpha_t^K(k)|^2, \quad (3.158)$$

and the macroscopic Ginzburg–Landau like parameter

$$\psi_t := \frac{1}{\hbar} \langle \alpha^* | \alpha_t \rangle. \quad (3.159)$$

The results are presented in Section C.4 of Chapter C.

To summarize them in a few words: For all values of  $\hbar$ , the linear approximation could not live up to its name. Whereas both  $|\psi_t|$  and  $\|\alpha_t\|_2^2$  decreased exponentially for the evolution of the linear equation, they oscillated around a finite value in the simulations of the full equations. Hence, the diffusion, which would be inherent to any Ginzburg–Landau type equation of motion on the macroscopic scale, can only be an artifact due to an unjustified linearization of the BCS equations. With these results, we could shed light on another important question in physics, this time in the realm of condensed matter physics.

Summarizing the summary, we can say that we achieved all the goals we had set ourselves in Chapter 2. However, the summary would not be complete without an illustration of the most arduous part of the thesis –the implementation of all the simulations we have conducted in the course of it.

## 3.3. On the particular hardships of implementation and simulation

As compared to publications in other fields, physical papers which report on the results of numerical studies tend to be concise. They focus on the results –mostly illustrative plots– and only state shortly on which physical setting the study in question is based. In order to get a feeling for the implementational effort behind a usual computational physics paper, consider our first work on spinning test particles, cf. Chapter A.

In the Mathisson-Papapetrou part, the relevant equations of motion (A.55) are given in their most compact form with the additional information that a Kerr background is used. But, already the single Riemann tensor  $R^\mu_{\nu\kappa\lambda}$  on its own in fact contains  $4 \times 4$  entries, each of which is a complicated function of the given Kerr metric  $g$  and its derivatives which, in turn, are functions of the positions  $x^\mu$ . The Christoffel symbols  $\Gamma^\mu_{\kappa\lambda}$ , too, are multivalued functions of the positions. As a consequence, the detailed expressions on the right side of the equations of

motion require pages and pages of analytical calculations. Even when painstakingly simplifying and merging as many terms as possible, the resulting subroutine of our *FORTRAN* code which, given some phase space variables  $x^\mu$ ,  $p_\mu$  and  $S^{\mu\nu}$ , calculates the right hand side of the equations of motion (A.55), ran up to more than thousand lines of code. The implementation of the right side of the formally very nice Hamiltonian equations of motion (A.45)-(A.47) for the compactly represented Hamiltonian (A.35) also requires hundreds of lines of codes. This is not surprising taking into account that, in order to arrive at the equations of motion, all the functions showing up in the Hamiltonian terms (A.53) have to be derived with regard to  $x^i$ ,  $P_i$  and  $S^I$  first. So it is easily understandable that, conventionally, the reader is spared the pain of reading through all this calculations. Furthermore, bearing this complexity in mind, it is not hard to see why progress in computational physics is perhaps somewhat slow compared to other fields. But how can one make sure that, at the end of the day, one has a reliable bug-free code calculating the correct quantities?

The first step of writing a simulation is, of course, the analytical calculation of the quantities appearing in the equations of motion's right hand side. In order to exclude implementation errors, i.e., in order to make sure that the code is actually calculating what the analytical formulas are saying, one can make use of a symbolical calculation tool such as Mathematica in our case. These programs take the equations in their compact form and, once all the quantities the compact formulations rely on are specified and a set of parameters is given, calculate the corresponding result. This result can then be compared with the numbers obtained via the implemented code. This requires a lot of patience but is by far the safest way of bug-finding.

Next, one has to make sure that the analytical calculations are correct in the first place. Here, it is of great help to have some quantities at hand which are known to be preserved under the exact evolution of the equations of motion. These are, for example, the energy (A.3) in case of the Mathisson–Papapetrou equations with a Kerr background metric or the Hamiltonian (A.35) in the work of Chapter A. For the schemes we have developed and implemented during this thesis, the constants of motion should almost be preserved, cf. Subsection 3.1.2. More precisely, their relative errors such as (A.83) are expected to be and stay small for not-too-large time steps and have to decrease in line with the step size. Hence, if the relative errors are large and do not decline for decreasing time steps, the evolution equations and the ‘constants of motion’ do not belong to each other. As implementation errors have been excluded before, the underlying calculations cannot be correct.

All told, we had to do a lot of cumbersome bug-finding but can now be very sure that the simulations which will be presented in detail in the following Chapters are based on correct calculations and bug-free implementations.

---

## Acknowledgements

I would like to use this opportunity to thank all the people who, in one way or another, contributed to this thesis or to my well-being while working on it. First and foremost, I want to thank my supervisor, Prof. Dr. Christian Lubich, for all his support over the last four years. In scientific and even more in personal aspects, I have learned a lot from him. Should I ever have to lead a group in the future, I hope I can do it as well as he does.

Working on this PhD, I closely collaborated with two nice people whom it always was a great pleasure to work with. One paper was written with my second supervisor, the amazing Prof. Dr. Christian Hainzl. I appreciated his advice very much. Besides, it was really fun having a beer together. Already from the time as a Diploma student, I know Georgios Lukes-Gerakopoulos, now in Prague, who in the meantime is a very good friend to me.

Christian, Christian and Georgios, thank you also especially for lending my an ear whenever necessary.

I also want to thank Daniela Kunst and Tomáš Ledvinka for the fruitful collaboration and for their essential work for “a really good paper one can be quite proud of having contributed to”, in the words of Georgios.

During my time as a PhD student I profited very much from the interaction with the nice people around. The Numerical Analysis Group can pride itself for a really and unusually good atmosphere among its members and every single member is contributing to this. Therefore, I want to thank Hanna Walach, Bernd Brumm, Dhia Mansour, Christian Power, Balázs Kovács, Marius Bruchhäuser, Anh Thy Tran, Raphael Rieber and, once again, our sociable boss Christian Lubich. Furthermore, I really enjoyed the lively discussions in my office with Bernd Brumm, Alexander Seizinger, Christopher Nerz, Markus Klein, Peter Vastag, Günter Lang and Daniel Thun. All this was of great help to stay in a good mood even when experiments turned out not to be as satisfactory as they were supposed to. But even more, it was real fun and I have found some more good friends for life.

Of course, the two persons I owe the most grateful thanks are my parents. For 28 years now they are around with their help and advice whenever necessary –and even when not.

For all the things I did, I do and I possibly will do in my life, there is one thing I am by far the most proud of. On the 27th of September in 2014, I married the love of my life, Elena. If I were asked to rank the achievements in my life, everything, including this work, will at most come a distant second to hearing her saying ‘Yes’. Thank you so much, this work is for you!

This work was partly supported by the DFG grants SFB/Transregio 7 and GRK 1838.

---

# A. Investigating spinning test particles: spin supplementary conditions and the Hamiltonian formalism

The content of this Section was published as [G. Lukes-Gerakopoulos, J. Seyrich, and D. Kunst, *Phys. Rev. D* **90**, 104019 (2014)] under lead-authorship of Georgios Lukes-Gerakopoulos. The physical studies, during which the plots in Figs A.1,A.2,A.3,A.4,A.5,A.6,A.7,A.8 were generated, were carried out by Georgios Lukes-Gerakopoulos with the codes of of J. S. . The studies are based on theoretical input by Daniela Kunst.

## Abstract

In this paper we report the results of a thorough numerical study of the motion of spinning particles in Kerr spacetime with different prescriptions. We first evaluate the Mathisson-Papapetrou equations with two different spin supplementary conditions, namely, the Tulczyjew and the Newton-Wigner, and make a comparison of these two cases. We then use the Hamiltonian formalism given by Barausse *et al.* (2009) to evolve the orbits and compare them with the corresponding orbits provided by the Mathisson-Papapetrou equations. We include a full description of how to treat the issues arising in the numerical implementation.

## A.1. Introduction

Since we expect that the centers of galaxies are occupied by super-massive black holes, relativistic binary systems with extreme mass ratios are of great interest. A first approximation to an extreme mass ratio inspiral (EMRI) is the geodesic motion where the spin of the smaller particle is ignored. More relevant models have to incorporate the spin. This, however, appears not to be so simple.

The equations of motion of a spinning particle were given by Mathisson (1937) and Papapetrou (1951) several decades ago. The Mathisson-Papapetrou (MP) equations are not a closed set of first order ordinary differential equations, i.e., there are less equations than necessary in order to evolve the system. To close the set, an extra spin supplementary condition (SSC) is required. Over the years, various such SSCs have been proposed (see, e.g., (Semerák, 1999; Kyrian and Semerák, 2007) for a review).

As a SSC fixes a center of reference, e.g., the center of the mass, and different SSCs define different centers, for each SSC we have a different world line (see, e.g., (Kyrian and Semerák, 2007)), and, hence, each SSC prescribes a different evolution of the MP equations. But, although this ambiguity appears to be a major issue in the modeling of an EMRI binary system, the difference in the evolution caused by different SSCs has not received the adequate attention. Our work aims at quantifying those evolution differences in a Kerr spacetime background.

The first part of the study addresses the above issue by examining how “similar” initial conditions diverge when they are evolved by using different SSCs. We focus on two SSCs,

---

namely the Tulczyjew (T) SSC (Tulczyjew, 1959) and the Newton-Wigner(NW) SSC (Newton and Wigner, 1949), as introduced by Barausse *et al.* (2009). T SSC is a standard SSC that has been used in several works concerned with different topics, see, e.g., (Semerák, 1999; Kyrian and Semerák, 2007; Dixon, 1970; Mino *et al.*, 1996; Hartl, 2003a; Steinhoff and Puetzfeld, 2012). On the other hand, NW SSC has been successfully implemented in the framework of the Post-Newtonian approximation (Steinhoff *et al.*, 2008; Steinhoff, 2011), and it is the only SSC allowing for a canonical Hamiltonian formalism, albeit only up to linear order in the spin of the particle in curved spacetimes. This Hamiltonian formalism has been derived in (Barausse *et al.*, 2009). As it has many practical advantages to have a Hamiltonian formulation of a given problem at hand, for example because it is part of the effective one body formulation (Barausse *et al.*, 2009; Barausse and Buonanno, 2010), it would be nice to see if orbits obtained via the Hamiltonian formalism of Barausse *et al.* (2009) stay close to those obtained with the help of the full MP equations in the case of NW SSC (a discussion on the topic can be found in Sec. IV of (Hinderer *et al.*, 2013)). Therefore, in the second part of our work, we compare both approaches numerically.

A numerical investigation of the equations considered in this work entails a bunch of interesting numerical challenges. To start with, a useful study of the divergence of different orbits should straddle a reasonably long time interval. The efficient integration of equations of motion over a long time interval requires structure preserving algorithms (see, e.g., (Hairer *et al.*, 2006) for an elaborate overview) such as symplectic schemes, which have been successfully applied for simulations in various fields of general relativity, e.g., (Seyrich and Lukes-Gerakopoulos, 2012; Seyrich, 2013; Zhong *et al.*, 2010; Mei *et al.*, 2013). Moreover, the MP equations have no Hamiltonian structure, wherefore one would expect usual symplectic integration schemes to lose their theoretical advantage over ordinary, not so efficient ones. What is more, in the NW SSC case part of the equations of motion will turn out to be known only implicitly. In this work we will explain how, notwithstanding the just mentioned obstacles, the MP equations can be evolved accurately in an efficient way for both SSCs. When comparing orbits calculated via the MP equations with those obtained by the Hamiltonian equations of (Barausse *et al.*, 2009), one is faced with the problem of different evolution parameters. We thus come up with a comfortable way of guaranteeing output at consistent times.

The paper is organized as follows. In Sec. A.2 we introduce the MP equations and give a brief discussion on the SSCs. Then, we turn to the Hamiltonian formalism in Sec. A.3, where the basic elements concerning the Hamiltonian function, which describes the motion of a spinning particle in curved spacetime, are summarized. In Sec. A.4 we explain how the simulations with the MP equations are done, and a comparison between the T and the NW SSC is provided, whilst Sec. A.5 quantifies the difference in the evolution of orbits between the MP equations and their Hamiltonian approximation. Finally, we discuss our main results in Sec. A.6. A detailed discussion of the numerical implementation is provided in the Appendix (Secs. A.7 and A.8).

The units we use are geometric ( $G = c = 1$ ), and the signature of the metric is  $(-, +, +, +)$ . Greek letters denote the indices corresponding to spacetime (running from 0 to 3), while Latin ones denote indices corresponding only to space (running from 1 to 3). We use capital letters for the indices when referring to a flat spacetime. In general, we try to follow the notation of Barausse *et al.* (2009) whenever this is possible.

## A.2. Mathisson-Papapetrou equations

The Mathisson-Papapetrou equations describe the motion of a particle with mass  $\mu$  and spin  $S^{\mu\nu}$  (pole-dipole approximation) in a given background  $g_{\mu\nu}$ . Their formulation in (Dixon, 1970) reads

$$\frac{D p^\mu}{d\tau} = -\frac{1}{2} R^\mu{}_{\nu\kappa\lambda} v^\nu S^{\kappa\lambda} \quad , \quad (\text{A.1})$$

$$\frac{D S^{\mu\nu}}{d\tau} = p^\mu v^\nu - v^\mu p^\nu \quad , \quad (\text{A.2})$$

where  $p^\mu$  is the four-momentum,  $v^\mu = dx^\mu/d\tau$  is the tangent vector to the world line along which the particle moves,  $\tau$  is the proper time along this world line, and  $R^\mu{}_{\nu\kappa\lambda}$  is the Riemann tensor. In the case of a stationary and axisymmetric spacetime, the energy

$$E = -p_t + \frac{1}{2} g_{t\mu,\nu} S^{\mu\nu} \quad , \quad (\text{A.3})$$

and the  $z$  angular momentum

$$J_z = p_\phi - \frac{1}{2} g_{\phi\mu,\nu} S^{\mu\nu} \quad , \quad (\text{A.4})$$

are preserved along the solutions of the MP equations.

Since we selected  $\tau$  to be the proper time, it holds that  $v^\nu v_\nu = -1$ . By multiplying Eq. (A.2) with  $v_\nu$  we get

$$p^\mu = m v^\mu - v_\nu \frac{D S^{\mu\nu}}{d\tau} \quad , \quad (\text{A.5})$$

where  $m = -p^\nu v_\nu$  is the rest mass of the particle with respect to  $v^\nu$ , while the measure of the four-momentum  $p^\nu p_\nu = -\mu^2$  provides the rest mass  $\mu$  with respect to  $p^\mu$ .  $m = \mu$  holds only if the tangent vector  $v^\nu$  coincides with the four-velocity  $u^\nu = p^\nu/\mu$ .

It is useful to stress that neither of the masses have to be a constant of motion. Namely, for  $m$  we get

$$\frac{dm}{d\tau} = \frac{D m}{d\tau} = -\frac{D v_\nu}{d\tau} p^\nu \quad ,$$

since from Eq. (A.1) we see that  $\frac{D p^\nu}{d\tau} v_\nu = 0$ , and by using Eq. (A.5) for replacing  $p^\nu$ , we arrive at

$$\frac{dm}{d\tau} = \frac{D v_\nu}{d\tau} v_\mu \frac{D S^{\nu\mu}}{d\tau} \quad . \quad (\text{A.6})$$

For  $\mu$  we have

$$\frac{d\mu}{d\tau} = \frac{D \mu}{d\tau} = -\frac{p_\nu}{\mu} \frac{D p^\nu}{d\tau} \quad ,$$

and again by using Eq. (A.5) for replacing  $p^\nu$ , we get

$$\frac{d\mu}{d\tau} = \frac{D p_\nu}{d\tau} \frac{p_\mu}{\mu m} \frac{D S^{\nu\mu}}{d\tau} \quad . \quad (\text{A.7})$$

---

The same holds for the spin measure

$$S^2 = \frac{1}{2} S_{\mu\nu} S^{\mu\nu} . \quad (\text{A.8})$$

Here, we have

$$\frac{d S^2}{d\tau} = \frac{D S^2}{d\tau} = S_{\mu\nu} \frac{D S^{\mu\nu}}{d\tau} , \quad (\text{A.9})$$

and by Eq. (A.2) we get

$$\begin{aligned} \frac{d S^2}{d\tau} &= S_{\mu\nu} (p^\mu v^\nu - v^\mu p^\nu) \\ &= 2S_{\mu\nu} p^\mu v^\nu , \end{aligned} \quad (\text{A.10})$$

which becomes zero if

$$S_{\mu\nu} p^\mu = 0 , \quad (\text{A.11})$$

or

$$S_{\mu\nu} v^\mu = 0 . \quad (\text{A.12})$$

Eq. (A.11) is the Tulczyjew SSC, while Eq. (A.12) is the Pirani SSC (Pirani, 1956). From Eq. (A.7) we see that  $d\mu/d\tau = 0$  for T SSC, while for Pirani SSC  $dm/d\tau = 0$ . The MP equations with Pirani SSC exhibit a “strange” helical motion (see, e.g., (Kyriani and Semerák, 2007)), which has been considered as unphysical. However, recently, Costa *et al.* (2012) argued that the helical motion can be interpreted by the concept of a hidden electromagnetic-like momentum. We will not discuss Pirani SSC further. Instead, we are going to focus on the Newton-Wigner SSC, which reads

$$S^{\mu\nu} \omega_\mu = 0 , \quad (\text{A.13})$$

where  $\omega_\mu$  is a time-like vector, or a sum of time-like vectors, e.g., of  $p_\mu$  and  $\varphi_\mu$ , i.e.,

$$\omega_\mu = p_\mu + \mu \varphi_\mu . \quad (\text{A.14})$$

In general, for NW SSC, neither the masses, Eqs. (A.6), (A.7), nor the spin, Eq. (A.8), are preserved. Thus, from this point of view it is a strange selection of a SSC. However, we should keep in mind that our framework is a pole-dipole approximation. Therefore it is somehow adequate for the just mentioned quantities to be conserved only up to linear order in the spin. For the spin, this can be seen from Eq. (A.9) but for the mass  $\mu$  the proof is quite more complicated and was provided by Barausse *et al.* (2009).

### A.2.1. Spin four-vector

Instead of the spin tensor  $S^{\mu\nu}$ , a spin four-vector  $S^\mu$  is used sometimes, since  $S^\mu$  is often considered more physically intuitive and more convenient than  $S^{\mu\nu}$ , see, e.g., (Suzuki and Maeda, 1997).

For the T SSC the four-vector is defined by

$$S_\mu = -\frac{1}{2}\eta_{\mu\nu\rho\sigma}u^\nu S^{\rho\sigma} \quad , \quad (\text{A.15})$$

where  $\eta_{\mu\nu\rho\sigma}$  is the Levi-Civita density tensor

$$\eta_{\mu\nu\rho\sigma} = \sqrt{-g} \epsilon_{\mu\nu\rho\sigma} \quad , \quad (\text{A.16})$$

and  $\epsilon_{\mu\nu\rho\sigma}$  is the Levi-Civita symbol with  $\epsilon_{0123} = -1$ . The inverse relation of Eq. (A.15) between the two spin forms is

$$S^{\rho\sigma} = -\eta^{\rho\sigma\gamma\delta} S_\gamma u_\delta \quad . \quad (\text{A.17})$$

By replacing the last equation in Eq. (A.8), we get

$$S^2 = S_\mu S^\mu \quad . \quad (\text{A.18})$$

From Eq. (A.15) we see that

$$S_\mu p^\mu = 0 \quad , \quad (\text{A.19})$$

so the spin four vector is perpendicular to the momentum.

For the NW SSC we define the four-vector as

$$S_\mu = -\frac{1}{2} \frac{1}{\mu} \eta_{\mu\nu\rho\sigma} \omega^\nu S^{\rho\sigma} \quad . \quad (\text{A.20})$$

By this definition we fix that

$$S_\mu \omega^\mu = 0 \quad . \quad (\text{A.21})$$

Thus, the spin four vector is perpendicular to the time-like vector  $\omega_\mu$ . In the NW case the inverse relation of Eq. (A.20) between the two spin forms is

$$S^{\rho\sigma} = \eta^{\rho\sigma\gamma\delta} S_\gamma \frac{\mu \omega_\delta}{\omega_\nu \omega^\nu} \quad . \quad (\text{A.22})$$

Now, the spin measure (A.8) reads

$$S^2 = -\frac{\mu^2}{\omega_\nu \omega^\nu} S_\sigma S^\sigma \quad . \quad (\text{A.23})$$

The measure of the spin divided by the rest mass, i.e.,  $S/\mu$  defines the minimal radius of a volume which a spinning body has to have in order not to rotate with superluminal speed. The same radius defines the upper bound of the separation between worldlines defined by various SSCs, i.e., a disc of centers of mass inside of which the worldlines have to lie. This radius was introduced by Møller (1949) and, therefore, is often referred to as the Møller radius.

In the next step, we explain how to calculate the tangent vector  $v^\mu$ .

---

### A.2.2. Calculating the tangent vector

The MP equations do not explicitly state how we can evaluate the tangent vector  $v^\mu$  throughout the evolution. To find  $v^\mu$  we use the SSCs.

In the case of T SSC,  $v^\mu$  is found via the relation

$$v^\mu = N(w^\mu + w^\mu) \ , \quad (\text{A.24})$$

where

$$w^\mu = \frac{2 S^{\mu\nu} u^\lambda R_{\nu\lambda\rho\sigma} S^{\rho\sigma}}{4 \mu^2 + R_{\alpha\beta\gamma\delta} S^{\alpha\beta} S^{\gamma\delta}} \ , \quad (\text{A.25})$$

and, because  $v^\mu v_\mu = -1$ , we get

$$N = \frac{1}{\sqrt{1 - w_\mu w^\mu}} \ . \quad (\text{A.26})$$

For more details on how to derive the above expression see, e.g., Semerák (1999).

In the case of NW SSC, according to our knowledge, there is no explicit expression which gives  $v^\mu$  as a function of  $p^\mu$  and  $S^{\mu\nu}$ . However, by taking the covariant derivative of Eq. (A.13), we obtain

$$v^\mu = \frac{1}{\omega_\nu p^\nu} \left( (\omega_\nu v^\nu) p^\mu + S^{\mu\nu} \frac{D \omega_\nu}{d\tau} \right) \ . \quad (\text{A.27})$$

A detailed discussion on how we solve the initial value problem numerically is provided in Appendix A.7.

### A.3. The Hamiltonian formalism for the spinning particle

The MP equations (A.1), (A.2) can be derived by means of Lagrangian mechanics, see, e.g., (Westpfahl, 1969; Bailey and Israel, 1975; Porto, 2006). If we want to apply a Legendre transformation in order to get a Hamiltonian canonical formulation<sup>54</sup> for a spinning particle moving in a curved spacetime, then the canonical structure holds only at linear order of the particle's spin (Barausse *et al.*, 2009).

The spin in the Hamiltonian formalism proposed by Barausse *et al.* (2009) comes from the projection of the spin tensor  $S^{\mu\nu}$  onto the spacelike part of a tetrad field  $\tilde{e}_\Delta^\mu$ . This tetrad consists of a timelike future oriented vector  $\tilde{e}_T^\mu$  (throughout the article we shall use T instead of 0) and three spacelike vectors  $\tilde{e}_I^\mu$ . For the tetrad it holds that

$$\tilde{e}_\Gamma^\mu \tilde{e}_\Delta^\nu g_{\mu\nu} = \eta_{\Gamma\Delta} \ , \quad (\text{A.28})$$

where  $\eta_{\Gamma\Delta}$  is the metric of the flat spacetime, and

$$\tilde{e}_\Delta^\mu \tilde{e}_\nu^\Delta = \delta_\nu^\mu \ , \quad (\text{A.29})$$

---

<sup>54</sup>There is also another Hamiltonian formulation for the spinning particle by Ramírez *et al.* (2014) who use a noncommutative position coordinate instead of the canonical one.

where  $\delta_\nu^\mu$  is the Kronecker delta. The capital indices are raised or lowered by the flat metric. When a tensor is denoted with capital indices, then the tensor has been projected onto this tetrad  $\tilde{e}_\Delta^\mu$ . In the case of the spin tensor  $S^{\mu\nu}$ , the projection reads

$$S^{IJ} = S^{\mu\nu} \tilde{e}_\mu^I \tilde{e}_\nu^J . \quad (\text{A.30})$$

The remaining components of this projection come from splitting the NW SSC (A.13) appropriately, and projecting the split on the tetrad, i.e.,

$$S^{TI} = S^{IJ} \frac{\omega_J}{\omega_T} , \quad (\text{A.31})$$

where  $\omega_\Delta = \tilde{e}^\nu_\Delta \omega_\nu$  is the projection of the time-like vector (A.14) of the NW SSC (A.13) as chosen in (Barausse *et al.*, 2009)

$$\omega_\nu = p_\nu - \mu \tilde{e}_\nu^T \quad (\text{A.32})$$

on the tetrad field, i.e.,

$$\begin{aligned} \omega_T &= p_\nu \tilde{e}_T^\nu - \mu , \\ \omega_J &= p_\nu \tilde{e}_J^\nu . \end{aligned} \quad (\text{A.33})$$

However, the Hamiltonian function of the spinning particle given by Barausse *et al.* (2009) does not use exactly the above described spin projection, instead the spin three vector is employed, i.e.,

$$S_I = \frac{1}{2} \epsilon_{IJJ} S^{JJ} \quad (\text{A.34})$$

(the inversion of Eq. (A.34) gives  $S^{JJ} = -\epsilon^{JLI} S_I$ ).

The Hamiltonian function  $H$  itself

$$H = H_{NS} + H^C S_C , \quad (\text{A.35})$$

splits in two parts. The first

$$H_{NS} = \beta^i P_i + \alpha \sqrt{\mu^2 + \gamma^{ij} P_i P_j} \quad (\text{A.36})$$

is the Hamiltonian for a non-spinning particle, and the second  $H^C S_C$

$$H^C = - \left( \beta^i F_i^C + F_0^C + \frac{\alpha \gamma^{ij} P_i F_j^C}{\sqrt{\mu^2 + \gamma^{ij} P_i P_j}} \right) \quad (\text{A.37})$$

includes the elements describing the spin, where

$$\alpha = \frac{1}{\sqrt{-g^{00}}} , \quad (\text{A.38})$$

$$\beta^i = \frac{g^{0i}}{g^{00}} , \quad (\text{A.39})$$

$$\gamma^{ij} = g^{ij} - \frac{g^{0i} g^{0j}}{g^{00}} . \quad (\text{A.40})$$

---

The canonical momenta  $P_i$  conjugate to  $x^i$  of the Hamiltonian (A.35) can be calculated from the momenta  $p_i$  of the MP formulation by using the relation

$$P_i = p_i + E_{i\Gamma\Delta} S^{\Gamma\Delta} = p_i + \left( 2E_{iTJ} \frac{\omega_C}{\omega_T} + E_{iJC} \right) \epsilon^{JCL} S_L \quad , \quad (\text{A.41})$$

where

$$E_{\nu\Gamma\Delta} = -\frac{1}{2} \left( g_{\kappa\lambda} \tilde{e}^\kappa_\Gamma \frac{\partial \tilde{e}^\lambda_\Delta}{\partial x^\nu} + \tilde{e}^\kappa_\Gamma \Gamma_{\kappa\nu\lambda} \tilde{e}^\lambda_\Delta \right) \quad (\text{A.42})$$

is a tensor which is antisymmetric in the last two indices, i.e.,  $E_{\nu\Gamma\Delta} = -E_{\nu\Delta\Gamma}$ .  $\Gamma_{\kappa\nu\lambda}$ , in turn, are the Christoffel symbols. This choice of momenta leads to a set of phase space variables that are canonical at linear order in the particle's spin.

Finally, the  $F_\mu^C$  tensor in Eq. (A.37) reads

$$F_\mu^C = \left( 2E_{\mu TI} \frac{\bar{\omega}_J}{\bar{\omega}_T} + E_{\mu IJ} \right) \epsilon^{IJC} \quad , \quad (\text{A.43})$$

where

$$\begin{aligned} \bar{\omega}_\Delta &= \bar{\omega}_\nu \tilde{e}^\nu_\Delta \quad , \\ \bar{\omega}_\nu &= \bar{P}_\nu - \mu \tilde{e}_\nu^T \quad , \\ \bar{P}_i &= P_i \quad , \\ \bar{P}_0 &= -\beta^i P_i - \alpha \sqrt{\mu^2 + \gamma^{ij} P_i P_j} \quad , \\ \bar{\omega}_T &= \bar{P}_\nu \tilde{e}^\nu_T - \mu \quad , \\ \bar{\omega}_J &= \bar{P}_\nu \tilde{e}^\nu_J \quad . \end{aligned} \quad (\text{A.44})$$

The equations of motion for the canonical variables as a function of coordinate time  $t$ , as derived in (Barausse *et al.*, 2009), read

$$\frac{dx^i}{dt} = \frac{\partial H}{\partial P_i} \quad , \quad (\text{A.45})$$

$$\frac{dP_i}{dt} = -\frac{\partial H}{\partial x^i} \quad , \quad (\text{A.46})$$

$$\frac{dS_I}{dt} = \epsilon_{IJC} \frac{\partial H}{\partial S_J} S^C \quad . \quad (\text{A.47})$$

The formulation provided up to this point is general, namely it does not depend on the coordinate or on the tetrad field choice. In the next section we specify the setup we use in the numerical sections of our work.

### A.3.1. The Hamiltonian for the Kerr spacetime

The line element of the Kerr spacetime in Boyer-Lindquist coordinates is

$$ds^2 = g_{tt} dt^2 + 2 g_{t\phi} dt d\phi + g_{\phi\phi} d\phi^2 + g_{rr} dr^2 + g_{\theta\theta} d\theta^2 \quad , \quad (\text{A.48})$$

where

$$\begin{aligned}
g_{tt} &= -1 + \frac{2Mr}{\Sigma} \ , \\
g_{t\phi} &= -\frac{2aMr \sin^2 \theta}{\Sigma} \ , \\
g_{\phi\phi} &= \frac{\Lambda \sin^2 \theta}{\Sigma} \ , \\
g_{rr} &= \frac{\Sigma}{\Delta} \ , \\
g_{\theta\theta} &= \Sigma \ ,
\end{aligned} \tag{A.49}$$

and

$$\begin{aligned}
\Sigma &= r^2 + a^2 \cos^2 \theta \ , \\
\Delta &= \varpi^2 - 2Mr \ , \\
\varpi^2 &= r^2 + a^2 \ , \\
\Lambda &= \varpi^4 - a^2 \Delta \sin^2 \theta \ .
\end{aligned} \tag{A.50}$$

In this section we reproduce the quantities already presented in (Barausse *et al.*, 2009). In the case of the small indices, we replace the numbers with the coordinates, i.e.,  $t$ ,  $r$ ,  $\theta$ ,  $\phi$  stand for 0, 1, 2, 3, respectively. The capital indices, meanwhile, are left unaltered.  $M$  denotes the mass and  $a$  the spin parameter of the central Kerr black hole.

The tetrad we use has been provided in (Barausse *et al.*, 2009) and reads

$$\begin{aligned}
\tilde{e}_\mu^T &= \delta_\mu^t \sqrt{\frac{\Delta \Sigma}{\Lambda}} \ , \\
\tilde{e}_\mu^1 &= \delta_\mu^r \sqrt{\frac{\Sigma}{\Delta}} \ , \\
\tilde{e}_\mu^2 &= \delta_\mu^\theta \sqrt{\Sigma} \ , \\
\tilde{e}_\mu^3 &= -\delta_\mu^t \frac{2aMr \sin \theta}{\sqrt{\Lambda \Sigma}} + \delta_\mu^\phi \sin \theta \sqrt{\frac{\Lambda}{\Sigma}} \ ,
\end{aligned} \tag{A.51}$$

while the inverse one reads

$$\begin{aligned}
\tilde{e}_T^\mu &= \delta_t^\mu \sqrt{\frac{\Lambda}{\Delta \Sigma}} + \delta_\phi^\mu \frac{2aMr}{\sqrt{\Delta \Lambda \Sigma}} \ , \\
\tilde{e}_1^\mu &= \delta_r^\mu \sqrt{\frac{\Delta}{\Sigma}} \ , \\
\tilde{e}_2^\mu &= \delta_\theta^\mu \frac{1}{\sqrt{\Sigma}} \ , \\
\tilde{e}_3^\mu &= \delta_\phi^\mu \frac{1}{\sin \theta} \sqrt{\frac{\Sigma}{\Lambda}} \ .
\end{aligned} \tag{A.52}$$

By calculating all the quantities mentioned in Sec. A.3, we finally obtain the coefficients  $H^C$  (Eq. (A.37)) as

$$\begin{aligned}
H^1 &= -\frac{\sqrt{\Delta} \cos \theta}{\sqrt{Q}(1+\sqrt{Q})\Lambda^2\sqrt{\Sigma} \sin^2 \theta} [(1+\sqrt{Q})(\Delta\Sigma^2 + 2Mr\varpi^4) + \sqrt{Q}2a^2Mr\varpi^2 \sin^2 \theta] \frac{P_\phi}{\mu} \\
&\quad + \frac{aM(2r^2\Sigma + \varpi^2\rho^2) \sin \theta}{\sqrt{Q}(1+\sqrt{Q})\Lambda^{3/2}\Sigma^2} \frac{\Delta P_r P_\theta}{\mu^2} + \frac{2a^3Mr \cos \theta \sin^2 \theta}{\sqrt{Q}(1+\sqrt{Q})\Lambda^{3/2}\Sigma} \frac{\Delta}{\mu^2} \left( 1 + \sqrt{Q} + \frac{2\Sigma}{\Lambda \sin^2 \theta} \frac{P_\phi^2}{\mu^2} + \frac{\Delta P_r^2}{\Sigma \mu^2} \right) , \\
H^2 &= \frac{\Delta(1+\sqrt{Q})(r\Sigma^2 - a^2M\rho^2 \sin^2 \theta) - M\sqrt{Q}(\rho^2\varpi^4 - 4a^2Mr^3 \sin^2 \theta)}{\sqrt{Q}(1+\sqrt{Q})\Lambda^2\sqrt{\Sigma} \sin \theta} \frac{P_\phi}{\mu} \\
&\quad + \frac{2a^3Mr \cos \theta \sin^2 \theta}{\sqrt{Q}(1+\sqrt{Q})\Lambda^{3/2}\Sigma^2} \frac{\Delta^{3/2} P_r P_\theta}{\mu^2} \\
&\quad + \frac{aM(2r^2\Sigma + \varpi^2\rho^2) \sin \theta}{\sqrt{Q}(1+\sqrt{Q})\Lambda^{3/2}\Sigma} \frac{\sqrt{\Delta}}{\mu^2} \left( 1 + \sqrt{Q} + \frac{2\Sigma}{\Lambda \sin^2 \theta} \frac{P_\phi^2}{\mu^2} + \frac{1}{\Sigma} \frac{P_\theta^2}{\mu^2} \right) , \\
H^3 &= -\frac{a^2\Delta \cos \theta \sin \theta}{\sqrt{Q}(1+\sqrt{Q})(\Lambda\Sigma)^{3/2}} (\Lambda + \sqrt{Q}\Delta\Sigma) \frac{P_r}{\mu} - \frac{r\Lambda\Delta + \varpi^2\Sigma\sqrt{Q}(r\Delta - M(r^2 - a^2))}{\sqrt{Q}(1+\sqrt{Q})(\Lambda\Sigma)^{3/2}} \frac{P_\theta}{\mu} \\
&\quad - \frac{aM\sqrt{\Delta}}{\mu^2\sqrt{Q}(1+\sqrt{Q})\Lambda^2\Sigma} [2a^2r\Delta \sin \theta \cos \theta P_r + (2r^2\Sigma + \varpi^2\rho^2)P_\theta] P_\phi , \quad (\text{A.53})
\end{aligned}$$

where

$$Q = 1 + \frac{\gamma^{ij} P_i P_j}{\mu^2} = 1 + \mu^{-2} \left( \frac{\Delta}{\Sigma} P_r^2 + \frac{1}{\Sigma} P_\theta^2 + \frac{\Sigma}{\Lambda \sin^2 \theta} P_\phi^2 \right) ,$$

and

$$\rho^2 = r^2 - a^2 \cos^2 \theta . \quad (\text{A.54})$$

For a full and detailed presentation of the derivation of  $H^C$ , we refer the reader to (Barausse *et al.*, 2009).

It is worth mentioning here that, contrary to the T SSC, the NW SSC (Eq. (A.32)) does not uniquely define the reference worldline. As already noted in the introduction the choice of the center of mass, i.e., the reference worldline, is observer dependent. When T SSC is applied the zero 3-momentum observer is chosen. However, when the NW SSC is used there is no unique choice because the observer and therewith the reference worldline depends on the tetrad. We have fixed our tetrad in Eqs. (A.51), (A.52). In the following we only consider the evolution of the orbit corresponding to this observer so that we do not have to worry about transforming the dynamical properties of the system to another reference frame.

## A.4. Comparison of Tulczyjew and Newton-Wigner SSC

### A.4.1. Preliminaries

When simulating the MP equations we in fact have to solve the initial value problem

$$\left\{ \begin{array}{l} \frac{d x^\mu}{d\tau} = v^\mu \quad , \\ \frac{d p^\mu}{d\tau} = -\frac{1}{2} R^\mu{}_{\nu\kappa\lambda} v^\nu S^{\kappa\lambda} - \Gamma^\mu{}_{\nu\kappa} v^\nu p^\kappa \quad , \\ \frac{d S^{\mu\nu}}{d\tau} = p^\mu v^\nu - v^\mu p^\nu + \Gamma^\mu{}_{\kappa\lambda} S^{\nu\kappa} v^\lambda - \Gamma^\nu{}_{\kappa\lambda} S^{\mu\kappa} v^\lambda \quad , \\ x^\mu(\tau = 0) = x_0^\mu \quad , \\ p^\mu(\tau = 0) = p_0^\mu \quad , \\ S^{\mu\nu}(\tau = 0) = S_0^{\mu\nu} \quad . \end{array} \right. \quad (\text{A.55})$$

As a first step, we have to provide initial conditions which comply with the constraints mentioned earlier (Sec. A.2).

In order to find these appropriate initial conditions, we follow the approach of Hartl (2003a), which implies that instead of the spin tensor  $S^{\mu\nu}$  we use the vector  $S^\mu$  for the initial setup. Without loss of generality, we set  $t = \phi = 0$  and provide initial values for  $r$ ,  $\theta$ ,  $p^r$  as well as for the two spin components  $S^r$  and  $S^\theta$ . The other initial conditions, namely  $p^t$ ,  $p^\theta$ ,  $p^\phi$ ,  $S^t$ , and  $S^\phi$ , are then fixed by the constraints. In the case of the T SSC, those constraints are

$$E = -p_t - \frac{1}{2\mu} g_{t\mu,\nu} \eta^{\mu\nu\gamma\delta} S_\gamma p_\delta \quad , \quad (\text{A.56})$$

$$J_z = p_\phi + \frac{1}{2\mu} g_{\phi\mu,\nu} \eta^{\mu\nu\gamma\delta} S_\gamma p_\delta \quad , \quad (\text{A.57})$$

$$\mu^2 = -g^{\mu\nu} p_\mu p_\nu \quad , \quad (\text{A.58})$$

$$S^2 = g^{\mu\nu} S_\mu S_\nu \quad , \quad (\text{A.59})$$

$$0 = g^{\mu\nu} S_\mu p_\nu \quad , \quad (\text{A.60})$$

where we have substituted Eq. (A.17) into the constants of motion (A.3), (A.4), and lowered the indices wherever needed. Thus, we specify an orbit by providing values for  $E$ ,  $J_z$ ,  $S^2$ , and  $\mu^2$ . We then solve the system (A.56)-(A.60) for  $p_t$ ,  $p_\theta$ ,  $p_\phi$ ,  $S_t$ , and  $S_\phi$  with the help of the Newton-Raphson method.

For comparing the effect of different SSCs in the evolution of MP, we need to find initial conditions for the NW SSC which are similar to the T SSC case. Hence, we parametrize the orbits by providing the same initial set of values for  $r$ ,  $\theta$ ,  $p^r$ ,  $S^r$ ,  $S^\theta$ ,  $E$ ,  $J_z$ ,  $S^2$  and  $\mu^2$ . The set of constraints for the NW SSC is similar to the one for the T SSC (Eqs. (A.56)-(A.60)). The constraints (A.56)-(A.57) remain unaltered. We use Eq. (A.58), and Eq. (A.23) instead of Eq. (A.59) for the initial setup, even though, in the case of the NW SCC, neither the spin  $S^2$  nor the rest mass  $\mu$  is preserved anymore. Finally, we replace constraint (A.60) by

$$g^{\mu\nu} S_\mu \omega_\nu = 0 \quad .$$

When solving the resulting system for  $p_t$ ,  $p_\theta$ ,  $p_\phi$ ,  $S_t$ , and  $S_\phi$  for the same provided  $r$ ,  $\theta$ ,  $p^r$ ,  $S^r$ ,  $S^\theta$ ,  $E$ ,  $J_z$ ,  $S^2$  and  $\mu^2$  as in the T case, we get what we referred to as similar initial conditions above. At last, by raising indices of the momenta and going from spin vectors to tensors with

the help of the transformations (A.17) and (A.22), respectively, we get suitable data to start the computation with. The orbits are evolved through the Eqs. (A.1), (A.2). A more detailed discussion about the techniques we have applied to evolve the MP equations is provided in Appendix A.7.

The timelike vector  $\omega_\nu$  in the NW SSC (A.13) is given by Eq. (A.32), where the  $\tilde{e}_\nu^T$  is the top equation from the set (A.51). By adapting the convention that times and lengths are measured in terms of  $M$ , we set  $M = 1$  throughout the paper.

Before we proceed with the numerical results, we want to discuss the initial setup for our evaluations in this section. We have chosen the orbits to start from the same point in the configuration space, i.e., both worldlines at  $\tau = 0$  lie at the same spacetime point. This means that both of the different corresponding observers see the center of the mass lying at the same place, even if the SSCs are different. This is not the usual way this subject is treated. In (Kyrian and Semerák, 2007), for example, the discussion about the transition between two different SSCs is based on the center of the mass worldline displacement. The latter approach would not be appropriate for our treatment, because apart from the shift in the value of the spin tensor, the initial point in the configuration space should be shifted as well (Kyrian and Semerák, 2007). In our treatment we want to change the order of magnitude of the spin while keeping the initial conditions as similar as possible during the scaling, in order to observe how the two different SSCs converge as the geodesic limit is approached. In other words we do not attempt to have initial conditions which would obey the transition between different SSCs for one particle, but rather conditions which represent similar orbits for two different SSCs.

#### A.4.2. Comparison for large spin

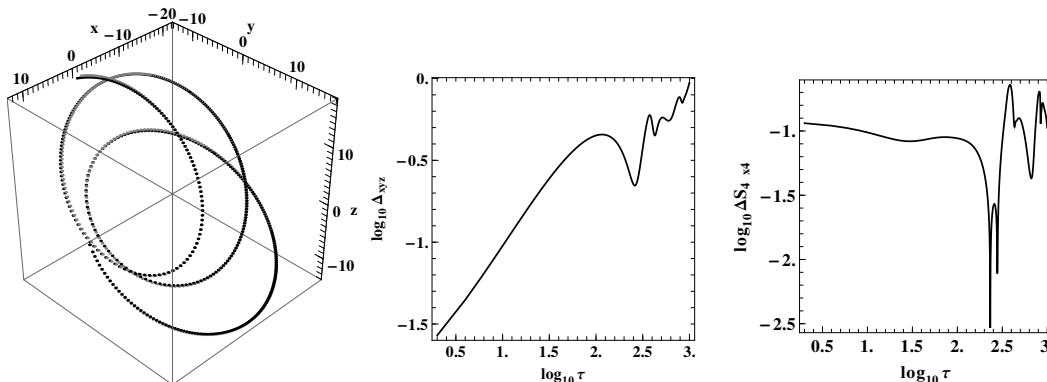


Figure A.1: The left panel shows a MP orbit with T SSC (black dots) and a MP orbit with NW SSC (gray dots) in the configuration space  $x, y, z$  (Cartesian coordinates). The common parameters for these orbits are  $a = 0.5$ ,  $r = 11.7$ ,  $\theta = \pi/2$ ,  $p^r = 0.1$ ,  $S = 1$ ,  $S^r = 0.1 S$ ,  $S^\theta = 0.01 S$ ,  $E = 0.97$ ,  $J_z = 3$ , and  $\mu = 1$ . The central panel shows the logarithm of the Euclidean distance in the configuration space between these two orbits as a function of the proper time. The right panel shows the logarithm of the difference  $\Delta S_{4 \times 4}$  between the spin tensors of these two orbits as a function of the proper time.

In our first example, the parameters read  $a = 0.5$ ,  $r = 11.7$ ,  $\theta = \pi/2$ ,  $p^r = 0.1$ ,  $S = 1$ ,

$S^r = 0.1 S$ ,  $S^\theta = 0.01 S$ ,  $E = 0.97$ ,  $J_z = 3$ , and  $\mu = 1$ . The left panel of Fig. A.1 shows how the two MP orbits with T SSC (black) and NW SSC (gray) evolve in the configuration space where the Cartesian coordinates

$$\begin{aligned} x &= r \cos \phi \sin \theta \quad , \\ y &= r \sin \phi \sin \theta \quad , \\ z &= r \cos \theta \quad , \end{aligned} \tag{A.61}$$

are employed.

The divergence between the two orbits is barely visible in the left panel, but if we take the Euclidean norm

$$\Delta_{xyz} = \sqrt{(x_T - x_{NW})^2 + (y_T - y_{NW})^2 + (z_T - z_{NW})^2} \quad , \tag{A.62}$$

we see that at the end of our run, the separation between the two orbits is of the order one (central panel of Fig. A.1), while the radial distance from the central black hole is of the order ten (left panel of Fig. A.1). Even if the Möller radius is not an appropriate tool for our setup (see the discussion at the last paragraph of Sec. A.4.1), it is worthy to note that the two orbits lie inside a Möller radius ( $S/\mu = 1$ ) for  $\tau = 10^3$ , even if their distance will grow out of this radius later on. This divergence in the orbit evolution follows the discrepancy in the spin space. To illustrate this, the norm of the difference between the spin tensor  $S_T^{\mu\nu}$  of the T SSC and the spin tensor  $S_{NW}^{\mu\nu}$  of the NW SSC,

$$\Delta S_{4 \times 4} = \sqrt{\left| g_{\mu\nu} g_{\kappa\lambda} (S_T^{\nu\kappa} - S_{NW}^{\nu\kappa})(S_T^{\mu\lambda} - S_{NW}^{\mu\lambda}) \right|} \quad , \tag{A.63}$$

is displayed in the right panel of Fig. A.1.  $\Delta S_{4 \times 4}$  is one tenth of the spin measure right from the beginning, and stays at this level during the evolution. Thus, from an orbital dynamic point of view when the spin of the test particle is of order  $S = 1$ , the choice of different SSCs leads to orbital evolutions which diverge significantly with time.

One thing that has to be discussed before we proceed is the meaning of a 'common' proper time, when two orbits with different SSCs are compared. Each SSC defines its own center of reference, which implies that with each SSC the proper time that is measured along the above orbits is different, even if the orbits start with similar initial conditions. Another issue that arises here is how we can measure the distance between two 'nearby' orbits in a curved spacetime. Above, we use the Euclidean norm, however the spacetime is not Euclidean. The same issues arise when geodesic chaos is studied in curved spacetimes, see, e.g., (Wu *et al.*, 2006; Lukes-Gerakopoulos, 2014). One of the suggestions in the aforementioned field is to use the two nearby orbits technique, i.e., to evolve two orbits with similar initial conditions and measure their distance when they reach the same proper time. This is, in few words, the approach we adapt in our study for the time issue. For the issue of the distance in the configuration space between the two orbits, we have chosen to employ the Euclidean metric. We could employ the local  $g_{\mu\nu}$  metric as well, even if the orbits depart from each other significantly (middle panel of Fig. A.5). However, for the evolution times  $\tau = 10^3$  the results coming from both approaches are almost identical, and therefore we went for the the simplest metric, which is the Euclidean.

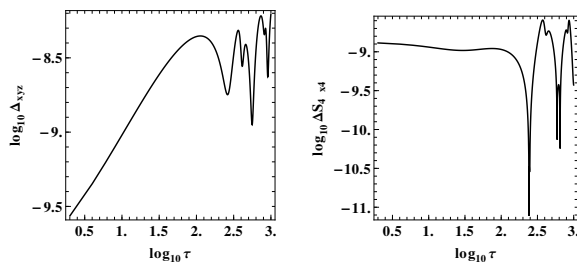


Figure A.2: The left panel shows the logarithm of the Euclidean distance in the configuration space between a MP orbit with T SSC and a MP orbit with NW SSC as a function of the proper time. The common parameters for these orbits read  $a = 0.5$ ,  $r = 11.7$ ,  $\theta = \pi/2$ ,  $p^r = 0.1$ ,  $S = 10^{-8}$ ,  $S^r = 0.1 S$ ,  $S^\theta = 0.01 S$ ,  $E = 0.97$ ,  $J_z = 3$ , and  $\mu = 1$ . The right panel shows the logarithm of the difference  $\Delta S_{4 \times 4}$  between the spin tensors of these two orbits as a function of the proper time.

#### A.4.3. Comparison for very small spin

Since we mentioned the geodesic orbits, we approach this limit by setting the measure of the spin in our initial conditions to  $S = 10^{-8}$ . All the other parameters are the same as in Fig. A.1. For this geodesic-like setup the orbits in the configuration space resemble the orbits shown in the left panel of Fig. A.1. However, the left panel of Fig. A.2 shows that the distance between the two orbits has dropped significantly, about 8 orders of magnitude. This drop is anticipated since we tend to the geodesic limit and the spin contribution is expected to be smaller. However, the level of the divergence in the configuration space (left panel of Fig. A.2) is again defined by the magnitude of the spin difference  $\Delta S_{4 \times 4}$  (right panel of Fig. A.2). Namely, even though the initial conditions in the configuration space are identical, i.e.,  $\Delta_{xyz} = 0$ , those of the spin components are not, i.e.,  $\Delta S_{4 \times 4} \approx 10^{-9}$ , and this initial divergence in the spin space is passed on to the configuration space.

#### A.4.4. Constants of motion

We now turn our attention to the conservation of the four-momentum (rest mass  $\mu$ ) and of the spin  $S$ . In order to check whether these quantities are preserved, we use the relative error of the four-momentum

$$\Delta \mu^2 = \left| 1 - \frac{\mu^2(\tau)}{\mu^2(0)} \right|, \quad (\text{A.64})$$

and the relative error of the spin  $S^2$

$$\Delta S^2 = \left| 1 - \frac{S^2(\tau)}{S^2(0)} \right|, \quad (\text{A.65})$$

where  $\mu^2(\tau)$ , and  $S^2(\tau)$  are calculated at time  $\tau$ .

We see from Fig. A.3 that both the rest mass  $\mu^2$  and the spin are conserved for the T SSC (black lines) as was expected (see Sec. A.2). On the other hand, in the case of the NW SSC (gray lines) the four-momentum scales with the magnitude of the spin  $S$ , while the square of

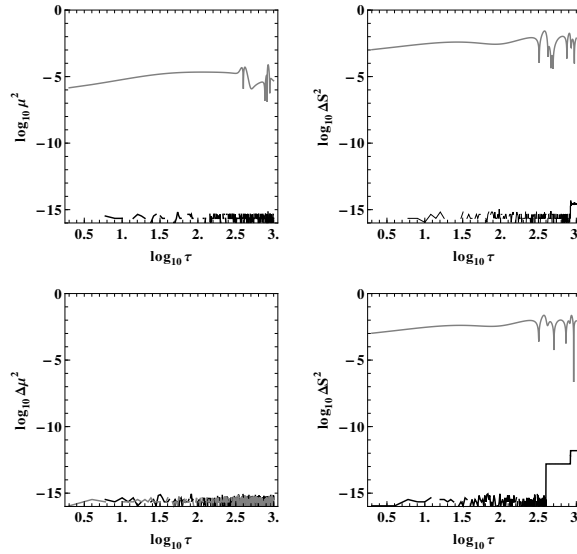


Figure A.3: The top row of panels corresponds to the orbits of Fig. A.1, while the bottom row of panels corresponds to the orbits of Fig. A.2. The black lines represent the evolution of the MP equations with T SSC, while the gray lines represent the NW SSC. The left column of panels shows the relative error in the preservation of the four-momentum, while the right depicts the preservation of the spin.

the spin itself stays at the same level indifferently from the spin’s magnitude. This scaling in the conservation of the mass is anticipated because, as  $S \rightarrow 0$ , the evolution of the MP equations approaches that of the geodesic motion.

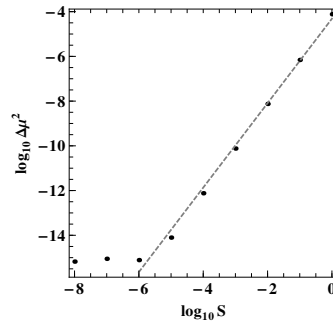


Figure A.4: The relative error of the four-momentum  $\Delta\mu^2$  as a function of the spin measure  $S$  for the NW SSC. The black dots correspond to the maximum values of  $\Delta\mu^2$  during the evolution for each  $S$ . The dashed line is a linear fit of the form  $\log_{10} \Delta\mu^2 = a \log_{10} S + b$  for data with  $S > 10^{-6}$ , where  $a = 1.995 \pm 0.004$ ,  $b = -4.136 \pm 0.013$ .

In order to better illustrate the above mentioned scaling, we run several simulations with initial setups similar to the one of Fig. A.1 where we only change the measure of the spin,  $S$ . For every simulation, we plot the maximum value of  $\Delta\mu^2$  along the trajectory against the initial spin measure (Fig. A.4). The resulting plot shows that, as we decrease  $S$ , the four-momentum for the NW SSC tends to be conserved up to the computational accuracy. There are two

effects that shape this figure. One is the theoretical scaling of  $\Delta\mu^2$  as a function of  $S$  and the other is the finite computational accuracy. From a linear fit of our data we get for  $S > 10^{-6}$  (dashed line in Fig. A.4)  $\Delta\mu^2 \propto S^2$ . For smaller spins a plateau appears because we reach the computational accuracy (in our runs we use double precision).

Since for T SSC the four-momentum is conserved and for the NW SSC the  $\sqrt{\Delta\mu^2}$  scales linearly with the spin, this scaling can be interpreted as the rate by which the two different SSCs converge to each other. Changing the value of the spin  $a$  of the central black hole does not alter qualitatively the results of our numerical comparison.

## A.5. Numerical comparison of the MP equations with the corresponding Hamiltonian equations

### A.5.1. Preliminaries

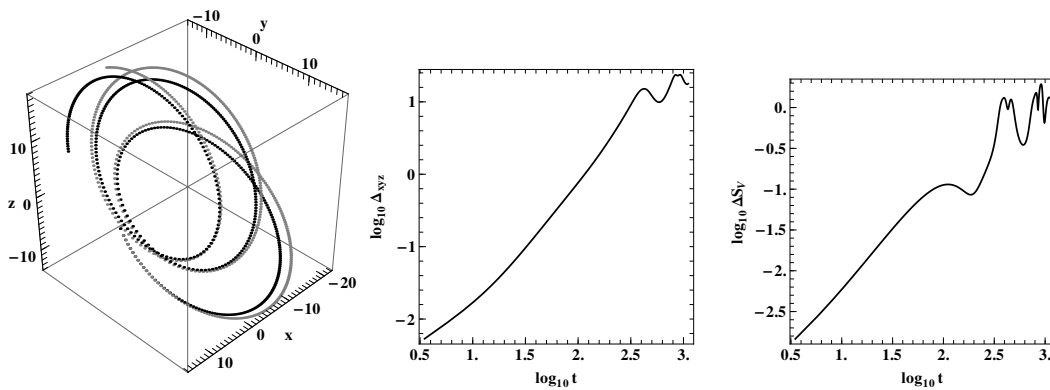


Figure A.5: The left panel shows how the orbit evolves through the MP equations (gray dots) and through the Hamilton's equations (black dots) in the configuration space  $x$ ,  $y$ ,  $z$ , when we use the initial conditions given in Fig. A.1. The central panel shows the logarithm of the Euclidean distance in the configuration space between these two orbits as a function of the coordinate time. The right panel shows the logarithm of the Euclidean norm of the difference between the spin vectors of these two orbits as a function of the coordinate time.

Since the MP equations are a pole-dipole approximation, multipoles of higher order than the spin dipole are already neglected. However, we can simplify the problem further by assuming that the physically relevant values for the particle spin are small and the terms quadratic in the spin correspond to the quadrupole contribution. Thus, a Hamiltonian which is accurate up to linear order of the spin should yield satisfactory results. This is the main idea on which the construction of such a Hamiltonian formalism for NW SSC in (Barausse *et al.*, 2009) is based.

According to this formalism (see the brief description in Sec. A.3), the evolution parameter is not the proper time like in the case of Sec. A.4, but the coordinate time. In order to perform a comparison between the MP equations and the corresponding Hamiltonian (Sec. A.3.1) equations, we could rewrite our MP code with respect to the coordinate time. However, the coordinate times, at which our quantities were calculated in the MP simulations, were

given as output anyway. With them at hand, there is an easier way out. One can evolve the Hamilton's equations of motion using constant steps in the coordinate time, and interpolate the solution around the required times of output. A more detailed discussion on this topic and the numerical methods we have used is given in Appendix A.8.

Moreover, in order to make the two formalisms comparable, we used the equations given in Sec. A.3 to go from the set of variables  $\{x^\mu, p^\mu, S^{\mu\nu}\}$  of the MP equations to the set of variables  $\{x^i, P^i, S^I\}$  in the Hamiltonian formalism. Note that this holds also for the initial conditions, thus both the MP equations and the corresponding Hamilton's equations start with exactly the same initial setup.

Before showing the results of comparisons between the two approaches, we want to point out that all simulations using the Hamiltonian equations were much faster than their equivalents based on the MP equations with NW SSC. More detailed information on this can be found in the Appendix Sections.

### A.5.2. Comparison for large spin

Using the initial conditions for the NW SSC given in Fig. A.1, we have evolved the orbit by using Hamilton's equations. The motion of the corresponding orbit in the configuration space is shown in the left panel of Fig. A.5 (black dots) together with the orbit evolved through the MP equations (gray dots). Even if the two orbits start with the same initial conditions they depart from each other quite quickly. This is seen more clearly in the central panel of Fig. A.5, where the Euclidean distance between the two orbits

$$\Delta_{xyz} = \sqrt{(x_H - x_{MP})^2 + (y_H - y_{MP})^2 + (z_H - z_{MP})^2} \quad , \quad (\text{A.66})$$

is displayed as a function of the coordinate time. Near the end of the calculation, the distance  $\Delta_{xyz}$  is almost as large as the radial distance of the particle from the central black hole. From the appearance of the left panel of Fig. A.5 one might wonder whether the divergence between the orbits is a ‘‘synchronization’’ issue. However, since both schemes use the same SSC, i.e., the NW SSC, and since the initial conditions for both schemes are exactly the same, i.e., the orbits correspond to the same particle, the proper time for both orbits has to tick at the same rate. Thus, it is reasonable to claim that this divergence results from the fact that the Hamiltonian is valid up to the linear order in the particle spin, and since the spin here is large, i.e.,  $S = 1$ , such divergence should be expected. Nevertheless, it is impressive that orbits corresponding to the same particle evaluated with different schemes, i.e., the MP equations and the corresponding Hamiltonian, give a divergence that is of one order of magnitude larger than the divergence of the MP equations with different SSCs (left panel of Fig. A.1). If we took the Möller radius as a criterion, for example, then, since the distance between the two orbits exceeds the diameter of the disc of centers of mass, according to this criterion, the orbits could not correspond to the same particle. Therefore, we can say that the Hamiltonian formalism is not valid for large spin values, just as expected.

The spin in the Hamiltonian formalism is given by the projection vector (Eq. (A.34)). The Euclidean norm of the difference between the spin vector  $S_H^I$  calculated by Hamilton's equations and the  $S_{MP}^I$  calculated by the MP equations

$$\Delta S_v = \sqrt{\sum_{I=1}^3 (S_H^I - S_{MP}^I)^2} \quad , \quad (\text{A.67})$$

is plotted as a function of the coordinate time in the right panel of Fig. A.5. This plot shows that the difference is quite high, even if the spin values are identical at first.

### A.5.3. Comparison for very small spin

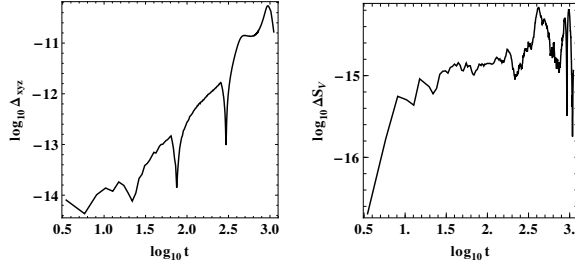


Figure A.6: The left panel shows the logarithm of the Euclidean distance in the configuration space between an orbit calculated with the MP equations and an orbit calculated with the Hamilton equations as a function of the coordinate time. For the orbits we have used the initial conditions given in Fig. A.2. The right panel shows the logarithm of the Euclidean norm of the difference between the spin vectors of these two orbits as a function of the coordinate time.

By decreasing the measure of the particle's spin to the level of  $S = 10^{-8}$ , we get the initial setup given in Fig. A.2. The Euclidean distance between the evolutions of the MP equations and the Hamilton equations (left panel of Fig. A.6) drops to a level which is near the precision of our simulations. Therefore, practically, the two orbits should not discern. This seems to be the picture we get from the Euclidean norm of the difference between the spin vectors as well (right panel of Fig. A.6). Moreover, it is also evident that the distance between the two orbits does not exceed the diameter of the disc of centers of mass defined by the Möller radius for the coordinate time we have computed. Therefore, it is reasonable to say that the two orbits obtained by two different formalisms do correspond to the same particle and thus infer that the Hamiltonian is indeed valid for small spin values. However, this picture might be a little bit illusive. The order of the spin is  $S = 10^{-8}$ , and, thus, what we see in fact is that the relative difference, i.e.,  $\Delta S_v/S \approx 10^{-8}$  is of the order of the spins' magnitude. In other words, in the spin space the evolution of the two orbits does not agree completely. The reason that in the configuration space the orbits appear to be identical, while in the spin space the agreement is not at the same level, is that we are in the geodesic limit, and the evolution of the orbits is almost independent from the spins.

The bottom row of Fig. A.7 supports the claim that when  $S = 10^{-8}$ , we are at the geodesic limit, and the evolution does not depend on the spins. In the left panel of the bottom row in Fig. A.7, the relative errors of the Hamiltonian function,

$$\Delta H = \left| 1 - \frac{H(t)}{H(0)} \right| , \quad (\text{A.68})$$

lie at the computation precision level for both the MP orbit (gray line) and the Hamiltonian orbit (black line), while the level of the relative error (A.65) in the measure of the spin vectors,

$$S^2 = S_I S^I , \quad (\text{A.69})$$

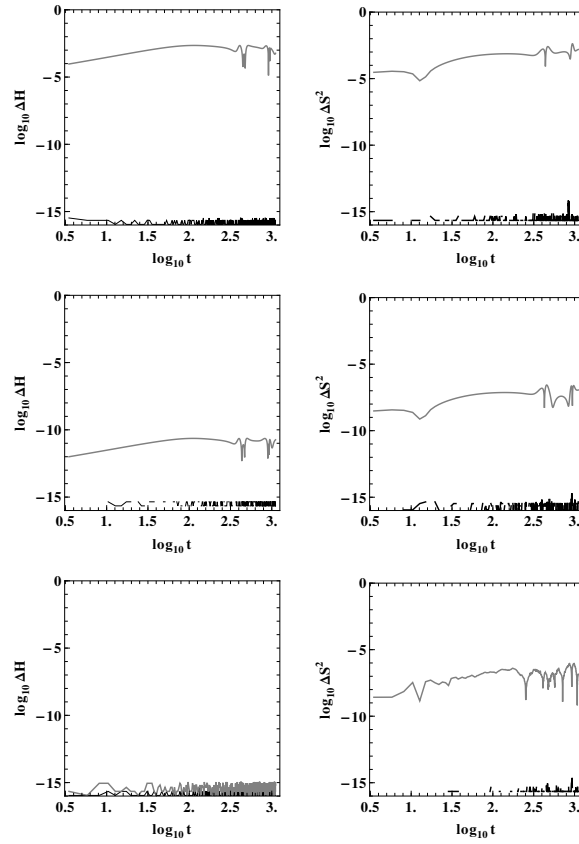


Figure A.7: The top row of panels corresponds to the orbits of Fig. A.5, while the bottom row of panels corresponds to the orbits of Fig. A.6. The middle row of panels corresponds to initial conditions similar to Fig. A.1 only instead of spin measure  $S = 1$  we set  $S = 10^{-4}$ . The gray lines represent the evolution of the MP equations, while the black lines represent the evolution of the Hamilton equations. The left column of panels shows the relative error in the preservation of the Hamiltonian function, while the right shows the preservation of the spin.

is not as well preserved for the MP case (gray line) as for the Hamiltonian case (black line in the right panel of the bottom row in Fig. A.7). Notice that, as stated above, in the case of the MP equation, we can get the value of the Hamiltonian function  $H$  and of the square of the spin measure  $S^2$  by transforming the set of variables  $\{x^\mu, p^\mu, S^{\mu\nu}\}$  into the set  $\{x^i, P^i, S^I\}$  and substituting the transformed set into Eq. (A.35) and Eq. (A.69) respectively.

#### A.5.4. Behavior of the constants of motion and scaling with the spin

When we raise the measure of the particle spin to  $S = 10^{-4}$ , then the relative error of the MP spin (Eq. (A.69)) remains practically at the same level (gray line in the right panel of the middle row in Fig. A.7) as in the  $S = 10^{-8}$  case. This does not hold for the relative error of the Hamiltonian function (gray line in the left panel of the middle row in Fig. A.7) which is not at the computation precision level anymore. This shows that the motion is no longer in the geodesic limit. However, both  $\Delta S^2$  and  $\Delta H$  for the MP orbit lie at acceptable levels, which shows that for this magnitude of the particle spin, the MP equations and the Hamilton equations seem to be in agreement.

This agreement breaks when  $S = 1$ . The top row of Fig. A.7 shows that when  $S = 1$ , the relative errors,  $\Delta H$  and  $\Delta S^2$  are at the same quite high level for the MP orbit. These relatively large values confirm the departure between the MP equations and the corresponding Hamiltonian that we see in Fig. A.5.

The black lines for all panels of Fig. A.7 are at the highest accuracy the computation accuracy allows, which means that apart from round-off error, the Gauss scheme we applied integrates accurately the system of the Hamilton equations, but also that the interpolation scheme we applied to match the coordinate times works quite well.

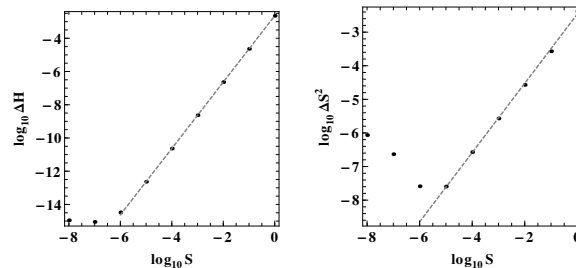


Figure A.8: The left panel shows the relative error of the Hamiltonian  $\Delta H$  of orbits evolved through the MP equations for different spin measures  $S$  of the particle, while the right panel shows the corresponding preservations of the measure of the 3-vector  $\Delta S^2$ . The black dots correspond to the maximum values of  $\Delta H$ ,  $\Delta S^2$ , respectively, for each  $S$ . The dashed lines are linear fits of the form  $\log_{10} \Delta H = a \log_{10} S + b$ , and

$$\log_{10} \Delta S^2 = c \log_{10} S + d, \text{ respectively, for data with } S > 10^{-6}, \text{ where } a = 1.9968 \pm 0.0015, b = -2.644 \pm 0.004, \text{ and } c = 1.031 \pm 0.015, d = -2.46 \pm 0.06.$$

As at the end of the previous Section, we can investigate the scaling of the constants of motion with the spin in more detail by taking the maxima of their relative errors the MP equations,

for different values of the measure of the particle's spin. The result is shown in Fig. A.8. Again, as in Fig. A.4, the precision of our computations and the scaling due to the spin measure shape the figure. We see a plateau at the left panel of Fig. A.8 for  $\Delta H$  due to the computational precision, while in the right panel of Fig. A.8 we see that  $\Delta S^2$  increases, which is due to the smallness of the spin components. Even if we had applied a special integration scheme respecting these small quantities, this scheme could not follow below a threshold either. This threshold is in our case  $S = 10^{-6}$ . When the scaling with the spin dominates ( $S > 10^{-6}$ ), the linear fits show that  $\Delta H \propto S^2$ , while  $\Delta S^2 \propto S$ . These proportionalities are expected as we explain next.

By construction the Hamiltonian function  $H$  of a spinning particle is accurate up to linear order of the particle spin. Hence, when compared with the value of the Hamiltonian function yielded from the evolution of the MP equations  $H_{MP}(t)$ , the difference between the two Hamiltonian function values should differ by terms of the order  $O(S^2)$ , i.e.,

$$H_{MP}(t) \approx H(t) + O(S^2) \quad . \quad (\text{A.70})$$

However, since we have chosen the same initial conditions for both evolution schemes, it holds that  $H_{MP}(0) = H(0)$ . Thus, the relative error (A.68) for the MP equations reads

$$\Delta H = \left| \frac{H_{MP}(t) - H_{MP}(0)}{H_{MP}(0)} \right| \approx \left| \frac{H(t) - H(0)}{H(0)} + \frac{O(S^2)}{H(0)} \right| \quad . \quad (\text{A.71})$$

Since we do not expect the relative error  $\frac{H(t)-H(0)}{H(0)}$  to depend on the value of the particle's spin, and this expectation is confirmed by the numerical findings (black lines in the left column of Fig. A.7), we get the scaling  $\Delta H \propto S^2$  of Fig. A.8.

In order to explain the scaling of the relative error  $\Delta S^2$ , we use a similar way of reasoning. The preservation of the spin for the Hamiltonian formalism (A.69) is  $S^2$ , thus a reasonable expectation is that for the MP case we should get values  $S^2_{MP}(t)$  from Eq. (A.69) which differ from the Hamiltonian case at order  $O(S^3)$ , i.e.,

$$S^2_{MP}(t) \approx S^2(t) + O(S^3) \quad . \quad (\text{A.72})$$

Furthermore, we have  $S^2_{MP}(0) = S^2(0)$ . Thus, the relative error (A.65) for the MP equations reads

$$\Delta S^2 = \left| \frac{S^2_{MP}(t) - S^2_{MP}(0)}{S^2_{MP}(0)} \right| \approx \left| \frac{S^2(t) - S^2(0)}{S^2(0)} + \frac{O(S^3)}{S^2(0)} \right| \quad , \quad (\text{A.73})$$

which explains why we see that  $\Delta S^2 \propto S$  in the right panel of Fig. A.8.

If we take as a criterion the convergence of the constants of motion shown in Fig. A.8, and consent that a relative error of the level of  $10^{-6}$  is adequate to state that the different formalisms have converged, then from our comparison the Hamiltonian formalism is in agreement with the MP equations for the NW SSC when the measure of the particle's spin is  $S < 10^{-4}$ . When we reach  $S \approx 10^{-6}$ , the effect of the spin appears not to be important anymore, and the orbit evolves like a geodesic, i.e., it does not depend on the spin.

## A.6. Conclusions

We have compared the evolutions of a spinning test particle in Kerr spacetime governed by different equations of motion. We first evolved the orbits prescribed by the MP equations, once

---

supplemented by the Tulczyjew SSC and once by the Newton-Wigner SSC. Our simulations indicate a linear in the spin scaling of the difference between the respective orbits. We also found that, in the case of the NW SSC, the four-momentum is conserved up to linear order in the square of the test particle’s spin, i.e.  $\Delta\mu^2 \propto S^2$ . In a second series of experiments we compared orbits given by the MP equations plus NW SSC with orbits obtained via the Hamiltonian formalism of Barausse *et al.* (2009). Here, too, the difference between the respective orbits, which is quite significant for large spins of the order of one, decreases linearly as a function of the square of the test particle’s spin, i.e.  $\Delta H \propto S^2$ , which agrees with the analysis given in (Barausse *et al.*, 2009). According to our analysis, the Hamiltonian formalism of the spinning particle appears to be relevant in the range  $10^{-6} < S < 10^{-4}$ . For values of the spin smaller than  $10^{-6}$  we can ignore the part of the Hamiltonian describing the spin evolution and keep the non-spinning part, and for spin values greater than  $10^{-4}$ , our numerical results show that the Hamiltonian formalism is not in good agreement with the MP equations. Anyhow, the aforementioned range, where the Hamiltonian formalism is relevant, is appropriate for astrophysical binary systems of extreme mass ratio. Moreover, as our simulations showed that the CPU effort for the Hamilton equations of motion is far smaller than the computational cost for the MP equations, we find appropriate the use of these equations for simulations of test particles with small spins. When, in addition, favorable numerical methods, such as the one presented in this work, are applied, reliable results can be obtained within a short period of time.

## Acknowledgements

This work was supported by the DFG grant SFB/Transregio 7, by the DFG Research Training Group 1620 “Models of Gravity ” and by the “Centre for Quantum Engineering and Space-Time Research (QUEST)”. We specially would like to thank Oldrich Semerák for his useful suggestions and remarks.

## A.7. Numerical integration of the MP equations

Seen from a numerical point of view, the initial value problem (A.55) reads

$$\frac{d\mathbf{y}}{d\tau} = f(\mathbf{y}) \quad , \quad (\text{A.74})$$

$$\mathbf{y}(\tau = 0) = \mathbf{y}_0 \quad . \quad (\text{A.75})$$

with  $\mathbf{y} = (t, r, \dots, S^{\theta\phi}, S^{\theta\theta})^T \in \mathbb{R}^{24}$  and  $f : \mathbb{R}^{24} \rightarrow \mathbb{R}^{24}$ . If this system was of Hamiltonian canonical form, symplectic integration schemes would be the most natural choice for their numerical solution. They almost exactly preserve a differential equation’s constants of motion and, unless for standard integration schemes, their overall numerical error grows only slowly as a function of the total integration time even for larger step sizes. Therefore, simulations over long time spans can be carried out efficiently. Unfortunately, the MP equations are not of Hamiltonian canonical form. But, they can be interpreted as the Euler-Lagrange equations of a suitable Lagrangian action, see, e.g., (Westpfahl, 1969; Bailey and Israel, 1975; Porto, 2006). What then saves the day is that the flow of symplectic integration schemes can be interpreted as the solution of the Euler-Lagrange equations of a discretization of the Lagrangian

action. Schemes with this property are called *variational integrators* and they only rely on the existence of a Lagrangian structure for their favorable behavior. For example they are known to exactly preserve an equation of motion's first integrals which are quadratic in the phase space variables. This implies that a variational integration scheme applied to the MP equations with T SSC will conserve the four-momentum  $\mu^2$  and the spin length  $S^2$  up to numerical round-off errors. An extensive discussion of this topic can be found in the monograph of Hairer *et al.* (2006), chapter VI.6. One prominent example of variational integrators are *Gauss Runge-Kutta methods* which have been shown to be the most efficient and accurate integrators in many general relativistic applications, see, e.g., (Seyrich and Lukes-Gerakopoulos, 2012; Seyrich, 2013). Motivated by these results, we choose this kind of variational integrator for the solution of the MP equations. Here we briefly summarize some of their properties.

An  $s$ -stage Gauss Runge-Kutta scheme is a collocation method, i.e., an implicit Runge-Kutta scheme

$$\mathbf{y}_{n+1} = \mathbf{y}_n + h \sum_{i=1}^s b_i f(\mathbf{Y}_i) \quad , \quad (\text{A.76})$$

$$\mathbf{Y}_i = \mathbf{y}_n + h \sum_{j=1}^s a_{ij} f(\mathbf{Y}_j), \quad i = 1, \dots, s \quad , \quad (\text{A.77})$$

with coefficients

$$a_{ij} = \int_0^{c_i} l_j(t) dt \quad , \quad (\text{A.78})$$

$$b_j = \int_0^1 l_j(t) dt \quad , \quad (\text{A.79})$$

where the stages  $c_1, \dots, c_s$  are chosen as

$$c_i = \frac{1}{2}(1 + \tilde{c}_i) \quad , \quad (\text{A.80})$$

with  $\tilde{c}_i$  being the roots of the Legendre-polynomial of degree  $s$ . Here,  $h$  denotes the time step size,  $\mathbf{Y}_i$ ,  $i = 1, \dots, s$ , are the so-called inner stage values and  $\mathbf{y}_n$  denotes the numerical approximation to the solution  $\mathbf{y}$  at time  $\tau = nh$ . The functions  $l_i(t)$  are the Lagrange-polynomials of degree  $s$ ,

$$l_i(t) = \prod_{i \neq j} \frac{t - c_j}{c_i - c_j} \quad . \quad (\text{A.81})$$

Gauss Runge-Kutta methods have a convergence order  $\mathcal{O}(h^{2s})$  which is the highest possible order among collocation schemes, e.g., (Hairer *et al.*, 1993). When integrating a time step with a Gauss Runge-Kutta scheme, one first solves the system of implicit equations (A.77) via a fixed-point iteration

$$\mathbf{Y}_i^{k+1} = \mathbf{y}_n + h \sum_{j=1}^s a_{ij} f(\mathbf{Y}_j^k) \quad . \quad (\text{A.82})$$

This, of course, requires more calculations per time step than an explicit scheme with the same number of stages. But, this extra effort is more than offset by the high accuracy of Gauss collocation methods which allows us to apply them with a much larger step size. Detailed information on their implementation is given in (Seyrich, 2013, Sec. 7), and (Hairer *et al.*, 1993, Chapters VIII.5 and VIII.6).

To illustrate the favorable behavior of Gauss collocation methods, we compare the performance of a 4-stage scheme with step size  $h = 1$  and a standard 5-th order explicit Cash-Karp scheme as proposed by Flannery *et al.* (1992) with a step size  $h = 0.1$ , when applied to the MP equations with T SSC and initial data given by  $E = 0.95$ ,  $J_z = 3.0$ ,  $S = 1$ ,  $M = 1$ ,  $\mu = 1$ ,  $a = 0.9$ ,  $r = 6.7$ ,  $\theta = \frac{\pi}{2} + 0.1$ ,  $p_r = 0.1$ ,  $S_r = 0.1$ ,  $S_\theta = 0.01$ . In Fig. A.9, we plot for both integrators the relative error in the energy,

$$\Delta E(\tau) = \frac{|E(\tau) - E(0)|}{|E(0)|}, \quad (\text{A.83})$$

and the corresponding relative error in the  $z$  angular momentum as a function of integration time  $\tau$ . We observe that the Gauss Runge-Kutta method, which is also faster, gives much more precise results.

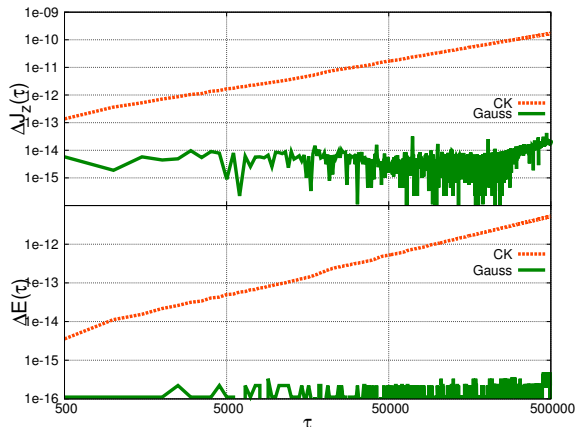


Figure A.9: The relative error of the  $z$  angular momentum,  $\Delta J_z$ , (top panel) and the relative error of the energy,  $\Delta E$ , (bottom panel) against integration time  $\tau$  for the 4-stage Gauss scheme with step size  $h = 1$  and the 5-th order Cash-Karp scheme with step size  $h = 0.1$  applied to the initial value problem (A.55) with initial data as stated in the text. CPU-time was 214.1s for the Gauss Runge-Kutta scheme and 422.7s for the Cash-Karp scheme.

An additional obstacle for simulations in the NW SSC case is that the tangential velocity  $v^\mu$  is only given implicitly by Eq. (A.27). (N.b.: Apart from the apparent  $v^\nu$  in the first term on the right hand side, the covariant derivative of  $\omega_\nu$  implies a linear dependence on  $v^\nu$  in the second term on the rhs as well, i.e.,  $\frac{D}{d\tau} \omega_\nu = \dot{\omega}_\nu - \Gamma_{\nu\mu}^\kappa \omega_\kappa v^\mu$ .) Setting  $\vec{v} := (v^t, v^r, v^\phi, v^\theta)^T \in \mathbb{R}^4$ , the implicit equation for  $v^\mu$  is qualitatively given by

$$\vec{v} = A(x^\mu, p^\mu, S^{\mu\nu})\vec{v} \quad (\text{A.84})$$

for a certain matrix  $A \in \mathbb{R}^{4 \times 4}$ . Theoretically there are two possibilities to cope with the implicitness in the velocities which we will describe now.

- Denoting the first four components of  $Y_i$  and  $f(Y_i)$  by  $Y_i^x$  and  $f^x(Y_i)$ , and the other components by  $Y_i^p$ ,  $Y_i^s$ ,  $f^p(Y_i)$ , and  $f^s(Y_i)$  we can augment the system of implicit equations (A.77) by adding the implicitly given quantity  $\vec{v}_i$  which denotes the tangential velocity  $v^\mu$  at the inner stage  $Y_i$ . This yields the system

$$\begin{pmatrix} \vec{v}_i \\ \mathbf{Y}_i^x \\ \mathbf{Y}_i^p \\ \mathbf{Y}_i^s \end{pmatrix} = \begin{pmatrix} A(Y_i^x, Y_i^p, Y_i^s) \vec{v}_i \\ \mathbf{y}_n^x + h \sum_{j=1}^s a_{ij} \vec{v}_i \\ \mathbf{y}_n^p + h \sum_{j=1}^s a_{ij} f^p(Y_i^x, Y_i^p, Y_i^s, \vec{v}_i) \\ \mathbf{y}_n^s + h \sum_{j=1}^s a_{ij} f^s(Y_i^x, Y_i^p, Y_i^s, \vec{v}_i) \end{pmatrix},$$

$$i = 1, \dots, s, \quad (\text{A.85})$$

to which, again, a fixed-point iteration can be applied. However, for this iteration to converge, it needs to satisfy

$$\left\| \begin{pmatrix} \vec{v}_i^{k+2} \\ \mathbf{Y}_i^{k+2} \end{pmatrix} - \begin{pmatrix} \vec{v}_i^{k+1} \\ \mathbf{Y}_i^{k+1} \end{pmatrix} \right\| \leq \left\| \begin{pmatrix} \vec{v}_i^{k+1} \\ \mathbf{Y}_i^{k+1} \end{pmatrix} - \begin{pmatrix} \vec{v}_i^k \\ \mathbf{Y}_i^k \end{pmatrix} \right\|, \quad (\text{A.86})$$

which cannot be guaranteed when  $A(Y_i^x, Y_i^p, Y_i^s)$  is of large norm. Numerical tests have shown that there are indeed problems with the convergence. Hence, for all its conceptual beauty, the approach of an augmented implicit system is of no practical use.

- With  $I$  denoting the  $4 \times 4$  identity matrix, we can rewrite the implicit equation for the velocities (A.84) as

$$0 = (I - A) \vec{v} =: B \vec{v}. \quad (\text{A.87})$$

Thus, from an algebraical point of view, the vector consisting of the components of the 4-velocity is an element of the nullspace  $\text{Ker}(B)$  of the matrix  $B$  which here is a one-dimensional subspace. Consequently, we can determine the tangential velocity at an internal stage by the following procedure

1. Calculate

$$B(Y_i^x, Y_i^p, Y_i^s) = I - A(Y_i^x, Y_i^p, Y_i^s). \quad (\text{A.88})$$

2. Calculate the singular-value-decomposition of  $B$ , i.e.,

$$B = U \Sigma V^T, \quad (\text{A.89})$$

with  $\Sigma = \text{diag}(\sigma_1, \sigma_2, \sigma_3, \sigma_4)$  and  $U^T U = V^T V = \delta_{ij}$ ,  $i, j = 1, \dots, 4$ . For more information on the singular value decomposition, see, e.g., (Flannery *et al.*, 1992, Chapter 2.6). The nullspace of  $B$  is then spanned by the column of the orthonormal matrix  $V_{.,i}$  that corresponds to the only singular value  $\sigma_i$  which is equal to 0.

3. The tangential velocity is now obtained by renormalizing  $V_{.,i}$  in order to have  $v^\mu v_\mu = -1$ .

This procedure is very robust and the computational cost for the calculation of the matrix  $B$  and the singular value decomposition is far less than the computational cost for the calculation of the other quantities which are needed anyway. This could be confirmed experimentally when comparing CPU times for simulations with T SSC and NW SSC for similar initial values. For all the simulations done in the preparation for this work, the CPU times in the NW SSC case were only slightly higher than those for the T SSC case where the velocities could be determined explicitly via Eq. (A.24).

---

Last, we turn to the numerical integration of the Hamiltonian formalism in the next section.

## A.8. Numerical integration of the Hamiltonian equations

The Hamiltonian equations considered in this study have a so-called *Poisson structure*, that is, with  $\mathbf{y} = (P_r, P_\theta, P_\phi, r, \theta, \phi, S_1, S_2, S_3)^T \in \mathbb{R}^9$ , they can be written as

$$\dot{\mathbf{y}} = B(\mathbf{y})\nabla H(\mathbf{y}) \quad , \quad (\text{A.90})$$

where  $B : \mathbb{R}^9 \rightarrow \mathbb{R}^{9 \times 9}$  is a skew-symmetric matrix-valued function. In our case, this function  $B(\mathbf{y})$  is given by

$$B(\mathbf{y}) = \begin{pmatrix} 0 & -I_{3 \times 3} & 0 \\ I_{3 \times 3} & 0 & 0 \\ 0 & 0 & B_1(\mathbf{y}) \end{pmatrix} \quad , \quad (\text{A.91})$$

with

$$I_{3 \times 3} = \begin{pmatrix} 1 & 0 & 0 \\ 0 & 1 & 0 \\ 0 & 0 & 1 \end{pmatrix} \quad , \quad (\text{A.92})$$

$$B_1(\mathbf{y}) = \begin{pmatrix} 0 & -S_3 & S_2 \\ S_3 & 0 & -S_1 \\ -S_2 & S_1 & 0 \end{pmatrix} \quad . \quad (\text{A.93})$$

For such  $B(\mathbf{y})$ , there exists a smooth transformation to new coordinates  $\mathbf{z}$ , for which the equations of motion are of symplectic form

$$\dot{\mathbf{z}} = J^{-1}\nabla H(\mathbf{z}) \quad , \quad (\text{A.94})$$

$$J = \begin{pmatrix} 0 & I_{4 \times 4} \\ -I_{4 \times 4} & 0 \end{pmatrix} \quad , \quad (\text{A.95})$$

see (Wu and Xie, 2010; Seyrich, 2013). The idea how to find this transformation is based on the conservation of the spin length  $S = \sqrt{S_1^2 + S_2^2 + S_3^2}$  by the eqs. (A.90). Thus, the three dimensional spin  $\mathbf{S} = (S_1, S_2, S_3)^T$  can be given as a function of two variables  $\alpha$  and  $\xi$  via

$$\mathbf{S} = S \begin{pmatrix} \sqrt{1 - \xi^2} \cos(\alpha) \\ \sqrt{1 - \xi^2} \sin(\alpha) \\ \xi \end{pmatrix} \quad . \quad (\text{A.96})$$

One can then show that

$$\dot{\xi} = -\frac{\partial H}{\partial \alpha} \quad , \quad (\text{A.97})$$

$$\dot{\alpha} = \frac{\partial H}{\partial \xi} \quad (\text{A.98})$$

hold, see, e.g., (Seyrich, 2013). Hence, for the variables  $\mathbf{z} = (P_r, P_\theta, P_\phi, \xi, r, \theta, \phi, \alpha)$ , the equations of motion indeed take the form (A.94). Whenever a system can be smoothly

transformed to symplectic form, it can be evolved by symplectic integration schemes. Therefore, for our studies of the Hamiltonian formalism of Barausse *et al.* (2009), we follow Seyrich (2013) and use Gauss Runge-Kutta schemes which have already been presented in the last section<sup>55</sup>. In order to show their favorable behavior, we evolve the Hamiltonian system for initial data  $M = 1$ ,  $m = 1$ ,  $a = \frac{1}{10}$ ,  $r = 15$ ,  $\theta = \frac{\pi}{2}$ ,  $\phi = 0$ ,  $P_r = 0$ ,  $P_\theta = 3.69336$ ,  $P_\phi = J_z = 3.8$ ,  $S_1 = \frac{1}{\sqrt{2}}$ ,  $S_2 = \frac{1}{\sqrt{3}}$ ,  $S_3 = \frac{1}{\sqrt{6}}$  and plot, in Fig. A.10, the relative error of the Hamiltonian (A.68) once for the Gauss Runge-Kutta method with  $s = 4$  inner stages and once for the 5th order explicit Cash-Karp scheme. For the explicit method we observe a linear growth in the error while there is no significant error during the whole simulation for the Gauss scheme. This is in spite of the latter's much smaller CPU time. With regard to the computational effort, we also notice that it is much smaller than in the case of the full MP equations, although both cases were tested on the same machine. This gives another practical reason to consider the Hamiltonian approximation.

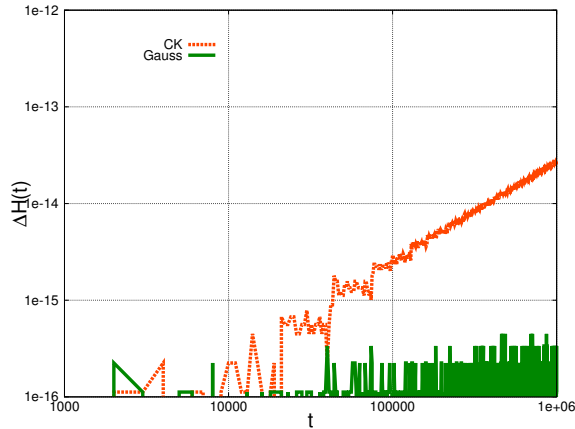


Figure A.10: The relative error of the Hamiltonian,  $\Delta H$  against integration time  $t$  for the 4-stage Gauss scheme with step size  $h = 2$  and the 5-th order Cash-Karp scheme with step size  $h = 0.2$  applied to the initial value problem (A.90) with initial data as stated in the text. CPU-time was 7.83s for the Gauss Runge-Kutta scheme and 24,7s for the Cash-Karp scheme.

In our comparison of the orbits given by the MP equations with those of the Hamiltonian formalism, the concerning simulations have to produce output for the same coordinate times. To avoid having to reformulate the MP equations for the coordinate time as evolution parameter, we proceed as follows. In the simulation of the MP equations, output is produced at uniform distances in the evolution parameter proper time. The output also comprises the corresponding coordinate times. These are then fed as input to the Hamiltonian simulations -for example under the name  $t_{\text{output required}}$ . Now, if in the simulation with uniform steps in the evolution parameter coordinate time  $t$ , between times  $t_i$  and  $t_{i+1}$  say, one passes one of the prescribed times for which output is required,  $t_{\text{output required}}$ , one can take use of the interpolation property of the collocation schemes to comfortably obtain output at no computational extra cost. It is well known that the interpolation polynomial  $\mathbf{u}(t)$  through the points  $(0, \mathbf{y}_n)$ ,  $(c_i, \mathbf{Y}_i)$ ,

<sup>55</sup>As opposed to the approach in (Seyrich, 2013) we did not bother to rewrite the system in the variables  $z$ , because in the present case the additional cost of the one extra variable is negligible in comparison to the other computational effort.

$i = 1, \dots, s$ , stays  $\mathcal{O}(h^s)$  close to the exact solution of the equation of motion, and, hence, also to the numerical calculated trajectory, see, e.g., (Hairer *et al.*, 1993). We thus only have to evaluate  $\mathbf{u}(t)$  at time  $t_{\text{output required}} - t_i$  which yields an approximation of the solution at time  $t_{\text{output required}}$  which is exact up to an error of  $\mathcal{O}(h^s)$ . The interpolation polynomial itself can be calculated very quickly with the so-called Horner scheme

$$\begin{aligned} \mathbf{u}(t) &= \mathbf{y}_i \\ &+ (t - 0) \left( \delta^1[0, hc_1] + (t - hc_1) \left( \delta^2[0, hc_1, hc_2] + (t - hc_2) \left( \dots (t - hc_{s-1}) \delta^s[0, hc_1, \dots, hc_s] \dots \right) \right) \right) , \\ \delta^1[0, hc_1] &= \frac{\mathbf{Y}_1 - \mathbf{y}_i}{hc_1 - 0} , \\ \delta^k[0, hc_1, \dots, hc_k] &= \frac{\delta^{k-1}[hc_1, \dots, hc_k] - \delta^{k-1}[0, hc_1, \dots, hc_{k-1}]}{hc_k - 0} . \end{aligned} \quad (\text{A.99})$$

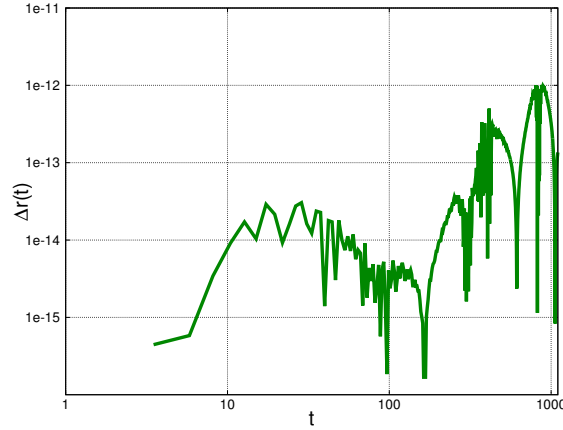


Figure A.11: The relative difference,  $\Delta r$ , between the radial distance calculated with the interpolation method and the radial distance calculated via the cumbersome method with extra integration steps plotted against output time  $t$ .

The more intricate way of producing output at the desired times would be the following:

- When having passed an output time  $t_{\text{output required}}$  between  $t_i$  and  $t_{i+1}$ , go back to  $t_i$ .
- Change  $h \rightarrow h_{\text{new}} = t_{\text{output required}} - t_i$ .
- Evolve the system until  $t = t_{\text{output required}}$  with step size  $h_{\text{new}}$  and produce output.
- Go back to  $t_i$  and go on integrating with step size  $h$ . (Note that this is necessary as the scheme would lose its symplectic structure when applied with different step sizes, see, e.g. (Hairer *et al.*, 2006), chapter VIII.)

In order to illustrate that this cumbersome procedure is not worth the additional effort, we again consider the data which yielded Fig. A.5 and, for every coordinate time  $t$ , for which  $\Delta_{xyz}$  was plotted in the central panel of that figure, we plot the relative difference in the radial distance at those times between the interpolation method and the cumbersome method,

$$\Delta r(t) = \frac{|r_{\text{interpolation}}(t) - r_{\text{cumbersome}}(t)|}{r} . \quad (\text{A.100})$$

In Fig. A.11, we can observe that the difference is negligible.

---

## B. Comparing Hamiltonians of a spinning test particle for different tetrad fields

The content of this Section was published as [D. Kunst, T. Ledvinka, G. Lukes-Gerakopoulos, and J. Seyrich *Phys. Rev. D* **93**, 044004 (2016)] under lead-authorship of Daniela Kunst. The theoretical work was done by Daniela Kunst and Tomáš Ledvinka. The simulations, which triggered the theoretical considerations and which corroborated the theoretical results, as well as the studies for integrability, were carried out by Georgios Lukes-Gerakopoulos and J. S. . The plots shown in the publication, c.f. Figs. B.1,B.2,B.3,B.4,B.5,B.6, were produced by Daniela Kunst and Georgios Lukes-Gerakopoulos.

### Abstract

This work is concerned with suitable choices of tetrad fields and coordinate systems for the Hamiltonian formalism of a spinning particle derived in Barausse *et al.* (2009). After demonstrating that with the originally proposed tetrad field the components of the total angular momentum are not preserved in the Schwarzschild limit, we analyze other hitherto proposed tetrad choices. Then, we introduce and thoroughly test two new tetrad fields in the horizon penetrating Kerr–Schild coordinates. Moreover, we show that for the Schwarzschild spacetime background the linearized in spin Hamiltonian corresponds to an integrable system, while for the Kerr spacetime we find chaos which suggests a nonintegrable system.

### B.1. Introduction

The motion of a spinning particle in the spacetime background of a black hole, particularly the Kerr spacetime, is of great astrophysical interest. Namely, it approximates the motion of a stellar compact object (e.g., a black hole) around a supermassive black hole. Such binary systems are expected to lie at the center of galaxies, see, e.g., (Amaro-Seoane *et al.*, 2015) and references therein, and to be good candidates for sources of gravitational radiation (Riles, 2013).

Even though the equations describing the motion of a spinning particle in a curved spacetime have been provided several decades ago by Mathisson (1937) and Papapetrou (1951), many issues of this motion are still open. The problem lies in the fact that the Mathisson-Papapetrou (MP) equations are not a closed system of first order differential equations. Hence, a spin supplementary condition (SSC) is needed in order to close them. Several such SSCs have been proposed, see, e.g., (Semerák, 1999; Kyrian and Semerák, 2007) for a review, each of which introduces a different reference frame. Physically, the ambiguity in the choice of a SSC is related to the fact that a spinning body cannot be treated as a point particle but must have a finite size in order to be prevented from rotating at superluminal speed (Møller, 1949). In particular, each SSC corresponds to an observer who sees the reference worldline fixed by the SSC as the center of mass of the extended body. Previous studies have shown that the choice of the SSC depends on the question one wants to investigate (Corinaldesi and Papapetrou, 1951; Costa *et al.*, 2012; Semerák, 1999; Kyrian and Semerák, 2007; Lukes-Gerakopoulos *et al.*, 2014; Møller, 1949; Pirani, 1956; Semerák and Šrámek, 2015).

---

Within the MP equations the motion of spinning test particles in the Schwarzschild or Kerr spacetime has been investigated by Hackmann *et al.* (2014); Plyatsko and Fenyk (2012, 2013), and several papers have been devoted to the investigation of the appearing chaotic motion (Hartl, 2003a,b; Suzuki and Maeda, 1997; Verhaaren and Hirschmann, 2010). Beyond the pole-dipole approximation, the quadrupole moment of the test particle has already been taken into account in (Steinhoff and Puetzfeld, 2012; Bini and Geralico, 2014).

The dynamics of spinning test particles has not only been worked out in Lagrangian formalisms (MP equations) (Bailey and Israel, 1975), but in Hamiltonian formalisms as well (Steinhoff *et al.*, 2008; Steinhoff, 2011; Barausse *et al.*, 2009; Tauber, 1988). Hamiltonian dynamics has a long tradition in astronomy and a large number of problems there (e.g. perturbative problems or chaotic motion) are typically studied from a Hamiltonian perspective (Contopoulos, 2002). In general relativity, the Hamiltonian formalisms have been applied, for example, in the framework of the canonical Arnowitt–Deser–Misner (ADM) formalism of Arnowitt *et al.* (1962) and in the effective one body approach (EOB) of Buonanno and Damour (1999), Damour *et al.* (2000) and Damour (2008), which studies the dynamics of spinning bodies of comparable masses using the Hamiltonian description of a one body problem (Blanchet, 2006).

Due to the significance of a Hamiltonian approach the Hamiltonian description of spinning particles is important despite the fact that it mostly neglects terms quadratic in spin.

In our previous work (Lukes-Gerakopoulos *et al.*, 2014), we have compared the Tulczyjew (T) SSC (Tulczyjew, 1959) with the Newton-Wigner (NW) SSC (Newton and Wigner, 1949) as supplements to the MP equations. In a second step, we compared the MP equations supplemented by the NW SSC to the corresponding Hamilton equations derived by Barausse *et al.* (2009) based on the same NW SSC. In this work we focus on the latter, i.e., on a canonical Hamiltonian formalism which should be equivalent to the MP equations up to the linear order of the test particle spin.

In contrast to the T SSC, the NW SSC, which is used within the framework of the Hamiltonian formalism, does not provide a unique choice of reference frame. It rather defines an entire class of observers, each characterized by a different tetrad field. Thus, the Hamiltonian formalism proposed in (Barausse *et al.*, 2009) depends on the choice of a reference basis given by such a tetrad field. Each choice of a tetrad field basically determines the form and the properties of the resulting Hamiltonian function. The fact that tetrads providing certain frames of reference are involved in a definition of the spin variable can also be seen as a consequence of the fact that in the Hamiltonian description the spin is a vector with prescribed canonical relations to coordinates and momenta. Still, one might conclude that the tetrad dependence of the Hamiltonian description of the spinning particle is against covariance principles of general relativity. Yet, when we numerically solve equations of motion we have to use some coordinates anyway. The involvement of tetrads simply means we use different coordinates for external and inner degrees of freedom of the spinning particle. As, e.g., Boyer-Lindquist coordinates are comfortable for solving equations of motion in Kerr geometry, there may well be some other tetrad fields more suitable for the definition of the Hamiltonian spin.

We discuss the advantages and the drawbacks of Hamiltonian functions arising from tetrad fields already proposed in (Barausse *et al.*, 2009; Barausse and Buonanno, 2010). Then, we introduce two new tetrad fields in Kerr–Schild coordinates which yield Hamiltonian functions with desirable properties using both analytical and numerical analysis. Namely in order to have a good choice of a tetrad field, the corresponding Hamiltonian should reflect the symmetries

of the background spacetime, i.e., preserve the integrals of motion, and avoid any coordinate effects evoked by coordinate dependent tetrad basis vectors.

For the above discussion, we focus on the Schwarzschild limit and show that the well behaving Hamiltonian functions based on our tetrads have as many integrals of motion as degrees of freedom. Thus, it is shown that in the Schwarzschild limit these Hamiltonians describe an integrable system. We view this as an important test, as in general, for different tetrad fields the description of Barausse *et al.* (2009) provides Hamiltonians non-equivalent beyond the given approximation. In any Hamiltonian system, the integrals of motion play a crucial role when the integrability issue is studied. If we have several possible descriptions of the same system in the given approximation, those respecting all background symmetries are the obvious choice. We use the case of spinning particle in Schwarzschild spacetime as such an exact problem with many integrals of motion to demonstrate shortcomings of certain coordinate-tetrad choices. Even though the considered approximations assume small spins, to clearly demonstrate (non-)integrability we also use large spin values in numerical tests.

As for the Kerr spacetime, it was shown by Rüdiger (1981) that if the MP equations supplemented by the T SSC are linearized in the spin, an integral of motion associated with a Killing-Yano tensor appears. This led to the impression that, up to linear order in the spin, the motion of a spinning particle is integrable in general (Hinderer *et al.*, 2013). However, according to our numerical calculations, this seems not to be the case for the Hamiltonian function depending on the tetrad field choice introduced in (Barausse and Buonanno, 2010).

This paper is organized as follows. In Sec. B.2 we give a short overview of the Hamiltonian formalism introduced in (Barausse *et al.*, 2009). After that, In Sec. B.3, we present two different choices of coordinate systems, Boyer-Lindquist and cartesian isotropic coordinates, for a tetrad corresponding to a ZAMO observer which is already given in (Barausse *et al.*, 2009; Barausse and Buonanno, 2010). We analyze the properties of both with the help of analytical calculations and numerical integrations. Then, we present our new tetrads in Kerr-Schild coordinates in Sec. B.4. Finally, in Sec. B.5, we summarize our results. We add a description of our numerical tools in Sec. B.6.

We use geometric units, i.e., ( $G = c = 1$ ), and the signature of the metric is  $(-, +, +, +)$ . Greek letters denote the indices corresponding to spacetime (running from 0 to 3), while Latin letters denote indices corresponding only to space (running from 1 to 3).

## B.2. The Hamiltonian formalism

The Hamiltonian formalism in (Barausse *et al.*, 2009) has been achieved by linearizing the MP equations of motion for the NW SSC. The MP equations describe the motion of a particle with mass  $m^2 = -p_\mu p^\mu$ , satisfying the mass shell constraint, and spin  $S^{\mu\nu}$  in a given spacetime background  $g_{\mu\nu}$ . Their reformulation in (Dixon, 1970) reads

$$\frac{D p^\mu}{d\sigma} = -\frac{1}{2} R^\mu{}_{\nu\kappa\lambda} v^\nu S^{\kappa\lambda} \quad , \quad (\text{B.1})$$

$$\frac{D S^{\mu\nu}}{d\sigma} = p^\mu v^\nu - v^\mu p^\nu \quad , \quad (\text{B.2})$$

---

where  $p^\mu$  is the four-momentum,  $v^\mu = dx^\mu/d\sigma$  is the tangent vector to the worldline along which the particle moves,  $\sigma$  is an evolution parameter along this worldline, and  $R^\mu{}_{\nu\kappa\lambda}$  is the Riemann tensor. The NW SSC reads

$$S^{\mu\nu} \omega_\mu = 0 \quad , \quad (\text{B.3})$$

where  $\omega_\mu$  is a sum of timelike vectors. This sum in (Barausse *et al.*, 2009) has the form

$$\omega_\nu = p_\nu - m \tilde{e}_\nu{}^T \quad , \quad (\text{B.4})$$

where  $\tilde{e}_\nu{}^T$  is a timelike future oriented vector (throughout the article we use T instead of 0), which together with three spacelike vectors  $\tilde{e}^\mu{}_I$ , denoted by capital latin indices, is part of a tetrad field  $\tilde{e}^\mu{}_\Delta$ .

This tetrad field has to satisfy two conditions: the first condition ensures the orthonormality of the tetrad given by

$$\tilde{e}^\mu{}_\Gamma \tilde{e}^\nu{}_\Delta g_{\mu\nu} = \eta_{\Gamma\Delta} \quad , \quad (\text{B.5})$$

where  $\eta_{\Gamma\Delta}$  is the metric of the flat spacetime and  $g_{\mu\nu}$  its analogon for the curved spacetime background. The capital indices are raised and lowered by the flat metric  $\eta_{\Gamma\Delta}$ , the small ones by  $g_{\mu\nu}$ . The second condition is implied by (B.5) and reads

$$\tilde{e}^\mu{}_\Delta \tilde{e}_\nu{}^\Delta = \delta_\nu^\mu \quad , \quad (\text{B.6})$$

where  $\delta_\nu^\mu$  is the Kronecker delta.

When a tensor is projected on the tetrad field, then it is denoted with capital indices. For example,  $\omega_\Delta = \tilde{e}^\nu{}_\Delta \omega_\nu$  is the projection of the time-like vector (B.4) on the tetrad field, i.e.,

$$\begin{aligned} \omega_T &= p_\nu \tilde{e}^\nu{}_T - m \quad , \\ \omega_J &= p_\nu \tilde{e}^\nu{}_J \quad . \end{aligned} \quad (\text{B.7})$$

Then, the spin tensor  $S^{\mu\nu}$  projection reads

$$S^{IJ} = S^{\mu\nu} \tilde{e}_\mu{}^I \tilde{e}_\nu{}^J \quad . \quad (\text{B.8})$$

In (Barausse *et al.*, 2009), the authors do not work with this tensor but rather employ the spin three vector

$$S_I = \frac{1}{2} \epsilon_{IJJL} S^{JJL} \quad , \quad (\text{B.9})$$

where  $\epsilon_{IJJL}$  is the Levi-Civita symbol.

Now, the Hamiltonian function  $H$  for a spinning particle

$$H = H_{NS} + H_S \quad , \quad (\text{B.10})$$

splits in two parts. The first,

$$H_{NS} = \beta^i P_i + \alpha \sqrt{m^2 + \gamma^{ij} P_i P_j} \quad , \quad (\text{B.11})$$

is the Hamiltonian for a nonspinning particle, where

$$\alpha = \frac{1}{\sqrt{-g^{00}}} , \quad (\text{B.12})$$

$$\beta^i = \frac{g^{0i}}{g^{00}} , \quad (\text{B.13})$$

$$\gamma^{ij} = g^{ij} - \frac{g^{0i}g^{0j}}{g^{00}} , \quad (\text{B.14})$$

and  $P_i$  are the canonical momenta conjugate to  $x^i$  of the Hamiltonian (B.10). They can be calculated from the momenta  $p_i$  with the help of the relation

$$\begin{aligned} P_i &= p_i + E_{i\Gamma\Delta} S^{\Gamma\Delta} , \\ &= p_i + \left( 2E_{iTJ} \frac{\omega_C}{\omega_T} + E_{iJC} \right) \epsilon^{JCL} S_L , \end{aligned} \quad (\text{B.15})$$

where the spin connection

$$E_{\nu\Gamma\Delta} = -\frac{1}{2} \left( g_{\kappa\lambda} \tilde{e}^\kappa{}_\Gamma \frac{\partial \tilde{e}^\lambda{}_\Delta}{\partial x^\nu} + \tilde{e}^\kappa{}_\Gamma \Gamma_{\kappa\nu\lambda} \tilde{e}^\lambda{}_\Delta \right) , \quad (\text{B.16})$$

is a tensor which is antisymmetric in the last two indices, i.e.,  $E_{\nu\Gamma\Delta} = -E_{\nu\Delta\Gamma}$ , and  $\Gamma_{\kappa\nu\lambda}$  are the Christoffel symbols. The second part of the Hamiltonian,

$$H_S = - \left( \beta^i F_i^C + F_0^C + \frac{\alpha \gamma^{ij} P_i F_j^C}{\sqrt{m^2 + \gamma^{ij} P_i P_j}} \right) S_C , \quad (\text{B.17})$$

provides the contribution of the particle's spin to the motion, with

$$F_\mu^C = \left( 2E_{\mu TI} \frac{\bar{\omega}_J}{\bar{\omega}_T} + E_{\mu IJ} \right) \epsilon^{IJC} , \quad (\text{B.18})$$

and

$$\begin{aligned} \bar{\omega}_\Delta &= \bar{\omega}_\nu \tilde{e}^\nu{}_\Delta , \\ \bar{\omega}_\nu &= \bar{P}_\nu - m \tilde{e}_\nu{}^T , \\ \bar{P}_i &= P_i , \\ \bar{P}_0 &= -\beta^i P_i - \alpha \sqrt{m^2 + \gamma^{ij} P_i P_j} , \\ \bar{\omega}_T &= \bar{P}_\nu \tilde{e}^\nu{}_T - m , \\ \bar{\omega}_J &= \bar{P}_\nu \tilde{e}^\nu{}_J . \end{aligned} \quad (\text{B.19})$$

The equations of motion for the canonical variables as a function of coordinate time  $t$  read

$$\frac{dx^i}{dt} = \frac{\partial H}{\partial P_i} , \quad (\text{B.20})$$

$$\frac{dP_i}{dt} = -\frac{\partial H}{\partial x^i} , \quad (\text{B.21})$$

$$\frac{dS_I}{dt} = \epsilon_{IJC} \frac{\partial H}{\partial S_J} S^C . \quad (\text{B.22})$$

---

The phase space of a canonical Hamiltonian system is equipped with a binary operation, i.e., the Poisson bracket. If the dynamical system is subject to (secondary) constraints  $\xi_i$ , the Poisson bracket has to be replaced by the Dirac bracket (Barausse *et al.*, 2009; Dirac, 1951)

$$\{Q, R\}_{DB} := \{Q, R\} - \{Q, \xi_i\} [C^{-1}]_{ij} \{\xi_j, R\} \quad , \quad (\text{B.23})$$

where  $Q$  and  $R$  are functions on phase space and  $C^{-1}$  is the inverse of the matrix consisting of the Poisson brackets of the set of constraints  $C = \{\xi_i, \xi_j\}$ . In the case of a spinning particle the constraints are given by the supplementary condition, here the NW SSC (B.3), and, in order to retain the symplectic structure, by the choice of the timelike body-fixed tetrad vector to be aligned with the four momentum

$$\chi_\mu := e_{\mu T} - \frac{p_\mu}{m} = 0 \quad ,$$

where  $e^\mu{}_A$  is related to the local frame  $\tilde{e}^\mu{}_A$  by a Lorentz transformation (for more details see (Barausse *et al.*, 2009)). In order to derive the canonical structure of the phase space variables, the new defined momenta  $P_\mu$  in eq. (B.15) are treated as functions of the kinematical momenta  $p_\mu$ , the position, and of the spin which result in the following bracket relations

$$\begin{aligned} \{x^i, P_j\}_{DB} &= \delta_j^i + \mathcal{O}(S^2) \quad , \\ \{S^I, S^J\}_{DB} &= \epsilon^{IJK} S^K + \mathcal{O}(S^2) \quad . \end{aligned} \quad (\text{B.24})$$

All the other bracket relations between the variables vanish at linear order in spin (Barausse *et al.*, 2009). At this approximation, even if the mass  $m^2 = -p_\nu p^\nu$  is not a constant of motion for the exact MP equations with NW SSC, it scales quadratically in the particle's spin, see, e.g., (Lukes-Gerakopoulos *et al.*, 2014), so that the mass is preserved at first order in the spin and treated as a constant in the linearized Hamiltonian formalism (Barausse *et al.*, 2009).

When we restrict the scheme to the linearized Hamiltonian formalism, and consider the  $P_i$  no longer as functions but as independent phase space variables, then the terms of  $\mathcal{O}(S^2)$  are dropped in all the above Dirac brackets, i.e., in (B.24) and all the other bracket relations between the variables  $\{x^i, P_i, S_I\}$ . Profoundly, in the linearized Hamiltonian formalism a quantity  $I$  is a constant of motion, if it holds for its Dirac bracket with the Hamiltonian function  $H$

$$\{I, H\}_{DB} = 0 \quad . \quad (\text{B.25})$$

This means if the system is evolved by the eqs. (B.20)-(B.22), then the quantity  $I$  is preserved during the evolution.

The formulation provided up to this point is general, namely it does not depend on the specific coordinate system or on the specific tetrad field. These two factors, however, are essential for the Hamiltonian function (B.10). In particular, the nonspinning part of the Hamiltonian function (B.11) depends on the coordinate system which the metric is written in, while the spinning part (B.17) depends on the tetrad we choose. In Sec. B.3 and Sec. B.4, we present three different combinations tetrad  $\leftrightarrow$  coordinates for the Kerr spacetime background and discuss the advantages and shortcomings of the respective setups.

## B.3. The Hamiltonian Function in Boyer-Lindquist coordinates compared with Cartesian Isotropic coordinates

### B.3.1. A tetrad in Boyer-Lindquist coordinates

A Hamiltonian function for the Kerr spacetime background in Boyer-Lindquist (BL) has been provided in (Barausse *et al.*, 2009). The line element of the Kerr spacetime in BL coordinates reads

$$ds^2 = g_{tt} dt^2 + 2 g_{t\phi} dt d\phi + g_{\phi\phi} d\phi^2 + g_{rr} dr^2 + g_{\theta\theta} d\theta^2 , \quad (\text{B.26})$$

with

$$\begin{aligned} g_{tt} &= -1 + \frac{2Mr}{\Sigma} , \\ g_{t\phi} &= -\frac{2aMr \sin^2 \theta}{\Sigma} , \\ g_{\phi\phi} &= \frac{\Lambda \sin^2 \theta}{\Sigma} , \\ g_{rr} &= \frac{\Sigma}{\Delta} , \\ g_{\theta\theta} &= \Sigma , \end{aligned} \quad (\text{B.27})$$

and

$$\begin{aligned} \Sigma &= r^2 + a^2 \cos^2 \theta , \\ \Delta &= \varpi^2 - 2Mr , \\ \varpi^2 &= r^2 + a^2 , \\ \Lambda &= \varpi^4 - a^2 \Delta \sin^2 \theta . \end{aligned} \quad (\text{B.28})$$

$M$  denotes the mass and  $a$  the spin parameter of the central Kerr black hole.

The tetrad field given in (Barausse *et al.*, 2009) reads

$$\begin{aligned} \tilde{e}_\mu^T &= \delta_\mu^t \sqrt{\frac{\Delta \Sigma}{\Lambda}} , \\ \tilde{e}_\mu^1 &= \delta_\mu^r \sqrt{\frac{\Sigma}{\Delta}} , \\ \tilde{e}_\mu^2 &= \delta_\mu^\theta \sqrt{\Sigma} , \\ \tilde{e}_\mu^3 &= -\delta_\mu^t \frac{2aMr \sin \theta}{\sqrt{\Lambda \Sigma}} + \delta_\mu^\phi \sin \theta \sqrt{\frac{\Lambda}{\Sigma}} , \end{aligned} \quad (\text{B.29})$$

where for the small indices the numbers have been replaced with the corresponding coordinates, i.e.,  $t$ ,  $r$ ,  $\theta$ ,  $\phi$  stand for 0, 1, 2, 3, respectively. The proposed tetrad corresponds to an

---

observer in the zero angular momentum frame (ZAMO) which intuitively yields a reasonable choice. Moreover, the coordinate system is based on the spherical coordinates in flat spacetime which respects the symmetries of the spacetime. In the Schwarzschild limit the above tetrad field reduces to ( $a \rightarrow 0$ )

$$\begin{aligned}
\tilde{e}_\mu^T &= \delta_\mu^t \sqrt{f(r)} \ , \\
\tilde{e}_\mu^1 &= \delta_\mu^r \sqrt{f(r)^{-1}} \ , \\
\tilde{e}_\mu^2 &= r \delta_\mu^\theta \ , \\
\tilde{e}_\mu^3 &= r \sin \theta \delta_\mu^\phi \ ,
\end{aligned} \tag{B.30}$$

where  $f(r) = 1 - \frac{2M}{r}$ . In the flat spacetime limit ( $M \rightarrow 0, a \rightarrow 0$ ) we get

$$\begin{aligned}
\tilde{e}_\mu^T &= \delta_\mu^t \ , \\
\tilde{e}_\mu^1 &= \delta_\mu^r \ , \\
\tilde{e}_\mu^2 &= r \delta_\mu^\theta \ , \\
\tilde{e}_\mu^3 &= r \sin \theta \delta_\mu^\phi \ .
\end{aligned} \tag{B.31}$$

This yields the flat spacetime in spherical coordinates.

Let's have a closer look at the dynamics in Schwarzschild spacetime. The corresponding metric in Schwarzschild spacetime results in

$$ds^2 = -f(r) dt^2 + f(r)^{-1} dr^2 + r^2 (d\theta^2 + \sin^2(\theta) d\phi^2) \ ,$$

with  $f(r) = 1 - 2M/r$  and the corresponding tetrad field is (B.30). The Hamiltonian

$$H = H_{NS} + H_S \ ,$$

is expressed in terms of the new phase space variables  $(r, \theta, \phi, P_r, P_\theta, P_\phi, S_I^{BL})$  where  $S_I^{BL}$  stands for the spin projected onto the spatial background tetrad in spherical coordinates (reduced from the Boyer-Lindquist coordinates). All told, we have

$$\begin{aligned}
H &= \frac{1}{\sqrt{f(r)}} \sqrt{Q} + \frac{M}{r^3 (1 + \sqrt{Q})} \left( P_\theta S_3^{BL} - \frac{P_\phi}{\sin(\theta)} S_2^{BL} \right) \\
&\quad - \frac{f(r)}{r^2 \sqrt{Q}} \left( \frac{\cos(\theta)}{\sin^2 \theta \sqrt{f(r)}} P_\phi S_1^{BL} - \frac{P_\phi}{\sin(\theta)} S_2^{BL} \right. \\
&\quad \left. + P_\theta S_3^{BL} \right) \ ,
\end{aligned} \tag{B.32}$$

where  $Q = m^2 + f(r) P_r^2 + \frac{1}{r^2} P_\theta^2 + \frac{1}{r^2 \sin^2(\theta)} P_\phi^2$ .

In (Barausse *et al.*, 2009), a criterion for the behavior of the Hamiltonian in the flat spacetime limit was introduced in order to check whether the choice of coordinates is a ‘‘good’’ one. Ideally, the contributions from the spin to the Hamiltonian  $H_S$  vanish, since we no longer have curvature which the spin could couple to and the trajectory of the spinning particle should

simply be the one of a straight line. Thus, the motion of the particle should be completely independent of the spin. However, in the case of spherical coordinates the Hamiltonian is given by (B.32) and the contribution from the spin part  $H_S$  does not vanish representing an evolution of the spin in the absence of spin-orbit coupling, as was noted in (Barausse *et al.*, 2009), which might imply a coordinate effect for this choice of tetrad. Following the latter line of thought, we might say that the basis vectors are coordinate dependent, since they are oriented along the direction of the coordinate basis vectors in spherical coordinates. Therefore, they introduce an additional evolution to the dynamical system which affects the equations of motion for the spinning particle, i.e., the equations of motion do not only contain the physical dynamics of the spinning object, but also the coordinate dynamics. On the other hand, the coordinate effect might not be the only interpretation, for instance for a long time the helical motion of a spinning particle with Pirani SSC in the flat spacetime was considered unnatural, until it was explained in terms of a hidden momentum by Costa *et al.* (2012). Anyhow, such effects make it harder to gain insights into the physical behavior of the particle's motion, since it is not so easy to distinguish between coordinate effects and physical effects in the results. Therefore, we prefer to focus on a more solid criterion for the Hamiltonian to check whether the choice of coordinates is a “good” one, and this criterion comes from the symmetries of the system.

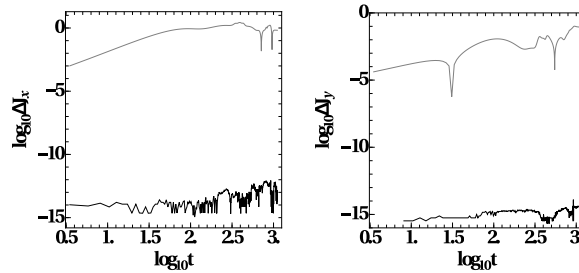


Figure B.1: The left panel shows the relative error of  $\Delta J_x$ , and the right of  $\Delta J_y$  as a function of time in logarithmic scale for the Schwarzschild background. The gray lines show the relative error of these quantities when the system is evolved using the Hamiltonian function corresponding to the tetrad (B.30), while the black lines show the relative error of these quantities when the system is evolved using the respective MP equations. Both evolutions share the same initial conditions conditions, where  $a = 0$ ,  $M = m = 1$ , and  $S = 1$ .

Generally, according to Noether's theorem each spacetime symmetry is related to a conserved quantity. In the case of spinning particles moving in a particular spacetime geometry equipped with a symmetry described by a Killing vector  $\xi_\mu$ , the associated quantity conserved by MP equations reads

$$C = p^\mu \xi_\mu - \frac{1}{2} S^{\mu\nu} \xi_{\mu;\nu} . \quad (\text{B.33})$$

In Schwarzschild spacetime we have three spatial Killing vectors yielding the three components of the total angular momentum (Suzuki and Maeda, 1997)

$$\begin{aligned} J_x = & -p_\theta \sin(\phi) - p_\phi \cot(\theta) \cos(\phi) \\ & + r^2 S^{\theta\phi} \sin(\theta)^2 \cos(\phi) + r S^{\phi r} \sin(\theta) \cos(\theta) \cos(\phi) \end{aligned}$$

---


$$\begin{aligned}
& - r S^{r\theta} \sin(\phi) \quad , \\
J_y &= p_\theta \cos(\phi) - p_\phi \cot(\theta) \sin(\phi) + r^2 S^{\theta\phi} \sin(\theta)^2 \sin(\phi) \\
& + r S^{\phi r} \sin(\theta) \cos(\theta) \sin(\phi) + r S^{r\theta} \cos(\phi) \quad , \\
J_z &= p_\phi - r \sin(\theta)^2 \left( S^{\phi r} - r S^{\theta\phi} \cot(\theta) \right) \quad ,
\end{aligned}$$

where  $p_i$  are the kinematical momenta and  $S^{ij}$  the spin components written in coordinate basis. In order to check whether the components of the total angular momentum are constants of motion within the Hamiltonian formulation we have to transform the expression to canonical variables  $P_i$  and  $S_i^{BL}$  with the relations given in (B.8) and (B.15). Therewith we obtain

$$\begin{aligned}
J_x &= \cos(\phi) (S_1^{BL} \csc(\theta) - P_\phi \cot(\theta)) - P_\theta \sin(\phi) \quad , \\
J_y &= P_\theta \cos(\phi) + \sin(\phi) (S_1^{BL} \csc(\theta) - P_\phi \cot(\theta)) \quad , \\
J_z &= P_\phi \quad ,
\end{aligned}$$

for the components of the total angular momentum, with which we may now compute the evolution equations for  $J_i$  via the Dirac brackets with the Hamiltonian. Indeed, they result in

$$\begin{aligned}
\{J_x, H\}_{DB} &= \mathcal{O}(S^2) \quad , \\
\{J_y, H\}_{DB} &= \mathcal{O}(S^2) \quad , \\
\{J_z, H\}_{DB} &= 0 \quad ,
\end{aligned}$$

and

$$\{J_x^2 + J_y^2 + J_z^2, H\}_{DB} = \mathcal{O}(S^2) \quad .$$

Although we consistently keep the linearization in the Hamiltonian and the corresponding bracket structure, we find that the Dirac brackets for  $J_x$ ,  $J_y$  and  $J_z$  contain contributions from higher orders in the particle's spin. Indeed,  $J_x$  and  $J_y$  start oscillating when the Hamiltonian system corresponding to the tetrad field (B.30) is numerically evolved through the the equations of motion (B.20)-(B.22). It is visible from the relative error

$$\Delta J_i = \left| 1 - \frac{J_i(t)}{J_i(0)} \right| \quad i = x, y \quad , \tag{B.34}$$

at time  $t$  of the  $J_x$  and  $J_y$  (gray line) in Fig. B.1, that the Hamiltonian function resulting from the tetrad (B.30) apparently violates the symmetry properties of the Schwarzschild spacetime. Consequently, the total angular momentum  $J^2$  is not preserved, because the  $x$  and  $y$  components of the total angular momentum exhibit inappropriate behavior. On the other hand, the respective evolution using the MP equation supplemented with NW SSC, instead, shows the expected preservation of the angular momentum components (black curves in Fig. B.1). This shows that even in the above linear in spin Hamiltonian approximation a quantity is a constant of motion only when its Dirac brackets with the Hamiltonian are exactly zero, while when the brackets have contributions from the higher in spin orders, the quantities show no constancy. The violation of the expected symmetries results in a system that exhibits chaotic motion (scattered dots in the left panel of Fig. B.2), which contradicts with the integrability of the Hamiltonian for the spinning particle on the Schwarzschild background we

prove in section B.3.2. It is true, however, that the relative error of the  $J_x$ ,  $J_y$  components, and therefore of  $J^2$  scale with  $S$  (right panel of Fig. B.2). However, this should be anticipated since as  $S \rightarrow 0$  the system basically ignores the spin contribution and tends to reproduce geodesic trajectories.

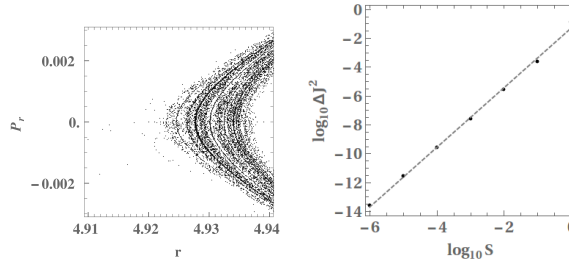


Figure B.2: In the left panel is a detail from the surface of section  $\theta = \pi/2$ ,  $P_\theta > 0$ . The parameters of the orbits are  $H = 0.95$ ,  $J_z = P_\phi = 3$ ,  $S = M = m = 1$ ,  $a = 0$ , the common initial conditions are  $\phi = 0$ ,  $P_r = 0$ ,  $S_1 = S_2 = 0$ ,  $S = S_3 = 10^{-2}$ , while the initial  $P_\theta$  is defined numerically by the Hamiltonian function  $H$ . The right panel shows how the maximal value of the relativity error  $\Delta J^2 = |1 - J^2(t)/J^2(0)|$  for evolution intervals  $t = 10^3$  scales with the spin measure  $S$ .

In this work we focus on the properties of the equations of motion, and not so much on the astrophysical implication of these equations. The spin of the particle makes the trajectories to deviate from their geodesic paths. Thus, we can interpret the spin as a perturbation parameter of the system. A constant of motion cannot depend on the magnitude of the spin, even if the given value might be astrophysically irrelevant. This independence from the spin magnitude holds also for the integrability of a spinning particle Hamiltonian (excluding of course the case when  $S = 0$ ). In our numerical calculations we measure the spin in units of  $m M$ , i.e.  $\sigma = S/(m M)$ , and set both masses to 1, thus the spin parameter  $\sigma = S$  is dimensionless. Large values of the dimensionless spin, like  $S = 1$ , might be astrophysically questionable, but do not have implications on the dynamics, see, e.g., Suzuki and Maeda (1997); Hartl (2003a) for relevant discussions. In our paper large values of the spin serve mainly as a tool to amplify the effects we want to point out, since these effects become less prominent when  $S \ll 1$ .

Moreover, we find that

$$\{L_x^2 + L_y^2 + L_z^2, H\}_{DB} = \mathcal{O}(S^2) \quad ,$$

with

$$L_x = -p_\theta \sin(\phi) - p_\phi \cot(\theta) \cos(\phi) \quad ,$$

$$L_y = p_\theta \cos(\phi) - p_\phi \cot(\theta) \sin(\phi) \quad ,$$

$$L_z = p_\phi \quad ,$$

which also have to be rewritten in terms of the canonical momenta  $P_i$ . The conservation of the measure of the orbital momentum  $L^2$  of the linearized in spin MP equation in the case of the Schwarzschild spacetime background has been thoroughly discussed in Apostolatos (1996) for the Pirani SSC (Pirani, 1956). When the measure of the spin  $S^2 = S_I S^I$  and the total angular momentum  $J^2$  are preserved, the integral of motion  $L^2$  is equivalent to the conservation of

---

$\vec{L} \cdot \vec{S}$ . However, as we have already seen for the total angular momentum, we recover the same numerical problems for the measure of the orbital angular momentum. These two kinds of oscillations can be traced back to the coordinate dependence of the basis vectors in the spherical coordinate system, as we will see in the next subsection.

So far, these coordinate effects have been investigated in Schwarzschild spacetime. Since the Schwarzschild spacetime is the nonrotating limit of the Kerr spacetime we would like to ensure that such coordinate effects can be eliminated in the nonrotating limit, i.e., the coordinate effects should vanish for nonrotating or slowly rotating black holes. Thus, we were wondering whether there are more suitable choices of a coordinate system and of a tetrad for rotating black holes which do not show any unphysical coordinate effects in the Schwarzschild limit. Hence, the question arises as to which coordinates are best used?

Therefore, in the rest of Sec. B.3 we study the Hamiltonian formulation in an isotropic coordinate systems for the same kind of observer (ZAMO), introduced by Barausse and Buonanno (2010).

### B.3.2. The Hamiltonian function in isotropic cartesian coordinates

A revised Hamiltonian function for the Kerr spacetime background in BL has been provided by Barausse and Buonanno (2010). The formulation starts in cartesian quasi-isotropic coordinates. The line element in these coordinates for an axisymmetric stationary metric is

$$\begin{aligned}
ds^2 &= g_{tt} dt^2 \\
&+ 2 g_{tX} dX dt + 2 g_{tY} dY dt + 2 g_{XY} dX dY \\
&+ g_{XX} dX^2 + g_{YY} dY^2 + g_{ZZ} dZ^2 ,
\end{aligned} \tag{B.35}$$

with

$$\begin{aligned}
g_{tt} &= e^{-2\nu} [B^2 \omega^2 (X^2 + Y^2) - e^{4\nu}] , \\
g_{tX} &= e^{-2\nu} \omega B^2 Y , \\
g_{tY} &= -e^{-2\nu} \omega B^2 X , \\
g_{XY} &= -\frac{(e^{-2\nu} B^2 - e^{2\mu}) XY}{X^2 + Y^2} , \\
g_{XX} &= \frac{e^{2\mu} X^2 + e^{-2\nu} B^2 Y^2}{X^2 + Y^2} , \\
g_{YY} &= \frac{e^{2\mu} Y^2 + e^{-2\nu} B^2 X^2}{X^2 + Y^2} , \\
g_{ZZ} &= e^{2\mu}
\end{aligned} \tag{B.36}$$

where  $\omega$ ,  $e^\mu$ ,  $e^\nu$ ,  $B$  are functions of  $X$ ,  $Y$ ,  $Z$ .

For this coordinate system the authors propose the tetrad field

$$\begin{aligned}
\tilde{e}_\beta{}^T &= e^\nu \delta_\beta^t , \\
\tilde{e}_\beta{}^1 &= \frac{B \omega Y}{e^\nu} \delta_\beta^t + \frac{e^\mu X^2 + e^{-\nu} B Y^2}{X^2 + Y^2} \delta_\beta^X \\
&\quad + \frac{(e^\mu - e^{-\nu} B)XY}{X^2 + Y^2} \delta_\beta^Y , \\
\tilde{e}_\beta{}^2 &= -\frac{B \omega X}{e^\nu} \delta_\beta^t + \frac{(e^\mu - e^{-\nu} B)XY}{X^2 + Y^2} \delta_\beta^X \\
&\quad + \frac{e^\mu Y^2 + e^{-\nu} B X^2}{X^2 + Y^2} \delta_\beta^Y , \\
\tilde{e}_\beta{}^3 &= e^\mu \delta_\beta^Z ,
\end{aligned} \tag{B.37}$$

corresponding to an infalling observer with zero 3-momentum. This tetrad becomes cartesian, i.e.,  $\tilde{e}_\beta{}^T = 1$ ,  $\tilde{e}_\beta{}^I = \delta_\beta^I$ , in the flat spacetime limit.

The cartesian quasi-isotropic coordinates relate with the BL coordinate system through the transformation

$$\begin{aligned}
X &= R(r) \sin \theta \cos \phi , \\
Y &= R(r) \sin \theta \sin \phi , \\
Z &= R(r) \cos \theta , \\
R(r) &= \frac{1}{2}(r - M + \sqrt{\Delta}) .
\end{aligned} \tag{B.38}$$

The above relation between  $r$  and  $R$  holds outside the black hole's horizon <sup>56</sup>.

When we go back to the Schwarzschild spacetime where  $a \rightarrow 0$ ,

$$ds^2 = -f(R)dt^2 + h(R)(dX^2 + dY^2 + dZ^2) , \tag{B.39}$$

the tetrad (B.37) reduces to the isotropic tetrad given in (Barausse *et al.*, 2009):

$$\begin{aligned}
\tilde{e}_\beta{}^T &= \sqrt{1 - \frac{2M}{r}} \delta_\beta^t = \sqrt{f(R)} \delta_\beta^t , \\
\tilde{e}_\beta{}^1 &= \frac{r}{R} \delta_\beta^X = \left(1 + \frac{M}{2R}\right)^2 \delta_\beta^X , \\
\tilde{e}_\beta{}^2 &= \frac{r}{R} \delta_\beta^Y = \left(1 + \frac{M}{2R}\right)^2 \delta_\beta^Y , \\
\tilde{e}_\beta{}^3 &= \frac{r}{R} \delta_\beta^Z = \left(1 + \frac{M}{2R}\right)^2 \delta_\beta^Z ,
\end{aligned} \tag{B.40}$$

---

<sup>56</sup>The general relation between  $r$  and  $R$  is

$$r = R + M + \frac{M^2 - a^2}{4R}$$

---

where

$$\begin{aligned}
r &= R \left( 1 + \frac{M}{2R} \right)^2 , \\
f(R) &= \frac{(2R-1)^2}{(2R+1)^2} , \\
h(R) &= \left( 1 + \frac{M}{2R} \right)^4 .
\end{aligned}$$

In order to check the behavior of these so called isotropic cartesian coordinates  $(X, Y, Z)$  we analyze the conservation of the constants of motion given by the symmetries of the system. The spherical symmetry of the spacetime can be described in Cartesian-like coordinates  $x^\mu$  by the three Killing vectors

$$\xi_K^\mu = \epsilon^{KLM} x^L \delta_M^\mu . \quad (\text{B.41})$$

Using (B.33) we thus get the three conserved components of the total angular momentum as a combination of kinematical momentum  $p_\mu$  and components of spin tensor  $S^{\mu\nu}$ . On the other hand, in the canonical description, the conservation of the total angular momentum

$$J_K = \epsilon^{KLM} x^L P_M + S_K , \quad (\text{B.42})$$

is demonstrated by vanishing Dirac brackets

$$\{J_K, H\}_{DB} = 0 . \quad (\text{B.43})$$

Contrary to the previous case the canonical momenta  $P_M$  and tetrad components of the spin appear in this formula. The relations between the two sets of quantities, the kinematical and the canonical, are given by (B.15) and (B.8). By computing the difference of projection of (B.33) and (B.42) it can be shown, that if the Lie derivatives of the three spatial tetrad vectors obey the Cartesian-like rule

$$(\mathcal{L}_{\xi_K} \tilde{e}^\mu_L) \tilde{e}_{\mu M} = -\epsilon_{KLM} \quad \wedge \quad \xi_K^0 \equiv 0 , \quad (\text{B.44})$$

the two conserved quantities, one in kinematical variables and the other in canonical ones, are identical. Indeed, this formula holds in flat Minkowski spacetime for Cartesian tetrad  $\tilde{e}_\mu^A = \delta_\mu^A$ , which naturally leads to the intuition, that a tetrad, that reduces to a cartesian one in flat spacetime, is a good tetrad choice. (In (B.44) the fact that the time component of the Killing vectors is required to vanish is explicitly stated, since it is written as a covariant, coordinate independent formula, but it was derived using this coordinate assumption.)

The general condition (B.44) can now be applied to the particular case of the Schwarzschild limit (B.39). As Lie derivatives can be written using partial rather than covariant derivatives, one can easily check, that the tetrad field (B.40) satisfies (B.44).

Yet, as an example, that the equivalence between total angular momentum expressed in kinematical and canonical variables is not so obvious, let us consider a symmetry of the Schwarzschild spacetime w.r.t. rotation along the  $z$ -axis

$$\xi_z^\mu = [0, -Y, X, 0] . \quad (\text{B.45})$$

It yields the related component of the total angular momentum

$$J_z = Xp_y - Yp_x + S^{xy} \left( h(R) + \frac{(h(R))'}{2R} (X^2 + Y^2) \right) - \frac{(h(R))'}{2R} Z (XS^{yz} + YS^{zx}) .$$

Here,  $p_i$  represents the kinematical MP momenta and  $S^{ij}$  the coordinate spin components, the prime denotes a derivative with respect to  $R$ . In the Hamiltonian approach we use the canonical momenta  $P_i$  and the projected spin components  $S^I$ , so it is necessary to perform a transformation from  $(p_i, S^{ij})$  to  $(P_I, S^I)$  using the relations given in (B.15) and (B.8). With these, terms proportional to  $h'(R)$  get absorbed into  $P_x$  and  $P_y$  and the corresponding component of the total angular momentum can be written as

$$J_z = XP_y - YP_x + S_3 . \quad (\text{B.46})$$

The corresponding Hamiltonian in these coordinates, cf. (Barausse *et al.*, 2009) reads

$$H = H_{NS} + H_S ,$$

with

$$H_{NS} = \frac{1}{\sqrt{f(R)}} \sqrt{Q} , \quad (\text{B.47})$$

$$H_S = \frac{1 - \frac{M}{2R} + 2 \left(1 - \frac{M}{4R}\right) \sqrt{Q}}{\left(1 + \frac{M}{2R}\right)^6 R^3 \sqrt{Q} (1 + \sqrt{Q})} \frac{M}{m} \left( \vec{L} \cdot \vec{S} \right) , \quad (\text{B.48})$$

and  $Q = m^2 + \frac{1}{h(R)} \vec{P}^2$ . Notice, that setting  $M \rightarrow 0$ , i.e., no gravitational field, we indeed obtain that the spin part of the Hamiltonian  $H_S$  becomes zero, as it should in Minkowskian spacetime.

Next, we can easily compute the evolution equations for the  $J_x$ ,  $J_y$  and  $J_z$  as

$$\begin{aligned} \{J_x, H\}_{DB} &= 0 , \\ \{J_y, H\}_{DB} &= 0 , \\ \{J_z, H\}_{DB} &= 0 , \end{aligned}$$

which is thus also true for the measure of the total angular momentum  $J^2$ . Moreover, it holds that  $\{L^2, H\} = 0$  where  $L^2 = L_x^2 + L_y^2 + L_z^2$  is the measure of the orbital angular momentum. Its respective components are defined as  $L_i = \varepsilon_{ijk} q^j P^k$ , with  $q^i = (X, Y, Z)$  and  $P^i = (P_x, P_y, P_z)$ .

In fact, since the Hamiltonian system of a spinning particle linearized in spin given by (B.47), (B.48) has five degrees of freedom, the five independent and in involution constants of motion  $(J_z, J^2, L^2, S^2, H)$  of the Schwarzschild limit make the system integrable. The integrability for the Schwarzschild background seems to result from the linearized in spin Hamiltonian approximation, because in Suzuki and Maeda (1997) it has been shown that for the full MP equations with T SSC chaos appears for a spinning particle in the Schwarzschild background. However, the integrability seems to vanish in the Hamiltonian approximation once we turn on

the spin of the central body. Namely, in the case of a Kerr spacetime background chaos appears again (scattered dots in Fig. B.3), which suggests the nonintegrability of the corresponding Hamiltonian system. The appearance of chaos in the Kerr background case for the Hamiltonian approximation is not just a confirmation of previous studies concerning the full MP equations with T SSC, see, e.g., (Hartl, 2003a,b). It shows that the linearized in spin Hamiltonian function given in (Barausse and Buonanno, 2010) is non-integrable. This result contradicts with statements in the literature saying that up to the linear order in spin, the motion of a spinning particle corresponds to an integrable system, see, e.g., (Hinderer *et al.*, 2013). A thorough investigation of chaos in the Kerr spacetime for the linearized in spin Hamiltonian function will be provided in a further work.

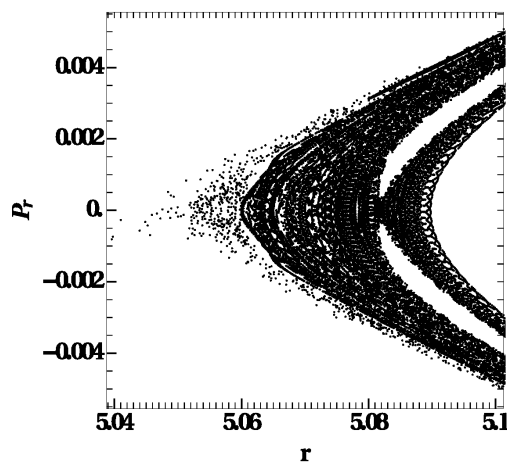


Figure B.3: A detail from the surface of section  $\theta = \pi/2$ ,  $P_\theta > 0$ . The parameters of the orbits are  $H = 0.9449111825230683$ ,  $J_z = 3.5$ ,  $S = M = m = 1$ ,  $a = 0.1$ , the common initial conditions are  $\phi = 0$ ,  $P_r = 0$ ,  $S_1 = 0$ , while by solving numerically the system  $P_\theta = -S_2$ ,  $J_z = P_\phi + S_3$ , and  $S = \sqrt{S_2^2 + S_3^2}$  we define the rest.

The above results match exactly the expectations we had from the symmetries.

We have investigated the properties of a ZAMO tetrad in spherical and cartesian coordinates in Schwarzschild spacetime. Taking the conservation of the constants of motion for numerical calculations as an important criterion to be satisfied, promising indicators for a “good” tetrad choice are the reduction to Cartesian tetrad in flat spacetime as well as the vanishing of the spin dependent Hamiltonian. Two questions arise with this statement: First, are there other coordinates we may choose providing us with “good” tetrads, and second, since we were focusing on a ZAMO tetrad, we ask whether a non-ZAMO tetrad yields the same properties if the coordinate basis is not changed. We expect the properties of the tetrad to depend on the choice of the coordinates, so that in the following we take Kerr-Schild coordinates and analyze two tetrads, one ZAMO and one non-ZAMO tetrad.

## B.4. The Hamiltonian function in Kerr-Schild coordinates

The Kerr-Schild coordinates have the great advantage that they are horizon penetrating so that they are well behaved in the vicinity of the horizon, which simplifies numerical calculations in

this domain, probably improving the numerical treatment compared to isotropic coordinates for events in the strong field. Here we shall introduce a Hamiltonian function using the Kerr-Schild (KS) coordinates. The line element in KS coordinates reads (Gualtierie and Ferrari, 2011)

$$ds^2 = g_{\mu\nu} d\bar{x}^\mu d\bar{x}^\nu , \quad (\text{B.49})$$

$$g_{\mu\nu} = \eta_{\mu\nu} + f l_\mu l_\nu , \quad (\text{B.50})$$

where  $(0, 1, 2, 3)$  correspond to  $(\bar{t}, \bar{x}, \bar{y}, \bar{z})$ ,

$$\begin{aligned} l_{\bar{t}} &= -1 , \\ l_{\bar{x}} &= -\frac{\bar{r} \bar{x} + a \bar{y}}{\bar{r}^2 + a^2} , \\ l_{\bar{y}} &= -\frac{\bar{r} \bar{y} - a \bar{x}}{\bar{r}^2 + a^2} , \\ l_{\bar{z}} &= -\frac{\bar{z}}{\bar{r}} , \end{aligned} \quad (\text{B.51})$$

$$(\text{B.52})$$

and

$$f = \frac{2 M \bar{r}^3}{\bar{r}^4 + a^2 \bar{z}^2} , \quad (\text{B.53})$$

$$\begin{aligned} \bar{r} &= \sqrt{\frac{\bar{\rho}^2 + \sqrt{\bar{\rho}^4 + 4a^2 \bar{z}^2}}{2}} , \\ \bar{\rho}^2 &= \bar{x}^2 + \bar{y}^2 + \bar{z}^2 - a^2 . \end{aligned} \quad (\text{B.54})$$

For simplicity in the rest of the section we drop the bar notation over the KS coordinates.

Independently on the tetrad field the choice of coordinates implies the non-spinning part of the Hamiltonian

$$H_{NS} = \alpha^2 f l_i P_i + \alpha \sqrt{m^2 + P_i P_i - f \alpha^2 (l_i P_i)^2} , \quad (\text{B.55})$$

where  $l_i P_i = \delta^{ij} l_i P_j$  and

$$\alpha = \frac{1}{\sqrt{1+f}} . \quad (\text{B.56})$$

In the following we present two tetrad choices corresponding to different types of observers.

#### B.4.1. ZAMO Tetrad

In the previous section, we focused on a tetrad field associated to the observers with vanishing momenta  $P_i = 0$ , i.e., zero angular momentum observers (ZAMO), in two different coordinate systems, isotropic cartesian and Boyer-Lindquist coordinates. Therefore, it is reasonable to first

consider such an observer in KS coordinates as well. Here, we choose a tetrad corresponding to an observer infalling with the radial velocity  $U^r = -\alpha f$ :

$$\begin{aligned}\tilde{e}_\beta^T &= \alpha \delta_t^0 , \\ \tilde{e}_\beta^I &= \delta_\beta^I + (\alpha^{-1} - 1 - \alpha f) l_I \delta_\beta^0 + (\alpha^{-1} - 1) l_I l_\beta .\end{aligned}$$

Again, this tetrad becomes cartesian, i.e.,  $\tilde{e}_\beta^T = \delta_\beta^T$ ,  $\tilde{e}_\beta^I = \delta_\beta^I$ , in the flat spacetime limit, which is a first indicator for being a good tetrad choice. The next step is to analyze the behavior in the Schwarzschild limit  $a \rightarrow 0$ . Then, following the procedure introduced in (Barausse *et al.*, 2009), we obtain the Hamiltonian  $\bar{H}^{\text{Schw}} = \bar{H}_{NS}^{\text{Schw}} + \bar{H}_S^{\text{Schw}}$  with

$$\bar{H}_{NS}^{\text{Schw}} = \alpha \left( \bar{m} - \frac{2M\alpha}{r^2} \vec{r} \cdot \vec{P} \right) , \quad (\text{B.57})$$

$$\bar{H}_S^{\text{Schw}} = \frac{M}{\bar{m}} \left[ \frac{2\alpha^2}{\alpha + 1} - \frac{\alpha^5 + 3\alpha^3}{r} \frac{\vec{r} \cdot \vec{P}}{\omega_T} - \alpha^4 \frac{\bar{m}}{\omega_T} \right] \frac{\vec{L} \cdot \vec{S}}{r^3} , \quad (\text{B.58})$$

where

$$\begin{aligned}\bar{m} &= \sqrt{m^2 + \vec{P}^2 - \frac{f\alpha^2}{r^2} (\vec{r} \cdot \vec{P})^2} , \\ \omega_T &= -m - \bar{m} .\end{aligned} \quad (\text{B.59})$$

Since the total Hamiltonian is merely a function of certain scalar combinations of  $(\vec{r}, \vec{P}, \vec{S})$  (where  $\vec{r} = (x, y, z)$ ), namely  $\bar{H} = \bar{H}(|\vec{r}|^2, |\vec{P}|^2, \vec{r} \cdot \vec{P}, \vec{L} \cdot \vec{S})$  with  $L_i = \varepsilon_{ijk} r^j P^k$ , we can deduce that

$$\left\{ \vec{L} + \vec{S}, H \right\}_{DB} = 0 , \quad (\text{B.60})$$

by using the canonical structure of the variables. Moreover, we would like to stress here again, that the conservation of  $L^2$  in Schwarzschild spacetime is equivalent to the conservation of  $\vec{L} \cdot \vec{S}$  so that it suffices to express the Hamiltonian in terms of  $\vec{L} \cdot \vec{S}$  in order to show (B.60). In fact, it reflects the integrability of the system at linear order in spin.

However, we cannot simply infer that  $\vec{J} = \vec{L} + \vec{S}$  is valid in the new canonical coordinates. The conserved total angular momentum is already given by (B.33) and by the Killing vectors (B.41) of the Schwarzschild spacetime we get

$$J_i = \tilde{L}_i + S_i , \quad (\text{B.61})$$

where the tilde denotes the quantities to be written in terms of the kinematical momenta  $p_i$  ( $L_i = \varepsilon_{ijk} r^j p^k$ ) and the index  $i$  in  $S_i$  refers to the coordinate basis. This relation is valid in KS coordinates, independent of the tetrad choice.

In order to relate the conserved quantities to the canonical momenta  $P_i$  and the tetrad components of the spin  $S_I$ , we have to perform a transformation from  $(p_i, S_i)$  to  $(P_i, S_I)$  using the relations given in (B.15) and (B.8). Therewith, we indeed find the components  $J_i$  to be given by (B.46), which yields vanishing Dirac brackets for each component of the total angular

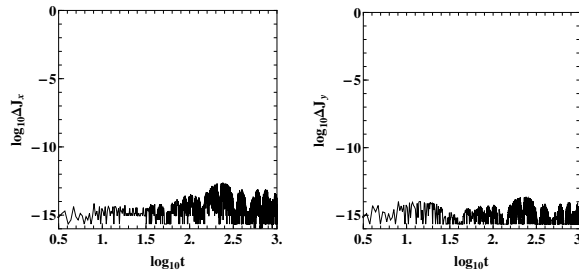


Figure B.4: The left panel shows the relative error of  $J_x$ , and the right of  $J_y$  as a function of time in logarithmic scale for the ZAMO tetrad in KS coordinates as evolved by the Hamiltonian with  $a = 0$ ,  $M = m = 1$ , and  $S = 1$ .

momentum according to the argument mentioned in Section B.3.2. In order to support this statement we performed a numerical check shown in Fig. B.4.

It is immediately obvious that the conservation of these components is ensured up to numerical errors which do not accumulate over the integration time but stay at the same level. These results are similar to the ones obtained in isotropic Cartesian coordinates, so that the quality of the outputs is comparable. Therefore, if one can choose between KS and isotropic Cartesian coordinates, there is no preferred choice between those two in Schwarzschild spacetime. However, if the dynamics of plunging orbits is considered in a Kerr spacetime background, it may be more sensible to change to KS coordinates since they are horizon penetrating and avoid numerical divergence close to the horizon (see Appendix B.7).

Secondly, we consider the contribution from the spin part of the Hamiltonian in flat spacetime. From (B.58) we see that for  $M \rightarrow 0$  the contributions from  $H_S$  vanish as it should. Hence, also additional coordinate effects which arise in spherical coordinates are avoided, further supporting such a choice of tetrad and coordinates.

#### B.4.2. Non-ZAMO tetrad

To simplify the Hamiltonian in Kerr-Schild coordinates we change to another tetrad field, which is not required to be a ZAMO observer. In particular, we take advantage of the fact that for certain observers no square roots appear due to normalization of the tetrad vectors

$$\tilde{e}_\mu{}^T = \left[ 1 - \frac{f}{2}, \frac{f}{2}l_x, \frac{f}{2}l_y, \frac{f}{2}l_z \right], \quad (\text{B.62})$$

$$\tilde{e}_\mu{}^X = \left[ -\frac{f}{2}l_x, 1 + \frac{f}{2}l_xl_x, \frac{f}{2}l_xl_y, \frac{f}{2}l_xl_z \right], \quad (\text{B.63})$$

$$\tilde{e}_\mu{}^Y = \left[ -\frac{f}{2}l_y, \frac{f}{2}l_yl_x, 1 + \frac{f}{2}l_yl_y, \frac{f}{2}l_yl_z \right], \quad (\text{B.64})$$

$$\tilde{e}_\mu{}^Z = \left[ -\frac{f}{2}l_z, \frac{f}{2}l_zl_x, \frac{f}{2}l_zl_y, 1 + \frac{f}{2}l_zl_z \right], \quad (\text{B.65})$$

where we use the definitions from above, cf. Eqs. (B.51)-(B.53). This is the tetrad of an infalling ‘non-ZAMO’ observer, as the observer’s specific angular momentum

$$\tilde{e}_{\phi T} = \left( \frac{\partial}{\partial \phi} \right)^\mu \tilde{e}_{\mu T} = -\frac{1}{2} \frac{fa}{r} \frac{x^2 + y^2}{r^2 + a^2} \neq 0 \quad , \quad (\text{B.66})$$

and the observer’s radial coordinate velocity

$$\tilde{e}^r{}_T = \left( \frac{\partial r}{\partial x^\mu} \right) \tilde{e}^\mu{}_T = -\frac{f}{2} < 0 \quad .$$

Thus, we again compute the Hamiltonian in canonical coordinates up to linear order in spin given by Barausse *et al.* (2009)

$$H = H_{NS} + H_{SO} + H_{SS} \quad , \quad (\text{B.67})$$

where  $H_{NS}$  is given by (B.55),

$$H_{SO} = \alpha f \frac{Mm - 2\tilde{m}(M - fr)}{2M \bar{m} \omega_T} \frac{r \epsilon^{ijk} l_i p_j S^k}{r^2 + a^2 l_z^2} \quad , \quad (\text{B.68})$$

and

$$H_{SS} = -\frac{af}{4\omega_T M \bar{m} (a^2 l_z^2 + r^2)} \times \left\{ \begin{aligned} & \left[ 4fl_z \tilde{m} ((\bar{m} - \alpha f \tilde{m})r + \alpha \tilde{m} M) - 2M l_z (\bar{m} m + \alpha m^2) \right. \\ & \quad \left. + 2\alpha [(M + 2r)mfl_z + (3M - 2fr)P_z] \tilde{m} \right] S^i l_i \\ & \quad + 2\alpha (m + \tilde{m}) [Ml_z S^i P_i - \tilde{m} (2fr - 3M) S^3] \\ & \quad - 2 \frac{al_z \tilde{m}}{r^2} (3Mr - a^2 fl_z^2 - 3fr^2) \left[ \alpha (S^1 P_y - S^2 P_x) \right. \\ & \quad \left. - (\alpha m + \bar{m} - \alpha f \tilde{m}) (S^1 l_y - S^2 l_x) \right] \end{aligned} \right\} \quad . \quad (\text{B.69})$$

Here, instead of (B.59), we used

$$\begin{aligned} \bar{m} &= \sqrt{m^2 + P_i P_i - f \alpha^2 (l_i P_i)^2} \quad , \\ \tilde{m} &= \alpha \bar{m} - \alpha^2 P_i l^i \quad , \\ \omega_T &= -m - \frac{\bar{m}}{\alpha} + \frac{f}{2} \tilde{m} \quad , \end{aligned} \quad (\text{B.70})$$

which together with the usage of components of  $l^\mu$  instead of coordinates significantly shortened expressions for  $H_{SO}$  and  $H_{SS}$ . All vector components are grouped in such a way that the relation  $\{L_z + S_z, H\}_{DB} = 0$  is obvious.

Again, the complete angular momentum conservation is restored in the Schwarzschild limit. Since  $\bar{H}_{NS}$  only depends on the chosen coordinate basis, it is still given by (B.57). The spinning part

$$\bar{H}_S = \left[ \alpha \frac{M}{\bar{m}} \left( 1 - \frac{M + 2r}{r(r + 2M)} \frac{\vec{r} \cdot \vec{P}}{\omega_T} \right) - \frac{M}{\omega_T} \frac{1 - \frac{M}{r}}{1 + \frac{2M}{r}} \right] \frac{\vec{L} \cdot \vec{S}}{r^3} \quad , \quad (\text{B.71})$$

where  $\bar{m}$  and  $\omega_T$  are given by (B.70), can again be written as a function  $\bar{H} = \bar{H}(|\vec{r}|^2, |\vec{P}|^2, \vec{r} \cdot \vec{P}, \vec{L} \cdot \vec{S})$  so that we can follow the reasoning of the preceding subsection to obtain vanishing Dirac brackets (B.60). Therefore, we only have to check the equations for the components of the total angular momentum  $J_i$  in canonical coordinates  $(P_i, S_I)$ . Using the expressions for the total angular momentum with respect to the coordinate basis (B.61), we again perform a transformation to the tetrad basis and the canonical momenta and recover relation (B.46). Thus, in the Schwarzschild limit, the non-ZAMO tetrad in KS coordinates has the same numerical properties as the ZAMO tetrad, as expected, which is also visible in Fig. B.5.

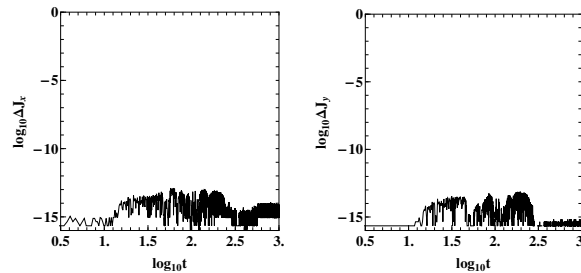


Figure B.5: The left panel shows the relative error of  $J_x$ , and the right of  $J_y$  as a function of time in logarithmic scale for the non-ZAMO tetrad in KS coordinates as evolved by the Hamiltonian with  $a = 0$ ,  $M = m = 1$ , and  $S = 1$ .

Consequently, it seems to be a good choice of coordinate system for numerical investigations.

It is of course also possible to rewrite the coefficients of the tetrad basis vectors in terms of any coordinate system without changing the general properties of the Hamiltonian system as long as the tetrad basis vectors remain oriented along the isotropic coordinate (cartesian like) basis vectors. In (Barausse *et al.*, 2009), it was already mentioned that the coordinate effects can be avoided by choosing the directions of the tetrad basis vectors along a cartesian coordinate system. However, if the tetrad corresponds to a cartesian frame, the spin variables remain cartesian whereas the position and momentum variables are spherical ones. This approach is used in effective-one-body theory or post-Newtonian methods in order to compare the dynamical contributions from different orders in spin, see e.g., (Porto, 2006; Barausse *et al.*, 2009), and may in fact also be used for the computation of the equations of motion from the Hamiltonian. Nevertheless, in that case it is more sensible to be consistent in the choice of coordinates and spin variables so that the Dirac brackets can be used for the calculation of the equations of motion. This coordinate system does not necessarily adapt to the symmetries of the spacetime as we have seen. Generally, it is very useful to choose a coordinate system and corresponding basis vectors that do not imply coordinate effects if one aims at the analysis of the equations of motion.

## B.5. Conclusions

In this work we have studied the Hamiltonian formalism of a spinning particle provided by Barausse *et al.* (2009) with regard to numerical investigations of the equations of motion. It was already discussed in (Barausse *et al.*, 2009) that this Hamiltonian formalism does not only depend on the tetrad field one uses, but also on the coordinate system one chooses in order to

---

express the tetrad field or the Hamiltonian function. Using the Dirac brackets to check the integrals of motion, we have shown that an unfortunate choice of the coordinate system can lead to a nonpreservation of quantities in numerical integration which should, according to the symmetries of the system and the linearized MP equations, be conserved. However, we find that the type of the tetrads, i.e., whether the observer is ZAMO or follows some other worldline which does not correspond to a ZAMO does not affect the general dynamical properties of the constants of motion. In fact, we have examined both kinds of tetrads and found no difference in their ability to be numerically applied, i.e., they possess the same properties with respect to numerical computations. However, the formulae for the spinning part of the Hamiltonian can be simplified and compactified, which we think is worth to be mentioned.

In order to obtain Hamiltonian systems without coordinate effects smearing the actual physical behavior in numerical solutions and still reliable in the vicinity of the central object's horizon, two new horizon penetrating Hamiltonian functions were introduced. Both of them were constructed on tetrad fields which were expressed in Kerr-Schild coordinates. In particular, the non-ZAMO tetrad allows us to express the Hamiltonian both in Schwarzschild and Kerr spacetime in a simple and compact form. Future (numerical) work may profit from this explicit Hamiltonian.

While studying the Dirac brackets in the Schwarzschild limit, we have shown that in this limit the Hamiltonian functions with acceptable properties are integrable. In particular, we have shown that the system's five degrees of freedom admit five independent and in involution integrals of motion. On the other hand, we have shown by a numerical example that chaos appears when we go to the Kerr background in the case of the Hamiltonian function proposed in (Barausse and Buonanno, 2010). This suggests that this linearized Hamiltonian function corresponds to a nonintegrable system in the case of the Kerr background. Indeed, the Hamiltonian formulation offers a wide range of applications in the context of chaos and perturbation theory, such as Poincaré sections or recurrence plots. In order to answer the question for chaos thoroughly, a detailed analysis of the motion of spinning particles in the Kerr spacetime described by the linearized in spin Hamiltonian approximation is in progress.

## Acknowledgements

G.L-G and J.S. were supported by the DFG grant SFB/Transregio 7. G.L-G is supported by UNCE-204020. T.L. and G.L-G were supported by GACR-14-10625S. D.K. gratefully acknowledges the support from the Deutsche Forschungsgemeinschaft within the Research Training Group 1620 “Models of Gravity” and from the “Centre for Quantum Engineering and Space-Time Research (QUEST)”.

## B.6. Numerical integration of the Hamiltonian equations

Our numerical integrators rely on the considerations of our previous work, cf. (Lukes-Gerakopoulos *et al.*, 2014, Secs. A and B), which can be extended to all Hamiltonians in this work. Let us briefly summarize the main points.

All Hamiltonian equations of this work possess a so-called *Poisson structure*, i.e., for  $\mathbf{y} =$

$(P_1, P_2, P_3, x^1, x^2, x^3, S_1, S_2, S_3)^T \in \mathbb{R}^9$ , they can be written as

$$\dot{\mathbf{y}} = B(\mathbf{y})\nabla H(\mathbf{y}) \quad , \quad (\text{B.72})$$

where  $B : \mathbb{R}^9 \rightarrow \mathbb{R}^{9 \times 9}$  is the skew-symmetric matrix-valued function

$$B(\mathbf{y}) = \begin{pmatrix} 0 & -I_{3 \times 3} & 0 \\ I_{3 \times 3} & 0 & 0 \\ 0 & 0 & B_1(\mathbf{y}) \end{pmatrix} \quad , \quad (\text{B.73})$$

with

$$I_{3 \times 3} = \begin{pmatrix} 1 & 0 & 0 \\ 0 & 1 & 0 \\ 0 & 0 & 1 \end{pmatrix} \quad , \quad (\text{B.74})$$

$$B_1(\mathbf{y}) = \begin{pmatrix} 0 & -S_3 & S_2 \\ S_3 & 0 & -S_1 \\ -S_2 & S_1 & 0 \end{pmatrix} \quad . \quad (\text{B.75})$$

Due to this special structure, the spin length  $S = \sqrt{S_1^2 + S_2^2 + S_3^2}$  is conserved along solutions of the equations of motion (B.72). Thus, the three dimensional spin  $\mathbf{S} = (S_1, S_2, S_3)^T$  can be represented by two variables  $\alpha$  and  $\xi$  via

$$\mathbf{S} = S \begin{pmatrix} \sqrt{1 - \xi^2} \cos(\alpha) \\ \sqrt{1 - \xi^2} \sin(\alpha) \\ \xi \end{pmatrix} \quad , \quad (\text{B.76})$$

see, e.g., (Wu and Xie, 2010; Seyrich, 2013). One can then show, cf. (Seyrich, 2013), that

$$\dot{\xi} = -\frac{\partial H}{\partial \alpha} \quad , \quad (\text{B.77})$$

$$\dot{\alpha} = \frac{\partial H}{\partial \xi} \quad , \quad (\text{B.78})$$

holds. Hence, in the transformed variables  $\mathbf{z} = (P_1, P_2, P_3, \xi, x^1, x^2, x^3, \alpha)$ , the equations of motion take the the symplectic form

$$\dot{\mathbf{z}} = J^{-1}\nabla H(\mathbf{z}) \quad , \quad (\text{B.79})$$

$$J = \begin{pmatrix} 0 & I_{4 \times 4} \\ -I_{4 \times 4} & 0 \end{pmatrix} \quad . \quad (\text{B.80})$$

As a nice consequence, we can evolve the system with *Gauss Runge–Kutta schemes* which have already been shown to yield very good results for little computational costs in previous studies, see, e.g., (Seyrich, 2013; Seyrich and Lukes-Gerakopoulos, 2012).

An  $s$ -stage Gauss Runge-Kutta scheme is a collocation method, i.e., an implicit Runge-Kutta scheme

$$\mathbf{y}_{n+1} = \mathbf{y}_n + h \sum_{i=1}^s b_i f(\mathbf{Y}_i) \quad , \quad (\text{B.81})$$

$$\mathbf{Y}_i = \mathbf{y}_n + h \sum_{j=1}^s a_{ij} f(\mathbf{Y}_j) \quad , \quad i = 1, \dots, s \quad , \quad (\text{B.82})$$

---

with coefficients

$$a_{ij} = \int_0^{c_i} l_j(t) dt \quad , \quad (\text{B.83})$$

$$b_j = \int_0^1 l_i(t) dt \quad , \quad (\text{B.84})$$

where the stages  $c_1, \dots, c_s$  are chosen as

$$c_i = \frac{1}{2}(1 + \tilde{c}_i) \quad , \quad (\text{B.85})$$

with  $\tilde{c}_i$  being the roots of the Legendre-polynomial of degree  $s$ . Here,  $h$  denotes the time step size,  $Y_i$ ,  $i = 1, \dots, s$ , are the so-called inner stage values and  $\mathbf{y}_n$  denotes the numerical approximation to the solution  $\mathbf{y}$  at time  $\tau = nh$ . The functions  $l_i(t)$  are the Lagrange-polynomials of degree  $s$ ,

$$l_i(t) = \prod_{j \neq i} \frac{t - c_j}{c_i - c_j} \quad . \quad (\text{B.86})$$

Gauss Runge-Kutta methods have a convergence order  $\mathcal{O}(h^{2s})$  which is the highest possible order among collocation schemes, e.g., (Hairer *et al.*, 1993). Detailed information on their implementation is given in (Seyrich, 2013, Sec. 7), and (Hairer *et al.*, 2006, Chapters VIII.5 and VIII.6).

Very importantly, Gauss Runge-Kutta schemes almost exactly preserve the Hamiltonian throughout the numerical evolution, cf. (Lukes-Gerakopoulos *et al.*, 2014, Fig. 10). Furthermore, it is known from numerical analysis that the solution  $\mathbf{y}_{n+1}$  coincides with the value at  $t = h$  of the interpolation polynomial  $\mathbf{U}(t)$  through the points  $(0, \mathbf{y}_n)$  and  $(c_1, \mathbf{Y}_1) \dots (c_s, \mathbf{Y}_s)$ . This interpolation polynomial can be shown to stay  $\mathcal{O}(h^s)$  close to the exact solution of the equations of motion, see, e.g., (Hairer *et al.*, 2006, Chapter II.1). Therefore, we can conveniently calculate  $\mathcal{O}(h^s)$  approximations to surface sections, such as the one presented in Fig. B.3 above (for the procedure details see, e.g., (Seyrich, 2013)).

## B.7. Plunging orbits

The analytical properties of equations of motion have also impact on the behavior of their numerical solution. In Fig. B.6 we plot the relative error of the Hamiltonian  $\Delta H = |1 - H(t)/H(0)|$  for plunging orbits using the Gauss Runge-Kutta method (Appendix B.6) with fixed time-step for equations of motion given by the Hamiltonian function discussed in Sec. B.3.2 (BL) (top plot) and the one discussed in section B.4.2 (KS) (bottom plot) as functions of the BL radius. The figure clearly shows that KS case covers smoothly the horizon of the Kerr black hole (vertical dashed gray line), while the BL fails to do so by definition.

The mass parameters are  $M = m = 1$  and the Kerr parameter is  $a = 0.9$ . As initial conditions for the BL orbit we use  $r = 25$ ,  $\theta = \pi/2$ ,  $\phi = 0$ , and  $\frac{dr}{dt} = \frac{d\phi}{dt} = \frac{d\theta}{dt} = 0$ . The first two conditions for the velocities determine the initial values of  $S_3$ , and  $P_r$ . The remaining initial conditions are  $P_\phi = S_x = S_y = P_\theta = 0$ . The timestep is  $\Delta t_{BL} = 0.1$ . The initial conditions for the KS

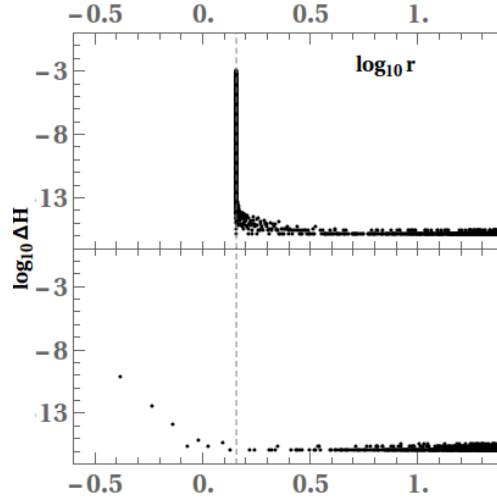


Figure B.6: The relative error of the Hamiltonian  $\Delta H$  as function of the BL radius  $r$  for two plunging orbits. The top plot shows the  $\Delta H$  of a plunging orbit evolved by the Hamiltonian function discussed in section B.3.2 (BL), while the bottom plot shows the  $\Delta H$  of a plunging orbit evolved by the Hamiltonian function discussed in section B.4.2 (KS). In both cases we used masses  $M = m = 1$  and Kerr parameter  $a = 0.9$ . For more about the initial conditions refer to the text. The horizon is depicted in both plots by a vertical dashed gray line.

orbit are  $x = 25, y = z = 0$ , and  $P_x = P_y = P_z = 0$  with spin  $S_x = S_y = 0, S_z = 0.9$ . The timestep is  $\Delta t_{KS} = 0.1$ .

In fact, to test how much the pole-dipole approximation of rotating body fails near the horizon has to be investigated by other studies. But, one can assume that not having equations of motion singular at the horizon helps to obtain the right numerical results within the range of spins allowed by the linear-in-spin approximation.

---

## C. Comparing the full time-dependent Bogoliubov–de-Gennes equations to their linear approximation: A numerical investigation

The content of this Section was published as [C. Hainzl, and J. Seyrich *Eur. Phys. J. B* **89** (5), 1-10 (2016)]. under lead-authorship of J. S. . The work is based on theoretical input by Christian Hainzl.

### Abstract

In this paper we report on the results of a numerical study of the nonlinear time-dependent Bardeen–Cooper–Schrieffer (BCS) equations, often also denoted as Bogoliubov–de-Gennes (BdG) equations, for a one-dimensional system of fermions with contact interaction. We show that, even above the critical temperature, the full equations and their linear approximation give rise to completely different evolutions. In contrast to its linearization, the full nonlinear equation does not show any diffusive behavior in the order parameter. This means that the order parameter does not follow a Ginzburg–Landau-type of equation, in accordance with a recent theoretical result in Frank *et al.* (2015). We include a full description on the numerical implementation of the partial differential BCS/BdG equations.

### C.1. Introduction

When Bardeen *et al.* (1957), shortly BCS, published one of the most famous papers in physics in 1957, giving the first microscopic explanation for superconductivity, a phenomenological theory for the phenomenon had already been around. Systems close to the critical temperature were described with the help of a macroscopic phase-transition parameter introduced by Landau and Ginzburg (1950). Their theory was the first one to allow for the description of the spatial dependence of the superconductivity inside superconducting alloys and the first with which to explain type-II superconductors and the hexagonally shaped penetrations by magnetic flux.

As the Ginzburg–Landau theory yields reliable results on the large scale, soon the question arose as to whether this model can be understood as a macroscopic limit of BCS theory for systems close to the critical temperature. Gorkov (1959) gave a positive answer to this question for the stationary case shortly after the publication of BCS. A rigorous mathematical proof of the convergence was achieved some years ago by Frank *et al.* (2012).

But what remains unclear and controversial up to this day, in particular in terms of a rigorous derivation, is the question whether the time evolution of superconducting systems close to the critical temperature are governed by a Ginzburg–Landau type of equation. After first attempts for a derivation of the macroscopic limit had been presented by Stephen and Suhl (1964); Schmid (1966); Abrahams and Tsuneto (1966), Gorkov and Eliashberg (1968) pointed out that a nonlinear equation could only be valid in a gapless regime. Still, in (Cyrot, 1973; De Melo

---

*et al.*, 1993; Randeria, 1995) the authors made a case for a time-dependent Ginzburg–Landau equation for superfluid gases at temperatures slightly above the critical one. The argument is based on the assumption that the nonlinear terms in the BCS/BdG equations only lead to small perturbations but do not quantitatively change the system’s behavior. In more detail, this would mean that the projection of the Cooper pair density onto the center of mass direction is governed by a nonlinear dispersive equation. However, it has been argued recently in (Frank *et al.*, 2015) that for a translation invariant homogeneous system close to equilibrium, the full BCS/BdG equations and their linearization do not yield the same behavior at temperatures close to the critical one. In particular, dissipative behavior can only be expected for the linear approximation of the BCS equations but not for the full equations.

With our work, we demonstrate this result by means of a thorough numerical study of the long-term evolution of the BCS equations and their linearization for spatially homogeneous systems close to equilibrium at temperatures slightly above the critical one. For decreasing values of the parameter  $h$ , defined via  $T = (1 + h^2)T_c$ , we evolve the full and the linear system over a long time span and track the behavior of the Cooper pair density and the order parameter. For each values of the small parameter  $h$ , we find clear differences between the full equation and its linearization. Additionally, we see that the full BCS /BdG equations yield oscillations in the order parameter about a constant value. Such a behavior has long been predicted for and already been observed in out-of-equilibrium systems, see, e.g., (Volkov and Kogan, 1974; Barankov *et al.*, 2004; Yuzbashyan *et al.*, 2006). Although the focus of our study is not on oscillations in particular but rather on the long-term behavior of the equations in general, it is interesting that we can replicate such oscillations for systems close to equilibrium.

In the realm of numerical analysis, the treatment of quantum dynamical systems has been of huge interest for many decades see (Lubich, 2008) for an extensive overview. Various evolution schemes for the linear Schrödinger equation in varying settings have been proposed, see, e.g., (Feit *et al.*, 1982; Gray and Manolopoulos, 1996; Blanes *et al.*, 2006; Tal-Ezer and Kosloff, 1984; Park and Light, 1986). Nonlinear Schrödinger equations such as the Gross–Pitaevskii equation and equations arising from the Hartree and Hartree–Fock approximation of the quantum state have also been devoted attention to, see, e.g., (Bao *et al.*, 2003; Caliari *et al.*, 2009; Tang *et al.*, 1996; Gauckler and Lubich, 2010) and (Lubich, 2004, 2005). Regarding the BCS regime, the stationary equations have been treated numerically by Lewin and Paul (2014) and the time-dependent BCS/BdG equations have been considered from an analytical perspective by Hainzl *et al.* (2010). But, the above-mentioned studies of the out-of-equilibrium dynamics of the BCS equations (Volkov and Kogan, 1974; Barankov *et al.*, 2004; Yuzbashyan *et al.*, 2006) notwithstanding, to the best of our knowledge the coupled nonlinear time-dependent BCS equations have not been paid much attention to from a numerical point of view. Therefore, we come up with a reliable integration algorithm for the evolution of the system.

The paper is organized as follows: First, we introduce the system we are considering and the physical background in Section C.2. This is followed by a brief summary of the theoretical results of Frank *et al.* (2015) in Section C.3. Then, we present our numerical results for the linear and the full equation in Section C.4. Finally, we summarize our main results in Section C.5. A detailed discussion of the initial setup of the system and the numerical implementation is provided in the Appendix Sections C.6 and C.7, respectively.

## C.2. Physical and mathematical background

### C.2.1. Energy functional and BCS equations

In mathematical terms, BCS theory is a special case of a generalized Hartree–Fock variational principle, itself described by Bogoliubov–theory, for the density operators  $\gamma : \mathcal{H} \mapsto \mathcal{H}$  and  $\alpha : \mathcal{H} \mapsto \mathcal{H}$  acting on the considered Hilbert space  $\mathcal{H}$ . Those matrices are put together to form the two-by-two operator-valued matrix

$$\Gamma := \begin{pmatrix} \gamma & \alpha \\ \bar{\alpha} & 1 - \gamma \end{pmatrix}, \quad (\text{C.1})$$

see, e.g., (Bach *et al.*, 1994) for an introduction. The entries of the matrix can be represented by means of their momentum distribution  $\hat{\gamma}(k) = \langle a_k^\dagger a_k \rangle$  and the pair density  $\hat{\alpha}(k) = \langle a_k a_{-k} \rangle$ , determining the Cooper pair wave-function via Fourier transform as  $\alpha(x - y) = (2\pi)^{-3/2} \int \hat{\alpha}(k) e^{ik \cdot (x-y)} d^3k$ . We suppress spin in our notation; the pair density  $\hat{\alpha}$  is assumed, for simplicity, to be a spin singlet. For a one-dimensional translation invariant system of fermions at temperature  $T$  interacting via a potential  $V$ , the BCS pressure functional per unit volume is given by

$$\mathcal{F}_T(\Gamma) = \int_{\mathbb{R}} (p^2 - \mu) \hat{\gamma}(p) dp + \int_{\mathbb{R}} |\alpha(x)|^2 V(x) dx - TS(\Gamma), \quad (\text{C.2})$$

where the entropy  $S$  is defined as

$$S(\Gamma) := - \int_{\mathbb{R}} \text{Tr}_{\mathbb{C}^2} (\Gamma(p) \log \Gamma(p)) dp. \quad (\text{C.3})$$

The evolutions of  $\alpha$  and  $\gamma$  are given by the time-dependent BCS equations which are also known as Bogoliubov–de–Gennes equations (De Gennes, 1966). In momentum space they can be written conveniently in the self-consistent form

$$i\dot{\Gamma}_t(p) = [H_{\Gamma_t}(p), \Gamma_t(p)]. \quad (\text{C.4})$$

Here, the subscript  $t$  indicates the time-dependence and the Hamiltonian  $H_{\Gamma_t}(p)$  is defined as

$$H_{\Gamma_t}(p) = \begin{pmatrix} p^2 - \mu & 2[\hat{V} * \hat{\alpha}_t](p) \\ 2[\hat{V} * \bar{\hat{\alpha}}_t](p) & \mu - p^2 \end{pmatrix}, \quad (\text{C.5})$$

with  $*$  denoting the convolution. Calculating the upper-left and upper-right entries of the matrix-valued equation (C.4), we arrive at the system of coupled nonlinear equations

$$i\dot{\hat{\gamma}}_t(p) = 2 \left[ (\hat{V} * \hat{\alpha}_t)(p) \bar{\hat{\alpha}}_t(p) - \overline{(\hat{V} * \hat{\alpha}_t)(p)} \hat{\alpha}_t(p) \right], \quad (\text{C.6})$$

$$i\dot{\hat{\alpha}}_t(p) = 2(p^2 - \mu) \hat{\alpha}_t(p) + 2(\hat{V} * \hat{\alpha}_t)(p) - 4(\hat{V} * \hat{\alpha}_t)(p) \hat{\gamma}_t(p). \quad (\text{C.7})$$

### C.2.2. Contact interactions

In this paper we concentrate on attractive contact interactions, i.e., potentials of the form

$$V(x) = -a\delta(x), \quad a > 0, \quad (\text{C.8})$$

---

which lead to exactly solvable systems in the stationary case. Not only is such a potential the most interesting one from a physical model point-of-view but also does it allow us to implement the terms including a convolution in the equations of motion conveniently as we will illustrate in the numerics Section C.7.

### C.2.3. Initial values

In this work we consider initial data which, in the stationary case, could be described by the Ginzburg-Landau energy functional for temperatures  $T$  close to the critical temperature  $T_c$ , i.e.,  $T = T_c + h^2$  for a small parameter  $h \in \mathbb{R}$ . For temperatures above  $T_c$ , the free energy is minimized by the so-called normal state  $\Gamma^N$  for which  $\alpha^N = 0$ ,  $\gamma^N = 1/1 + \exp((p^2 - \mu)/T)$ . For initial data  $\Gamma_0$  to be within the range of Ginzburg–Landau, they have to satisfy

$$\mathcal{F}_T(\Gamma_0) - \mathcal{F}_T(\Gamma^N) \leq \mathcal{O}(h^4). \quad (\text{C.9})$$

This condition can be complied with by choosing

$$\Gamma_0 = \frac{1}{1 + e^{H_{\Delta_0}/T}} \quad (\text{C.10})$$

with

$$H_{\Delta_0} = \begin{pmatrix} p^2 - \mu & -\Delta_0 \\ -\Delta_0 & \mu - p^2 \end{pmatrix}, \quad (\text{C.11})$$

where  $\Delta_0$  is a small parameter of the order of  $h$ , see, e.g., (Frank *et al.*, 2012). Calculating the right-hand side of the matrix equation (C.10) gives

$$\Gamma_0 = \begin{pmatrix} \hat{\gamma}_0 & \hat{\alpha}_0 \\ \hat{\alpha}_0 & 1 - \hat{\gamma}_0 \end{pmatrix} \quad (\text{C.12})$$

where  $\hat{\gamma}_0$  and  $\hat{\alpha}_0$  take the special form

$$\hat{\gamma}_0 = \frac{1}{2} - \frac{p^2 - \mu}{2} \frac{\tanh\left(\frac{\sqrt{(p^2 - \mu)^2 + |\Delta|^2}}{2T}\right)}{\sqrt{(p^2 - \mu)^2 + |\Delta|^2}} \quad (\text{C.13})$$

$$\hat{\alpha}_0 = \frac{\Delta_0}{2} \frac{\tanh\left(\frac{\sqrt{(p^2 - \mu)^2 + |\Delta|^2}}{2T}\right)}{\sqrt{(p^2 - \mu)^2 + |\Delta|^2}}. \quad (\text{C.14})$$

In our simulations we choose a temperature which is slightly above the critical temperature for the setting under consideration and set the initial value for the gap parameter  $\Delta_0$  to a non-vanishing value. We explain how to obtain the critical temperature for our setting and how to find physically reasonable initial values for  $\Delta$  in the Appendix Section C.6.

### C.2.4. Ginzburg–Landau and macroscopic parameter

For the stationary case it is well known that the Ginzburg–Landau theory emerges as the macroscopic limit of the BCS theory. To be more specific, define  $|\alpha^*\rangle$  as the translation

invariant minimizer of the BCS functional which, in case of the contact interaction (C.8), can be calculated via

$$\hat{\alpha}^*(p) = \frac{\Delta}{2} \frac{\tanh\left(\frac{\sqrt{(p^2 - \mu)^2 + |\Delta|^2}}{2T}\right)}{\sqrt{(p^2 - \mu)^2 + |\Delta|^2}}. \quad (\text{C.15})$$

Then, for the Cooper pair density  $|\alpha\rangle$  corresponding to the non-translation invariant minimizer of  $\mathcal{F}_T$ , the quantity

$$\psi := \frac{1}{h} \langle \alpha^* | \alpha \rangle \quad (\text{C.16})$$

is an approximate solution of the stationary Ginzburg–Landau equation, see, e.g., Frank *et al.* (2013). This told, if there were an analogous relation between the time-dependent BCS and the GL equations, the order parameter

$$\psi_t := \frac{1}{h} \langle \alpha^* | \alpha_t \rangle \quad (\text{C.17})$$

should, close to  $T_c$ , approximately satisfy a conventional time-dependent Ginzburg–Landau (TDGL) equation. In the spatially homogeneous case we are studying in this work, the conventional TDGL equation takes the form

$$\dot{\psi}_t = -c_{\text{GL},1} \psi_t - c_{\text{GL},2} |\psi_t|^2 \psi_t, \quad (\text{C.18})$$

with some appropriate parameters  $c_{\text{GL},1}$  and  $c_{\text{GL},2}$ , see, e.g., (Cyrot, 1973) and (Randeria, 1995, Eq. (18)). The parameter  $c_{\text{GL},1}$  depends on  $(T - T_c)/(h^2 T_c)$ . Crucially,  $c_{\text{GL},1}$  has the same sign as  $(T - T_c)$ . Thus, the TDGL equation is dissipative for temperatures above  $T_c$  by definition. This implies that if  $\psi_t$  could be described by the TDGL for small  $h$  it should decay over time. However, we will demonstrate in Section C.4 that this is not the case, at least for the full non-linear equation. The same conclusion has been reached by an analytical investigation recently as we will outline in Section C.3.

### C.2.5. The linear approximation

Let us decompose the particle density as

$$\gamma_t = \gamma_0 + \eta_t. \quad (\text{C.19})$$

For states satisfying (C.9)  $\eta_t$  appears to depend quadratically on  $\hat{\alpha}_t$ , see, e.g., (Frank *et al.*, 2015, Eq. 11), and it seems legitimate to approximate the full equation by its linearization

$$i\dot{\hat{\alpha}}_t(p) = 2(p^2 - \mu)\hat{\alpha}_t(p) + 2(\hat{V} * \hat{\alpha}_t)(p)(1 - 2\hat{\gamma}_0(p)). \quad (\text{C.20})$$

However, close to the Fermi-surface the quantity  $\eta_t$  is not small but the dominant part in the non-linear evolution. Consequently, the full BCS equations (C.6)-(C.7) and the linearization (C.20) give rise to very different evolutions. Namely, Eq. (C.20) yields a dissipative behavior in  $\psi_t$  whereas the full equations do not as is shown formally in Frank *et al.* (2015) and as we confirm by our numerical experiments below. Let us briefly summarize the results of Frank *et al.* (2015) in the next Section.

---

### C.3. Recent mathematical results

The BCS time-evolution (C.4) is studied analytically in Frank *et al.* (2015). Based on the work of Frank *et al.* (2012) the authors prove in (Frank *et al.*, 2015, Theorem 1) that  $|\psi_t|$  does not vanish for any times. More precisely, it is shown in a very general setting that, if the initial state  $\Gamma_0$  is close to the energy of the normal state, i.e.,  $\mathcal{F}_T(\Gamma_0) - \mathcal{F}_T(\Gamma^N) \leq O(h^4)$ , then the corresponding  $\psi_t$  satisfies

$$\| |\psi_t| - |\psi_0| \| \leq Ch^{1/2}, \quad (\text{C.21})$$

for an appropriate constant  $C$  independent of  $h$ .

On the other hand, it is shown in Frank *et al.* (2015) that the solution of the linearized equation (C.20) tends to 0 exponentially fast compared to the system's time scale of  $1/h^2$ . In detail, using strategies from perturbation theory, it can be derived that

$$|\psi_t| \approx |\psi_0| e^{t \text{Im} \lambda} \quad (\text{C.22})$$

holds, where  $\lambda$  is a resonance of order  $1/h^2$  which emerges from the zero-eigenvalue at  $T = T_c$  of the linear operator  $\mathcal{O} = (k^2 - \mu) \tanh^{-1} \left( \frac{k^2 - \mu}{2T} \right) + V$ .

The combination of the bounds (C.21) and (C.22) shows clearly that the non-dissipative behavior of  $\psi_t$  is a purely non-linear effect which takes place solely in a tiny neighborhood of the Fermi surface.

Furthermore, using the methods of Frank *et al.* (2015), it is straightforward to derive the following bound on the derivative

$$|\dot{\psi}_t| = \mathcal{O}(1/h). \quad (\text{C.23})$$

In other words, although the solution  $|\psi_t|$  tends to the constant  $|\psi_0|$  in the limit  $h \rightarrow 0$ , its derivative might well oscillate more and more –in line with according predictions for systems which are suddenly perturbed out of equilibrium (Volkov and Kogan, 1974). These findings are well reproduced in our numerical experiments as we show now.

### C.4. Simulations

In this work we are interested in a qualitative study of the differences between the full BCS/BdG equations and their linearization. Thus, without loss of generality, we can work in dimensionless units and set the constant  $a$  of the contact interaction and the chemical potential  $\mu$  to  $a = 1$  and  $\mu = 1$ , respectively. The initial data for the simulations are obtained as outlined in the Appendix Section C.6. For this, we approximate the integrals in Eqs. (C.25) and (C.26) by the sum over the discrete momenta we take into account. For the sake of reproducibility we add the thus-obtained values for  $T_c$  and  $\Delta_0$  to the results of our simulations. For more details on the discretization of the equations under consideration we refer the interested reader to the Appendix Section C.7.

#### C.4.1. Gap as a function of $h$

In order not to have to calculate the initial value of the gap parameter which depends on the crucial parameter  $h$  at the start of each evolution again, we calculate  $\Delta_0$  with the procedure

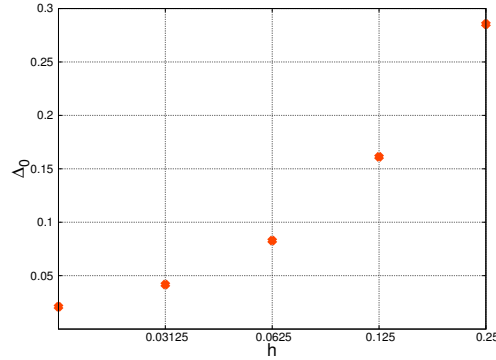


Figure C.1: The gap  $\Delta_0$  as a function of the semiclassical parameter  $h$  in semilogarithmic scale.

outlined in the Appendix Section C.6 for various  $h$  once. The interesting result is illustrated in Fig. C.1 where we can see that  $\Delta_0$  depends more or less linearly on the crucial parameter.

Finally, with both  $T_c$  and  $\Delta_0$  at hand, we are able to present the results of the simulations. Doing so, we take into account that at temperatures  $T = T_c + h^2$ , physically interesting dynamics are expected to occur on a time-scale of  $\mathcal{O}(1/h^2)$ . Therefore, we always set  $t_{\text{end}} = 1/h^2$  or  $t_{\text{end}} = 2/h^2$  in the following.

#### C.4.2. Results for $h = 1/4$

We plot the scaled  $L^2$ -norm of  $\alpha$ , which in the discrete setting is given by the sum over the  $K$  discrete momenta as

$$\frac{1}{h^2} \|\alpha_t\|_2^2 = \frac{1}{h^2} \sum_{k=-K/2}^{K/2-1} |\alpha_t^K(k)|^2, \quad (\text{C.24})$$

as well as the modulus of the interesting macroscopic parameter  $\psi_t$  introduced in Eq. (C.17). We plot the results for both the BCS equation (C.7) and its linear approximation (C.20), see Fig. C.2 and Fig. C.3. For both quantities, the linear equation leads to exponential decay. The full equation, in contrast, coincides with the linear approximation only for a short period after which both  $\|\alpha_t\|$  and  $|\psi_t|$  grow again.

#### C.4.3. Results for $h = 1/8$

Here, too, we consider the scaled norm of the Cooper pair density and the modulus of the parameter  $\psi_t$ . The results are shown in Fig C.4 and Fig. C.5. Again, the linear evolution equation is clearly diffusive while the full equation yields a similar behavior only for very small times. After a short decline in the beginning of the simulation,  $\|\alpha_t\|$  and  $|\psi_t|$  seem to oscillate. Similar oscillations have been predicted by Volkov and Kogan (1974) and observed for suddenly perturbed non-equilibrium systems in Yuzbashyan *et al.* (2006). Although, as compared to these studies, we work on systems close to equilibrium and slightly above the critical temperature, it is interesting to see that our long-term evolutions show oscillations which resemble the ones predicted for the out-of-equilibrium case.

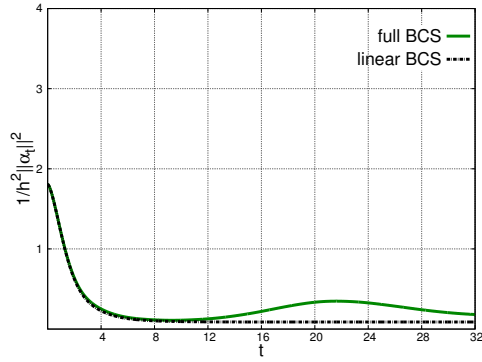


Figure C.2:  $1/h^2 \|\alpha_t\|_2^2$  as a function of integration time  $t$  for  $h = 1/4$ . The physical parameters are  $T_c = 0.19$  and  $\Delta_0 = 0.29$ .

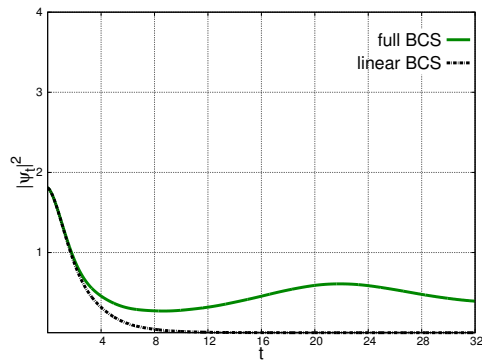


Figure C.3:  $|\psi_t|^2$  as a function of integration time  $t$  for  $h = 1/4$ . The physical parameters are  $T_c = 0.19$  and  $\Delta_0 = 0.29$ .

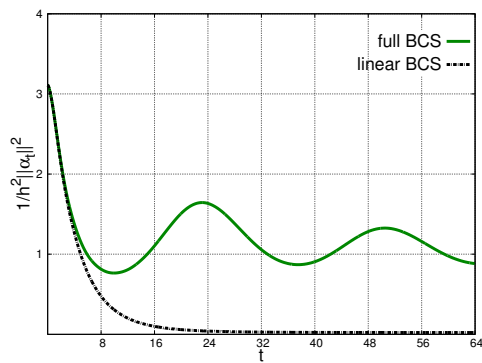


Figure C.4:  $1/h^2 \|\alpha_t\|_2^2$  as a function of integration time  $t$  for  $h = 1/8$ . The physical parameters are  $T_c = 0.19$  and  $\Delta_0 = 0.16$ .

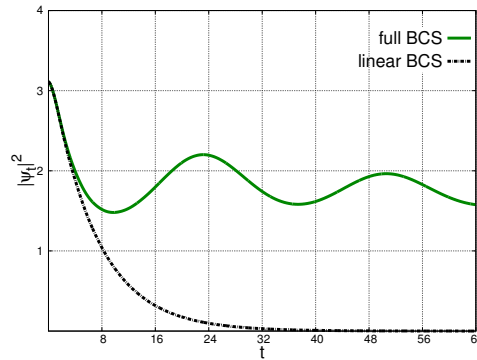


Figure C.5:  $\psi_t$  as a function of integration time  $t$  for  $h = 1/8$ . The physical parameters are  $T_c = 0.19$  and  $\Delta_0 = 0.16$ .

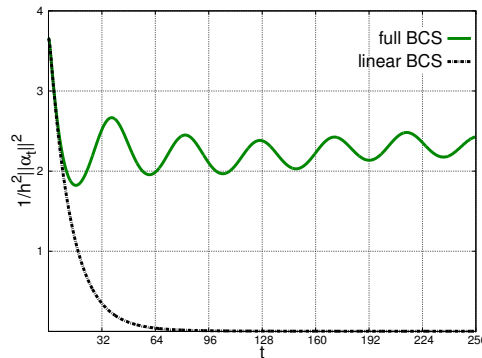


Figure C.6:  $1/h^2 \|\alpha_t\|_2^2$  as a function of integration time  $t$  for  $h = 1/16$ . The physical parameters are  $T_c = 0.19$  and  $\Delta_0 = 0.083$ .

#### C.4.4. Results for $h = 1/16$

Once more, we depict the time evolution of  $\|\alpha_t\|$  and  $|\psi_t|$ , cf. Figs. C.6 and C.7. The conclusions we can draw from these two plots are the same as for  $h = 1/8$ , the only difference being the faster oscillations in line with the bound (C.23). Most importantly, even for this small value of  $h$ , we only observe diffusion for the linear approximation which, belying its name, does not approximate the BCS equation for reasonably long time intervals. Let us summarize our results in the concluding Section.

## C.5. Summary

We have introduced a reliable integration scheme for the time-dependent BCS equation and its linear approximation in spatially homogeneous settings. With the help of these algorithms, we could perform numerical long-term studies for systems close to equilibrium in order to investigate the time-evolution of the order parameter at the limit close to the critical temperature. The study shows very clearly that, opposed to the linear case, the full BCS equation does not yield any decay over time in the order parameter  $\psi_t$ . Since the conventional

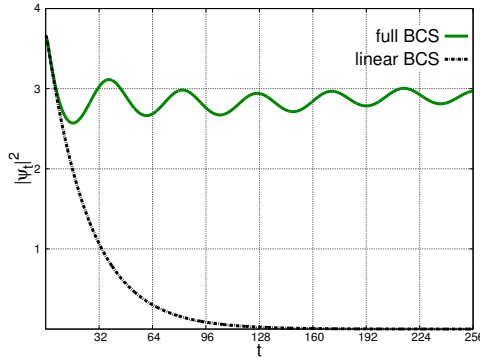


Figure C.7:  $\psi_t$  as a function of integration time  $t$  for  $h = 1/16$ . The physical parameters are  $T_c = 0.19$  and  $\Delta_0 = 0.083$ .

time dependent Ginzburg–Landau equation is dissipative above the critical temperature by definition, it cannot give a valid macroscopic limit of the full time-dependent BCS/BdG equations. It can only be seen as the limit of the linearization of the full equations but the effects of this linearization could clearly be shown not to be negligible in the considered regime. We thus confirm the analysis provided in Frank *et al.* (2015).

In addition, when evolving the system as described by the non-linear BCS/BdG equations, we observed oscillations in the Cooper pair density and in the order parameter about a finite value which are similar to oscillations which have been observed for out-of-equilibrium systems in various works.

## Acknowledgements

We want to thank Christian Lubich for useful remarks and discussions. This work was partially funded by the DFG grant GRK 1838.

**Declaration of contribution** Contribution to the original manuscript was: C. H. 30%, J. S. 70%.

Contribution to the update of the manuscript was: C. H. 50%, J. S. 50%.

## C.6. Critical temperature and initial energy gap

For translation invariant systems with contact interaction, the critical temperature  $T_c$  is well-known to be given implicitly by

$$\frac{2\pi}{a} = \int_{\mathbb{R}} \frac{\tanh\left(\frac{p^2 - \mu}{2T_c}\right)}{p^2 - \mu} dp, \quad (\text{C.25})$$

see, e.g. (Leggett, 1980; Nozieres and Schmitt-Rink, 1985; Randeria, 1995). The energy gap  $\Delta$  between the superconducting state and the normal state at temperatures beneath the critical

temperature, in turn, can be obtained from the relation

$$\frac{2\pi}{a} = \int_{\mathbb{R}} \frac{\tanh\left(\frac{\sqrt{(p^2-\mu)^2+|\Delta|^2}}{2T}\right)}{\sqrt{(p^2-\mu)^2+|\Delta|^2}} dp. \quad (\text{C.26})$$

In order to calculate the critical temperature and a realistic initial value for the gap parameter we thus proceed as follows: For a given value of the small crucial parameter  $h$ , we first determine the critical temperature  $T_c$  and set  $T = T_c - h^2$ . For this temperature we then search the corresponding gap  $\Delta$  following the above definition (C.26) and set  $\Delta_0 = \Delta$  as its initial state. Finally, as we are interested in simulations for temperatures slightly above the critical temperature, we put  $T = T_c + h^2$  and insert this into Eq. (C.12) together with the just-determined  $\Delta_0$ . This yields physically realistic conditions which satisfy the energy constraint (C.9).

## C.7. Numerical treatment of the equations

We want to model a system of infinite spacial extension, which, of course, is not possible to achieve on a machine. Therefore, we pretend our system to be periodic in space but with a large enough period.

### C.7.1. Finite extension and discrete system

In the Ginzburg-Landau regime, one often takes into account external potentials that vary on a scale of  $\mathcal{O}(1/h)$  and, consequently, lead to variations of the system which occur over intervals of that very scale. Thus, a valid model system should have an extension no smaller than those physical variations. But, in order to avoid artificial effects due to the periodicity, it is necessary to enlarge this extensions by some multiples of  $1/h$ . For convenience we furthermore include a factor of  $2\pi$ , wherefore we consider systems with period  $2\pi N/h$ ,  $1 < N \in \mathbb{N}$ . The kernels of the density operators are now functions on  $L^2([0, 2\pi N/h] \mapsto \mathbb{R})$ . In order to simplify the notation, we introduce macroscopic variables via  $x_{\text{mac}} := h/Nx$ . We end up in a  $2\pi$ -periodic setting for which the inner product of two functions  $f$  and  $g$  is just

$$\langle f | g \rangle = \sum_{k \in \mathbb{Z}} \widehat{f} \widehat{g}. \quad (\text{C.27})$$

The self-consistent BCS equations are now given by

$$i\dot{\Gamma}_t(k) = [H_{\Gamma_t}(k), \Gamma_t(k)], \quad k \in \mathbb{Z}, \quad (\text{C.28})$$

with the Hamiltonian

$$H_{\Gamma_t} = \begin{pmatrix} \left(\frac{h^2}{N^2}k^2 - \mu\right) & 2[\widehat{V}_{Nh} * \widehat{\alpha}_t]_k \\ 2[\widehat{V}_{Nh} * \widehat{\alpha}_t]_k & \left(\mu - \frac{h^2}{N^2}k^2\right) \end{pmatrix} \quad (\text{C.29})$$

and the Fourier transform  $\widehat{V}_{Nh}$  of  $V_{Nh}(\cdot) := V(N/h \cdot)$ . Please note that in the present discrete case the convolution of two summable series  $a_k$  and  $b_k$  has to be understood as

$$(a * b)_k = \sum_{j \in \mathbb{Z}} a_{k-j} b_j. \quad (\text{C.30})$$

---

### C.7.2. The equations for a delta potential

For systems on a large torus with a contact interaction (C.8), we can easily see that

$$\hat{V}_{Nh} * \hat{\alpha}_t = -a \langle \phi | \alpha \rangle, \quad (\text{C.31})$$

where  $\phi$  is the state given by  $\phi(k) = 1$  for all integers  $k$ . With this, the equations of motion take the convenient form

$$i\dot{\hat{\gamma}}_t(k) = 2a \left[ \overline{\langle \phi | \alpha \rangle} \hat{\alpha}_t(k) - \langle \phi | \alpha \rangle \overline{\hat{\alpha}_t(k)} \right], \quad (\text{C.32})$$

$$i\dot{\hat{\alpha}}_t(k) = 2 \left( \frac{\hbar^2}{N^2} k^2 - \mu \right) \hat{\alpha}_t(k) + 2a \langle \phi | \alpha \rangle (2\hat{\gamma}_t(k) - 1) \quad (\text{C.33})$$

for the nonlinear case and

$$i\dot{\hat{\alpha}}_t(k) = 2 \left( \frac{\hbar^2}{N^2} k^2 - \mu \right) \hat{\alpha}_t(k) + 2a \langle \phi | \alpha \rangle (2\hat{\gamma}_0(k) - 1) \quad (\text{C.34})$$

for the linear case.

Up to now we are still left with an infinite-dimensional system of equations. In order to solve these numerically, we have to introduce a suitable finite-dimensional subspace.

### C.7.3. Space discretization

As the BCS equations are given in their momentum space representation, it is most convenient to use the so-called *Fourier collocation*. This means that a  $2\pi$ -periodic function  $f(x) = \sum_{j \in \mathbb{Z}} \hat{f}(j) e^{ikx}$  is approximated by

$$f^K(x) = \sum_{j=-\frac{K}{2}}^{\frac{K}{2}-1} \hat{f}^K(j) e^{ikx}, \quad (\text{C.35})$$

where the coefficients  $\hat{f}^K(j)$  are obtained by the discrete Fourier transform of the values  $f_j = f(2\pi/Kj)$ ,  $j = -K/2, \dots, K/2 - 1$ . Mathematically speaking we work on the subspace spanned by the first  $K$  eigenfunctions of the Laplacian on  $[0, 2\pi]$ . As a consequence, the evolution of the system is given by the  $K$ -dimensional system of ordinary differential equations (ODE)

$$i\dot{\hat{\gamma}}_t^K(k) = 2a \left[ \overline{\langle \phi^K | \alpha^K \rangle} \hat{\alpha}_t^K(k) - \langle \phi^K | \alpha^K \rangle \overline{\hat{\alpha}_t^K(k)} \right], \quad (\text{C.36})$$

$$-\frac{K}{2} \leq k \leq \frac{K}{2} - 1,$$

$$i\dot{\hat{\alpha}}_t^K(k) = 2 \left( \frac{\hbar^2}{N^2} k^2 - \mu \right) \hat{\alpha}_t^K(k) + 2a \langle \phi^K | \alpha^K \rangle (2\hat{\gamma}_t^K(k) - 1), \quad (\text{C.37})$$

$$-\frac{K}{2} \leq k \leq \frac{K}{2} - 1,$$

and accordingly for the linear case. From numerical analysis it is well known that (C.35) yields a very good approximation to  $2\pi$ -periodic functions with the discretization error decreasing rapidly as a function of  $K$ , see, e.g. (Lubich, 2008), Chapter III.1.3.

For practical reasons we set  $K$  to be an integer power of 2 so that for a given  $\hat{\alpha}_t^K(j)$ ,  $j = -K/2, \dots, K/2 - 1$ , the corresponding distribution  $\alpha_t^K(x)$  at the discrete points  $x_j = \frac{2\pi}{K}j$  can be computed efficiently with the well-known fast Fourier transform (FFT). As we want to resolve phenomena happening on the microscopic scale  $\mathcal{O}(h/N)$ , we choose

$$K = M \frac{N}{h} \quad (\text{C.38})$$

for a large enough integer  $M$ . Let us now explain how we solve the system of ODE (C.36)–(C.37).

#### C.7.4. Solving the system of ordinary differential equations

We first notice that the Hamiltonian  $H_{\Gamma_t}$  is self-adjoint. Thus, the time-evolution of  $\Gamma_t$  is a unitary transformation and, hence, its eigenvalues are preserved. With regard to definition (C.1), the eigenvalues can be readily computed as

$$\lambda_{1,2}(p) = \frac{1}{2} \pm \sqrt{\left(\hat{\gamma}_t(p) - \frac{1}{2}\right)^2 + |\hat{\alpha}_t(p)|^2}, \quad (\text{C.39})$$

and we see that the equality

$$\left(\hat{\gamma}_t(p) - \frac{1}{2}\right)^2 + |\hat{\alpha}_t(p)|^2 = \left(\hat{\gamma}_0(p) - \frac{1}{2}\right)^2 + |\hat{\alpha}_0(p)|^2 \quad (\text{C.40})$$

holds. Solving this for  $\hat{\gamma}_t$ , we get

$$\hat{\gamma}_t(p) = \begin{cases} \frac{1}{2} + \sqrt{h(p) - |\hat{\alpha}_t(p)|^2} & \text{for } p^2 < \mu, \\ \frac{1}{2} - \sqrt{h(p) - |\hat{\alpha}_t(p)|^2} & \text{for } p^2 \geq \mu, \end{cases} \quad (\text{C.41})$$

where we have defined the auxiliary function

$$h(p) := \left(\hat{\gamma}_0(p) - \frac{1}{2}\right)^2 + |\hat{\alpha}_0(p)|^2. \quad (\text{C.42})$$

The signs in Eq. (C.41) can be inferred from the initial values we use in this work, cf. (C.12). They are such that  $\hat{\gamma}_0(p)$  is greater than  $1/2$  for  $\mu > p^2$  and less than or equal to  $1/2$  for  $\mu \leq p^2$ .

Inserting the discrete analogon of Eq. (C.41) into the relevant equation of motion (C.37), we get the nonlinear coupled system of equations

$$\begin{aligned} i\dot{\hat{\alpha}}_t^K(k) &= 2 \left( \frac{h^2}{N^2} k^2 - \mu \right) \hat{\alpha}_t^K(k) \\ &\quad \pm 4a \langle \phi^K | \alpha^K \rangle \sqrt{h(k) - |\hat{\alpha}_t^K(k)|^2}, \quad -\frac{K}{2} \leq k \leq \frac{K}{2} - 1. \end{aligned} \quad (\text{C.43})$$

This said, we now present our time integration algorithm.

---

### C.7.5. Time discretization

Putting it in a formal way, the system we have to integrate is given by

$$\begin{cases} \frac{d\mathbf{y}(t)}{dt} = f(\mathbf{y}(t)), \\ \mathbf{y}(0) = \mathbf{y}_0, \end{cases} \quad (\text{C.44})$$

with

$$\mathbf{y} = (\hat{\alpha}^K(-K/2) \quad \dots \quad \hat{\alpha}^K(K/2 - 1))^T \in \mathbb{R}^K. \quad (\text{C.45})$$

The right hand side of our initial problem can be written as the sum of two terms,

$$f(\mathbf{y}) = f_1(\mathbf{y}) + f_2(\mathbf{y}), \quad (\text{C.46})$$

where  $f_1$  represents the linear part which resembles the kinetic part in the Schrödinger-equation and  $f_2$  is the nonlinear part. Let  $\tau$  denote a time step and  $\Phi_{\tau,f}$  the smooth map between  $\mathbf{y}(0)$  and  $\mathbf{y}(\tau)$ . Given the special form (C.46) of the differential equation, one can approximate  $\Phi_{\tau,f}$  numerically by

$$\Phi_{\tau,f}^{\text{num}}(\mathbf{y}_0) = (\Phi_{\tau/2,f_1} \circ \Phi_{\tau,f_2} \circ \Phi_{\tau/2,f_1})(\mathbf{y}_0). \quad (\text{C.47})$$

This is the well-known *Strang splitting*. Applying it successively yields an approximation to the exact solution at times  $t = n\tau$ ,  $n = 1, 2, \dots$ , the error of which decreases quadratically as a function of the step size  $\tau$ , see, e.g. (Hairer *et al.*, 2006), Chapter II.5.

The advantage of the Strang splitting is that  $\Phi_{\tau,h}$  can be calculated exactly as

$$\Phi_{\tau,f_1}(\cdot) = e^{-i2\left(\frac{h^2}{N^2}k^2 - \mu\right)\tau} \cdot \quad (\text{C.48})$$

As for  $\Phi_{\tau,f_2}$ , it has to be approximated due to the nonlinearity. For this, we choose a simple Runge-Kutta scheme as proposed by Flannery *et al.* (1992) whose numerical error is small compared to the error expected from the splitting<sup>57</sup>. Before starting the simulations, we still need to fix the mentioned discretization parameters  $\tau$  and  $K$ . In our case,  $K$  itself depends on three parameters, cf. Eq. (C.38). As  $h$  is the semiclassical parameter we want to vary throughout the study, we have to choose reasonable values for the remaining quantities  $M$ ,  $N$  and  $\tau$ . We first consider  $\tau$ .

### C.7.6. Fixing the time discretization parameter

The step size has to be chosen small enough for both the numerical approximation of  $\Phi_{\tau,f_2}$  and the Strang splitting to give accurate results. For our simulations it turned out that reliable results can only be expected for a step size inversely proportional to  $K$ . Playing safe we include a small factor and set  $\tau = 0.1/K$ . As a measure for the time integrator's accuracy, we consider the discrete analogon of the free energy introduced in Eq. (C.2) above, which is given

---

<sup>57</sup>Note that in the linear case  $\Phi_{\tau,f_2}$  can also be calculated exactly, cf. Chapter D

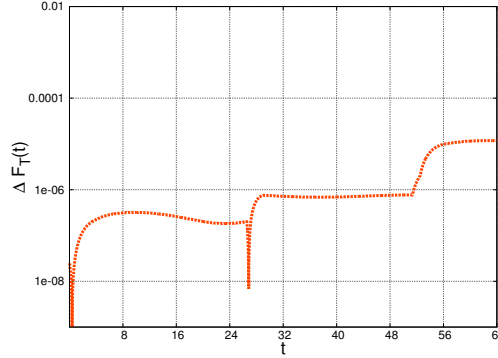


Figure C.8: Relative error  $\Delta F_T$  of the discretized free energy against integration time  $t$  in semilogarithmic scale for  $h = 1/8$ . The physical parameters are  $T_c = 0.19$  and  $\Delta_0 = 0.16$ .

by

$$\begin{aligned}
 F_T^K(\Gamma^K) &= \sum_{k=-K/2}^{K/2-1} \left( \frac{h^2}{N^2} k^2 - \mu \right) \hat{\gamma}^K(k) \\
 &+ \frac{1}{2\pi} \int_0^{2\pi} V(x_{\text{mac}}) |\alpha^K(x_{\text{mac}})|^2 dx_{\text{mac}} - TS(\Gamma^K).
 \end{aligned} \tag{C.49}$$

A short calculation yields that this quantity is conserved under the exact flow of the corresponding initial value problem. Therefore, the reliability of a numerical integration scheme can be checked by tracking the relative error  $\Delta F_T$ , defined by

$$\Delta F_T(t) = \left| \frac{F_T(\Gamma_t^K) - F_T(\Gamma_0^K)}{F_T(\Gamma_0^K)} \right|, \tag{C.50}$$

along the numerical evolution. Recurring to a constant of motion as a criterion of accurateness is a much applied procedure in various computational fields, see, e.g. (Seyrich, 2013; Lukes-Gerakopoulos, 2014). Following this line of reasoning, we have verified the accuracy of our time integrator for every simulation presented below. As an example, we show the plot of  $\Delta F_T$  corresponding to the simulations of Subsection C.4.3 in Fig. C.8.

### C.7.7. Fixing the space discretization parameters

We have seen in the previous Subsection that the time step has to be inversely proportional to the dimension of the subspace we are approximating our system on. Furthermore, every time step requires a computational effort which grows linearly with  $K$ . Consequently, the complete CPU time for a simulation over a given time interval  $[0, t_{\text{end}}]$  is quadratic in  $K$ . So the dimension of the subspace and, thus, the related  $N$  and  $M$  should be the smallest possible. In order to check how small a  $M$  we can choose without any significant loss of accuracy, we fix  $N = 8$  and  $h = 1/4$  and calculate the critical temperature via the discretized version of

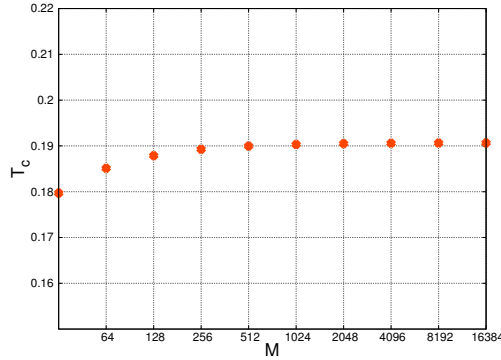


Figure C.9: Critical temperature  $T_c$  as a function of the number of momenta per unit volume  $M$  for  $N = 8$  and  $h = 1/4$ .

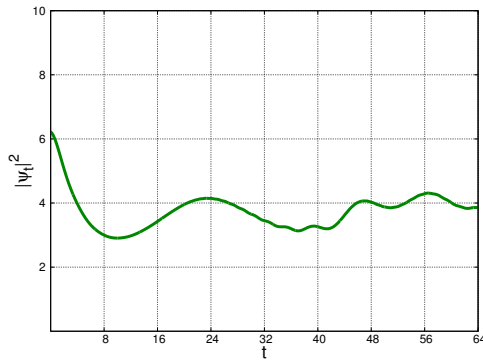


Figure C.10:  $|\psi_t|$  as a function of integration time  $t$  for  $N = 4$  and  $h = 1/8$ . The physical parameters are  $T_c = 0.19$  and  $\Delta_0 = 0.16$ .

Eq. (C.25),

$$\frac{2\pi}{a} = \sum_{k=-K/2}^{K/2-1} \frac{\tanh\left(\frac{\frac{h^2}{N^2}k^2 - \mu}{2T_c}\right)}{\frac{h^2}{N^2}k^2 - \mu}, \quad (\text{C.51})$$

for different values of  $M$ . The result can be seen in Fig. C.9. For different values of  $N$  and  $h$  we get the same plot. We see that for  $M = 256$  the critical temperature is still slightly too small. However, when comparing the evolutions obtained with  $M = 256$  to the according ones for  $M = 512$ , the relevant figures are indistinguishable from each another. For the sake of efficiency, we thus fix  $M = 256$  for the rest of this work.

As for the extension of our interval,  $N$ , we have to choose it large enough so that the solution cannot reach the boundaries during the simulation. As, by construction, we work with a periodic setting, a solution reaching one end of the interval would enter again at the other end, thus leading to unphysical interference. As an example of this numerical artifact, we consider the case  $h = 1/8$ ,  $N = 4$  and plot the modulus of  $\psi_t$  in Fig. C.10. We observe oscillations for larger  $t$  which should not show up in reality, cf. Subsection C.4.3. Whenever we encountered such an artifact, we successively increased  $N$  by factors of 2 until the artifact vanished.

# D. Splitting integrators for the BCS equations of superconductivity

The content of this Section will be submitted as a single-author paper by J. S. . The corresponding preprint can be found at arXiv:1505.03417.

## Abstract

The BCS equations are the centerpiece of the microscopic description of superconductivity. Their space discretization yields a system of coupled ordinary differential equations. In this work, we come up with fast time evolution schemes based on a splitting approach. One of the schemes only requires basic operations. For the physically important case of the BCS equations for a contact interaction potential, the computational cost of the schemes grows only linearly with the dimension of the space discretization. The schemes' accuracy is demonstrated in extensive numerical experiments. These experiments also show that the physical energy of the system is preserved up to very small errors.

## D.1. Introduction

In this work, we consider the time-dependent BCS equations, often also referred to as Bogoliubov–de-Gennes (BdG) equations for the particle density and the Cooper pair density in superconductors. These equations, named after *Bardeen, Cooper and Schrieffer*, the pioneers of the microscopic description of superconductivity in metals, see (Bardeen *et al.*, 1957), were first introduced for the single-particle wave functions  $u$  and  $v$  of fermionic systems by De Gennes (1966) based on the transformations of Bogoliubov (1947). Being a fundamental part of condensed matter physics, the time-dependent BCS/BdG equations have been paid a lot of attention from different perspectives, see, e.g., (Volkov and Kogan, 1974; Barankov *et al.*, 2004; Yuzbashyan *et al.*, 2006). Most studies are based on the evolution equations of the single-particle wave functions  $u$  and  $v$ . But often, especially in works concerning macroscopic limits, it is more convenient to work with the equations for the particle density  $\gamma$  and the Cooper pair density  $\alpha$  directly, see, e.g., (Frank *et al.*, 2012; Hainzl and Seiringer, 2012; Hainzl and Schlein, 2013; Hainzl *et al.*, 2010). A detailed introduction to the corresponding formalism is given by Bach *et al.* (1994). A numerical scheme for the minimization of a stationary problem in this formalism has been presented in (Lewin and Paul, 2014). The present work is motivated by studies on the macroscopic limit of the time-dependent BCS/BdG equations close to the critical temperature (Frank *et al.*, 2015; Hainzl and Seyrich, 2016). In order to study the behavior of the time-evolutions of the particle density and the pair density in the considered limit, the coupled partial differential equations for  $\gamma$  and  $\alpha$  had to be solved numerically. Thus, two reliable and efficient integration algorithms for these equations based on a splitting approach have been developed and will be presented in this work.

The evolution equations for the Cooper pair density resembles the linear Schrödinger equation for quantum dynamical systems. One important aspect of these systems is that, after a space discretization, the right hand side of the resulting ordinary differential equations has a very large Lipschitz constant due to the Laplacian in the kinetic part. As a consequence, standard

---

explicit integration schemes, such as the ones presented in (Flannery *et al.*, 1992), although very popular in computational physics, are of no use in quantum mechanical applications. Therefore, the treatment of such quantum dynamical systems has been of huge interest in the numerical analysis community for many decades, see, e.g., (Lubich, 2008, Chapter II.1). Various evolution schemes for the linear Schrödinger equation in varying settings have been proposed over the years, see, e.g., (Gray and Manolopoulos, 1996; Blanes *et al.*, 2006; Tal-Ezer and Kosloff, 1984; Park and Light, 1986; Hochbruck and Lubich, 1997, 2003). Nonlinear Schrödinger equations such as the Gross–Pitaevskii equation and equations arising from the Hartree and Hartree–Fock approximation of the quantum state have also been devoted attention to, see, e.g., (Tang *et al.*, 1996; Bao *et al.*, 2003; Gauckler and Lubich, 2010) and (Lubich, 2004, 2005), respectively.

All these methods have in common that the partial differential equations are first discretized in space. This means that the system is restricted to a suitable subspace spanned by a finite number of basis functions. Here, we do this with the help of a *Fourier collocation* method which is the straightforward approach for the problem we look at, see, e.g., (Lubich, 2008, Chapter III.1). This yields a system of coupled ordinary differential equations, on the solution of which we focus in the present work.

What, in many applications, turned out to be the most promising tool for the solution of the space discretized system was the splitting of the equations under consideration into some subproblems, each of which can be solved more easily than the system of equations as a whole. This idea was first employed for advection equations by Strang (1968) and Marchuk (1968). In the realm of quantum dynamics, it was applied for the first time by Feit *et al.* (1982) where the linear Hamiltonian was split into a kinetic and a potential part. The respective solutions were then concatenated in a suitable way in order to obtain a reliable integration method. Here, we use this ansatz to introduce two schemes for the evolution of the space discretized BCS equations. The coupling terms depend on the convolution of the particle density with the Cooper pair density. We use the well-known *fast Fourier transform (FFT)* to swiftly compute these terms. As a consequence, the CPU effort per time step of our schemes grows only mildly with the number of basis functions. This is very important since in most physical applications the BCS system requires a discretization space of very high dimension.

For the first scheme, we exploit that the eigenvalues of the density operator, which are functions of the particle density and the Cooper pair density, are conserved along exact solutions to the BCS equations. Hence, we can express the particle density as a function of the Cooper pair density. We end up with a decoupled nonlinear system for the evolution of the Cooper pair density  $\alpha$ . The thus obtained equations are split into a linear part, which can be solved exactly, and into a nonlinear part, the flow of which can be approximated by some standard numerical scheme. In the rest of this work, we will refer to the resulting integrator as *BCSInt*. It is very accurate and preserves the physically interesting eigenvalues of the density operator by construction. The integrator has already been employed in a numerical study of the physical behavior of the BCS equations in (Hainzl and Seyrich, 2016).

For the second integrator, we do not decouple the system at all. Instead, thanks to the system’s particular structure, we can aptly split it into three subproblems for which the flows can be calculated very efficiently. These calculations require only basic operations. Recombining the thus obtained flows in a suitable way results in a very accurate and efficient scheme which conserves the system’s constants of motion, such as the energy, up to very small errors. In the following, we will denote the new scheme by *SplitBCS*. In the physically important case of a contact interaction, i.e., when the potential is given by a delta function, the flows of the

subproblems can all be calculated exactly with an effort linear in the number of basis functions.

We demonstrate our integrators' favorable behavior with the help of numerical experiments and numerical comparisons to standard integration schemes. We mention that an error estimate similar to the one of Gauckler (2011) for splitting schemes applied to the Gross–Pitaevskii equations is expected to hold for SplitBCS. However, such an analysis is out of the scope of this work.

Our presentation is organized as follows: We start with a short introduction to the BCS equations for the particle density and Cooper pair density in Section D.2. Afterwards, we recall the Fourier collocation for the partial differential equations in Section D.3. After introducing some notation in Section D.3.4, we first introduce our splitting scheme BCSInt for the decoupled nonlinear system in Section D.5. Then, we present our fast integration scheme SplitBCS for the coupled system in Section D.6. This is followed by numerical tests in Section D.7. Finally, we summarize our results in Section D.8.

## D.2. The BCS Equations

A superconducting translation invariant system in one spatial dimension is characterized by the particle density  $\gamma : \mathbb{R} \times \mathbb{R} \mapsto \mathbb{R}$  which describes the probability at time  $t$  of finding a particle at position  $x$  and the Cooper pair density  $\alpha : \mathbb{R} \times \mathbb{R} \mapsto \mathbb{C}$  which gives the probability at time  $t$  of having a Cooper pair of electrons at distance  $x$ . For a given particle interaction  $V$ , the evolution of  $\alpha$  and  $\gamma$  is governed by the BCS equations, sometimes also called Bogoliubov–De-Gennes equations,

$$i\dot{\gamma}(t, x) = -2 \int_{\mathbb{R}} V(y) \operatorname{Im} \left[ \alpha(t, x - y) \overline{\alpha(t, y)} \right] dy, \quad (\text{D.1})$$

$$i\dot{\alpha}(t, x) = 2 \left( -\frac{d^2}{dx^2} - \mu + V(x) \right) \alpha(t, x) - 4 \int_{\mathbb{R}} \gamma(t, x - y) V(y) \alpha(t, y) dy, \quad (\text{D.2})$$

with  $\mu$  denoting the chemical potential of the physical system and  $\dot{\cdot} = \partial/\partial t$ . Conventionally, the BCS equations are given in terms of the Fourier transforms, i.e., the momentum space representations

$$\hat{\gamma}(t, p) = \frac{1}{2\pi} \int_{\mathbb{R}} \gamma(t, x) e^{ipx} dx, \quad (\text{D.3})$$

$$\hat{\alpha}(t, p) = \frac{1}{2\pi} \int_{\mathbb{R}} \alpha(t, x) e^{ipx} dx. \quad (\text{D.4})$$

Please note that for the momentum distributions, we have  $\hat{\gamma}(k) = \langle a_k^\dagger a_k \rangle$  and  $\hat{\alpha}(k) = \langle a_k a_{-k} \rangle$ , where  $a_k^\dagger$  and  $a_k$  are the creation and annihilation operators of particles with momentum  $k$ . In the momentum space representation, the equations of motion can be written in the compact, self-consistent form

$$i\dot{\Gamma}(t, p) = [H_{\Gamma(t,p)}, \Gamma(t, p)], \quad p \in \mathbb{R}, \quad (\text{D.5})$$

see, e.g., Frank *et al.* (2015).  $\Gamma(t, p)$  is the  $2 \times 2$ -matrix

$$\Gamma(t, p) = \begin{pmatrix} \hat{\gamma}(t, p) & \hat{\alpha}(t, p) \\ \hat{\alpha}(t, p) & 1 - \hat{\gamma}(t, p) \end{pmatrix} \quad (\text{D.6})$$

and  $H_{\Gamma(t,p)}$  is the Hamiltonian

$$H_{\Gamma(t,p)}(p) = \begin{pmatrix} p^2 - \mu & 2[\hat{V} * \hat{\alpha}](t, p) \\ 2[\hat{V} * \hat{\alpha}](t, p) & \mu - p^2 \end{pmatrix}. \quad (\text{D.7})$$

Here,  $*$  denotes the convolution of  $\hat{V}$  with  $\hat{\alpha}(t, p)$ .

### D.2.1. Superconductivity

It can be shown, see e.g. (Hainzl *et al.*, 2008), that the free energy functional

$$F_T(\Gamma(t)) = \int_{\mathbb{R}} (p^2 - \mu) \hat{\gamma}(t, p) dp + \int_{\mathbb{R}} |\alpha(t, x)|^2 V(x) dx + \int_{\mathbb{R}} \text{Tr}_{\mathbb{C}^2} (\Gamma(p) \log \Gamma(p)) dp \quad (\text{D.8})$$

is conserved along solutions of the evolution equations (D.5) for any given temperature of the system  $T$ . If, for a given temperature  $T$ , the minimizer  $\Gamma$  of  $\mathcal{F}_T$  has a non vanishing Cooper pair density  $\alpha$ , then the system is said to be in a superconducting state.

### D.2.2. The discrete BCS equations

In order to render the system computationally palpable, one restricts it to a domain  $D = [0, L2\pi]$ ,  $L \in \mathbb{N}$ , and assumes periodic boundary conditions. In most applications,  $L$  is a large integer as the extension of the system is considered to be huge compared to the microscopic scale which here is  $\mathcal{O}(1)$ . On the finite domain  $D$ , the momenta consist of the discrete set  $k \in 1/L\mathbb{Z}$ . The momentum space representations of  $\alpha$  and  $\gamma$  are given by

$$\hat{\gamma}_k(t) = \frac{1}{L2\pi} \int_0^{L2\pi} \gamma(t, x) e^{ikx} dx, \quad (\text{D.9})$$

$$\hat{\alpha}_k(t) = \frac{1}{L2\pi} \int_0^{L2\pi} \alpha(t, x) e^{ikx} dx. \quad (\text{D.10})$$

In terms of these representations, the BCS equations read

$$i\dot{\Gamma}_k(t) = [H_{\Gamma_k(t)}, \Gamma_k(t)], \quad k \in \frac{1}{L}\mathbb{Z}, \quad (\text{D.11})$$

where the convolution appearing in the Hamiltonian is now to be understood as

$$\left( \hat{V} * \hat{\alpha} \right)_k(t) = \sum_{j \in \mathbb{Z}} \hat{V}_{k-j} \hat{\alpha}_j(t). \quad (\text{D.12})$$

The first step towards a numerical solution is to introduce a finite basis. This process is called *space discretization*.

### D.3. Space Discretization

As the BCS equations are given in their momentum space representation anyway, it is most convenient to use the so-called *Fourier collocation*. This means that for a fixed number  $K \in \mathbb{N}$ , a  $L2\pi$ -periodic function  $f(x) = \sum_{k \in \mathbb{Z}} \hat{f}(k) e^{ik/Lx}$  is approximated by

$$f^K(x) = \sum_{k=-\frac{K}{2}}^{\frac{K}{2}-1} \hat{f}_k^K e^{i\frac{k}{L}x}, \quad (\text{D.13})$$

where the coefficients  $\hat{f}_k^K$  are obtained by the discrete Fourier transform of the values  $f_j = f(L2\pi/K \cdot j)$ ,  $j = -K/2, \dots, K/2 - 1$ . From numerical analysis, cf. (Lubich, 2008, Chapter III.1), it is known that for an  $s$ -times differentiable function  $f$ , the bound

$$\|f(x) - f^K(x)\| \leq CK^{-s} \left\| \frac{d^s f}{dx^s} \right\| \quad (\text{D.14})$$

holds for some constant  $C$  independent of the number of basis functions  $K$ .

Mathematically speaking, we work on the subspace spanned by the first  $K$  eigenfunctions of the Laplacian on  $[0, L2\pi]$ . The approximation of the particle density on this subspace is given by

$$\gamma^K(t, x) = \sum_{k=-\frac{K}{2}}^{\frac{K}{2}-1} \hat{\gamma}_k^K(t) e^{i\frac{k}{L}x} \quad (\text{D.15})$$

and the approximation of the Cooper pair density reads

$$\alpha^K(t, x) = \sum_{k=-\frac{K}{2}}^{\frac{K}{2}-1} \hat{\alpha}_k^K(t) e^{i\frac{k}{L}x}. \quad (\text{D.16})$$

Inserting these approximations into the infinite dimensional BCS equations (D.11) yields a finite dimensional system of ordinary differential equations (ODEs).

#### D.3.1. System of ordinary differential equations

The system of ordinary differential equations we end up with after applying the Fourier collocation is given by

$$i\dot{\gamma}_k(t) = 2 \left[ \alpha_k(t) \overline{(\hat{V} * \alpha)_k} - \overline{\alpha_k(t)} (\hat{V} * \alpha)_k \right], \quad (\text{D.17})$$

$$i\dot{\alpha}_k(t) = 2 \left( \frac{k^2}{L^2} - \mu \right) \alpha_k(t) - 2(2\gamma_k(t) - 1) (\hat{V} * \alpha)_k, \quad (\text{D.18})$$

$$-\frac{K}{2} \leq k \leq \frac{K}{2} - 1,$$

where, for the sake of readability, we have replaced  $\hat{\gamma}^K$  and  $\hat{\alpha}^K$  by  $\gamma$  and  $\alpha$ , respectively.

---

### D.3.2. System for a contact interaction

For a contact interaction  $V(x) = -a\delta(x)$ ,  $a > 0$ , which is the most popular interaction model in physics, we have

$$\hat{V}(k) = -\frac{a}{2L\pi}, \quad -\frac{K}{2} \leq k \leq \frac{K}{2} - 1. \quad (\text{D.19})$$

Hence, the convolution term in the self-consistent Hamiltonian on the  $K$  dimensional subspace is given by

$$\left(\hat{V} * \hat{\alpha}\right)_k(t) = -\frac{a}{2L\pi} \sum_{j=-\frac{K}{2}}^{\frac{K}{2}-1} \hat{\alpha}_j(t). \quad (\text{D.20})$$

With this relation, the equations of motion become

$$i\dot{\gamma}_k(t) = -\frac{a}{L\pi} \left( \alpha_k(t) \sum_{j=-K/2}^{K/2-1} \alpha_j(t) - \overline{\alpha_k(t)} \sum_{j=-K/2}^{K/2-1} \alpha_j(t) \right), \quad (\text{D.21})$$

$$i\dot{\alpha}_k(t) = 2 \left( \frac{k^2}{L^2} - \mu \right) \alpha_k(t) + \frac{a}{L\pi} \sum_{j=-K/2}^{K/2-1} \alpha_j(t) (2\gamma_k(t) - 1), \quad (\text{D.22})$$

$$-\frac{K}{2} \leq k \leq \frac{K}{2} - 1.$$

With

$$p_k(t) := \text{Re } \alpha_k(t), \quad (\text{D.23})$$

$$q_k(t) := \text{Im } \alpha_k(t), \quad (\text{D.24})$$

we can rewrite the equation of motion for  $\gamma_k(t)$  as

$$\dot{\gamma}_k(t) = \frac{2a}{L\pi} \left( q_k(t) \sum_{j=-K/2}^{K/2-1} p_j(t) - p_k(t) \sum_{j=-K/2}^{K/2-1} q_j(t) \right). \quad (\text{D.25})$$

From this expression we can see very easily that  $\gamma_k(t)$  is a real quantity whenever  $\gamma_t(0)$  is so. As  $\gamma$  represents the physical particle density, which is real by definition, we can safely assume  $\gamma_k(t)$  to be real in the following.

### D.3.3. Constants of motion

For later use we mention that the coupled system (D.17),(D.18) possesses some important constants of motion:

- It can readily be seen that the matrix  $H_{\Gamma(t)}$  in the BCS equations (D.11) is self-adjoint. Together with the commutator structure of the equations of motion (D.11), this implies that the evolution of  $\Gamma(t)$  is unitary. Consequently, its eigenvalues are preserved along the evolution. A little bit of algebra shows that these eigenvalues are given by

$$\lambda_k^\pm = \frac{1}{2} \pm \sqrt{\left(\gamma_k(t) - \frac{1}{2}\right)^2 + |\alpha_k(t)|^2}. \quad (\text{D.26})$$

- The discretized analog of the free energy functional (D.8) in the case of an interaction potential is given by

$$\begin{aligned}
F^K(\gamma(t), \alpha(t)) &:= \sum_{k=-K/2}^{K/2-1} \left( \frac{k^2}{L^2} - \mu \right) \gamma_k(t) + \frac{1}{L2\pi} \int_0^{L2\pi} V(x) |\alpha(t, x)|^2, \\
&+ T \sum_{k=-K/2}^{K/2-1} [\lambda_k^+ \log(\lambda_k^+) + \lambda_k^- \log(\lambda_k^-)],
\end{aligned} \tag{D.27}$$

and can be shown to be preserved, too.

### D.3.4. Numerical notation

From a numerical point of view, the coupled system (D.17),(D.18), when supplemented by some initial data, represents an initial value problem

$$\begin{cases} \frac{d\mathbf{y}(t)}{dt} = f(\mathbf{y}(t)), \\ \mathbf{y}(0) = \mathbf{y}_0, \end{cases} \tag{D.28}$$

with  $\mathbf{y} \in \mathbb{C}^{2K}$ . Formally, the aim of this paper is to find a numerical approximation to the exact flow of such an initial value problem. For this, we denote a time step by  $\tau$  and the flow over such a time, i.e., the smooth map between  $\mathbf{y}(t)$  and  $\mathbf{y}(t + \tau)$ , by  $\Phi_{\tau, f}(\mathbf{y}(t))$ . Its numerical approximation will be denoted by  $\Phi_{\tau, f}^{\text{num}}$ .

Both of the numerical flows we present in this work rely on the fast calculation of the convolutions appearing on the right hand side of the equations of motion (D.17),(D.18). Let us turn towards this now.

## D.4. Calculating the Convolution Terms

We denote by  $\mathcal{F}$  the Fourier transform of a vector of length  $K = 2^N$ ,  $N \in \mathbb{N}$ , and by  $\mathcal{F}^{-1}$  its inverse. With the help of the fast Fourier transform (FFT) algorithms, these operations can be calculated efficiently in  $\mathcal{O}(N \cdot K)$  operations, see, e.g., (Flannery *et al.*, 1992, Chapter 12).

Furthermore, the convolution of two  $K$  dimensional vectors  $a$  and  $b$  can be computed by

$$a * b = \mathcal{F}^{-1}((\mathcal{F}a) \cdot (\mathcal{F}b)), \tag{D.29}$$

with  $\cdot$  denoting pointwise multiplication. Taking this into account, we can efficiently calculate the convolution terms as outlined in Fig. D.1. There, we have defined

$$V_j := V(L2\pi/K \cdot j), \quad j = -K/2, \dots, K/2 - 1. \tag{D.30}$$

The algorithm only takes  $\mathcal{O}(N \cdot K)$  operations. When considering systems with a contact interaction, i.e., when integrating the evolution equations (D.25),(D.22), the convolution terms are just a sum over the entries of the vector  $\alpha$ . Hence, the CPU effort in this case is only  $\mathcal{O}(K)$ .

---



---

**Algorithm 1: calc\_convolution**


---

```

conv = FFT( $\alpha$ )
for  $j = -K/2$  to  $K/2 - 1$  do
  | conv( $j$ ) = conv( $j$ ) ·  $V(j)$ .
|
conv = invFFT(conv)

```

---

Figure D.1: Sketch of the algorithm `calc_convolution`, which uses the FFT and its inverse to efficiently calculate the convolution between  $\hat{\alpha}$  and  $\hat{V}$ .

## D.5. Nonlinear Splitting Integrator

BCSInt, the integrator we present in this Section, is based on the conservation of the eigenvalues of  $\Gamma(t)$ . These eigenvalues being conserved, the following equality holds

$$\left(\gamma_k(t) - \frac{1}{2}\right)^2 + |\alpha_k(t)|^2 = \left(\gamma_k(0) - \frac{1}{2}\right)^2 + |\alpha_k(0)|^2. \quad (\text{D.31})$$

With the help of this relation, we can eliminate  $\gamma_k(t)$  in the equations of motion for  $\alpha_k(t)$  as we show now.

### D.5.1. Decoupled system

Solving Eq. (D.31) for  $\gamma_k$  yields

$$\gamma_k(t) = \frac{1}{2} \pm \sqrt{h(k) - |\alpha_k(t)|^2}, \quad (\text{D.32})$$

with the auxiliary function

$$h(k) := \left(\gamma_k(0) - \frac{1}{2}\right)^2 + |\alpha_k(0)|^2. \quad (\text{D.33})$$

The sign in relation (D.32) can usually be inferred from physical information. In our study (Hainzl and Seyrich, 2016), for example, the initial values had to be such that  $\gamma_k(0)$  was greater than  $1/2$  for  $\mu > k^2/L^2$  and less than or equal to  $1/2$  for  $\mu \leq k^2/L^2$ .

Inserting the just-derived expression (D.32) for  $\gamma_k(t)$  into the equations of motion for  $\alpha_k(t)$ , we get the nonlinear system

$$i\dot{\alpha}_k(t) = 2 \left(\frac{k^2}{L^2} - \mu\right) \alpha_k(t) \pm \frac{a}{L\pi} \sqrt{h(k) - |\alpha_k(t)|^2} \sum_{j=-K/2}^{K/2-1} \alpha_t(j), \quad (\text{D.34})$$

$$-\frac{K}{2} \leq k \leq \frac{K}{2} - 1.$$

Having decoupled the system, we can now turn towards its time evolution.

### D.5.2. BCSInt

The nonlinear system (D.34), together with some suitable initial data, gives an initial value problem

$$\begin{cases} i \frac{d\vec{\alpha}(t)}{dt} &= \tilde{f}(\vec{\alpha}(t)), \\ \vec{\alpha}(0) &= \vec{\alpha}_0, \end{cases} \quad (\text{D.35})$$

for

$$\vec{\alpha} = (\alpha_{-K/2}(t) \quad \dots \quad \alpha_{K/2-1}(t))^T \in \mathbb{C}^K. \quad (\text{D.36})$$

The right hand side of the differential equation can be written as the sum of two terms,

$$\tilde{f}(\vec{\alpha}) = A\vec{\alpha} + f_1(\vec{\alpha}), \quad (\text{D.37})$$

where  $f_1$  represents the nonlinear term and where  $A$  is the matrix

$$A = \text{diag} \left( 2 \left( \frac{(-K/2)^2}{L^2} - \mu \right), \dots, 2 \left( \frac{(K/2-1)^2}{L^2} - \mu \right) \right). \quad (\text{D.38})$$

This linear part resembles the kinetic part of the linear Schrödinger equation. Its flow  $\Phi_{\tau,A}$  can be calculated exactly as

$$\Phi_{\tau,A}(\vec{\alpha}) = \text{diag} \left( e^{-i2 \left( \frac{(-K)^2}{4L^2} - \mu \right) \tau}, \dots, e^{-i2 \left( \frac{(K-2)^2}{4L^2} - \mu \right) \tau} \right) \vec{\alpha}. \quad (\text{D.39})$$

With regard to  $f_1$ , it has a much smaller Lipschitz constant than the complete right hand side  $f$ , wherefore  $\Phi_{\tau,f_1}$  can be approximated by some standard integration scheme. We then follow the idea of Strang (1968) and set

$$\Phi_{\tau,\tilde{f}}^{\text{num}}(\vec{\alpha}(0)) = (\Phi_{\tau/2,A} \circ \Phi_{\tau,f_1}^{\text{num}} \circ \Phi_{\tau/2,A})(\vec{\alpha}(0)). \quad (\text{D.40})$$

Applying this operation successively yields an approximation to the exact solution at times  $t = n\tau$ ,  $n = 1, 2, \dots$ . Its error decreases quadratically as a function of the step size  $\tau$  as long as  $\Phi_{\tau,f_1}^{\text{num}}$  is a second-or-higher order approximation to  $\Phi_{\tau,f_1}$ , see, e.g. (Hairer *et al.*, 2006, Chapter II.5).

Just as every exact flow,  $\Phi_{\tau,A}$  satisfies

$$\Phi_{t,A} \circ \Phi_{s,A} = \Phi_{t+s,A}. \quad (\text{D.41})$$

Hence, when applying many time steps of the numerical scheme in a row, one can combine the last sub-step of the previous step with the first sub-step of the next step, thus saving computational costs. We illustrate the resulting procedure in Fig. D.2.

Concerning  $\Phi_{\tau,f_1}^{\text{num}}$ , in the study Hainzl and Seyrich (2016) it has been calculated via the fifth order explicit Cash–Karp Runge–Kutta scheme proposed by Flannery *et al.* (1992). In the experiment Section D.7 below, we will also test the second order explicit midpoint rule. In this case,  $\Phi_{\tau,f_1}^{\text{num}}$  is calculated as outlined in Fig. D.3.

---



---

**Algorithm 2: BCSInt**


---

```

 $\vec{\alpha} = \Phi_{\tau/2,A}(\vec{\alpha}_0)$ 
for  $n = 0$  to  $N$  do
   $\vec{\alpha} = \Phi_{\tau,f_1}^{\text{num}}(\vec{\alpha})$ .
   $\vec{\alpha} = \Phi_{\tau,A}(\vec{\alpha})$ .
 $\vec{\alpha} = \Phi_{-\tau/2,A}(\vec{\alpha})$ 

```

---

Figure D.2: Sketch of our algorithm BCSInt which for a given initial value  $\vec{\alpha}_0$  and a given step size  $\tau$  approximates  $\vec{\alpha}(N\tau) = \Phi_{N\tau,\vec{f}}(\vec{\alpha}_0)$ .

---

**Algorithm 3: calc $\Phi_{f_1}$** 


---

```

 $\dot{Y} = \text{calc}_{f_1}(\vec{\alpha})$ 
for  $k = -K/2$  to  $K/2 - 1$  do
   $Y(k) = \alpha_k(t) + \tau/2 \dot{Y}(k)$ 
 $\dot{Y} = \text{calc}_{f_1}(Y)$ 
for  $k = -K/2$  to  $K/2 - 1$  do
   $\alpha_k(t) = \alpha_k(t) + \tau \dot{Y}(k)$ 

```

---



---

**Algorithm 4: calc $f_1$** 


---

```

 $c = \text{calc\_convolution}(V, \alpha)$ 
for  $k = -K/2$  to  $K/2 - 1$  do
   $d = \sqrt{h(k) - |\alpha_k(t)|^2}$ 
   $f_1(k) = -ic \cdot d$ 

```

---

Figure D.3: The left panel shows the algorithm which for a given value  $\vec{\alpha}(n\tau)$  and a given time step  $\tau$  calculates  $\vec{\alpha}((n+1)\tau) = \Phi_{\tau,f_1}^{\text{num}}(\vec{\alpha}(n\tau))$  with the explicit midpoint rule. The right panel shows the algorithm which for a given value  $\vec{\alpha}$  calculates  $f_1(\vec{\alpha})$ .

### D.5.3. Number of operations

In order to analyze BCSInt's efficiency, we count the number of real operations which are executed per call of our implementations, which, to the best of our knowledge, have been implemented in the most efficient way possible. We do not weight the costs of different operations, i.e., the square root in  $\text{calc}_{f_1}$ , cf. Fig. D.3, also counts as a single operation. The number of operations as a function of the number of basis functions  $K$  for the various sub-algorithms and BCSInt as a whole are listed in Tab. D.1. We mention that, if we substitute the fifth order Cash–Karp scheme for the explicit midpoint rule in  $\text{calc}\Phi_{f_1}$ , the number of operations for  $\text{calc}\Phi_{f_1}$  will increase slightly to  $6 \times \text{calc\_convolution} + 38K$ .

Algorithm	#Operations per call
Calculation of $\Phi_{\tau,A}$	$14 \cdot K + 14$
Calc $f_1$	$1 \times \text{calc\_convolution} + 12 \cdot K + 20$
calc $\Phi_{f_1}$	$2 \times \text{calc}_{f_1} + 8 \cdot K + 9 = 2 \times \text{calc\_convolution} + 32 \cdot K + 49$
BCSInt	$2 \times \text{calc\_convolution} + 46 \cdot K + 63$
BCSInt for contact interaction	$58 \cdot K + 63$

Table D.1: The required number of operations per step as a function of the dimension of the ODE system (D.34) for the sub-algorithms of BCSInt and for BCSInt itself.

Let us now introduce our second integration scheme.

## D.6. Triple Splitting Integrator

For our second scheme, we consider the coupled system (D.17),(D.18) as a whole. From a numerical perspective, we have an initial value problem for

$$\mathbf{y}(t) = \begin{pmatrix} \vec{\gamma}(t) \\ \vec{\alpha}(t) \end{pmatrix} \in \mathbb{C}^{2K}, \quad (\text{D.42})$$

$$\vec{\gamma}(t) = (\gamma_{-K/2}(t) \ \dots \ \gamma_{K/2-1}(t))^T \in \mathbb{R}^K, \quad (\text{D.43})$$

$$\vec{\alpha}(t) = (\alpha_{-K/2}(t) \ \dots \ \alpha_{K/2-1}(t))^T \in \mathbb{C}^K, \quad (\text{D.44})$$

$$(\text{D.45})$$

whose right hand side  $f(\mathbf{y})$  can be split into three parts,

$$f(\vec{\gamma}, \vec{\alpha}) = \tilde{A}\mathbf{y} + g(\vec{\alpha}) + h(\vec{\gamma}, \vec{\alpha}). \quad (\text{D.46})$$

Here,  $\tilde{A}\mathbf{y}$  is the first term of the equation of motion (D.18) for  $\alpha$ , i.e.,

$$\tilde{A} \begin{pmatrix} \vec{\gamma} \\ \vec{\alpha} \end{pmatrix} = \begin{pmatrix} \vec{\gamma} \\ A\vec{\alpha} \end{pmatrix}, \quad (\text{D.47})$$

which means that it represents the same action on  $\alpha$  as  $A$  in the nonlinear case above. The function  $g(\vec{\alpha})$  represents the right hand side of the evolution equation for  $\gamma$  and  $h(\vec{\gamma}, \vec{\alpha})$  is the second term of Eq. (D.18).

We will now show that we can efficiently calculate the flows for all three subproblems. The calculation of  $\Phi_{\tau, \tilde{A}}$  is nothing other than  $\Phi_{\tau, A}$  acting on  $\vec{\alpha}$  with  $\vec{\gamma}$  held constant. We thus, in fact, only have to consider the other two subproblems.

### D.6.1. Calculating $\Phi_{\tau, g}$

For the subsystem

$$\begin{cases} \frac{d\vec{\gamma}(t)}{dt} = g(\vec{\alpha}(t)), \\ \vec{\gamma}(0) = \vec{\gamma}_0, \end{cases} \quad (\text{D.48})$$

the right hand side does not depend on the quantity to be evolved. Therefore, the solution of the initial value problem (D.48) at time  $t$  is trivially given by

$$\vec{\gamma}(t) = \Phi_{t, g}(\vec{\gamma}(0)) = \vec{\gamma}(0) + t \cdot g(\vec{\alpha}(0)). \quad (\text{D.49})$$

Bearing in mind the reformulation (D.25), we calculate a step of  $\Phi_{\tau, g}$  with the algorithm illustrated in Fig. D.4. Please note that in the case  $V(x) = -a\delta(x)$ , the convolution is replaced by the sum (D.20). Hence,  $\Phi_{\tau, g}$  can even be calculated in  $\mathcal{O}(K)$  operations.

---



---

**Algorithm 5:** calc $\Phi_g$ 


---

```

c = calc_convolution(V,  $\vec{\alpha}$ )
for k = -K/2 to K/2 - 1 do
   $\gamma_k(t) = \gamma_k(0) + 2\tau \cdot (\text{Im}(\alpha_k) \cdot \text{Re}(c) - \text{Re}(\alpha_k) \cdot \text{Im}(c))$ 

```

---

Figure D.4: Sketch of the algorithm which for given values  $\vec{\gamma}(0)$ ,  $\vec{\alpha}(0)$  and a given step size  $\tau$  calculates the solution  $\vec{\gamma}(\tau) = \Phi_{\tau,g}(\vec{\gamma}(0))$  to the initial value problem (D.48).

### D.6.2. Calculating $\Phi_{\tau,h}$

We consider the subproblem

$$\begin{cases} i \frac{d\vec{\alpha}(t)}{dt} = h(\vec{\gamma}(0), \vec{\alpha}(t)), \\ \vec{\alpha}(0) = \vec{\alpha}_0. \end{cases} \quad (\text{D.50})$$

The linear right hand side's Lipschitz constant is small. This gives us two possibilities to swiftly calculate the flow  $\Phi_{\tau,h}$ . The first option is to use the Lanczos method described in (Lubich, 2008, Chapter II.2.2) with some iterations. According to the analysis of Hochbruck and Lubich (1997), this yields an approximation with vanishingly small error. The more convenient and still faster option is the use of an explicit standard integration scheme such as the explicit midpoint rule or the classical Runge–Kutta scheme. Thanks to the favorable properties of the subproblem, the resulting numerical error is much smaller than the already small splitting error. In our tests, the schemes with this faster implementation were as accurate as the ones using the Lanczos method. We outline the algorithm for the example of the explicit midpoint rule in Fig. D.5.

---

**Algorithm 6:** calc $\Phi_h$ 


---

```

 $\dot{\mathbf{Y}} = \text{calc}_h(\vec{\alpha})$ 
for k = -K/2 to K/2 - 1 do
   $Y(k) = \alpha_k(t) + \tau/2 \dot{Y}(k)$ 
 $\dot{\mathbf{Y}} = \text{calc}_h(\mathbf{Y})$ 
for k = -K/2 to K/2 - 1 do
   $\alpha_k(t) = \alpha_k(t) + \tau \dot{Y}(k)$ 

```

---



---

**Algorithm 7:** calc $_h$ 


---

```

c = calc_convolution(V,  $\vec{\alpha}$ )
for k = -K/2 to K/2 - 1 do
   $d = 2 \cdot \gamma_k - 1$ 
   $h(k) = -ic \cdot d$ 

```

---

Figure D.5: The left panel shows the algorithm which for a given value  $\vec{\alpha}(n\tau)$  and a given time step  $\tau$  calculates  $\vec{\alpha}((n+1)\tau) = \Phi_{\tau,h}^{\text{num}}(\vec{\alpha}(n\tau))$  with the explicit midpoint rule. The right panel shows the algorithm which for a given value  $\vec{\alpha}$  calculates  $h(\vec{\gamma}, \vec{\alpha})$ .

The most appealing fact about our triple splitting is that in the case of a contact interaction, the subproblem (D.50) can be solved exactly in  $\mathcal{O}(K)$  operations as we show now.

Introducing  $\vec{b} \in \mathbb{R}^K$  via

$$b_k = \frac{a}{L\pi} (2\gamma_k(0) - 1), \quad (\text{D.51})$$

and the  $K \times K$ -matrix

$$B = \underbrace{\begin{pmatrix} b_{-K/2} & \cdots & b_{-K/2} \\ \vdots & \ddots & \vdots \\ b_{K/2-1} & \cdots & b_{K/2-1} \end{pmatrix}}_K, \quad (\text{D.52})$$

we can write

$$h(\vec{\gamma}(0), \vec{\alpha}(t)) = B\vec{\alpha}(t). \quad (\text{D.53})$$

Hence, the solution to the initial value problem (D.50) is given by

$$\vec{\alpha}(\tau) = \Phi_{\tau,h}(\vec{\alpha}(0)) = e^{-iB\tau}\vec{\alpha}(0) =: e^{\tilde{B}}\vec{\alpha}(0). \quad (\text{D.54})$$

We now show that for a given  $\vec{\alpha}(0)$ ,  $\vec{\alpha}(\tau)$  can be calculated in  $\mathcal{O}(K)$  operations.

For a given  $n \in \mathbb{N}$ , we have

$$\tilde{B}^n = \underbrace{\begin{pmatrix} -ib_{-K/2}\tau c^{n-1} & \cdots & -ib_{-K/2}\tau c^{n-1} \\ \vdots & \ddots & \vdots \\ -ib_{K/2-1}\tau c^{n-1} & \cdots & -ib_{K/2-1}\tau c^{n-1} \end{pmatrix}}_K, \quad (\text{D.55})$$

with

$$c = -i\tau \sum_{j=-\frac{K}{2}}^{\frac{K}{2}-1} b_j. \quad (\text{D.56})$$

Consequently, with Id denoting the  $K \times K$  identity matrix, we have

$$\exp(-i\tau B) = \text{Id} + \sum_{n=1}^{\infty} \frac{1}{n!} \begin{pmatrix} -ib_{-K/2}\tau c^{n-1} & \cdots & -ib_{-K/2}\tau c^{n-1} \\ \vdots & \ddots & \vdots \\ -ib_{K/2-1}\tau c^{n-1} & \cdots & -ib_{K/2-1}\tau c^{n-1} \end{pmatrix} \quad (\text{D.57})$$

$$= \text{Id} + \frac{1}{c} \begin{pmatrix} -ib_{-K/2}\tau(\exp(c) - 1) & \cdots & -ib_{-K/2}\tau(\exp(c) - 1) \\ \vdots & \ddots & \vdots \\ -ib_{K/2-1}\tau(\exp(c) - 1) & \cdots & -ib_{K/2-1}\tau(\exp(c) - 1) \end{pmatrix}. \quad (\text{D.58})$$

With this, the matrix-vector multiplication in Eq. (D.54) yields

$$\exp(-i\tau B)\vec{\alpha}(0) = \vec{\alpha}(0) - \frac{i\tau}{c} \begin{pmatrix} b_{-K/2}(\exp(c) - 1) \sum_{j=-\frac{K}{2}}^{\frac{K}{2}-1} \alpha_j(0) \\ \vdots \\ b_{K/2-1}(\exp(c) - 1) \sum_{j=-\frac{K}{2}}^{\frac{K}{2}-1} \alpha_j(0) \end{pmatrix}. \quad (\text{D.59})$$

Thus, the solution of the initial value problem (D.50) can efficiently be calculated by the algorithm illustrated in Fig. D.6.

Having found efficient algorithms for all three subproblems we have split the system into, we can now recompose them.

---



---

**Algorithm 8:** calc $\Phi_h$ 


---

```

 $c = -i\tau \sum_{k=-\frac{K}{2}}^{\frac{K}{2}-1} b_k$ 
 $s = \sum_{k=-\frac{K}{2}}^{\frac{K}{2}-1} \alpha_k(0)$ 
 $e = \exp(c) - 1$ 
for  $k = -K/2$  to  $K/2 - 1$  do
  |  $\alpha_k(t) = \alpha_k(0) - i\tau \cdot e \cdot s \cdot b_k / c$ 
  |

```

---

Figure D.6: Sketch of the algorithm which for given values  $\vec{\gamma}(0)$ ,  $\vec{\alpha}(0)$  and a given step size  $\tau$  calculates the solution  $\vec{\alpha}(\tau) = \Phi_{\tau,h}(\vec{\alpha}(0))$  to the initial value problem (D.50) for the case of a contact interaction.

### D.6.3. SplitBCS

As all the three flows  $\Phi_{\tau,A}$ ,  $\Phi_{\tau,g}$ , and  $\Phi_{\tau,h}$  are at least of second order, each symmetric composition of them gives rise to a second order integration scheme, see, e.g. (Hairer *et al.*, 2006, Chapter II.5). We propose the composition

$$\Phi_{\tau,f}^{\text{num}} = \Phi_{\tau,AghgA} := \Phi_{\tau/2,A} \circ \Phi_{\tau/2,g} \circ \Phi_{\tau,h} \circ \Phi_{\tau/2,g} \circ \Phi_{\tau/2,A}, \quad (\text{D.60})$$

as this yields the fastest and most accurate scheme among the possible combinations as we will see in the next Section. If even more accuracy were required, we could use a suitable composition of the scheme (D.60); see (Suzuki, 1990; Yoshida, 1990) for more information on compositions.

In the same way as for the algorithm of Section D.5, the last sub-step of each step can be combined with the first sub-step of the following step which reduces the CPU effort. Even more computational costs can be saved by paying heed to the following points.

- From Eq. (D.25) it can be deduced that

$$\frac{d}{dt} \left( \sum_{j=-\frac{K}{2}}^{\frac{K}{2}-1} \gamma_k(t) \right) = 0. \quad (\text{D.61})$$

Thus, the sum over all  $\gamma_k(t)$ , and, as a consequence, also the quantities  $c$  and  $e$  appearing in the calculation of  $\Phi_{\tau,h}$ , cf. Fig. D.6, are preserved along evolutions of the equations of motion. Hence,  $c$  and  $e$  only need to be calculated once at the start of the simulation when considering a contact interaction.

- Both  $\Phi_{\tau,g}$  and  $\Phi_{\tau,h}$  require the computation of the convolution, cf. Figs. D.4 and D.6. However,  $\Phi_{\tau,g}$  does not modify  $\vec{\alpha}$  which means that the convolution in the first call of calc\_h is the same as the one already calculated in calc $\Phi_g$ . Hence, by suitably combining the calculation of

$$\Phi_{\tau,ghg} := \Phi_{\tau/2,g} \circ \Phi_{\tau,h} \circ \Phi_{\tau/2,g} \quad (\text{D.62})$$

into one algorithm, one can avoid redundancies.

- The calculation of  $\Phi_{\tau,A}$  can be made more efficient for both BCSInt and SplitBCS when a fixed step size is used. In this case, during each call of  $\Phi_{\tau,A}$ ,  $\cos$  and  $\sin$  of  $2(k^2/L^2 - \mu)\tau$ ,  $k = K/2, \dots, K/2 - 1$ , have to be calculated. But, if storage is not a problem, one only has to calculate the  $\cos$  and  $\sin$  once at the beginning of the simulation as the arguments are the same in each step. This is what we did in our implementations. Accordingly, the number of operations specified in Tabs. D.1 and D.2 refer to this efficient version. Please note that this point, together with the first point, means that the time steps for a system with a contact interaction can be calculated without having to call any mathematical function but only require basic computational operations.

Putting everything together, we obtain our integrator SplitBCS as outlined in Fig. D.7.

---

**Algorithm 9: SplitBCS**


---

```

 $\vec{\alpha} = \Phi_{\tau/2,A}(\vec{\alpha}(0))$ 
for  $n = 0$  to  $N$  do
   $(\vec{\gamma}, \vec{\alpha}) = \Phi_{\tau,ghg}(\vec{\gamma}, \vec{\alpha})$ .
   $\vec{\alpha} = \Phi_{\tau,A}(\vec{\alpha})$ .
 $\vec{\alpha} = \Phi_{-\tau/2,A}(\vec{\alpha})$ 

```

---

Figure D.7: Sketch of our algorithm SplitBCS which for given initial values  $\vec{\gamma}(0)$ ,  $\vec{\alpha}(0)$  and a given step size  $\tau$  approximates  $(\vec{\gamma}(N\tau), \vec{\alpha}(N\tau))^T = \Phi_{N\tau,f}(\vec{\gamma}(0), \vec{\alpha}(0))$ .

#### D.6.4. Number of operations

In order to compare the efficiency of SplitBCS to the one of BCSInt, we count the number of operations required for the respective sub-algorithms and for SplitBCS as a whole, too. The result can be found in Tab. D.2. If the explicit midpoint rule is replaced by the Cash–Karp scheme, the number of operations in the calculation of  $\Phi_{\tau,h}$  will increase just as for BCSInt. We see that SplitBCS calculates one convolution more than BCSInt. Thus, BCSInt is expected

Algorithm	#Operations per call
Calculation of $\Phi_{\tau,A}$	$14 \cdot K + 14$
Calc_h	$1 \times \text{calc\_convolution} + 7 \cdot K + 12$
calc $\Phi_{f_1}$	$2 \times \text{calc\_h} + 8 \cdot K + 9 = 2 \times \text{calc\_convolution} + 22 \cdot K + 33$
calc $\Phi_g$	$1 \times \text{calc\_convolution} + 6 \cdot K + 12$
Calculation of $\Phi_{\tau,ghg}$ for contact interaction	$18 \cdot K + 39$
SplitBCS	$3 \times \text{calc\_convolution} + 34 \cdot K + 53$
SplitBCS for contact interaction	$32 \cdot K + 53$

Table D.2: The required number of operations per step as a function of the dimension of the ODE system (D.17),(D.18) for the sub-algorithms of SplitBCS and for SplitBCS itself.

to be faster for general settings with a huge number of basis functions. For the important case of a contact interaction, however, we are able to calculate  $\Phi_{\tau,ghg}$  very efficiently. This is why we choose the composition (D.60) over other possible sequences of the subflows. With this, SplitBCS is even faster than BCSInt in the physically important setting.

---

Let us now subject the schemes to numerical tests.

## D.7. Numerical Experiments

All the numerical experiments presented here were run on a Core 2 Duo E6600 machine with 2.4GHz and 4GB RAM. In order to have physically realistic data to start our experiments with, we chose a system which is slightly superconducting. Such a system can be obtained by setting

$$\hat{\gamma}_k(0) = \frac{1}{2} - \frac{k^2/L^2 - \mu}{2} \frac{\tanh\left(\frac{\sqrt{(k^2/L^2 - \mu)^2 + h^2}}{2T}\right)}{\sqrt{(k^2/L^2 - \mu)^2 + h^2}} \quad (\text{D.63})$$

$$\hat{\alpha}_k(0) = \frac{h}{2} \frac{\tanh\left(\frac{\sqrt{(k^2/L^2 - \mu)^2 + h^2}}{2T}\right)}{\sqrt{(k^2/L^2 - \mu)^2 + h^2}}, \quad (\text{D.64})$$

where  $h = 0.1$  is a small parameter, see, e.g., (Hainzl and Seyrich, 2016). The critical temperature  $T$  of the system depends on the chemical potential  $\mu$  and on the interaction potential  $V$ . In the simulations presented here, we considered a system with a contact interaction  $V(x) = -a\delta(x)$ . In this case,  $T$  can be calculated from the implicit formula, cf. (Hainzl and Seyrich, 2016),

$$\frac{2\pi}{a} = \int_{\mathbb{R}} \frac{\tanh\left(\frac{p^2 - \mu}{2T}\right)}{p^2 - \mu} dp. \quad (\text{D.65})$$

For our simulations, we chose  $a = \mu = 1$  which yields  $T = 0.19$ .

As a measure of an integrator's accuracy, we used the discrete energy (D.27) which is conserved along the exact solution of the ODE system (D.17),(D.18). Thus, the reliability of a numerical integration scheme can be checked by tracking the relative error  $\Delta F^K$ , defined by

$$\Delta F^K(t) = \left| \frac{F^K(\vec{\gamma}(t), \vec{\alpha}(t)) - F^K(\vec{\gamma}(0), \vec{\alpha}(0))}{F^K(\vec{\gamma}(0), \vec{\alpha}(0))} \right|, \quad (\text{D.66})$$

along the numerical evolution.

We first used this tool to compare SplitBCS to BCSInt with  $\Phi_{\tau, f_1}$  calculated via the fifth order Cash–Karp method. For this, we fixed  $L = 32$ ,  $K = 256 \cdot L$  and chose a step size  $\tau = 0.1/K$ . We evolved the system until  $t = \mathcal{O}(L)$  with both integrators and plotted the relative error in the energy,  $\Delta F^K$ , against integration time  $t$  in the left panel of Fig. D.8. We repeated the procedure for  $L = 64$  and plotted the result in the right panel of Fig. D.8. Although the error increases slightly at the end of the integration for BCSInt, both schemes seem to be very accurate. When comparing BCSInt with  $\Phi_{\tau, f_1}$  calculated via the fifth-order Cash–Karp method to BCSInt where  $\Phi_{\tau, f_1}$  was calculated with the explicit midpoint rule, we found no differences in the relative error of the energy. Hence, we recommend the use of the latter method as it is much faster.

Other physically relevant constants of motion are the eigenvalues  $\lambda_k$  of the particle density matrix  $\Gamma$ . BCSInt preserves them by construction. In order to check their behavior when using

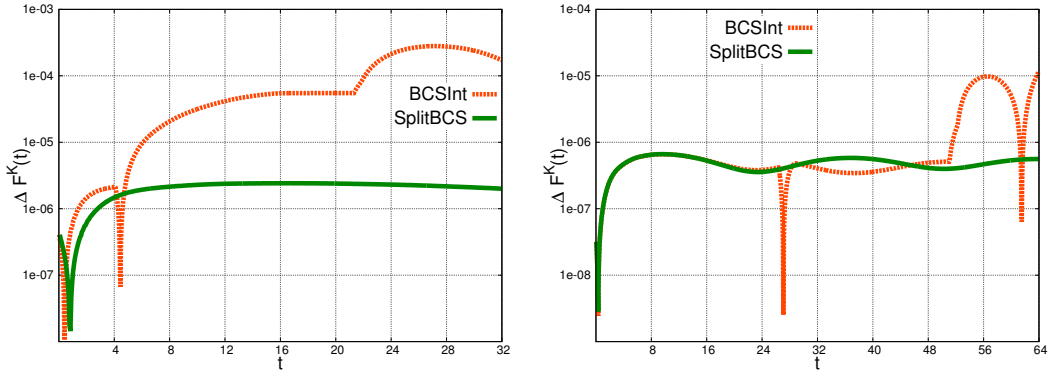


Figure D.8: The relative error  $\Delta F^K$  of the free energy as a function of integration time  $t$  for SplitBCS and BCSInt in semilogarithmic scale. The left panel shows the result for  $L = 32$ , the right panel depicts the corresponding result for  $L = 64$ .

SplitBCS, we also tracked the eigenvalues together with their corresponding relative error,

$$\Delta \lambda_k(t) = \left| \frac{\lambda_k(t) - \lambda_k(0)}{\lambda_k(0)} \right|, \quad (\text{D.67})$$

along the evolution. We found out that, up to very small rounding errors, all eigenvalues were preserved for SplitBCS, too. As an illustration, we plot some eigenvalues and the relative error of  $\lambda_0$  in Fig. D.9.

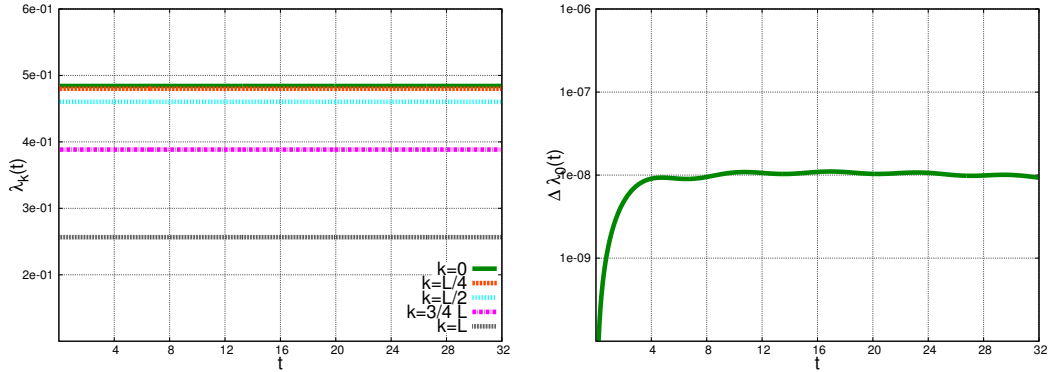


Figure D.9: The left panel shows some eigenvalues  $\lambda_k$  of the density matrix as a function of integration time  $t$  for SplitBCS applied to the system with  $L = 32$ . The right panel shows the corresponding relative error  $\Delta \lambda_0$  of the density matrix' first eigenvalue in semilogarithmic scale.

With regard to SplitBCS, the question remains as to whether we could have done even better by choosing another sequence of the sub-flows than composition (D.60). In order to go into this matter, we also evolved the systems for  $L = 32$  and  $L = 64$  for various other compositions of the sub-flows  $\Phi_{\tau,A}$ ,  $\Phi_{\tau,g}$  and  $\Phi_{\tau,h}$ , and again plotted  $\Delta F^K$  as a function of the integration time  $t$ . The resulting plots are shown in Fig. D.10. We also tested the other possible sequences which are not shown in the plots. However, we found out that the relative error in the energy

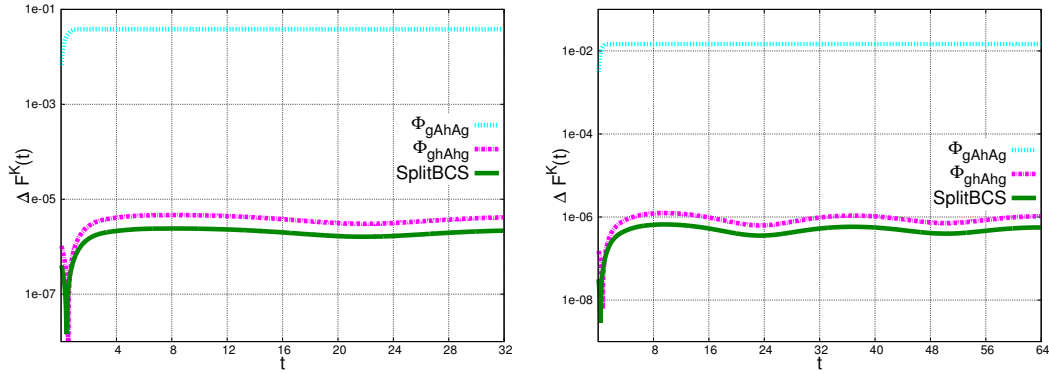


Figure D.10: The relative error  $\Delta F^K$  of the free energy as a function of integration time  $t$  for SplitBCS and other possible compositions in semilogarithmic scale. The left panel shows the result for  $L = 32$ , the right panel depicts the corresponding result for  $L = 64$ .

seems only to depend on the spot of  $\Phi_{\tau,A}$  in the composition. This means that  $\Phi_{\tau,AhghA}$  is as accurate as SplitBCS. But we could not find an equally efficient implementation for  $\Phi_{\tau,hgh}$  as the one for  $\Phi_{\tau,ghg}$ . This is why we strongly recommend the use of the composition (D.60), shortly SplitBCS, in simulations of the discrete BCS equations with a contact interaction.

In order to show, as a last point, why standard integration schemes are of no use for the discrete BCS equations, we apply the popular fifth order Cash–Karp scheme of Flannery *et al.* (1992) to the equations with the same  $L$  and the same step size as for the splitting methods. When plotting the resulting  $\Delta F^K$ , cf. Fig D.11, we observe an exponential growth in the error. This is in accordance with theoretical expectations, see, e.g. (Hairer *et al.*, 1993).

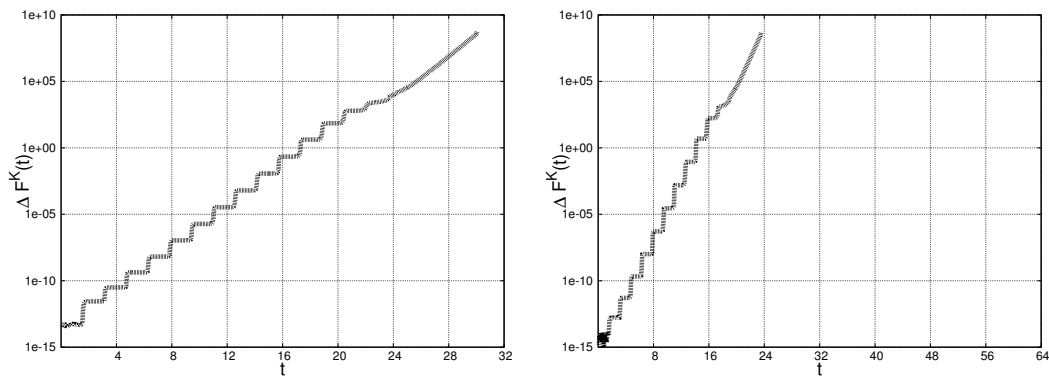


Figure D.11: The relative error  $\Delta F^K$  of the free energy as a function of integration time  $t$  for the explicit Cash–Karp scheme in semilogarithmic scale. The left panel shows the result for  $L = 32$ , the right panel depicts the corresponding result for  $L = 64$ .

Let us now summarize our results.

## D.8. Conclusion

In this work, we have presented two fast and accurate evolution schemes, BCSInt and SplitBCS, for the coupled discrete BCS equations which arise from a Fourier space discretization of the BCS equations for superconducting materials. BCSInt uses the preservation of the density matrix' eigenvalues to decouple the system and a subsequent splitting of the decoupled system into two terms. SplitBCS is based on a splitting of the coupled equations into three subproblems which for the important case of a contact interaction can all be solved exactly by employing basic operations only. Crucially, the CPU effort for these exact solutions grows only linearly in the dimension of the spatial discretization. Further computational costs could be saved by aptly recombining the flows of the subproblems. In numerical tests, the schemes have been shown to be very accurate. Additionally, they preserve the discrete analog of the physical energy and the eigenvalues of the particle density matrix up to very small errors. We have, thus, come up with very useful tools for simulations in the field of superconductivity.

## Acknowledgements

I would like to thank Ch. Hainzl and Ch. Lubich for useful discussions and suggestions. This work was partially funded by the DFG grant GRK 1838.

---

---

## References

- Abbott, B., R. Abbott, T. Abbott, M. Abernathy, F. Acernese, K. Ackley, C. Adams, T. Adams, P. Addesso, R. Adhikari, et al. 2016.  
Observation of gravitational waves from a binary black hole merger.  
*Physical review letters* 116(6), 061102.
- Abrahams, E., and T. Tsuneto 1966.  
Time variation of the ginzburg-landau order parameter.  
*Physical Review* 152(1), 416.
- Abramovici, A., W. E. Althouse, R. W. Drever, Y. Gürsel, S. Kawamura, F. J. Raab, D. Shoemaker, L. Sievers, R. E. Spero, K. S. Thorne, et al. 1992.  
Ligo: The laser interferometer gravitational-wave observatory.  
*Science* 256(5055), 325–333.
- Amaro-Seoane, P., J. R. Gair, A. Pound, S. A. Hughes, and C. F. Sopuerta 2015.  
Research update on extreme-mass-ratio inspirals.  
In *Journal of Physics: Conference Series*, Volume 610, pp. 12002–12018. IOP Publishing.
- Apostolatos, T. A. 1996.  
A spinning test body in the strong field of a schwarzschild black hole.  
*Classical and Quantum Gravity* 13(5), 799.
- Arnowitt, R., S. Deser, and C. W. Misner 1962.  
Republication in 2008 of: The dynamics of general relativity.  
*General Relativity and Gravitation* 40, 1997–2027.
- Bach, V., E. H. Lieb, and J. P. Solovej 1994.  
Generalized hartree-fock theory and the hubbard model.  
*Journal of statistical physics* 76(1-2), 3–89.
- Bailey, I., and W. Israel 1975.  
Lagrangian dynamics of spinning particles and polarized media in general relativity.  
*Communications in Mathematical Physics* 42(1), 65–82.
- Bao, W., D. Jaksch, and P. A. Markowich 2003.  
Numerical solution of the gross-pitaevskii equation for bose-einstein condensation.  
*Journal of Computational Physics* 187(1), 318–342.
- Barankov, R., L. Levitov, and B. Spivak 2004.  
Collective rabi oscillations and solitons in a time-dependent bcs pairing problem.  
*Physical review letters* 93(16), 160401.
- Barausse, E., and A. Buonanno 2010.  
Improved effective-one-body hamiltonian for spinning black-hole binaries.  
*Physical Review D* 81(8), 084024.
- Barausse, E., E. Racine, and A. Buonanno 2009.  
Hamiltonian of a spinning test particle in curved spacetime.  
*Phys. Rev. D* 80, 104025.

- Bardeen, J., L. N. Cooper, and J. R. Schrieffer 1957.  
Theory of superconductivity.  
*Physical Review* 108(5), 1175.
- Bini, D., and A. Geralico 2014.  
Deviation of quadrupolar bodies from geodesic motion in a kerr spacetime.  
*Physical Review D* 89(4), 044013.
- Blanchet, L. 2002.  
Gravitational Radiation from Post-Newtonian Sources and Inspiralling Compact Binaries.  
*Living Reviews in Relativity* 5, 3.
- Blanchet, L. 2006.  
Gravitational radiation from post-newtonian sources and inspiralling compact binaries.  
*Living Reviews in Relativity* 9, 4.
- Blanes, S., F. Casas, and A. Murua 2006.  
Symplectic splitting operator methods for the time-dependent schrödinger equation.  
*The Journal of chemical physics* 124(23), 234105.
- Bogoliubov, N. 1947.  
On the theory of superfluidity.  
*J. Phys* 11(1), 23.
- Buonanno, A., and T. Damour 1999.  
Effective one-body approach to general relativistic two-body dynamics.  
*Physical Review D* 59(8), 084006.
- Caliari, M., C. Neuhauser, and M. Thalhammer 2009.  
High-order time-splitting hermite and fourier spectral methods for the gross-pitaevskii equation.  
*J. Comput. Phys* 228(3), 822–832.
- Contopoulos, G. 2002.  
*Order and chaos in dynamical astronomy*.  
Springer Science & Business Media.
- Corinaldesi, E., and A. Papapetrou 1951.  
Spinning test-particles in general relativity. ii.  
*Proceedings of the Royal Society A* 209, 259–268.
- Costa, L. F., C. Herdeiro, J. Natário, and M. Zilhao 2012.  
Mathisson’s helical motions for a spinning particle: Are they unphysical?  
*Physical Review D* 85(2), 024001.
- Cyrot, M. 1973.  
Ginzburg-landau theory for superconductors.  
*Reports on Progress in Physics* 36(2), 103.
- Damour, T. 2008.  
Introductory lectures on the effective one body formalism.  
*International Journal of Modern Physics A* 23(08), 1130–1148.

- 
- Damour, T., P. Jaranowski, and G. Schaefers 2000.  
Determination of the last stable orbit for circular general relativistic binaries at the third post-newtonian approximation.  
*Physical Review D* 62(8), 084011.
- De Gennes, P.-G. 1966.  
*Superconductivity of metals and alloys*, Volume 86.  
WA Benjamin New York.
- De Melo, C. S., M. Randeria, and J. R. Engelbrecht 1993.  
Crossover from bcs to bose superconductivity: Transition temperature and time-dependent ginzburg-landau theory.  
*Physical review letters* 71(19), 3202.
- Dirac, P. A. M. 1951.  
*Lectures on Quantum Mechanics*.  
Canadian Journal of Mathematics.
- Dixon, W. 1964.  
A covariant multipole formalism for extended test bodies in general relativity.  
*Il Nuovo Cimento* 34(2), 317–339.
- Dixon, W. G. 1970.  
Dynamics of extended bodies in general relativity. i. momentum and angular momentum.  
*Proceedings of the Royal Society of London. A. Mathematical and Physical Sciences* 314(1519), 499–527.
- Einstein, A. 1915.  
Die Feldgleichungen der Gravitation.  
*Sitzungsberichte der Königlich Preußischen Akademie der Wissenschaften (Berlin)*, Seite 844-847., 844–847.
- Einstein, A. 1916.  
Näherungsweise integration der feldgleichungen der gravitation.  
*Sitzungsberichte der Königlich Preußischen Akademie der Wissenschaften (Berlin)*, Seite 688-696. 1, 688–696.
- Feit, M., J. Fleck, and A. Steiger 1982.  
Solution of the schrödinger equation by a spectral method.  
*Journal of Computational Physics* 47(3), 412–433.
- Flannery, B., W. Press, S. Teukolsky, and W. Vetterling 1992.  
*Numerical Recipes in C. The art of scientific computing (2 ed.)*.  
Cambridge: Cambridge University Press.
- Frank, R., C. Hainzl, R. Seiringer, and J. Solovej 2012.  
Microscopic derivation of ginzburg-landau theory.  
*Journal of the American Mathematical Society* 25(3), 667–713.
- Frank, R. L., C. Hainzl, B. Schlein, and R. Seiringer 2015.  
Time-dependent bogolubov–de-gennes equations and non-validity of ginzburg–landau theory.  
*arXiv preprint arXiv:1504.05885*.

- Frank, R. L., C. Hainzl, R. Seiringer, and J. P. Solovej 2013.  
Derivation of ginzburg-landau theory for a one-dimensional system with contact interaction.  
In *Operator Methods in Mathematical Physics*, pp. 57–88. Springer.
- Gauckler, L. 2011.  
Convergence of a split-step hermite method for the gross–pitaevskii equation.  
*IMA Journal of Numerical Analysis* 31(2), 396–415.
- Gauckler, L., and C. Lubich 2010.  
Splitting integrators for nonlinear schrödinger equations over long times.  
*Foundations of Computational Mathematics* 10(3), 275–302.
- Giazotto, A. 1992.  
Wide-band measurement of gravitational waves: thevirgo project.  
*Il Nuovo Cimento C* 15(6), 955–971.
- Golub, G., and W. Kahan 1965.  
Calculating the singular values and pseudo-inverse of a matrix.  
*Journal of the Society for Industrial & Applied Mathematics, Series B: Numerical Analysis* 2(2), 205–224.
- Gorkov, L., and G. Eliashberg 1968.  
Generalization of the ginzburg-landau equations for non-stationary problems in the case of alloys with paramagnetic impurities.  
*Soviet Journal of Experimental and Theoretical Physics* 27, 328.
- Gorkov, L. P. 1959.  
Microscopic derivation of the ginzburg-landau equations in the theory of superconductivity.  
*Sov. Phys. JETP* 9(6), 1364–1367.
- Gray, S. K., and D. E. Manolopoulos 1996.  
Symplectic integrators tailored to the time-dependent schrödinger equation.  
*The Journal of chemical physics* 104(18), 7099–7112.
- Gualtierie, L., and V. Ferrari 2011.  
Lecture notes for a graduate course on black holes in general relativity.
- Hackmann, E., C. Lämmerzahl, Y. N. Obukhov, D. Puetzfeld, and I. Schaffer 2014.  
Motion of spinning test bodies in kerr spacetime.  
*Physical Review D* 90(6), 064035.
- Hainzl, C., E. Hamza, R. Seiringer, and J. P. Solovej 2008.  
The bcs functional for general pair interactions.  
*Communications in Mathematical Physics* 281(2), 349–367.
- Hainzl, C., E. Lenzmann, M. Lewin, and B. Schlein 2010.  
On blowup for time-dependent generalized hartree–fock equations.  
In *Annales Henri Poincaré*, Volume 11, pp. 1023–1052. Springer.
- Hainzl, C., and B. Schlein 2013.  
Dynamics of bose–einstein condensates of fermion pairs in the low density limit of bcs theory.  
*Journal of Functional Analysis* 265(3), 399–423.

- 
- Hainzl, C., and R. Seiringer 2012.  
Low density limit of bcs theory and bose–einstein condensation of fermion pairs.  
*Letters in Mathematical Physics* 100(2), 119–138.
- Hainzl, C., and J. Seyrigh 2016.  
Comparing the full time-dependent bogoliubov-de-gennes equations to their linear approximation: a numerical investigation.  
*The European Physical Journal B* 89(5), 1–10.
- Hairer, E., C. Lubich, and G. Wanner 2006.  
*Geometric Numerical Integration: Structure-Preserving Algorithms for Ordinary Differential Equations (2 ed.)*.  
Berlin: Springer Verlag.
- Hairer, E., S. P. Nørsett, and G. Wanner 1993.  
*Solving Ordinary Differential Equations I (2 ed.)*.  
Berlin: Springer Verlag.
- Hartl, M. D. 2003a.  
Dynamics of spinning test particles in kerr spacetime.  
*Physical Review D* 67(2), 024005.
- Hartl, M. D. 2003b.  
Survey of spinning test particle orbits in kerr spacetime.  
*Physical Review D* 67(10), 104023.
- Hinderer, T., A. Buonanno, A. H. Mroué, D. A. Hemberger, G. Lovelace, H. P. Pfeiffer, L. E. Kidder, M. A. Scheel, B. Szilagyi, N. W. Taylor, et al. 2013.  
Periastron advance in spinning black hole binaries: comparing effective-one-body and numerical relativity.  
*Physical Review D* 88(8), 084005.
- Hochbruck, M., and C. Lubich 1997.  
On krylov subspace approximations to the matrix exponential operator.  
*SIAM Journal on Numerical Analysis* 34(5), 1911–1925.
- Hochbruck, M., and C. Lubich 2003.  
On magnus integrators for time-dependent schrödinger equations.  
*SIAM Journal on Numerical Analysis* 41(3), 945–963.
- Hulse, R. A., and J. H. Taylor 1975.  
Discovery of a pulsar in a binary system.  
*The Astrophysical Journal* **195**, L51–L53.
- Katsanikas, M., and P. A. Patsis 2011.  
The Structure of Invariant Tori in a 3d Galactic Potential.  
*International Journal of Bifurcation and Chaos* **21**, 467.
- Kerr, R. P., and A. Schild 1963.  
Republication in 2009 of: A new class of vacuum solutions of the Einstein field equations.  
*General Relativity and Gravitation* **41**, 2485–2499.
-

- Kuroda, K., L. collaboration, et al. 2010.  
Status of lqgt.  
*Classical and Quantum Gravity* 27(8), 084004.
- Kyrian, K., and O. Semerák 2007.  
Spinning test particles in a kerr field–ii.  
*Monthly Notices of the Royal Astronomical Society* 382(4), 1922–1932.
- Landau, L. D. 1937.  
On the theory of phase transitions. i.  
*Zh. Eksp. Teor. Fiz.* 11, 19.
- Landau, L. D., and V. Ginzburg 1950.  
On the theory of superconductivity.  
*Zh. Eksp. Teor. Fiz.* 20, 1064.
- Leggett, A. 1980.  
Diatomic molecules and cooper pairs.  
In A. Pełalski and J. Przystawa (Eds.), *Modern Trends in the Theory of Condensed Matter*, Volume 115 of *Lecture Notes in Physics*, pp. 13–27. Springer Berlin Heidelberg.
- Lewin, M., and S. Paul 2014.  
A numerical perspective on hartree- fock- bogoliubov theory.  
*ESAIM: Mathematical Modelling and Numerical Analysis* 48(01), 53–86.
- London, F., and H. London 1935.  
Supraleitung und diamagnetismus.  
*Physica* 2(1), 341–354.
- Lubich, C. 2004.  
A variational splitting integrator for quantum molecular dynamics.  
*Applied numerical mathematics* 48(3), 355–368.
- Lubich, C. 2005.  
On variational approximations in quantum molecular dynamics.  
*Mathematics of computation* 74(250), 765–779.
- Lubich, C. 2008.  
*From quantum to classical molecular dynamics: reduced models and numerical analysis*.  
European Mathematical Society.
- Lück, H., G. Team, et al. 1997.  
The geo600 project.  
*Classical and quantum gravity* 14(6), 1471.
- Lukes-Gerakopoulos, G. 2014.  
Adjusting chaotic indicators to curved spacetimes.  
*Physical Review D* 89(4), 043002.
- Lukes-Gerakopoulos, G., J. Seyrich, and D. Kunst 2014.  
Investigating spinning test particles: Spin supplementary conditions and the hamiltonian formalism.  
*Physical Review D* 90(10), 104019.

- 
- Marchuk, G. I. 1968.  
Some application of splitting-up methods to the solution of mathematical physics problems.  
*Aplikace Matematiky* 13(2), 103–132.
- Marsden, J. E., and M. West 2001.  
Discrete mechanics and variational integrators.  
*Acta Numerica 2001* 10, 357–514.
- Mathisson, M. 1937.  
Republication in 2010 of: New mechanics of material systems.  
*General Relativity and Gravitation* 42(4), 1011–1048.
- Mei, L., M. Ju, X. Wu, and S. Liu 2013.  
Dynamics of spin effects of compact binaries.  
*Royal Astronomical Society, Monthly Notices* 435, 2246–2255.
- Meissner, W., and R. Ochsenfeld 1933.  
Ein neuer effekt bei eintritt der supraleitfähigkeit.  
*Naturwissenschaften* 21(44), 787–788.
- Mino, Y., M. Shibata, and T. Tanaka 1996.  
Gravitational waves induced by a spinning particle falling into a rotating black hole.  
*Physical Review D* 53(2), 622.
- Møller, C. 1949.  
Sur la dynamique des systemes ayant un moment angulaire interne.  
In *Annales de l'institut Henri Poincaré*, Volume 11, pp. 251–278. Presses universitaires de France.
- Newton, T. D., and E. Wigner 1949.  
Localized states for elementary systems.  
*Reviews of Modern Physics* 21(3), 400.
- Nozieres, P., and S. Schmitt-Rink 1985.  
Bose condensation in an attractive fermion gas: From weak to strong coupling superconductivity.  
*Journal of Low Temperature Physics* 59(3-4), 195–211.
- Onnes, H. K. 1911.  
The resistance of pure mercury at helium temperatures.  
*Commun. Phys. Lab. Univ. Leiden* 12(120), 1.
- Papapetrou, A. 1951.  
Spinning test-particles in general relativity. i.  
In *Proceedings of the Royal Society of London A: Mathematical, Physical and Engineering Sciences*, Volume 209, pp. 248–258. The Royal Society.
- Park, T. J., and J. Light 1986.  
Unitary quantum time evolution by iterative lanczos reduction.  
*The Journal of chemical physics* 85(10), 5870–5876.
-

Pirani, F. 1956.

On the physical significance of the riemann tensor.  
*Acta Physica Polonica* **15**, 389–405.

Plyatsko, R., and M. Fenyk 2012.

Highly relativistic spinning particle in the schwarzschild field: Circular and other orbits.  
*Physical Review D* **85**(10), 104023.

Plyatsko, R., and M. Fenyk 2013.

Highly relativistic circular orbits of spinning particle in the kerr field.  
*Physical Review D* **87**(4), 044019.

Porto, R. A. 2006.

Post-newtonian corrections to the motion of spinning bodies in nonrelativistic general relativity.  
*Physical Review D* **73**(10), 104031.

Ramírez, W. G., A. A. Deriglazov, and A. M. Pupasov-Maksimov 2014.

Frenkel electron and a spinning body in a curved background.  
*Journal of High Energy Physics* **2014**(3), 1–19.

Randeria, M. 1995.

*Bose-Einstein Condensation*, Volume 355.  
Cambridge University Press Cambridge.

Riles, K. 2013.

Searches for continuous gravitational waves with the LIGO and Virgo detector.  
In J. van Leeuwen (Ed.), *IAU Symposium*, Volume 291 of *IAU Symposium*, pp. 477–479.

Rüdiger, R. 1981.

Conserved quantities of spinning test particles in general relativity. i.  
*Proceedings of the Royal Society of London. Series A, Mathematical and Physical Sciences*,  
185–193.

Schmid, A. 1966.

A time dependent ginzburg-landau equation and its application to the problem of resistivity in the mixed state.  
*Physik der kondensierten Materie* **5**(4), 302–317.

Schwarzschild, K. 1916.

On the Gravitational Field of a Mass Point According to Einstein's Theory.  
*Abh. Königl. Preuß. Akad. Wissenschaften Jahre 1906,92, Berlin,1907*, 189–196.

Semerák, O. 1999.

Spinning test particles in a kerr field—i.  
*Monthly Notices of the Royal Astronomical Society* **308**(3), 863–875.

Semerák, O., and M. Šrámek 2015.

Spinning particles in vacuum space-times of different curvature types—i.  
*arXiv preprint arXiv:1505.01069*.

- 
- Seyrich, J. 2012.  
Numerical Long-Time Analysis of Compact Binary Systems.  
Diploma thesis, Eberhard Karls Universität Tübingen.
- Seyrich, J. 2013.  
Gauss collocation methods for efficient structure preserving integration of post-newtonian equations of motion.  
*Physical Review D* 87(8), 084064.
- Seyrich, J., and G. Lukes-Gerakopoulos 2012.  
Symmetric integrator for nonintegrable hamiltonian relativistic systems.  
*Physical Review D* 86(12), 124013.
- Steinhoff, J. 2011.  
Canonical formulation of spin in general relativity.  
*Annalen der Physik* 523(4), 296–353.
- Steinhoff, J., and D. Puetzfeld 2012.  
Influence of internal structure on the motion of test bodies in extreme mass ratio situations.  
*Physical Review D* 86(4), 044033.
- Steinhoff, J., G. Schäfer, and S. Hergt 2008.  
Adm canonical formalism for gravitating spinning objects.  
*Physical Review D* 77(10), 104018.
- Stephen, M., and H. Suhl 1964.  
Weak time dependence in pure superconductors.  
*Physical Review Letters* 13(26), 797.
- Strang, G. 1968.  
On the construction and comparison of difference schemes.  
*SIAM Journal on Numerical Analysis* 5(3), 506–517.
- Suzuki, M. 1990.  
Fractal decomposition of exponential operators with applications to many-body theories and monte carlo simulations.  
*Physics Letters A* 146(6), 319–323.
- Suzuki, S., and K.-i. Maeda 1997.  
Chaos in schwarzschild spacetime: The motion of a spinning particle.  
*Physical Review D* 55(8), 4848.
- Tal-Ezer, H., and R. Kosloff 1984.  
An accurate and efficient scheme for propagating the time dependent schrödinger equation.  
*The Journal of chemical physics* 81(9), 3967–3971.
- Tang, Y.-F., L. Vázquez, F. Zhang, and V. Pérez-García 1996.  
Symplectic methods for the nonlinear schrödinger equation.  
*Computers & Mathematics with Applications* 32(5), 73–83.
- Tauber, G. E. 1988.  
Canonical formalism and equations of motion for a spinning particle in general relativity.  
*International journal of theoretical physics* 27(3), 335–344.
-

- Tulczyjew, W. 1959.  
Motion of multipole particles in general relativity theory.  
*Acta Phys. Pol* **18**, 393.
- Verhaaren, C., and E. W. Hirschmann 2010.  
Chaotic orbits for spinning particles in schwarzschild spacetime.  
*Physical Review D* *81*(12), 124034.
- Volkov, A., and S. M. Kogan 1974.  
Collisionless relaxation of the energy gap in superconductors.  
*Soviet Journal of Experimental and Theoretical Physics* **38**, 1018.
- Walther, B., B. Brüggemann, and D. Müller 2009.  
Numerical black hole initial data with low eccentricity based on post-newtonian orbital parameters.  
*Physical Review D* *79*(12), 124040.
- Westpfahl, K. 1969.  
Relativistische bewegungsprobleme. vi rotator-spinteilchen und allgemeine relativitätstheorie.  
*Annalen der Physik* *477*(7-8), 361–371.
- Wu, X., T.-Y. Huang, and H. Zhang 2006.  
Lyapunov indices with two nearby trajectories in a curved spacetime.  
*Physical Review D* *74*(8), 083001.
- Wu, X., and Y. Xie 2010.  
Symplectic structure of post-newtonian hamiltonian for spinning compact binaries.  
*Phys. Rev. D* **81**, 084045.
- Yang, K.-H., and J. O. Hirschfelder 1980.  
Generalizations of classical poisson brackets to include spin.  
*Physical Review A* *22*(5), 1814.
- Yoshida, H. 1990.  
Construction of higher order symplectic integrators.  
*Physics Letters A* *150*(5), 262–268.
- Yuzbashyan, E. A., O. Tsyplatyev, and B. L. Altshuler 2006.  
Relaxation and persistent oscillations of the order parameter in fermionic condensates.  
*Physical review letters* *96*(9), 097005.
- Zhong, S.-Y., X. Wu, S.-Q. Liu, and X.-F. Deng 2010.  
Global symplectic structure-preserving integrators for spinning compact binaries.  
*Physical Review D* *82*(12), 124040.

# List of Figures

1.1.	Sketch of the resistance $R$ as a function of the temperature $T$ for superconducting materials. . . . .	20
3.1.	Illustration of a Poincaré section for an integrable orbit (left panel) and a chaotic orbit (right panel). Courtesy of Seyrich (2012). . . . .	44
3.2.	The relative error of the Hamiltonian, $\Delta H_{\text{section}}$ , calculated for the phase space points of the sections of Fig. B.3. . . . .	45
A.1.	The left panel shows a MP orbit with T SSC (black dots) and a MP orbit with NW SSC (gray dots) in the configuration space $x, y, z$ (Cartesian coordinates). The common parameters for these orbits are $a = 0.5$ , $r = 11.7$ , $\theta = \pi/2$ , $p^r = 0.1$ , $S = 1$ , $S^r = 0.1 S$ , $S^\theta = 0.01 S$ , $E = 0.97$ , $J_z = 3$ , and $\mu = 1$ . The central panel shows the logarithm of the Euclidean distance in the configuration space between these two orbits as a function of the proper time. The right panel shows the logarithm of the difference $\Delta S_{4 \times 4}$ between the spin tensors of these two orbits as a function of the proper time. . . . .	74
A.2.	The left panel shows the logarithm of the Euclidean distance in the configuration space between a MP orbit with T SSC and a MP orbit with NW SSC as a function of the proper time. The common parameters for these orbits read $a = 0.5$ , $r = 11.7$ , $\theta = \pi/2$ , $p^r = 0.1$ , $S = 10^{-8}$ , $S^r = 0.1 S$ , $S^\theta = 0.01 S$ , $E = 0.97$ , $J_z = 3$ , and $\mu = 1$ . The right panel shows the logarithm of the difference $\Delta S_{4 \times 4}$ between the spin tensors of these two orbits as a function of the proper time. . . . .	75
A.3.	The top row of panels corresponds to the orbits of Fig. A.1, while the bottom row of panels corresponds to the orbits of Fig. A.2. The black lines represent the evolution of the MP equations with T SSC, while the gray lines represent the NW SSC. The left column of panels shows the relative error in the preservation of the four-momentum, while the right depicts the preservation of the spin. . . . .	76
A.4.	The relative error of the four-momentum $\Delta \mu^2$ as a function of the spin measure $S$ for the NW SSC. The black dots correspond to the maximum values of $\Delta \mu^2$ during the evolution for each $S$ . The dashed line is a linear fit of the form $\log_{10} \Delta \mu^2 = a \log_{10} S + b$ for data with $S > 10^{-6}$ , where $a = 1.995 \pm 0.004$ , $b = -4.136 \pm 0.013$ . . . . .	77
A.5.	The left panel shows how the orbit evolves through the MP equations (gray dots) and through the Hamilton's equations (black dots) in the configuration space $x, y, z$ , when we use the initial conditions given in Fig. A.1. The central panel shows the logarithm of the Euclidean distance in the configuration space between these two orbits as a function of the coordinate time. The right panel shows the logarithm of the Euclidean norm of the difference between the spin vectors of these two orbits as a function of the coordinate time. . . . .	78
A.6.	The left panel shows the logarithm of the Euclidean distance in the configuration space between an orbit calculated with the MP equations and an orbit calculated with the Hamilton equations as a function of the coordinate time. For the orbits we have used the initial conditions given in Fig. A.2. The right panel shows the logarithm of the Euclidean norm of the difference between the spin vectors of these two orbits as a function of the coordinate time. . . . .	80

<p>A.7. The top row of panels corresponds to the orbits of Fig. A.5, while the bottom row of panels corresponds to the orbits of Fig. A.6. The middle row of panels corresponds to initial conditions similar to Fig. A.1 only instead of spin measure <math>S = 1</math> we set <math>S = 10^{-4}</math>. The gray lines represent the evolution of the MP equations, while the black lines represent the evolution of the Hamilton equations. The left column of panels shows the relative error in the preservation of the Hamiltonian function, while the right shows the preservation of the spin. . . .</p>	81
<p>A.8. The left panel shows the relative error of the Hamiltonian <math>\Delta H</math> of orbits evolved through the MP equations for different spin measures <math>S</math> of the particle, while the right panel shows the corresponding preservations of the measure of the 3-vector <math>\Delta S^2</math>. The black dots correspond to the maximum values of <math>\Delta H</math>, <math>\Delta S^2</math>, respectively, for each <math>S</math>. The dashed lines are linear fits of the form <math>\log_{10} \Delta H = a \log_{10} S + b</math>, and <math>\log_{10} \Delta S^2 = c \log_{10} S + d</math>, respectively, for data with <math>S &gt; 10^{-6}</math>, where <math>a = 1.9968 \pm 0.0015</math>, <math>b = -2.644 \pm 0.004</math>, and <math>c = 1.031 \pm 0.015</math>, <math>d = -2.46 \pm 0.06</math>. . . . .</p>	82
<p>A.9. The relative error of the <math>z</math> angular momentum, <math>\Delta J_z</math>, (top panel) and the relative error of the energy, <math>\Delta E</math>, (bottom panel) against integration time <math>\tau</math> for the 4-stage Gauss scheme with step size <math>h = 1</math> and the 5-th order Cash-Karp scheme with step size <math>h = 0.1</math> applied to the initial value problem (A.55) with initial data as stated in the text. CPU-time was 214.1s for the Gauss Runge-Kutta scheme and 422.7s for the Cash-Karp scheme. . . . .</p>	86
<p>A.10. The relative error of the Hamiltonian, <math>\Delta H</math> against integration time <math>t</math> for the 4-stage Gauss scheme with step size <math>h = 2</math> and the 5-th order Cash-Karp scheme with step size <math>h = 0.2</math> applied to the initial value problem (A.90) with initial data as stated in the text. CPU-time was 7.83s for the Gauss Runge-Kutta scheme and 24,7s for the Cash-Karp scheme. . . . .</p>	89
<p>A.11. The relative difference, <math>\Delta r</math>, between the radial distance calculated with the interpolation method and the radial distance calculated via the cumbersome method with extra integration steps plotted against output time <math>t</math>. . . . .</p>	90
<p>B.1. The left panel shows the relative error of <math>\Delta J_x</math>, and the right of <math>\Delta J_y</math> as a function of time in logarithmic scale for the Schwarzschild background. The gray lines show the relative error of these quantities when the system is evolved using the Hamiltonian function corresponding to the tetrad (B.30), while the black lines show the relative error of these quantities when the system is evolved using the respective MP equations. Both evolutions share the same initial conditions conditions, where <math>a = 0</math>, <math>M = m = 1</math>, and <math>S = 1</math>. . . . .</p>	99
<p>B.2. In the left panel is a detail from the surface of section <math>\theta = \pi/2</math>, <math>P_\theta &gt; 0</math>. The parameters of the orbits are <math>H = 0.95</math>, <math>J_z = P_\phi = 3</math>, <math>S = M = m = 1</math>, <math>a = 0</math>, the common initial conditions are <math>\phi = 0</math>, <math>P_r = 0</math>, <math>S_1 = S_2 = 0</math>, <math>S = S_3 = 10^{-2}</math>, while the initial <math>P_\theta</math> is defined numerically by the Hamiltonian function <math>H</math>. The right panel shows how the maximal value of the relativity error <math>\Delta J^2 =  1 - J^2(t)/J^2(0) </math> for evolution intervals <math>t = 10^3</math> scales with the spin measure <math>S</math>. . . . .</p>	101

---

B.3.	A detail from the surface of section $\theta = \pi/2$ , $P_\theta > 0$ . The parameters of the orbits are $H = 0.9449111825230683$ , $J_z = 3.5$ , $S = M = m = 1$ , $a = 0.1$ , the common initial conditions are $\phi = 0$ , $P_r = 0$ , $S_1 = 0$ , while by solving numerically the system $P_\theta = -S_2$ , $J_z = P_\phi + S_3$ , and $S = \sqrt{S_2^2 + S_3^2}$ we define the rest. . . . .	106
B.4.	The left panel shows the relative error of $J_x$ , and the right of $J_y$ as a function of time in logarithmic scale for the ZAMO tetrad in KS coordinates as evolved by the Hamiltonian with $a = 0$ , $M = m = 1$ , and $S = 1$ . . . . .	108
B.5.	The left panel shows the relative error of $J_x$ , and the right of $J_y$ as a function of time in logarithmic scale for the non-ZAMO tetrad in KS coordinates as evolved by the Hamiltonian with $a = 0$ , $M = m = 1$ , and $S = 1$ . . . . .	111
B.6.	The relative error of the Hamiltonian $\Delta H$ as function of the BL radius $r$ for two plunging orbits. The top plot shows the $\Delta H$ of a plunging orbit evolved by the Hamiltonian function discussed in section B.3.2 (BL), while the bottom plot shows the $\Delta H$ of a plunging orbit evolved by the Hamiltonian function discussed in section B.4.2 (KS). In both cases we used masses $M = m = 1$ and Kerr parameter $a = 0.9$ . For more about the initial conditions refer to the text. The horizon is depicted in both plots by a vertical dashed gray line. . . . .	114
C.1.	The gap $\Delta_0$ as a function of the semiclassical parameter $h$ in semilogarithmic scale. . . . .	123
C.2.	$1/h^2 \ \alpha_t\ _2^2$ as a function of integration time $t$ for $h = 1/4$ . The physical parameters are $T_c = 0.19$ and $\Delta_0 = 0.29$ . . . . .	123
C.3.	$\psi_t$ as a function of integration time $t$ for $h = 1/4$ . The physical parameters are $T_c = 0.19$ and $\Delta_0 = 0.29$ . . . . .	124
C.4.	$1/h^2 \ \alpha_t\ _2^2$ as a function of integration time $t$ for $h = 1/8$ . The physical parameters are $T_c = 0.19$ and $\Delta_0 = 0.16$ . . . . .	124
C.5.	$\psi_t$ as a function of integration time $t$ for $h = 1/8$ . The physical parameters are $T_c = 0.19$ and $\Delta_0 = 0.16$ . . . . .	125
C.6.	$1/h^2 \ \alpha_t\ _2^2$ as a function of integration time $t$ for $h = 1/16$ . The physical parameters are $T_c = 0.19$ and $\Delta_0 = 0.083$ . . . . .	125
C.7.	$\psi_t$ as a function of integration time $t$ for $h = 1/16$ . The physical parameters are $T_c = 0.19$ and $\Delta_0 = 0.083$ . . . . .	125
C.8.	Relative error $\Delta F_T$ of the discretized free energy against integration time $t$ in semilogarithmic scale for $h = 1/8$ . The physical parameters are $T_c = 0.19$ and $\Delta_0 = 0.16$ . . . . .	131
C.9.	Critical temperature $T_c$ as a function of the number of momenta per unit volume $M$ for $N = 8$ and $h = 1/4$ . . . . .	132
C.10.	$\psi_t$ as a function of integration time $t$ for $N = 4$ and $h = 1/8$ . The physical parameters are $T_c = 0.19$ and $\Delta_0 = 0.16$ . . . . .	132
D.1.	Sketch of the algorithm <code>calc_convolution</code> , which uses the FFT and its inverse to efficiently calculate the convolution between $\hat{a}$ and $\hat{V}$ . . . . .	140
D.2.	Sketch of our algorithm <code>BCSInt</code> which for a given initial value $\vec{\alpha}_0$ and a given step size $\tau$ approximates $\vec{\alpha}(N\tau) = \Phi_{N\tau, f}(\vec{\alpha}_0)$ . . . . .	142
D.3.	The left panel shows the algorithm which for a given value $\vec{\alpha}(n\tau)$ and a given time step $\tau$ calculates $\vec{\alpha}((n+1)\tau) = \Phi_{\tau, f_1}^{\text{num}}(\vec{\alpha}(n\tau))$ with the explicit midpoint rule. The right panel shows the algorithm which for a given value $\vec{\alpha}$ calculates $f_1(\vec{\alpha})$ . . . . .	142

---

D.4. Sketch of the algorithm which for given values  $\vec{\gamma}(0), \vec{\alpha}(0)$  and a given step size  $\tau$  calculates the solution  $\vec{\gamma}(\tau) = \Phi_{\tau,g}(\vec{\gamma}(0))$  to the initial value problem (D.48). 144

D.5. The left panel shows the algorithm which for a given value  $\vec{\alpha}(n\tau)$  and a given time step  $\tau$  calculates  $\vec{\alpha}((n+1)\tau) = \Phi_{\tau,h}^{\text{num}}(\vec{\alpha}(n\tau))$  with the explicit midpoint rule. The right panel shows the algorithm which for a given value  $\vec{\alpha}$  calculates  $h(\vec{\gamma}, \vec{\alpha})$ . . . . . 144

D.6. Sketch of the algorithm which for given values  $\vec{\gamma}(0), \vec{\alpha}(0)$  and a given step size  $\tau$  calculates the solution  $\vec{\alpha}(\tau) = \Phi_{\tau,h}(\vec{\alpha}(0))$  to the initial value problem (D.50) for the case of a contact interaction. . . . . 146

D.7. Sketch of our algorithm SplitBCS which for given initial values  $\vec{\gamma}(0), \vec{\alpha}(0)$  and a given step size  $\tau$  approximates  $(\vec{\gamma}(N\tau), \vec{\alpha}(N\tau))^T = \Phi_{N\tau,f}(\vec{\gamma}(0), \vec{\alpha}(0))$ . . . . . 147

D.8. The relative error  $\Delta F^K$  of the free energy as a function of integration time  $t$  for SplitBCS and BCSInt in semilogarithmic scale. The left panel shows the result for  $L = 32$ , the right panel depicts the corresponding result for  $L = 64$ . 149

D.9. The left panel shows some eigenvalues  $\lambda_k$  of the density matrix as a function of integration time  $t$  for SplitBCS applied to the system with  $L = 32$ . The right panel shows the corresponding relative error  $\Delta\lambda_0$  of the density matrix' first eigenvalue in semilogarithmic scale. . . . . 149

D.10. The relative error  $\Delta F^K$  of the free energy as a function of integration time  $t$  for SplitBCS and other possible compositions in semilogarithmic scale. The left panel shows the result for  $L = 32$ , the right panel depicts the corresponding result for  $L = 64$ . . . . . 150

D.11. The relative error  $\Delta F^K$  of the free energy as a function of integration time  $t$  for the explicit Cash–Karp scheme in semilogarithmic scale. The left panel shows the result for  $L = 32$ , the right panel depicts the corresponding result for  $L = 64$ . 150

## List of Tables

D.1. The required number of operations per step as a function of the dimension of the ODE system (D.34) for the sub-algorithms of BCSInt and for BCSInt itself. 142

D.2. The required number of operations per step as a function of the dimension of the ODE system (D.17),(D.18) for the sub-algorithms of SplitBCS and for SplitBCS itself. . . . . 147